The Dissertation Committee for Zhu-Lin Xie Certifies that this is the approved version of the following Dissertation:

Bio-inspired Iron Pincers: from [Fe]-hydrogenase Mimics to Hydrogen Activation Reactivity

Committee:

Michael J. Rose, Supervisor

Emily L. Que

Richard A. Jones

Michael J. Krische

Benjamin K. Keitz

Bio-inspired Iron Pincers: from [Fe]-hydrogenase Mimics to Hydrogen Activation Reactivity

by

Zhu-Lin Xie

Dissertation

Presented to the Faculty of the Graduate School of

The University of Texas at Austin

in Partial Fulfillment

of the Requirements

for the Degree of

Doctor of Philosophy

The University of Texas at Austin

May 2019

Dedication

To my family

and most importantly

to Him who covered me along this path

Acknowledgements

It is difficult for me to imagine the multitude of people who have helped me along this path and encouraged me in my pursuit of this dream. Time would fail me to mention the occasions I benefitted from my PhD advisor, Dr Michael J. Rose. It would be impossible for me to reach this goal without your dedicated guidance, encouragement and patience, inside or outside academia. I must thank you for being my incredible source of knowledge and teaching me how to be a scientist.

I would like to thank all my fellow group members — you guys created an encouraging, agreeable and supportive environment in the Rose group and made my PhD study an unforgettable journey with a lot of joy. Acknowledgement is deserved to Dr GDP for his mentorship and instruction when I first joined the Rose group. Thank you for your numerous helpful discussions and demonstrations. I am also grateful to Dr Feng Li for graciously sharing his expertise in organic synthesis with me as well as being my friend outside the lab who offered a lot of wonderful suggestions on living. To Dr Kuppu and Dr Seo, for their incredible discussions on my research and generously sharing chemicals with me. To Dylan, Doran and James, for their devoted assistance on ligand synthesis and tolerance for my "tough" leadership. Actually, they taught me how to be an advisor. To Chris, for being a caring "neighbor" and offering me ride after group meetings without charging me. To Patrick, for your sympathetic comforting words when I made an April-fool's-day prank and sharing your incredible music knowledge with me. To Spencer, for being a great companion along the journey and helping with my PhD study. With a special mention to Keren, Dr Cho, Dr Manes, Dr Pekarek, Dr Taylor, Joey,

Brenna, Sean, Jordan, Brittany, Anh, Clarisse, Eileen, Dan, Azim, Chase to name a few, It was fantastic to have the opportunity to work with you.

I would also like to thank the people who have also been incredible supportive in the chemistry department throughout this endeavor. To Vince, Ian, Kristin, Steve, Angela, Garrett and Betsy, for all your assistance with my graduate studies. Without you, it would be impossible for me to achieve this milestone.

To my friends, Gang, Junpeng, Yan, Weiran, Yawei, Jiajie, Wandi, Meng, Da, Hongyu, Shichao, you guys are amazing and have made my graduate life full of wonderful memories.

A very special gratitude goes out to my brothers and sisters in Christ, especially Pastor Chen and Ruth. Thank you for all your encouragement and inspiration, as well as every act of kindness and selflessness, which have motivated me to keep up and move forward.

I am grateful to my parents who have offered me steadfast support and sympathetic ear. You were always there for me no matter how I was and what challenge I was going through. Thank you for your unconditional love and persistent prayers.

Finally, I would like to thank someone who is very dear to me, an angel sent by God at the right time. To Pu, thank you so much for taking the brave step to embrace me even though that meant long term physical separation. However, I would like to say that oceans have never conquered the power of love and my heart has never been so close to you. Your words of comfort and strength have carried me though many challenging times, and I would not be able to make it without you. Thank you!

Zhulin Xie

Austin, May 6, 2019

Abstract

Bio-inspired Iron Pincers: from [Fe]-hydrogenase Mimics to Hydrogen Activation Reactivity

Zhu-Lin Xie, Ph.D.

The University of Texas at Austin, 2019

Supervisor: Michael J. Rose

The enzyme [Fe]-hydrogenase catalyzes the heterolytic cleavage of H_2 and hydride transfer to the substrate methenyl-tetrahydromethanopterin (methenyl-H_4MPT^+), a C_1 carrier during the methanogenic carbon dioxide (CO_2) reduction. This metalloenzyme (also called Hmd: H_2-forming H_4MPT dehydrogenase) plays an obligate role in the 'nickel-free' metabolism of CO_2 to methane ($CO_2 \rightarrow CH_4$) in the absence of bio-available nickel ([NiFe] hydrogenase) and is the only known biological example of H_2 activation by a mononuclear iron site. The active site of [Fe]-hydrogenase exhibits a distinctive array of non-proteinaceous ligands (except for Cys_{176}), including the *cis*-dicarbonyl, the bidentate pyridone-acyl unit that presents a unique (to biology) organometallic Fe–C bond, a cysteine thiolate, and a substrate binding site weakly occupied by H_2O in the resting state. Although computational studies of [Fe]-hydrogenase have shown that H_2 splitting is achieved by metal-ligand cooperation between iron and the pyridone-oxygen, there are few synthetic models that have sufficiently investigated this process.

In order to shed light on the mechanism of [Fe]-hydrogenase, we developed three families of models that mimic different aspects the enzyme active site. The first family consisted of carbamoyl thioether pincer complexes ($^{O=}C^{py}NS^{Me}$) wherein the carbamoyl group (-NH-$C^{=O}$-) mimics the acyl unit in the enzyme. The reactivities of the $^{O=}C^{py}NS^{Me}$ complexes with hydride sources and strong base were investigated. The H_2 activation reaction with the pentacoordinate $^{O=}C^{py}NS^{Me}$ complex revealed that the *fac-C, N, S* arrangement is a critical factor to reactivity with H_2. The second family was Schiff base $^{py}N^{C=}NS^{H}$ complexes, in which a variety of iron Schiff base thiol complexes were synthesized with the non-bulky thiolate ligands and bulky thiolate ligand. The thermal stability of the complexes and the role of anionic thiolate donors in stabilizing the *cis*-$Fe(CO)_2$ unit were investigated. The third family includes the carbamoyl phosphine pincer complexes ($^{O=}C^{py}NP^{R2}$), in which a phosphine donor was incorporated in place of the biomimetic sulfur donor. The phosphine donor is ideal for stabilizing Fe(II) carbonyl core, and promises the best path forward to a functional catalyst. The reactivity toward H_2 activation and catalytic efficacy of the carbamoyl Fe(II) phosphine complexes were investigated.

Table of Contents

List of Tables

List of Figures

List of Schemes

Chapter 1: Mononuclear Iron Complexes for (De)hydrogenation: an Overview of Iron Pincer Chemistry and the Synthetic Mimics for [Fe]-Hydrogenase

1.1 Introduction

Hydrogenation reactions broadly describes a class of reactions involving the addition of hydrogen, either in atomic form or in the form of a proton and hydride, to molecules, or the reverse reactions involving abstraction of hydrogen.[1–4] Hydrogenation reactions may be further categorized by hydrogen sources, wherein direct hydrogenation utilizes gaseous H_2 molecules and transfer hydrogenation utilizes organic hydrogen sources. These two fundamental reactions are intensively researched and widely applied in chemical industries, such as fine chemical synthesis and the pharmaceutical industry.[5]

In recent decades, the study of (de)hydrogenation has been further motivated due to its critical applications in the energy industry.[6] With multiple advantages over fossil fuels, such as zero-carbon emission and high specific energy, hydrogen is often called the energy of the future and is expected to be one of the renewable energy carriers to replace conventional fossil fuels.[7] However, the application of hydrogen energy is limited by the efficiency of hydrogen production and hydrogen storage.[8–11] Large attention has been devoted to the development of sustainable hydrogen production using dehydrogenation of organic molecules from biomass, or efficient hydrogen energy storage by (de)hydrogenation of small molecular carriers, including alcohols, metal borohydrides, amine-borane adducts, formic acid, hydrous hydrazine, metal hydrides, etc.[6] The practicality of these technologies relies on the choice of (de)hydrogenation strategy. It is notable that the area of homogeneous transition metal-catalyzed (de)hydrogenation has

undergone exciting developments and furnished valuable results, many of which have been applied in industry.

The first homogeneous transition metal-catalyzed hydrogenation was reported by Melvin Calvin in 1938.[7] This report showed that copper acetate catalyzed the reduction of 1,4-benzoquinone to 1,4-hydroquinone under 1 atm of H_2 and 100 °C. Later, in 1965, Wilkinson reported the hydrogenation of unactivated alkenes and alkynes catalyzed by [$RhCl(PPh_3)_3$], which is the well-known Wilkinson's catalyst.[12] For about 50 years, catalyst technology has witnessed explosive growth and many of the catalysts have been deployed widely in synthetic contexts. So far, existing catalysts mostly rely on noble transition metals, such as Pd, Rh, Ru, Pt, and Ir, which usually display efficient reactivity, high selectivity, ease of handling and apply to a broad scope of substrates.[13] However, the application of these catalysts is hindered by limited availability, high cost and sometimes toxicity of noble transition metals. During the past decade, with the increasing emphasis on environmental impact of chemical processes and development of sustainable chemistry, the focus of transition metal-catalyzed catalysis has switched to the use of first-row transition metals, which are abundant in the Earth's lithosphere, economical in practice and with reliable accessibility. Nonetheless, first-row transition metal catalysts are often inferior to the noble metal counterparts due to their narrow energy gap between d-orbitals, their propensity for one electron chemistry, and their kinetic lability in nature.[6] To overcome these obstacles, strategies such as rational ligand design, cooperative catalysis (e.g. ligand-metal cooperation) and manipulation of electronic structure of catalysts to suit certain reactivities have been employed, leading to an escalating number of first-row transition metal catalysts with high reactivity comparable to noble metal catalysts.[14] More interestingly, due to the unique properties of first-row transition metals,

new reactivities are enabled, which results in new frontiers in synthetic organometallic chemistry.

Among the impressive progress of first-row transition metal-catalyzed (de)hydrogenation, iron-catalyzed hydrogenation has experienced rapid advancement within the recent decade. While various types of homogeneous iron catalysts with different nuclearity (mono-Fe, di-Fe and multinuclear Fe)[15–17] have been developed and the reactivities have expanded to most major transformations[18] and functionalization[19] of molecules, it is amazing to note that mononuclear iron catalysis plays a major role in this field. Early in the 1960s, pioneering works about alkenes and alkynes hydrogenation were reported using $[Fe(CO)_5]$[20–23] and $Fe(acac)_3$[24]. However, these reactions often require harsh conditions and exhibit poor selectivity and narrow a scope of substrates.[25,26] Soon after that, the first iron-catalyzed transfer hydrogenation of alkenes and alkynes were reported, in which $[Fe(Br)_2(PPh_3)_2]$[27] and $[Fe(Cl)_2(PPh_3)_2]$[27,28] were used to reduce 1,5-cyclooctadiene (COD). Importantly, the use of dihydroxybenzene as a hydrogen source under harsh conditions (160-240 ℃) made the procedures less favorable in synthetic contexts. Followed by the pioneering works of Markó[29], the procedures of first iron-catalyzed hydrogenation of aldehydes and ketones were described in 1983. The reduction was carried out using 10 mol% of $[Fe(CO)_5]$ in the presence of tertiary amine at 150 ℃ under 100 bar of a mixture of H_2 and CO. It was proposed that the active species of the catalyst was likely $[HFe(CO)_4]^-$ and protonated amine. After about 40 years of development, studies of new synthetic methodologies of (de)hydrogenation using mononuclear iron catalysts has been fruitful; numerous examples of catalysts have been published, among which primarily includes pnictogen-containing bidentate-ligand catalysts[30,31], tridentate pincer-type catalysts[32,33], tripod-derived catalysts[34], tetradentate PNNP catalysts[35,36] and bifunctional piano-stool catalysts[37] (**Scheme 1.1**).

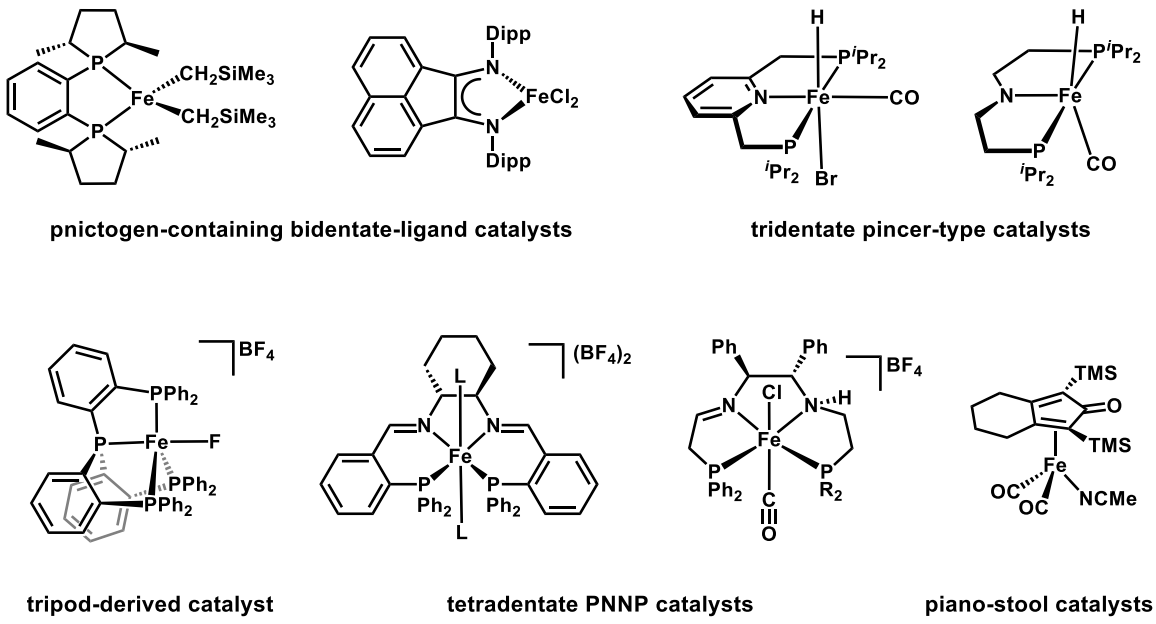

Scheme 1.1 Selective mononuclear iron catalysts for (de)hydrogenation reactions.

Interestingly, Nature has created a powerful toolbox with various biological catalysts — enzymes — to perform various chemical transformations relevant to humankind.[38] It is not surprising to realize that most of the metalloenzymes that catalyze hydrogen-related reactivities contain earth-abundant iron in the active centers.[16] For example, the nitrogenase active site which is specialized in the reduction of N_2 to ammonia is composed of a [Fe_7MoS_9C] cluster (**Scheme 1.2**).[39] The Carbon Monoxide Dehydrogenase/Acetyl CoA Synthase (CODH/ACS) is significant in the world carbon cycle by oxidizing CO to CO_2 and producing H_2 as a byproduct.[40,41] Although multimetallic, the CODH/ACS enzyme uses Fe as a key component which participates in the CODH reaction (**Scheme 1.2**). Most relevantly, hydrogenases are types of enzymes catalyzing the metabolism of H_2 molecules in biological systems.[42] These enzymes can

be classifieded into three types, namely, [FeNi]-, [FeFe]- and [Fe]-hydrogenases (**Scheme 1.2**). Among the hydrogenases, [Fe]-hydrogenase is the least studied so far and bears most important similarities with synthetic hydrogenation catalysts (not redox active). Therefore, keen interest in functional studies on the native enzyme or synthetic modelling has been witnessed recently.

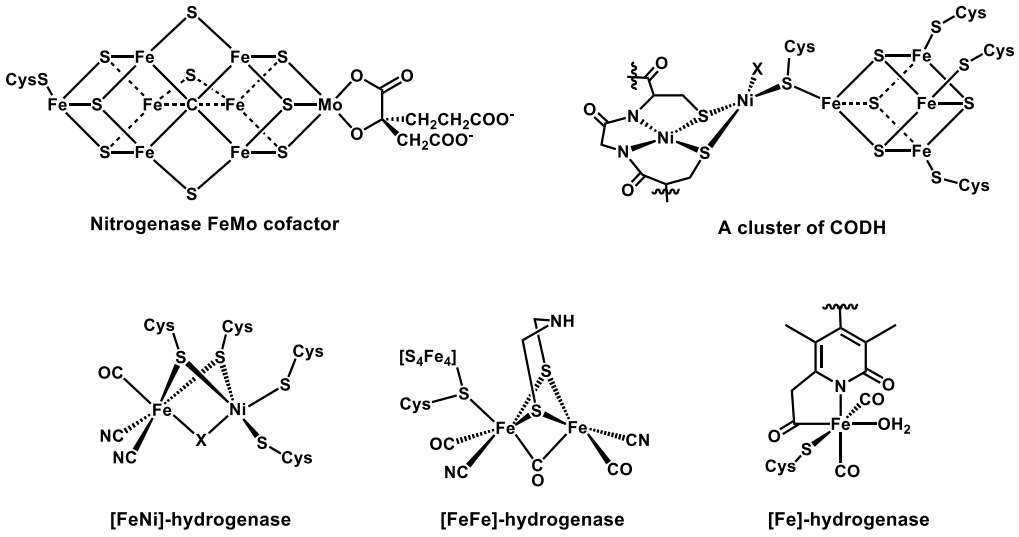

Scheme 1.2 Representative metalloenzymes that contain iron.

It is amazing to witness the on-going convergence of Nature and human society in catalysis, especially in hydrogenation. In addition to society's push towards bioavailable metals, there are common strategies that synthetic catalysts and Nature's metalloenzyes share, e.g. cooperative catalysis and resemblance in structure and ligand design.[43] However, there are also divergences between the biological enzyme systems and synthetic catalysts due to different supermolecular environments and the availability of elements. By improving the understanding of enzymatic catalysis and fundamental organometallic catalysis, it is promising that hydrogenation catalysis using iron will

progress at a faster pace in the near future, and more outstanding bio-inspired iron-based catalysts benefitting the academic and industrial spheres will be prepared.

In this chapter, the fundamental concepts of dihydrogen reactivity will first be described (section 1.2). These concepts include the theory of metal-H_2 interaction established by Kubas[44], fundamental principles of heterolytic cleavage of H_2 molecules which are pivotal for hydrogenation catalysis, and metal-ligand cooperation that has been utilized in both enzymatic activity and synthetic catalysis. In section 1.3, we will summarize some seminal works and recent progress of hydrogenation catalysis in organometallic chemistry catalyzed by mononuclear iron pincer complexes. The reactions covered will be (de)hydrogenation of olefins, carbonyls and C1 substrates (CO_2, formic acid and methanol). The aim of section 1.4 is to provide readers with a bioinorganic perspective on hydrogenase. We will discuss the structure and functionality of [Fe]-hydrogenase, the DFT studies of hydrogenase reactivity, and the synthetic modelling of [Fe]-hydrogenase. In this chapter, we hope to show the readers the convergences and divergences between enzymatic catalysis and organometallic (de)hydrogenation and lay the foundation for future directions.

1.2 THEORY, REACTIVITY OF H_2 ACTIVATION

1.2.1 Historical Background and Theoretical Aspects of Metal–H_2 Ligation

Numerous reviews about dihydrogen (H_2) complexes have been published.[9,44–49] In the early stage of transition metal-catalyzed hydrogenation studies, the H_2–M adduct was considered not observable and certainly not isolable under ambient conditions due to the perceived poor σ-donor ability of the H_2 molecule. It was difficult to envision that the smallest diatomic molecule H_2 which strongly holds two electrons between each other would be able to share electrons with metal centers. This bias continued partially because

many authentic dihydrogen complexes were usually transient such that they were never structurally observed at that time, despite some spectroscopic data of the putative hydride complexes occasionally yielding perplexing information that could not be rationalized by simple hydride models. For example, in 1971, Aresta[50] reported a "tetrahydride Fe(IV) complex $[Fe(H)_4(PEtPh_2)_3]$" with a mysterious IR band at 2380-2400 cm^{-1}, which ultimately was determined to emanate from the iron-bound H–H stretch, and the oxidation state of Fe was in fact +2. In another example described by Ashworth and Singleton[51] in 1976, "$[Ru(H)_4(PPh_3)_3]$" gave rise to a perplexing broad hydride resonance in NMR spectrum, accompanied by the detection of H_2 generation in experimental study. The authors even assumed a H–H bond in their complex. It was not until Kubas serendipitously isolated the first crystal structure of a tungsten dihydrogen complex which was structurally characterized to be the intact side-on dihydrogen complex $[W(CO)_3(P^iPr_3)_2(H_2)]$ (**1**) (**Scheme 1.3**)[52]. This begot a completely new era was ushered in. Later more and more dihydrogen complexes were discovered with various metal centers, and the side-on interaction of H_2 with metal prevails in most cases.

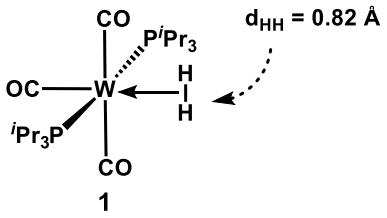

1

H-H bond distances corresponding to types of complexes

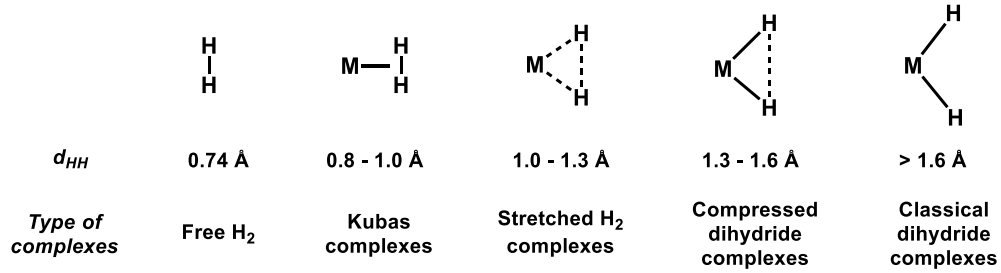

Scheme 1.3 Structure of $[W(CO)_3(P^iPr_3)_2(H_2)]$ (**1**) and the diagram of H–H distances corresponding to types of complexes.

The evidence of dihydrogen ligation rather than dihydride was confirmed by the slightly elongated H–H distance (0.82 Å) in **1**, compared to the free H–H distance (0.74 Å). As more examples of dihydrogen complexes were uncovered, Kubas was able to map out four types of complexes in the reaction coordinates of dihydrogen binding (**Scheme 1.3**).[44] The true H_2 complexes are usually termed 'Kubas complexes' with H–H bond distance less than 1.0 Å. In less common cases, a stretched H_2 complex would be observed with H–H distance in the range of 1.0-1.3 Å. Complexes with H–H distance between 1.3-1.6 Å are called compressed dihydride complexes, and classical dihydride complexes have a H–H distance larger than 1.6 Å. The continuum of d_{HH} clearly demonstrates the process of H_2 rupture. Nevertheless, the classification of dihydrogen complexes represents a continuum and varies depending on specific systems of complexation.

The stability of 'Kubas-type' complexes under ambient conditions indicates that the bonding interaction of H_2 with a metal ion should not be a classical Werner-type interaction where lone pair electrons on ligands are donated to empty orbitals of the metal center. The bonding of H_2 to metal is best described[44] as a combination of a σ bonding interaction in which the σ orbital of H_2 donates electron density to the empty d_{z2} orbital, and a π bonding orbital in which electron density in the metal d_{xz} orbital backdonates to the empty σ* orbital of H_2 (**Scheme 1.4**). The special bonding interaction is analogous to the Dewar-Chatt-Duncanson model[53,54] for M–ethylene complexes. The backdonation has a synergistic effect, by which the excess electron density on the metal can be relieved by the ligand and in turn stabilize the π acidic ligand, e.g. H_2, CO, N_2 etc. Indeed, the weakly Lewis basic H_2 molecule is insufficient to coordinate to metal center without the backdonation of the metal center.

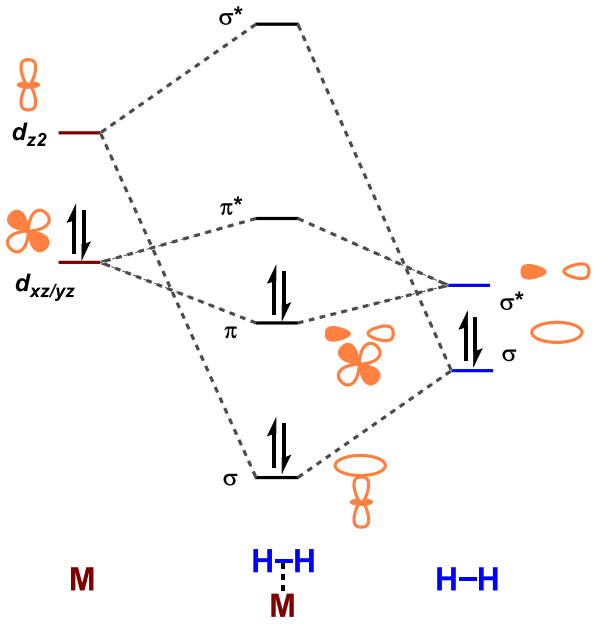

Scheme 1.4 Molecular orbital (MO) diagram of metal interacting with H_2 forming [M(H_2)] complex.

The d orbital configuration of the metal center affects the formation of dihydrogen complexes due to the importance of backdonation.[45] Metals that are not π basic enough, e.g. d^0 or high valent metals, usually cannot furnish stable H_2 complexes. Other configurations, such as d^2, d^4, and d^8, have been reported to generate isolable H_2 complexes. A majority number of dihydrogen complexations occur with octahedral d^6 metals because of their ideal geometry for backdonation and strong back donor capabilities.

Ligands tune the electronics of the metal center, which largely impacts the complexation of H_2, as well. As the electronic density on the metal center increases, backdonation to H_2 is improved and the H–H bond distance elongates. At the extreme, rupture of the H_2 molecule takes place. This is the reason why many catalysts showing H_2 reactivity contain strong field ligands, such as phosphines or carbenes. A good example demonstrating a ligand's effect on H_2 complexation is the complex $[Mo(CO)(R_2PC_2H_4PR_2)_2]$, in which the R groups on the phosphine donors control whether H_2 binds as an intact ligand or dihydride.[55] The less electron donating phosphine ligand with aromatic substituents (phenyl) favors H_2 ligation, whereas strong electron donors (R = Et and ^{i}Bu) produce the dihydride congeners.

A very special ligand effect often observed in dihydrogen complexes is *trans*-influence from ligands positioned *trans* to H_2. When strong π acceptors (or σ donors), e.g. CO and H^-, coordinate to the trans position of H_2, the H–H distance usually remains short (< 0.9 Å). The d orbital that participates in backdonation is shared by two π acidic ligands *trans* to each other, leading to weak backdonation to H_2 and short H–H distance, as in the case of **1**.[52] For weak σ donating and strong π donating trans-ligands, the H–H bond disctance is usually longer. One good example of this are the two isomers of $[Ir(Cl)_2(H)(H_2)(PR_3)_2]$ (**Scheme 1.5**).[56] The strong σ donor, H^-, is trans to H_2 in the *trans*-

$[Ir(Cl)_2(H)(H_2)(PR_3)_2]$ (**2**) isomer, which shows a H–H distance of 0.9 Å, but the weak σ-donor and good π-donor Cl^- is trans to H_2 in the *cis*-$[Ir(Cl)_2H(H_2)(PR_3)_2]$ (**3**) isomer, resulting in an elongated H_2 complex (d_{HH} = 1.11 Å).

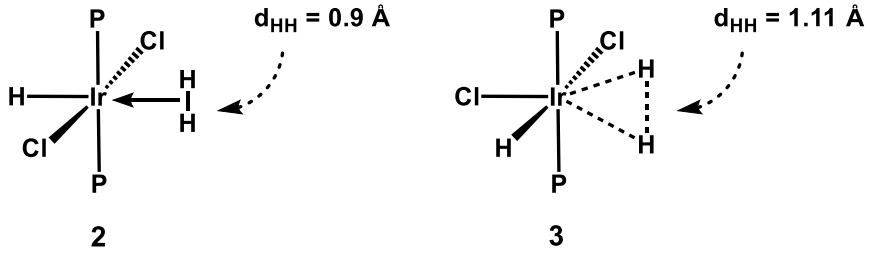

Scheme 1.5 Trans-influence on H–H distances in *trans/cis*-$[Ir(Cl)_2(H)(H_2)(PR_3)_2]$ (**2** and **3**).

Lastly, steric effects occasionally also play a role in protecting the binding site from being occupied by exogenous ligands, while still allowing H_2 binding due to its small steric profile. Another probable effect from steric crowding is proposed to be prevention of oxidative addition of H_2 because of the change of coordination geometry and coordination number after oxidative addition, however, there is no obvious example showing this effect.

1.2.2 H_2 Activation: Heterolytic Cleavage of H_2

The revelation of molecular orbital interaction in M–H_2 adducts provides fundamental principles for researchers to understand H_2 reactivity, i.e. how H_2 is activated and what controls the type of H_2 activation. There are two major types of H_2 activation: homolytic cleavage, where H_2 undergoes oxidative addition forming dihydride complexes, and heterolytic cleavage, where H_2 is split into a proton and hydride generating monohydride complexes.

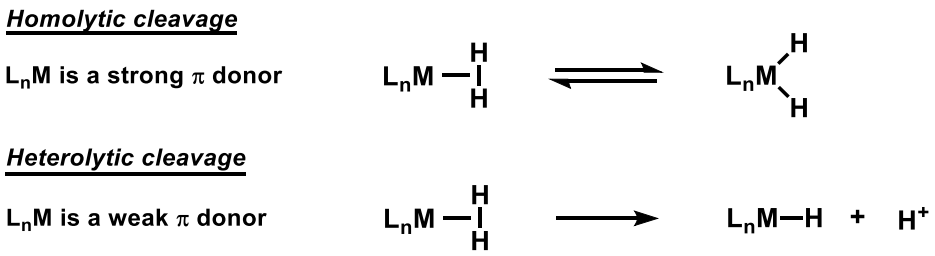

Scheme 1.6 Two types of H_2 activation

The type of H_2 activation is determined by the bonding interaction between M and H_2. When L_nM is a strong π donor, backdonation from the metal to H_2 dominates the interaction, resulting in elongation of the H–H bond. This is characteristic of 4d/5d transition metal centers in lower oxidation states, neutral complexes, or with strong ligand donor sets (e.g. phosphine). Strong π donor metal centers would promote homolytic cleavage of H_2 generating dihydride species. The fluxional behavior observed in the hydride dihydrogen complexes — in which tautomerization between H–H and hydride occurs — can also be attributed to strong backdonation.

On the other hand, when L_nM is a weak π donor, σ interaction between M and H_2 dominates and Kubas complexes are observed (d_{HH} < 1.0 Å). In this scenario, the metals are typically in higher oxidation states, contain 3d transition metals, in complexes with high cationic charge, or with strong π accepting ligand set (e.g. CO) and tend to facilitate heterolytic cleavage of H_2. Thus far, heterolytic cleavage of H_2 is more common in catalysis than homolytic cleavage of H_2.

The Dewar-Chatt-Duncanson model suggests that when σ donation is dominating and π backdonation is minimal, the H–H ligand carries net positive charge which leads to proton loss.[45] This is consistent with the fact that most of the catalysts are carbonyl complexes as CO ligand enhances σ interaction and diminishes π backdonation in M–H_2.

In addition, this explains why heterolytic cleavage of H_2 could still occur even if M–H_2 interaction is weak (d_{HH} is short).

To quantify the ease of heterolytic cleavage, the pK_a of the M–H_2 adduct is often measured. In contrast to the high pK_a of free H_2 (~50 in THF[57,58]), indicating very difficult deprotonation, the metal-bound H_2 exhibits a drastic decrease in pK_a value. Heinekey[59] reported the deprotonation of $[Cp^*Ru(CO)_2(H_2)]^+$ with a pK_a as low as –2, as result of the positive charge of the complex as well as the π accepting CO ligand. This complex is so acidic that it even protonates diethyl ether. Another example of trans-$[Ru(H_2)(H)(R_2PCH_2CH_2PR_2)_2]$ complexes reported by Morris[60] showed decreasing pK_a values (from 16 to 9) as R groups change from *p*-$MeOC_6H_4$ to *p*- $CF_3C_6H_4$. The increase of π accepting ability of phosphine ligand set improves the heterolytic H_2 activation.

1.2.3 Metal-Ligand Cooperation towards H_2 Activation

The heterolytic cleavage of H_2 requires a Lewis acidic site to accept the hydride anion as well as a Lewis/Brønsted basic atom to receive the proton cation. As H_2 binds to M, it can be cleaved by either metal centers and exogenous bases, or metal centers and basic atoms on the ligand backbone, commonly referred to as metal-ligand cooperation. The proton-accepting atom on the ligand backbone is called the pendant base, and are usually neutral amines, anionic oxygen atoms, or sulfur atoms. Due to the different catalytic properties of 3d transition metals compared with their heavier 4d/5d transition metals, 3d transition metal hydrogenation benefits substantially from metal-ligand cooperation. Presently, numerous (de)hydrogenation catalysts developed or metalloenzymes discovered utilize metal-ligand cooperation to facilitate catalysis.[16,43,61–66] While the debate about the definitions of terminologies about metal-ligand cooperation and metal-ligand bifunction is unsettled,[67–69] this chapter will use metal-ligand

cooperation to describe both cases, in which a basic atom actually accepts a proton from H_2 and a basic atom changes the electronic properties of metal centers without protonation. Metal-ligand cooperation has also been the topic of several reviews that provide more details.[16,43,61–66]

The greatest benefit of metal-ligand cooperation in catalysis is the attenuated kinetic penalty paid by catalytic systems in orienting substrate molecules with the active site during the transition state. The pre-organization of Lewis/Brønsted acids and bases within catalysts acts to mediate a reaction that is otherwise slow in kinetics. Therefore, positioning acids and bases in proximity with correct geometry is extremely important in designing catalysts with metal-ligand cooperation.

Nature provides numerous examples of implementing this strategy to perform various type of catalysis. [FeFe]-hydrogenase[42], found in anaerobic prokaryotes and in some anaerobic eukaryotes, fungi, ciliates, is functional for both H_2 generation and H_2 activation, with preference to catalyze the former reaction. The dimetallic center of [FeFe]-hydrogenase is coordinated to COs, CN^-s, and a unique azadithiolate (adt) bridging two Fe centers through two thiolate Fe–S bonds. The basic amine group in the bridging ligand has long been considered to participate in catalysis as a proton relay to facilitate H_2 production or activation. Reconstitution of synthetic models of [FeFe]-hydrogenase cofactor with the cofactor-free [FeFe]-hydrogenase apo-enzyme produced different reactivity from the native enzyme, depending on the dithiolate ligands used in the synthetic model.[70–73] Only the semisynthetic enzyme with azadithiolate bridge achieved the full recovery of reactivity, confirming the participation of the amine group in H_2 reacitivity.

Despite having one iron atom, [Fe]-hydrogenase presents exceptional activity towards H_2 splitting.[42] The key feature that contributes to the catalysis is the ligation of a

guanylylpyridinol ligand where the deprotonated form of pyridone-O atom functions as a proton acceptor in cooperation with the Fe center during the H_2 heterolysis. The pyridone-O is ideally directed towards the H_2 binding site, primed for receiving protons. The function of pyridone-O was supported by Shima and Hu in the reconstitution study of [Fe]-hydrogenase with small-molecule mimics.[74] H_2 reactivity was achieved by a reconstituted mimic containing a 2-hydroxypyridine group, whereas the semisynthetic enzyme with a 2-methoxypyridine complex was essentially inactive. DFT calculations performed on the 2-hydroxypyridne mimic discovered that the activation energy for H_2 splitting with the deprotonated $–O^-$ group was as low as 2 kJ/mol, in contrast to the high activation energy (39.6 kJ/mol) with the protonated –OH group. The accessible energy barrier is consistent with the facile heterolysis observed in the experimental study and further exemplifies the critical role of the basic pyridone-O atom in the catalysis.

Inspired by the metal-ligand cooperation in the biological system, biomimetic hydrogenation catalysts which employed ligand sets similar to those observed in biology were developed. Hu[75] developed a bioinspired catalyst (**4**) based on [Fe]-hydrogenase which contains an methoxypyridinylacyl ligand set and a bidentate diphosphine chelate with an internal nitrogen base (**Scheme 1.7**). Interestingly, the reactivity of the analogous complex with NH instead of NMe was first studied by DFT calculation[76] which shows an accessible energetic profile with low/moderate activation barriers for H_2 cleavage (3.5 kcal/mol) and hydride transfer (4-16 kcal/mol) to neutral hydride acceptors (aldehyde or iminiums). The experimental results for complex **4** displayed facile H/D scrambling in THF at room temperature under a mixture of H_2 and D_2 (8 bar and 18 bar, respectively), indicative of H_2 activation. Although no protonation of the internal nitrogen base was observed, the cooperative mechanism is highly feasible. Complex **4** can catalyze hydrogenation of *para*-fluorobenzaldehyde with high yields under 50 bar of H_2 gas.

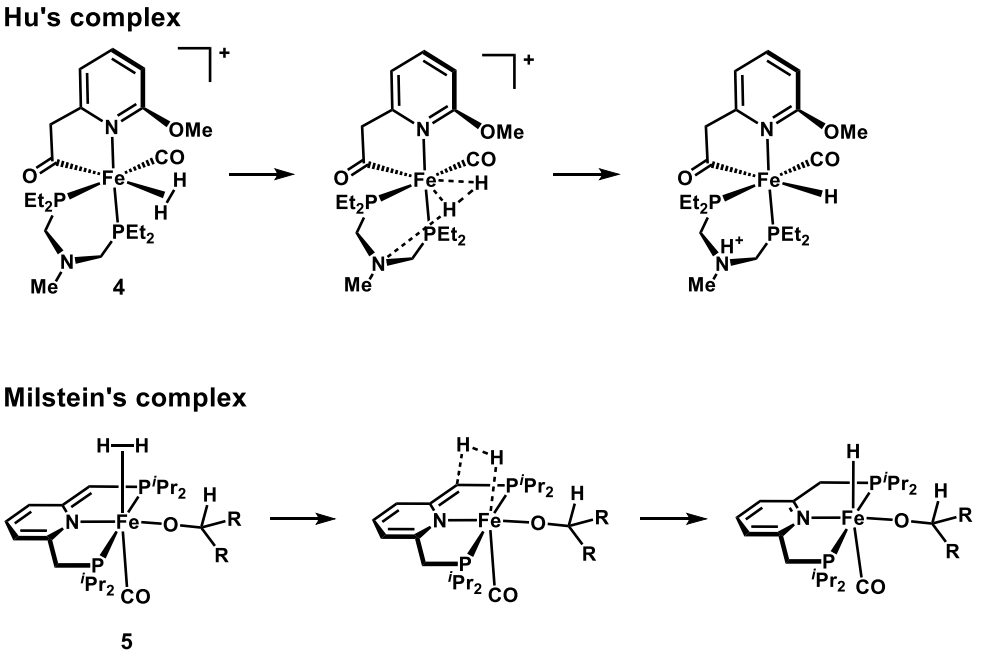

Scheme 1.7 Metal-ligand cooperation in bioinspired acylpyridine iron complex (**4**) and lutidine-based PNP pincer complex (**5**).

Metal-ligand cooperation is also prevalently observed in the hydrogenation catalysis of organometallic systems. One of the prominent ligand platforms is pincer ligands, which are comprised of a central donor with two sidearms. The lutidine-based PNP complex (**5**) developed by Milstein[62,77,78] contains a proton-responsive methylene spacer which enables dearomatization of the pyridine ring upon deprotonation, and its Ru/Fe complexes exhibit great reactivity for hydrogenation catalysis (**Scheme 1.7**). Originally, the dearomatization of the ligand backbone could act as a proton relay during catalysis, but further mechanistic studies[79] and DFT studies[80,81] showed that it is more likely that the hydrogenation occurs when the ligand is in the protonated state. Nevertheless, metal-ligand cooperation is still a probable pathway for hydrogenation[82]

and the deprotonated methylene spacer could serve as an intramolecular proton shuttle or a contact point to enable stabilizing non-covalent interactions.[63]

1.3 (De)hydrogenation in Organometallic Chemistry with Pincer-Type Iron Catalysts

Pincer-type ligands are a family of ligand sets with one central donor (e.g. pyridine or secondary amine) and two sidearms (e.g. phosphines or imines). The first member of this ligand family was synthesized in the 1970s[83,84] and went on to be coined by van Koten as 'Pincer' ligands in 1989.[85] Over the course of 50 years, different kind of pincer ligands and their complexes of various transition metals (Ru, Fe, Co, Rh, Ir, Ni, Pd, Pt, and Re) have been reported.[86] The key feature of the pincer ligand is the ability to enforce meridional coordination and provide great stability to complexes.[87] Thus, the applications of pincer complexes to organic synthesis have been studied intensively.[86] The first iron-catalyzed pincer catalyst for ketone hydrogenation was reported by Milstein in 2011, based on his experiences on the synthesis of Ru complexes.[88] Since then, numerous Fe pincer complexes for (de)hydrogenation of olefins, ketones, aldehydes and C1 compounds have been synthesized (**Scheme 1.8**). Depending on the ligand type, they can be divided into four classes: PNP complexes with –CH_2– spacer (**A**), PNP complexes with –N*H*– spacer (**B**), PNP complexes with –O– spacer (**C**), aliphatic amine PNP complexes (**D**) and other pincer complexes (**M**). The following discussion describes the recent advancement of hydrogenation catalysis using these iron pincer complexes, starting with hydrogenation of carbonyl compounds, followed by the hydrogenation of olefins, and finally pincer-catalyzed hydrogenation of C1 compounds.

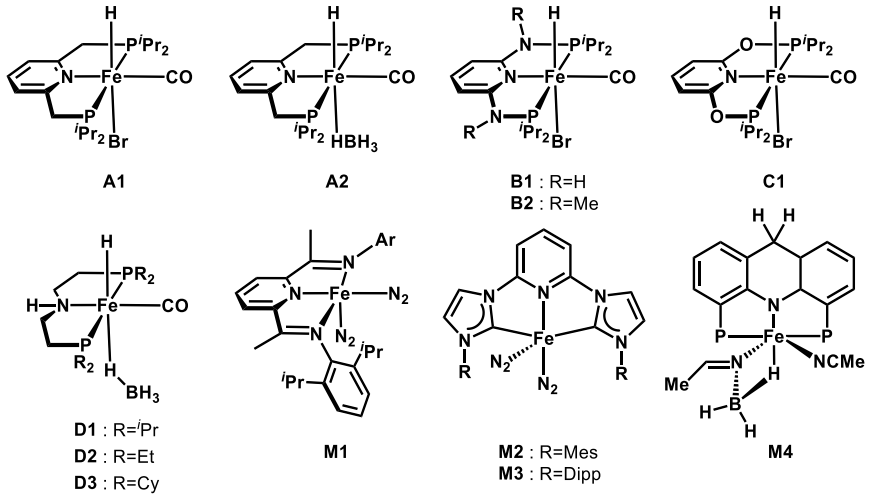

Scheme 1.8 Selective Iron Pincer Complexes for (de)hydrogenation.

1.3.1 Hydrogenation of C=O bonds

In 2011, Milstein reported the first iron pincer complex (**A1**) that can catalyze hydrogenation of ketones (**Scheme 1.9**).[88] Complex **A1** was highly active at 40 ℃ under 4.1 atm of H_2 in EtOH. The catalyst exhibited a turnover number (TON) as high as 1880 and TOF as high as 425 h^{-1}. The reaction was initiated with the addition of 2 equivalents of KO^{t}Bu as base. The substrate scope of **A1** included nitrile ketones with C=C bonds, conjugated diketones and substituted acetophenones. Noticeably, the activity of **A1** was prohibited when substrates contain nitrile or amine functional groups. Also, the hydrogenation of C=C bonds of the unsaturated ketones was observed at 20% conversion to product.

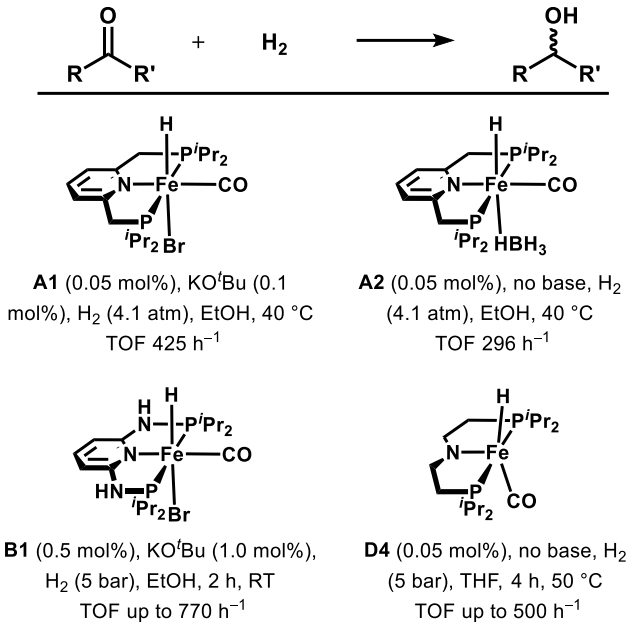

Scheme 1.9 Hydrogenation of ketones with pincer catalyst. Ref: **A1**[88], **A2**[89], **B1**[32], **D4**[33].

In 2012, Milstein[89] described an Fe(II) pincer complex (**A2**) with a borohydride ligand coordinated. This catalyst exhibited similar catalytic activity to **A1** in the hydrogenation of acetophenone. It is noteworthy that the catalysis was able to proceed without the addition of exogenous base. The TON of **A2** achieved up to 1780 for the hydrogenation of 2-acetylpyridine. However, **A2** exhibited a lower TOF (up to 296 h^{-1}) than that of **A1** (425 h^{-1}).

Upon changing the spacer of ligand backbone from CH_2 to NH, Kirchner[32] reported a new type of iron pincer complex (**B1**), showing good catalytic activity in the hydrogenation of ketones with 0.5 mol% catalyst loading and 1.0 mol% KO^{t}Bu, under 5 atm of H_2 at room temperature in EtOH.

The aliphatic pincer (aminopincer) family features a secondary central NH donor which upon deprotonation can function as a base atom while ligating with iron center. Generation of the five-coordinate aminopincer complex **D4**, reported by Fairweather and

Guan[90], was access by treating with KO^{t}Bu. Later, Jones and Schneider[33] described the high catalytic activity of **D4** in the hydrogenation of ketones (TOF up to 500 h^{-1}).

The first iron pincer complex that was able to catalyze the reduction of aldehyde was **B1** reported by Kirchner (**Scheme 1.10**).[32,91] The reaction was catalyzed with 5 mol% of **B1** and 10 mol% KO^{t}Bu under 5 bar H_2 at room temperature in EtOH. The TOF reached up to 120 h^{-1} in the reduction of substituted benzaldehydes. Notably, the analogous catalyst with NMe spacer (**B2**) resulted in drastic increase in the ketone hydrogenation activity with TOF and TON up to 20000 h^{-1} and 80000, respectively.[92] The high reactivity of **B2** was comparable to noble transition metal catalysis, making **B2** among the most active catalysts for hydrogenation of aldehydes.

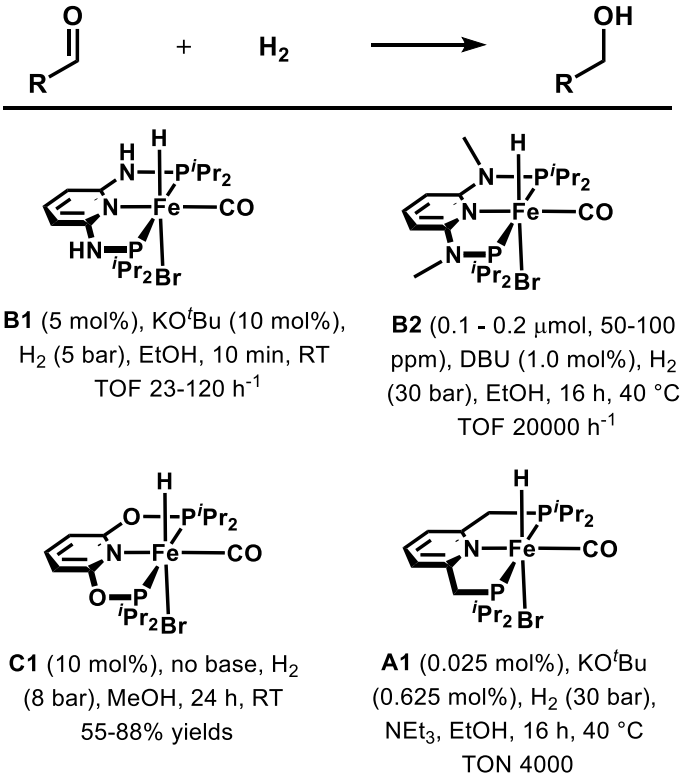

Scheme 1.10 Hydrogenation of aldehydes with pincer catalyst. Ref: **B1**[32,91], **B2**[92], **C1**[93], **A1**[94].

The iron complex **C1** derived from 2,6-bis(phosphinito)pyridine developed by Hu[93] exhibited good activity in the hydrogenation of aldehyde with 10 mol% catalyst loading. Fair to good yields (60-90%) were achieved under 8 bar of H_2 in methanol at RT for 24 h. The addition of sodium formate (10 mol%) could accelerate the reaction as well as decrease the catalyst amount to 5 mol%.

Interestingly, the Milstein[94] pincer **A1** which had originally low activity for aldehyde reduction was afterwards found to exhibit increased catalytic reactivity for the hydrogenation of aldehyde. The improvement was attributed to the addition of triethylamine or acetophenone, which was proposed to prevent the transient formation of carboxylic acid.

The hydrogenation of esters or carboxylic acids (**Scheme 1.11**) are synthetically challenging but desirable reactions for applications in industrial synthesis. Milstein[95] reported in 2014 that complex **A3** could catalyze the hydrogenation of activated trifluoroacetic acid esters to trifluoroethanol and the corresponding alcohols. The reaction was carried out with 1 mol% of catalyst in the presence of 5 mol% of NaOMe under 25 bar of H_2 in dioxane at 40 ℃. After 16 h, moderate to excellent yields were observed (52-99%) based on NMR. At the same time, Beller[96] and Guan[90] independently reported complex **D1** catalyzed the hydrogenation of esters under mild conditions without the addition of base. Later, the less steric complex **D2** reported by Beller[97] gave rise to superior catalysis under milder conditions. This suggested that the steric hindrance has negative effect for catalysis.

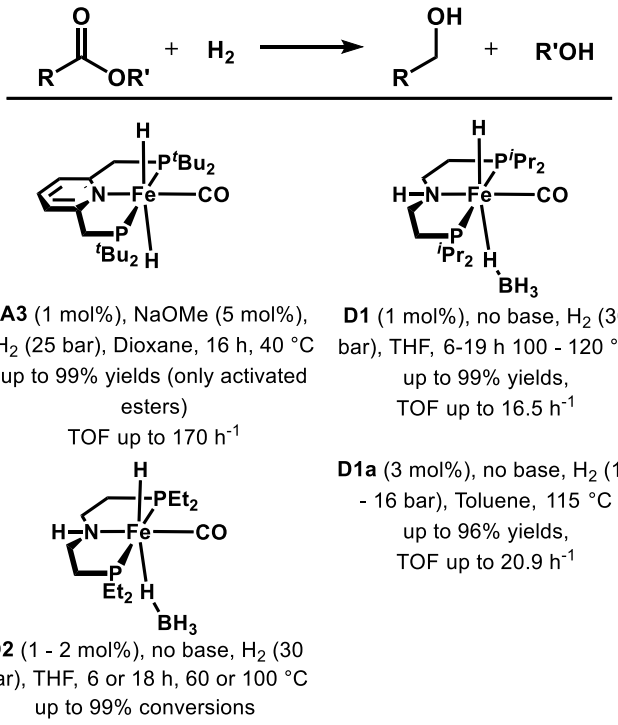

Scheme 1.11 Hydrogenation of esters with pincer catalyst. Ref: **A3**[95], **D1**[96], **D1a**[90], **D2**[97].

Being most difficult to reduce among carboxylic acid derivatives, carboxamides are targets for synthetic chemists who study transition metal-catalyzed hydrogenation. However, up to now iron-catalyzed hydrogenations are still scarce and only four examples have been reported (**Scheme 1.12**). The first iron catalyzed hydrogenation of amides was reported by Milstein[98] in 2016. The PNP pincer complex **A2** catalyzed the reaction in the presence of KHMDS (6 mol%) under 60 bar at 140 ℃ in THF, in which a series of activated N-substituted trifuoroacetamides were reduced to trifluoroethanol and the corresponding amines.

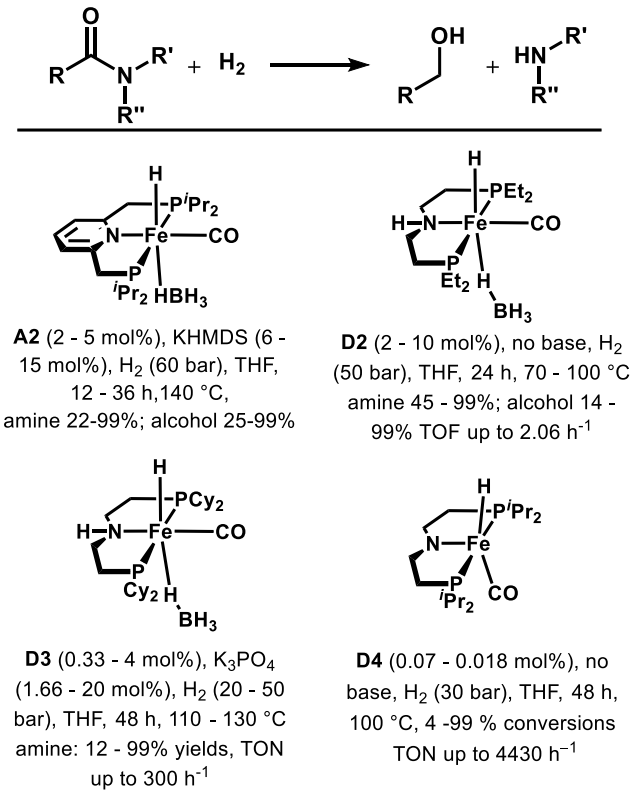

Scheme 1.12 Hydrogenation of amides with pincer catalyst. Ref: **A2**[98], **D2**[99], **D3**[100], **D4**[101].

Later, Langer[99] described a method to hydrogenate unactivated amides with complex **D2** under slightly milder conditions (2-10 mol% cat; 50 bar H_2; 70-100 °C). This reaction was achieved without the addition of base. Subsequently, Sanford[100] displayed the catalytic activity of an analogous complex **D3** with cyclohexyl (Cy) group. The catalysis was improved by K_3PO_4, allowing for formamides to achieve full conversion to amines and alcohols at 0.33 mol% cat. Followed by Bernskoetter[101], the hydrogenation of amides by **D4** was reported, where high activity was reached with TON up to 4430 and conversion in the range of 4-99% under the conditions of 0.07-0.018 mol% of **D4** in THF under 30 atm of H_2 for 4 h. Noticeably, co-catatyst such as

formanilide and LiOTf showed enhancing effect for the productivity of acetamide and benzamides.

One of the key features in pincer chemistry is the ability for ligand backbones to deprotonate/dearomatize and participate in H_2 activation through metal-ligand cooperation. The ligands with CH_2 or NH linkers (Milstein-type, Kirchner-type and aminopincer ligands) are proposed to function as proton-responsive positions and be deprotonated in basic conditions. Based on mechanistic studies and DFT calculations, two types of mechanisms for hydrogenation of ketones involving metal-ligand cooperation have been proposed. Although there are still ongoing debates on whether metal-ligand cooperation occurs during catalysis[13,17,49,62,63,102], the proton responsiveness of ligand backbones should to some extend affect, if not participate in, the reactivity by electronic effects or acting as a proton relay.

Due to the coordination of substrates, the first mechanism is called inner-sphere mechanism (**Scheme 1.13**). The active species (**I-1**) is produced by reacting with base KO^{t}Bu and the dissociation of bromide ion[103]. The coordination of carbonyl generates intermediate **I-2**, followed by the insertion of hydride into C=O double bond to give the species **I-3**. This 16 e^- species binds H_2, which is heterolytically cleaved, leading to the hydrido alkoxy complex **I-4**. The elimination of the alcohol regenerates the active species **I-1**.

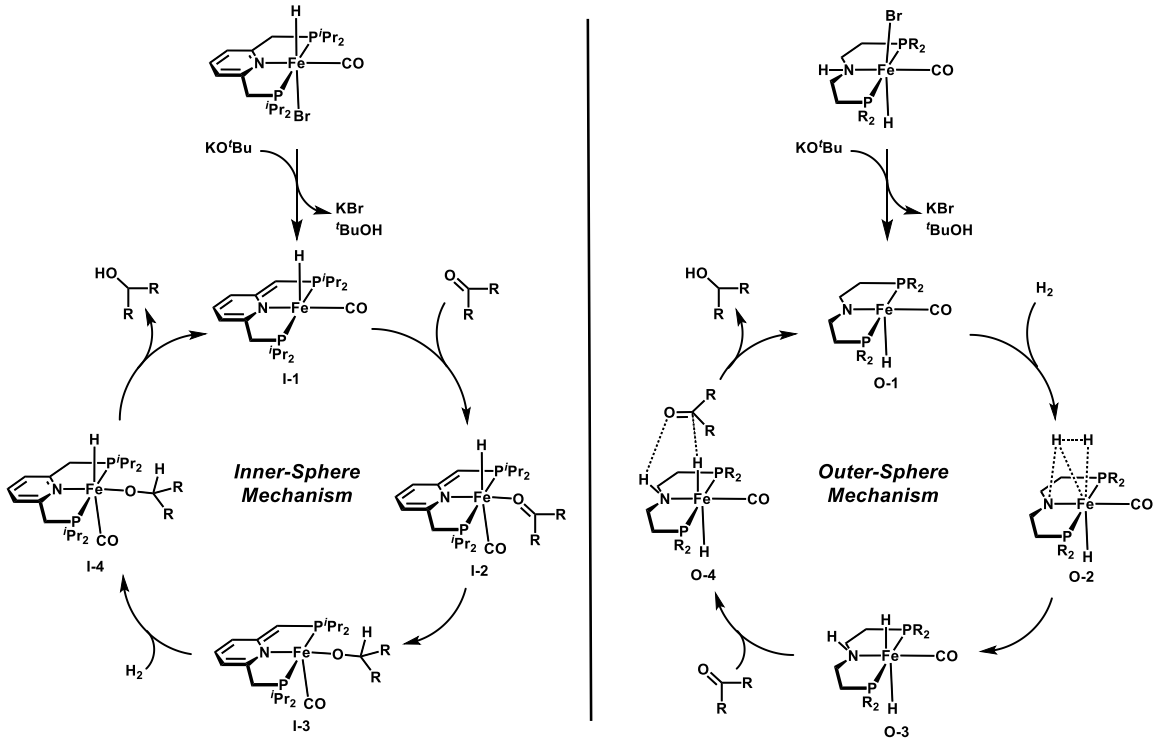

Scheme 1.13 Proposed mechanisms of iron pincer complexes for hydrogenation of ketones involving metal-ligand cooperation.

The second plausible mechanism for hydrogenation of ketones are outer-sphere mechanism (**Scheme 1.13**) because of the outer-sphere process in the step of hydride transfer and usually observed in aminopincer systems and pincers without deprotonation site, e.g. **B2**. In a aminopincer system, the reaction is initiated by the deprotonation of amine proton, which generates five-coordinate species (**O-1**). H_2 is cleaved between amide-N and Fe center, leading to the trans-dihydride species (**O-3**). The synergetic process of transferring proton from the central amine and hydride from the iron center to carbonyl regenerates the active amide **O-4**.[104]

1.3.2 Hydrogenation of C=C and C≡C bonds

Chirik developed a series of iron (0, II) complexes with CNC, NNN, and PNP ligand backbone, which are high active in hydrogenation of alkenes (**Scheme 1.14**). In 2004, Chirik[105] reported a pioneering work of pyridine diimine (PDI) iron(0) complexes (**M1**). The complex was able to catalyze the hydrogenation of alkenes with 0.33 mol% of catalyst at 22 ℃ under 4 atm of H_2. The catalyst was highly reactive achieving TOFs up to 1814 h^{-1}. Importantly, the PDI ligand was redox non-innocent. During catalysis, it was able to accept up to three electrons.

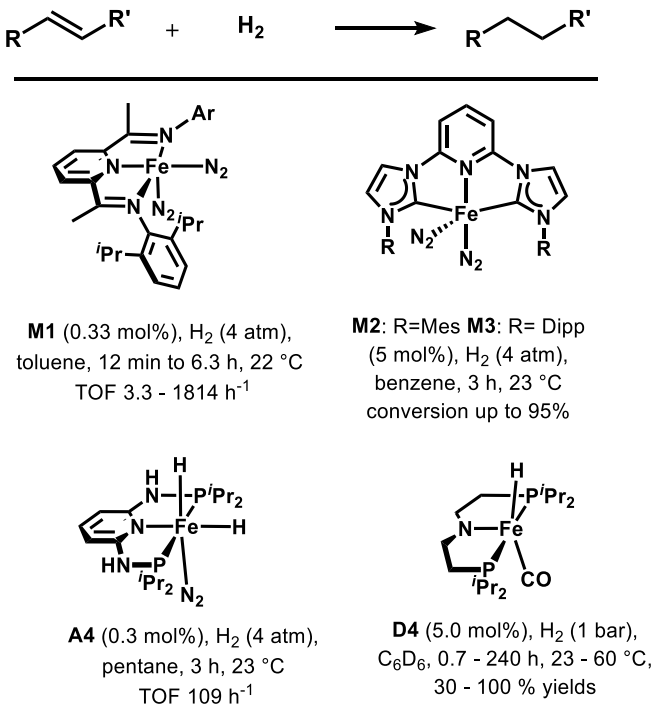

Scheme 1.14 Hydrogenation of alkenes with pincer catalyst. Ref: **M1**[105], **M2**[106], **M3**[106], **A4**[107], **D4**[108].

In 2012, Chirik[106] developed NHC-containing pincer iron(0) complexes (**M2**, **M3**). The high activity of these catalysts rendered them among the best catalysts in

hydrogenation of the most challenging unactivated, tri- and tetrasubstituted alkenes. Also, the same group[107] published a PNP iron(II) hydrido complex (**A4**) analogous to the Milstein complexes. This catalyst was able to promote hydrogenation of 1-hexene and cyclohexene.

Jones[108] reported the activity of **D4** used in the hydrogenation of alkenes. This reaction occurred in ambient conditions. However, the catalyst loading was slightly higher than that in the previous hydrogenation reactions catalyzed by this complex.

Milstein[109], in 2013, published an elegant contribution to the semi-hydrogenation of alkynes to *E*-alkenes (**Scheme 1.15**) using an acridine-based PNP Fe(II) complex (**M4**) bearing a noval imino borohydride ligand. The reaction was conducted with 0.6-4.0 mol% of cat. and 4-10 atm of H_2. The reduction was controlled to afford primarily *E*-alkenes with tiny amount of over reduced alkanes.

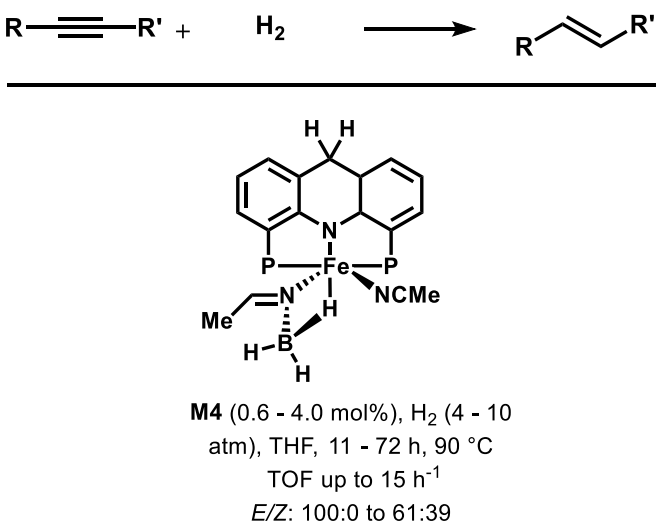

M4 (0.6 - 4.0 mol%), H_2 (4 - 10 atm), THF, 11 - 72 h, 90 °C
TOF up to 15 h^{-1}
E/*Z*: 100:0 to 61:39

Scheme 1.15 Semi-hydrogenation of alkyne to *E*-alkenes with pincer catalyst. Ref: **M4**[109].

1.3.3 (De)hydrogenation of C1 Substrates

Catalytic (de)hydrogenation can be extremely important in the energy conversion studies. The hydrogenation of C1 molecules, including CO_2 hydrogenation, formate dehydrogenation, and methanol dehydrogenation, can be applied to hydrogen storage, by which gaseous dihydrogen molecules are transformed into liquid, safely transported to places, and finally regenerated when to be used.[6,110] As the increasing amount of global greenhouse gases, CO_2 hydrogenation is one of the important ways to decrease atmospheric CO_2 concentration to fight against climate change. Researchers have been focused on developing efficient catalyst for these reactions. It is amazing to notice that in the past decade, we have witnessed a rapid and fruitful progress in the iron pincer-catalyzed (de)hydrogenation of C1 substrates, demonstrating the huge power of earth-abundant metal in catalysis and the significance of ligand design.

The Milstein pincer complexes were among the first iron catalysts that shown catalytic activity in the CO_2 hydrogenation and bicarbonate hydrogenation (**Scheme 1.16**). In 2011, Milstein[111] reported a trans-dihydrido pincer complex **A3**, exhibiting high activity in the hydrogenation of bicarbonate to formate under the conditions of 0.1 mol% of catalyst under 8.3 bar of H_2 in the solvent mixture of H_2O and THF (10:1). The CO_2 hydrogenation was achieved in the presence of NaOH (2 M) under similar conditions (0.1 mol% cat.; 6.66 bar H_2; H_2O/THF = 10:1). High TOF and TON comparable to noble metal catalysts were reached (156 h^{-1} and 788, respectively). Based on the observations, it is also proposed that the direct coordination of H_2 followed by heterolytic cleavage through hydroxide or ligand dearomatization and hydride insertion to CO_2 are plausible pathway for hydrogenation. In 2013, the complex **A3** was discovered to catalyze formic acid dehydrogenation to CO_2 and H_2, which performed under ambient conditions in the presence of NEt_3 with TON up to 500.[112]

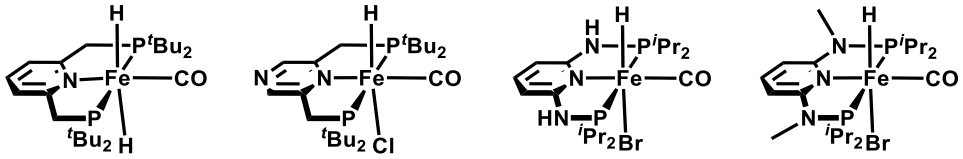

Scheme 1.16 Aromatic pincer catalysts employed in (de)hydrogenation of C1 substrates. Ref: **A3**[111], **A4**[113], **B1**[114,115], **B2**[114,115].

In 2015, A pyrazine-based iron pincer complex **A4** was described.[113] The pyrazine ligand backbone bears a coordinating N on the para-position, which upon deprotonation of the sidearm, binding of the N to adjacent iron and forming a six-membered aggregate was observed in the crystal structure. The dearomatized species was able to activate CO_2 and H_2 by metal-ligand cooperation (MLC) leading to hydrogenation of CO_2 to formate with TON up to 388.

In the Kirchner pincer system, CO_2 hydrogenation was also observed.[115] Both NH complex **B1** and the NMe complex **B2** showed high catalytic activity (TON: up to 1220 and up to 10275, respectively) for CO_2 hydrogenation under mild conditions. Noticeably, the two catalysts required different conditions. In **B1**, inorganic base NaOH and a combination of H_2O and THF (4:1) was added to the reaction. EtOH drastically decreased the catalytic activity due to ligation to the iron center. In **B2**, bulky organic base DBU and EtOH as the solvent gave rise to the optimal reactivity. Mechanistic study showed that the dihydride species was the active species in both catalysts and the use of protic solvent pushed the dissociation of formate from the iron center and the formation of formic acid.

Notably, the same catalysts[114] were also able to catalyze the selective dehydrogenation of formic acid to CO_2 under mild conditions in the presence of NEt_3 at

~60 ℃. Excellent performance for both catalysts was observed, wherein TON up to 10000 for **B2** was achieved.

The aliphatic pincer family exhibited superior reactivity in the (de)hydrogenation of C1 substrates (**Scheme 1.17A**). In 2015, Hazari and Bernskoetter[116] demonstrated that complexes **D4**-**D9** exhibited exceptional activity for CO_2 hydrogenation in THF with DBU as base at 80 ℃. Remarkably, the central methylated complexes (**D6**-**D9**) performed much more actively than their NH analogues; the TOF values for the former ones were recorded over 23000 h^{-1}, leading to a nearly 60000 turnovers. Interestingly, the similar complex **D10** was reported to be highly active in the dehydrogenation of formic acid. This reaction requires no addition of base and TOF was reached over 196000 h^{-1}.[117]

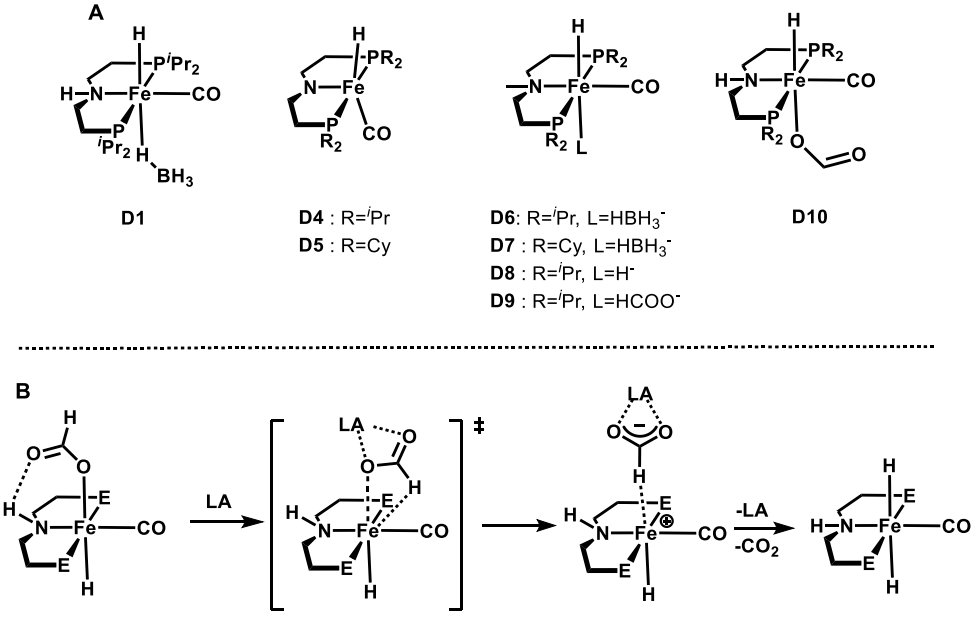

Scheme 1.17 (A) The aliphatic pincer catalysts employed in (de)hydrogenation of C1 molecules. Ref: **D1**[118], **D4**-**D9**[116], **D10**[117]. (B) Pathway for Lewis acid assisted decarboxylation of catalysts.

The outstanding performance of the aminopincer complexes can be attributed to the Lewis acid effect, whereby the presence of Lewis acids in the reaction aids in

stabilizing the transition states and intermediates (**Scheme 1.17B**).[119,120] In the dehydrogenation of formic acid, the negative charge of the formate adduct is stabilized by Lewis acid, which facilitates the decarboxylation generating CO_2.

The Lewis acid enhancement of the catalytic activity are prevalent in the aminopincer-catalyzed (de)hydrogenation of C1 substrates. Likewise, Beller[118] demonstrated the first aminopincer-catalyzed methanol dehydrogenation using **D1** (**Scheme 1.17A**). The reaction was later improved by Hazari, Bernskoetter and Holthausen,[121] which described a base-free protocol for methanol dehydrogenation to CO_2 and H_2 with Lewis acid additive $LiBF_4$. The facile dehydrogenation process resulted in TON up to 51000. DFT calculation elucidated that Li^+ decreased the energy barrier for the decarboxylation step and promoted the generation of CO_2.[121]

1.4 Hydrogenation in Biology: [Fe]-Hydrogenase and the Relevant Synthetic Modelling

H_2 plays a significant role in Nature's carbon cycle.[122,123] As a small diatomic molecule, H_2 can freely diffuse through cytoplasmic membranes, making it an ideal electron carrier.[124,125] In methanogenic archaea, a phylogenetically diverse group of strictly anaerobic Euryarchaeota, H_2 is utilized as the electron source in the reduction of CO_2 to methane ($4H_2 + CO_2 \rightarrow CH_4 + 2H_2O$; $\Delta G°' = -131$ kJ/mol).[122,123] It has been estimated that approximately 1 billion tons of methane is formed annually by methanogenic archaea (2% of the CO_2 fixed by photosynthesis per year globally).[126] This means that about 150 million tons of H_2 are used to fuel methanogens, accounting for approximately half of the H_2 produced in Nature.[122]

Due to high H–H bond dissociation energy (120 kcal/mol[127]) and high pK_a (~50 in THF[57,58]), chemical reactions involving H_2 molecules are unfeasible without dihydrogen

activation. After nearly 14 billion years of history, Nature is adept at H_2 reactivity. Hydrogenases, as is indicated by the name, are metalloenzymes that mediate H_2 activation or generation[42] and are commonly found in bacteria, archaea, and some eukarya. In contrast to most synthetic catalysts that employ noble transition metals, hydrogenases exclusively rely on earth abundant transition metals—more specifically, they all contain iron in their active sites. Based on the identity of metal, hydrogenases can be categorized into three types: [FeFe]-, [NiFe]-, and [Fe]-hydrogenase.[42]

Unlike the two dimetallic hydrogenases, [Fe]-hydrogenase is only expressed in methanogenic archaea, and catalyzes the reversible reaction of heterolytic cleavage of H_2 followed by the transfer of H^- to the substrate methenyltetrahydromethanopterin (methenyl-H_4MPT$^+$), producing methylenetetrahydromethanopterin (methylene-H_4MPT).[122,123] Hence, [Fe]-hydrogenase is also called H_2-forming methylenetetrahydromethanopterin (methylene-H_4MPT) dehydrogenase or Hmd. The highly reactive [Fe]-hydrogenase renders the forward and reverse reactions extremely facile ($TOF_{forward}$ = 215 s^{-1} in pH 7.5 and $TOF_{reverse}$ = 555 s^{-1} in pH 6.5).[128] The reaction catalyzed by [Fe]-hydrogenase is one of the intermediate steps for CO_2 reduction in methanogenic process (**Scheme 1.18**).[122,129] Importantly, [Fe]-hydrogenase is not a redox active enzyme, and thus common electron transfer units such as iron-sulfur clusters are not found in the enzyme, differentiating it from the other two dimetallic hydrogenases.[130] Therefore, [Fe]-hydrogenase does not show reactivity in the reduction of electron acceptors, such as artificial dyes;[131] however, it displays other typical reactivities of hydrogenases, which are H_2O/H_2 exchange and *para*-H_2 to *ortho*-H_2 conversion.[131] These activities are dependent on the presence of the substrate (methenyl-H_4MPT$^+$).

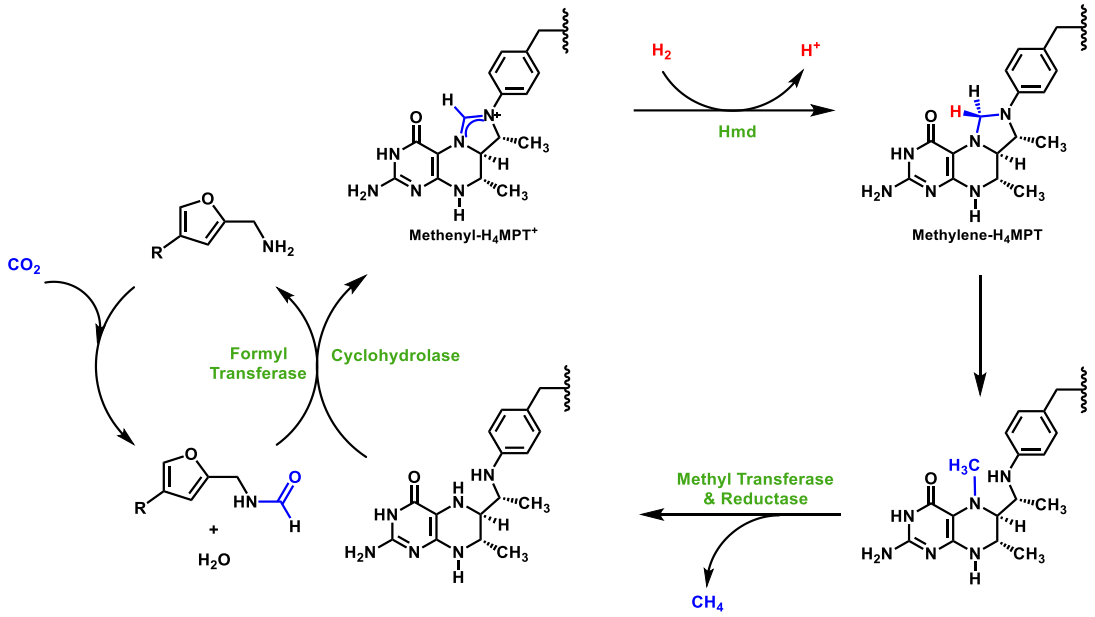

Scheme 1.18 Methanogenesis pathway in methanogens

The active site of [Fe]-hydrogenase is a non-proteinaceous iron guanylylpyridinol (FeGP) cofactor (except for Cys176), which is comprised of a pyridinol iron complex unit linked to a guanosine base by a phosphodiester (**Scheme 1.19**).[132,133] The guanosine base unit is necessary for binding site recognition when the FeGP non-covalently docks into the protein scaffold, and the pyridinol iron complex exhibits an iron center octahedrally coordinated to one cysteine sulfur atom, two COs, one solvent molecule (H_2O), a pyridinol nitrogen atom, and an acyl carbon atom.

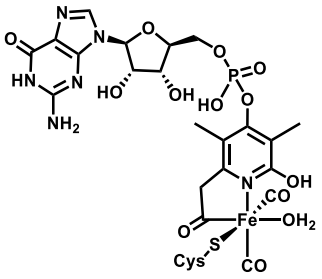

Scheme 1.19 Structure of iron guanylylpyridinol (FeGP) cofactor.

In this section, we will first discuss the spectroscopic studies and the structural determination of [Fe]-hydrogenase (section 1.4.1), then cover computational mechanistic studies on H_2 reactivity (section 1.4.2) and conclude by the recent updates on the synthetic modelling (section 1.4.3).

1.4.1 Spectroscopy and Structure of [Fe]-hydrogenase

In the early days of Hmd studies, the structural and electronic elucidation was highly dependent on spectroscopic methods.[42] A dramatic turn was undertaken in the understanding of Hmd. For over a decade, Hmd was thought to be "metal free", and the H_2 activation was considered to be induced by a purely organic interaction of the Lewis-acidic substrate, methenyl-H_4MPT^+, and a Brønsted base in the active site.[128,134–138] However, the purification of Hmd was always accompanied by the isolation of iron species with up to 1 mol Fe per 40 kDa subunit.[139] The iron species was thought to be a contamination until it was discovered that the release of iron was correlated with the inactivation of Hmd activity upon illumination by UV-A (320-400 nm) or blue light (400-500 nm).[139] The UV/vis spectrum of active Hmd showed a maximum absorbance at 360 nm. This band was bleached by white light, associated by the inactivation of Hmd and the release of iron. The rate of inactivation of Hmd was slowed down in the presence of CO. These results can be explained by the hypothesis that iron is responsible for the reactivity and can form Fe–CO complex which protects Hmd from light inactivation. Thus, the term of "metal-free" hydrogenase was proven inappropriate.

The organic residue of the cofactor (the active site of Hmd) was structurally determined by NMR and mass spectroscopy.[140] Since NMR and mass spectrometry studies of the intact cofactor failed due to its instability, the organic part of the cofactor was extracted after light inactivation. These spectra showed that the organic residue was a

derivative of pyridone and guanosine monophosphate (GMP). Although the exact binding mode of iron to the cofactor was still unknown at that time, it was proposed that the pyridone unit could be the chelating ligand bonded with iron.

The IR spectrum of Hmd suggested two intrinsic COs ligated to the iron center at an angle of 90°, exhibiting two bands of equal intensity at 2011 and 1944 cm^{-1}.[141] The binding of CO ligand excluded the possibility of Fe with high oxidation states, e.g. Fe(III), Fe(IV). The Mössbauer spectrum of Hmd was consistent with the presence of a single iron in a low oxidation state (0, +1, +2).[142] The fact that Hmd was EPR-silent further ruled out the occurrence of Fe(I), and the final oxidation state of Fe was determined as low-spin Fe(II) by comparing Mössbauer data and X-ray absorption spectra with those of the model complexes.[143,144]

Later, extended X-ray absorption fine structure (EXAFS) uncovered that the immediate coordination sphere of Fe was composed of cysteine-S, two COs, two N/O atoms from either pyridone or water.[145] The coordination environment was confirmed by nuclear resonance vibrational spectroscopy (NRVS) applied to ^{57}Fe-labeled [Fe]-hydrogenase. The simulation of the NRVS data is in agreement with a five-coordinate *cis*-CO Fe(II) model.[146]

The exact coordinating motif of the pyridone with iron was uncovered by single crystal X-ray diffraction to be a bidentate chelate through pyridine-N and acyl-C.[133] Electrospray ionization FT ion cyclotron resonance mass spectroscopy (ESI-FT-ICR-MS) confirmed the ligation of the acyl-C to Fe and IR spectroscopy assigned the stretching band at 1697 cm^{-1} to the acyl ligand (C=O) in the cofactor.[147] Iron-chromophore CD analysis supported that the binding of substrate and inhibitors to the Hmd induced a conformation change to close the active site cleft.[148]

The spectroscopic data provided indirect structural information about [Fe]-hydrogenase, which complemented the direct structural determination by single crystal X-ray diffraction. The first two protein crystal structures of [Fe]-hydrogenase reported were the apoenzyme (without FeGP cofactor and the substrate) structures isolated from *Methanocaldococcus jannaschii* and *Methanopyrus kandleri*, which were heterologously produced in *E. coli*.[145] Both crystal structures displayed homodimeric motif with one central globular unit and two N-terminal peripheral units. The central unit involves two C-terminal fragments from two subunits intertwined with each other, causing each N-terminal to face the C-terminal from the other subunit. Two clefts on both sides of the central unit were thus formed. Importantly, the cleft size of *M. kandleri* is larger than that of *M. jannaschii*, displaying two conformations (the open form and the closed form) in [Fe]-hydrogenase.

Two years later, the apoenzyme from *M. jannaschii* was reconstituted with FeGP cofactor, resulting in the first structurally-elucidated wild-type holoenzyme (with FeGP cofactor but without substrate) of [Fe]-hydrogenase.[132] This holoenzyme was found in the open conformation. Interestingly, when published for the first time, the structure of FeGP cofactor was erroneously modeled in that the acyl moiety was depicted as a carbonyl ligand with a hydroxy group on the pyridinol ring, and the hydroxy group on the other side was changed to carboxymethyl group.[132] However, the electron density at the carboxymethyl group did not match with the modeled structure. Soon after that, a revision of the previous structure was reported, showing that the FeGP cofactor contained an acyl–Fe bond, and the carboxymethyl group was modified to hydroxy to fit the observed electron density.[133] This acyl ligation was consistent with the spectroscopic study (*vide supra*)[133] and was the third example of a stable carbon-metal σ-bond in a biological system (others are methylcobalamine and adenosylcobalamin). In addition to

the wild-type holoenzyme structure, a mutant enzyme, where the Cys176 was replaced by an alanine, was also published. A dithiothreitol (DTT) molecule acting as a bidentate ligand occupied the sites of the solvent and cysteine sulfur in the previous structure.[133] Noticeably, this holoenzyme was completely inactive in the H_2 reactivity due to the loss of H_2 binding site.[133]

To study the mechanism of H_2 activation in the [Fe]-hydrogenase, it was desirable to obtain the crystal structure of [Fe]-hydrogenase complexed with the substrate, methenyl-H_4MPT^+, which clearly shows how FeGP cofactor and methenyl-H_4MPT^+ interact with each other and how a H_2 molecule binds to the enzyme and is activated.[149] The structure of holoenzyme-substrate binary complex was reported[150] soon after the structure of FeGP cofactor was revealed[132,133]. The crystal of the binary complex was obtained by co-crystallizing the DTT-bound inactive mutant holoenzyme with methenyl-H_4MPT^+, leading to the isolation of an open form protein structure. The closed form of the binary complex was then computationally modeled by superimposing the "open" binary complex onto the "closed" apoenzyme. In the modeled closed form of the binary complex, FeGP cofactor was located in a cavity with the iron center facing the *Re*-face of methenyl-H_4MPT^+. The hydride-accepting C14a atom from methenyl-H_4MPT^+ was close to the coordination site of Fe *trans* to the acyl group with a distance of 3 Å. A narrow hydrophobic channel from the periphery leading to the active site was discovered with a length of approximately 10 Å and a diameter of approximately 4 Å. This channel was believed to be the pathway for H_2 to access to the active site. The structure of the binary complex revealed the binding and activation environment of H_2 in [Fe]-hydrogenase, leading to the proposal of a H_2 activation mechanism involving: i) binding of methenyl-H_4MPT^+ leading to the close form; ii) H_2 entering the cavity through the hydrophobic channel and captured by Fe, iii) H_2 heterolytically cleaved by Fe and pyridone-O or

cysteine-S, and iv) the hydride transferred to C14 a and the proton passed to bulk solvent.[150]

In 2013, two structures of [Fe]-hydrogenase holoenzyme inhibited with *p*-toluenesulfonylmethylisocyanide (TosMIC) and 2-naphthylisocyanide (NIC) were reported.[151] X-ray crystallography and X-ray absorption spectroscopy (XAS) revealed that TosMIC and NIC coordinated to the proposed H_2-binding site of Fe *trans* to the acyl group. Surprisingly, the ligated isocyanides were also covalently bound to the pyridone-O atom. The discovery underlined the significance of pyridone-O atom as a pendant base in H_2 activation.

1.4.2 Computational Mechanistic Studies on H_2 Reactivity of [Fe]-hydrogenase

Computational modelling was used to study the catalytic cycle of H_2 reaction of Hmd. Hall et al.[152] carried out a DFT calculation of a truncated active site and proposed a *stepwise* pathway for H_2 reactivity (**Scheme 1.20**). The reaction started with the coordination of H_2 to the pentacoordinate iron species at the vacant site trans to the acyl ligand *trans* to the acyl group (**S-1**). Two pathways of H_2 cleavage were compared; one was by Fe and pyridone-O (**S-2** to **S-3**) and the other was by Fe and cysteine-S (**S-4** to **S-3**). The activation energy of the former pathway was lower than the latter (3.3 kcal/mol and 6.6 kcal/mol, respectively), indicating the cooperation of Fe and pyridone-O was the major pathway for H_2 cleavage. Next, the hydride migrated to the methenyl-H_4MPT$^+$ (**S-5** to **S-6**), generating methylene-H_4MPT. The catalytic cycle restarted by release of methylene-H_4MPT followed by binding of H_2. Noticeably, the calculation suggested that H_2 cleavage was achieved without the participation of methenyl-H_4MPT$^+$, while the experimental results showed the enzyme remained inactive until the substrate was bound to the FeGP cofactor[131,141]. In addition, the hydride intermediate (**S-3**) was at the lowest

energy in the entire reaction trajectory, while the hydride migration gave rise to the highest energy state, indicating the fair stability of **S-3**. However, the results contradict to the experimental evidence, in that no hydride species has been observed in the enzyme system.

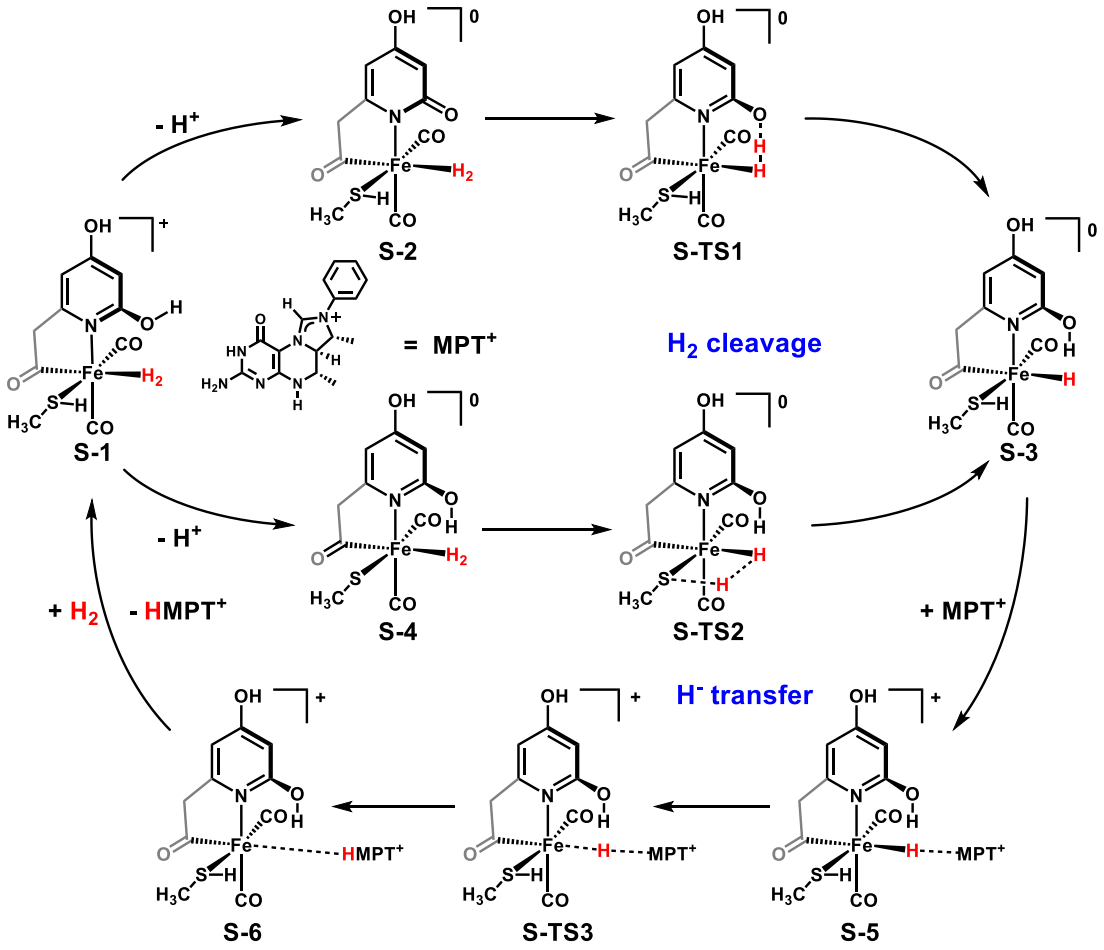

Scheme 1.20 Stepwise mechanism for H_2 activation and hydride transfer performed by Hmd.

Reiher and Senn[153] employed molecular dynamics (MD) simulations and quantum mechanical/molecular mechanical (QM/MM) calculations on the full protein structure of Hmd, which offered a *concerted* mechanism for the enzymatic reactivity (**Scheme 1.21**).

In this mechanism, H_2 molecule was cleaved with the cooperation of Fe site, pyridone-O and the cationic carbon atom on the substrate (**C-TS**), and concurrently hydride was transferred to the substrate and proton to the pyridone-O. PES scan was unable to locate a stable minimum for hydride intermediate. The mechanism indicated that not only the FeGP cofactor, but also the substrate, was also responsible for H_2 cleavage. The interactions between the substrate and the cofactor in H_2 cleavage was reminiscent of the function of frustrated Lewis pairs[154].

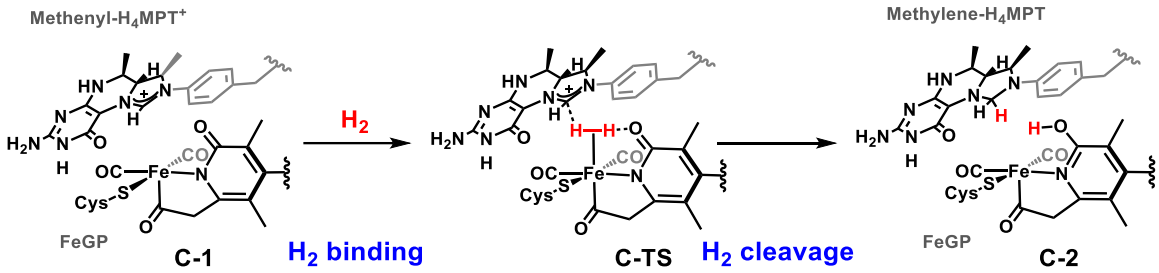

Scheme 1.21 Concerted mechanism for H_2 activation and hydride transfer performed by Hmd.

Although somewhat contradictory, the two mechanisms agree on the significance of iron and pyridone-O for H_2 reactivity. As we will proceed to the discussion of synthetic modelling, readers will notice the rationality for each mechanism.

1.4.3 Synthetic Modelling of [Fe]-hydrogenase

The discovery of the X-ray crystal structures for Hmd motivated the development of synthetic model complexes. Rauchfuss[155,156] reported the first acyl-containing iron carbonyl model complexes featuring phosphine derivatives (**Scheme 1.22**). The synthesis involved a phosphine thioester ligand reacting with $[Fe_2(CO)_{19}]$, in which oxidative addition of the thioester to Fe(0) occurred, generating acyl thiolate Fe(II) complexes. Due

to the bridging promiscuity of thiolate-S, a dinuclear Fe complex bridged by the thiolate-S was furnished first, and under high pressure CO atmosphere (1600 psi) the mononuclear complex **H1** was afforded. Importantly, the formation of acyl unit via oxidative addition of thioester is biomimetic as the guanylylpyridinol (GP) cofactor is also originated from a thioester during the biogenesis.[157] Although some of the structural features were not present in **H1**, such as pyridinol and cis-COs, the ν_{CO} bands were close to those of the enzyme (**H1**[155]: 2075, 2020, 1981 cm^{-1}; Hmd[141]: 2011, 1944 cm^{-1}; $Hmd_{CO\text{-}inhibited}$[141]: 2074, 2020, 1981 cm^{-1}). Complex **H1** was also treated with NEt_4CN or (*p*-tolylsulfonyl)methyl isocyanide ($TsCH_2NC$), producing the CN-bound or $TsCH_2NC$ bound complexes (**H2** and **H3**) relevant to the CN-inhibited Hmd.[156] Notably, ^{31}P NMR indicated that the CO ligand *trans* to acyl unit was replaced by L, suggesting the strong trans-influence of the acyl donor.

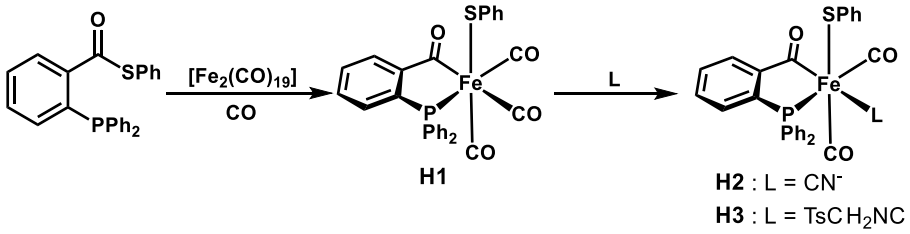

Scheme 1.22 Phosphine-based synthetic models for Hmd featuring acyl moiety.

Hu[124,158,159] developed the high-fidelity structural models containing acylpyridine moieties (**Scheme 1.23**). The acyl iron complex **H4** was produced by treating $[Fe(CO)_5]$ with activated ligand, followed by oxidation of the Fe center by I_2. The carbanion generated from deprotonation nucleophilically attacked one of the COs, forming acyl unit in-situ. Surprisingly, the installation of bulky aryl thiolate by replacing iodide afforded a novel pentacoordinate thiolate acylpyridine iron complex **H5**.[124,158] In order to synthesize

pyridinol model complexes, **H6** with ^{t}butyloxy group was accessed through similar route with **H5**. Deprotonation of ^{t}butyl group followed by ligand substitutions led to the formation of the first mononuclear pentacoordinate acylpyridinol model complexes **H9**-**H13** which were highly faithful to the active site.[159] The pyrdinol complexes were characterized by IR and NMR, but could not be characterized by X-ray crystallography due to the extreme sensitivity to heat and light. While similar to the active site, these pyridinol complexes could not activate H_2, which suggested the secondary interaction of FeGP cofactor with the protein scaffold, the presence of methenyl-H_4MPT^+ and derivation of the pyridinol ring are significant aspects in H_2 reactivity.[130]

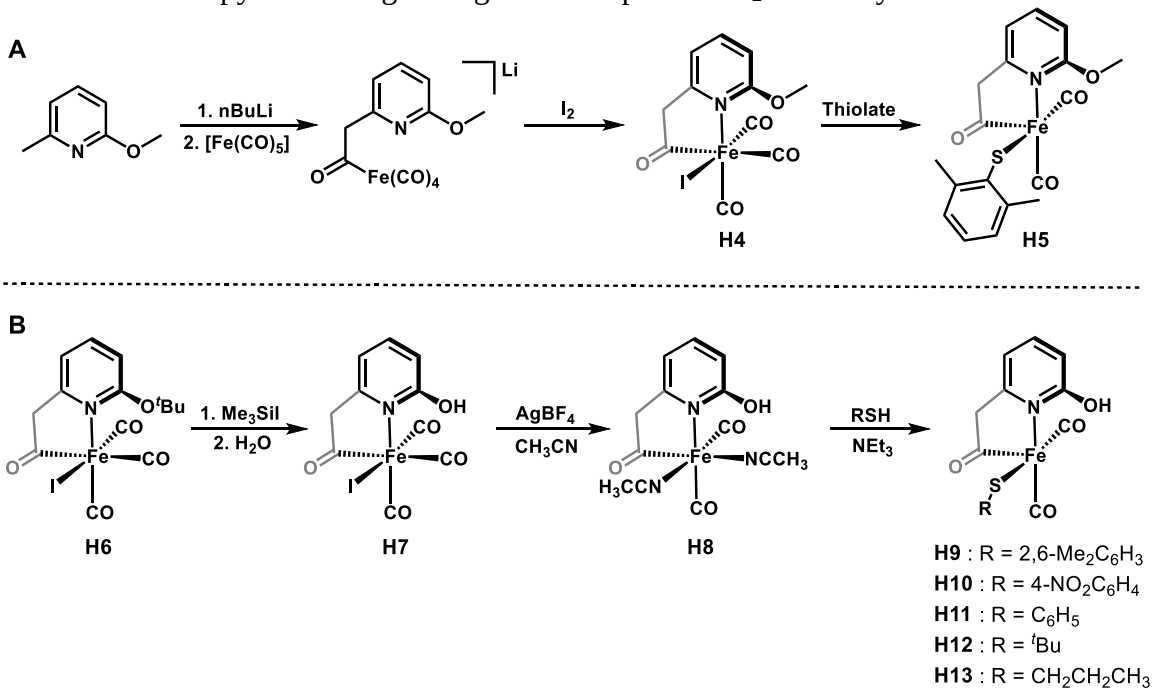

Scheme 1.23 Acylpyridine and acylpyridinol models for Hmd.

Based on the synthetic modelling studies by Hu, Shima and Hu[74] reported the first semisynthetic [Fe]-hydrogenases comprised of apo-enzyme reconstituted with pyridine- and pyridinol-containing iron complexes (**H4** and **H7**). The construct containing 2-

hydroxypyridine (**H7**; conjugate base: pyridone) exhibited detectable turnover frequencies in the forward and reverse reactions of [Fe]-hydrogenase (2 s^{-1} and 1 s^{-1}, respectively). In contrast, the methoxy analogue (**H4**) exhibited catalytic reactivity below the detection limit. These results revealed the importance of the protein environment, methenyl-H_4MPT^+, and the 2-hydroxy group — presumably as a pendant base that accepts the H^+ during H_2 cleavage. In addition, the effects of the guanosine monophosphate (GMP) moiety and the methyl groups of pyridinol ring on H_2 reactivity were evaluated by reconstructing the GMP-cleaved FeGP cofactor into the apoenzyme. The reactivity exhibited a ten-fold decrease compared to that of the wild enzyme, but a five-fold increase relative to the enzyme reconstructed with **H7**. The differences were attributed to the electronic effects of the GMP and two methyl groups of the GP ligand.

Similar to Hu, Li[160–165] focused on synthesizing acylpyridine/acylpyridinol iron model complexes (**Scheme 1.24**). The equatorial CNX complexes (**H14**) showed structural and spectroscopic similarities to Hmd.[160] The attempts to access pyridinol model complexes yielded dinuclear (**H15**)[163] and mononuclear (**H16**)[162] products depending on the sulfur ligand employed. However, due to the saturation of coordination positions, no reactivity related to H_2 activation was investigated.

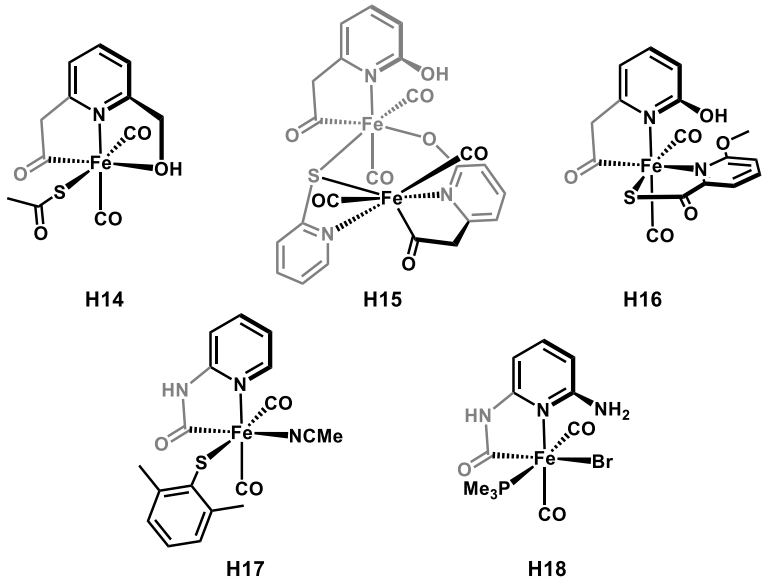

Scheme 1.24 Other model complexes containing acyl or carbamoyl moiety.

Pickett[166,167] reported the study of carbamoyl-containing iron model complexes (**H17** and **H18**). The carbamoyl moiety, akin to the acyl in Hmd, was generated in-situ by reacting 2-aminopyridine with $[Fe(CO)_4X_2]$ in base-free conditions. Despite of the similar coordination environment with Hu's complexes, complex **H17** was not pentacoordinate; the coordination site *trans* to the carbamoyl was occupied by acetonitrile, which indicated that carbamoyl had a lower trans-influence than acyl.[166] In addition, Pickett reported the synthesis of a phosphine-modified carbamoyl iron complex featuring an amine group on the 6-position of pyridine ring (**H18**), which was used to mimic the 2-hydroxy group in pyridinol. However, H_2 reactivity of **H18** was not reported.[167]

Distinctive from the previous synthetic models, Rose focused on developing novel tridentate ligand sets that restrict donor atoms to chelate metal centers in a *facial* orientation (**Scheme 1.25**).[168] The foray started with the model systems based on an 'anthracene scaffold'.[169,170] The implementation of the anthracene scaffold tethers the C,

N, S donors to form a unique tridentate ligand which not only increases the stability of the synthetic model through chelating effects, but also restricts the chelation to a facial motif. Reactivity studies showed that the thioether complex **H19** is bifunctional towards H_2 activation and C–H hydride abstraction, and the thiolate complex **H20** performs H_2 activation and hydride transfer to a model substrate, which is the first CNS biomimetic molecule that achieves structural integrity and functional reactivity. The synthetic model complex studies suggest that the CNS facial motif is pivotal for H_2 activation regardless of the binding of the substrates or protein scaffold, and the reactivity of the model complexes can be tuned by the charge of the donor atoms.

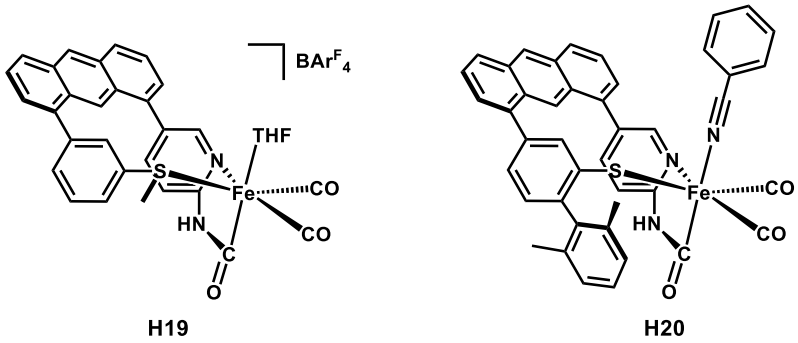

Scheme 1.25 Anthracene-based facial-chelating synthetic models for Hmd.

Finally, some bioinspired model complexes (**Scheme 1.26**) were also reported including an acylpyridine iron complex (**H21**) with a PNP ligand that was able to catalyze H/D scrambling and aldehyde hydrogenation[75], a cyclopentadiene (Cp) ruthenium carbonyl complex (**H22**) that displayed reactivity of H_2 cleavage with imidazolinium substrate[171], and some ruthenium/osmium-based carbamoyl complexes (**H23** and **H24**)[172]. In addition, the bioconjugation study of ruthenium carbamoyl complexes into papain was also recently reported.[173]

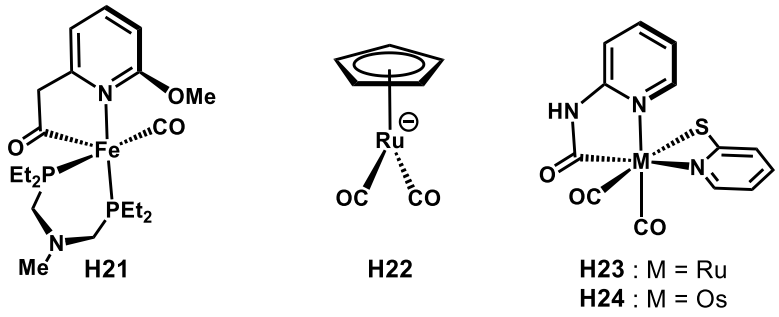

Scheme 1.26 Bio-inspired complexes for Hmd.

1.5 CONCLUDING REMARKS

(1) Hydrogenation plays a pivotal role in organic transformation and energy conversion. Mononuclear Iron catalysis exhibits great potential in the application of transition metal-catalyzed hydrogenation. We have witnessed a convergence between synthetic catalyst and Nature's metalloenzymes in utilizing mononuclear iron species as the active catalysts in hydrogenation.

(2) In the mononuclear iron-catalyzed hydrogenation, iron centers are usually electron deficient due to at the oxidation state of +2 and binding of strong π acidic ligands. In this way, H_2 tends to undergo heterolytic cleavage pathway through the Kubas interaction.

(3) Metal-ligand cooperation has been commonly employed in Nature's metalloenzymes and synthetic catalysts. Through this cooperation, H_2 is split into a proton, which is transferred to the basic atoms on the ligand backbone and a hydride, resulting in a metal hydride complex. The pre-organization of the acid-base pair greatly reduces the entropy of H_2 activation, and thus facilitates hydrogenation.

(4) Exciting advancements in pincer chemistry have shown that iron is a good candidate in various type of hydrogenations. More achievements are expected in the near future such that more efficient iron catalysts will be reported, larger substrate scope will be included, and more diverse ligand platform will be discovered.

(5) The synthetic modelling of [Fe]-hydrogenase has uncovered the unique properties of H_2 activation. The special donor arrangement and high efficiency has motivated researchers to develop various synthetic models and bio-inspired catalysts in hydrogenation. As real functional models outside the protein environment still await discovery, the synthetic modelling of [Fe]-hydrogenase still leaves large area to explore. Hopefully, more bio-inspired functional models that can be applied in organic synthesis will be uncovered soon.

Chapter 2: Carbamoyl Complexes with a *mer*-CNS Chelate as Structural Mimics for Mono-Iron Hydrogenase: Mechanistic Study of H_2 Cleavage*

2.1 INTRODUCTION

The H_2 activation has been well studied in organometallic chemistry and is an important elemental step in hydrogenation reactions.[1] Two modes of H_2 activation have been investigated, i.e. homolytic cleavage and heterolytic cleavage.[2,3] As the homolytic cleavage of H_2 often involves redox chemistry, metal should be soft, low-valent, and with accessible higher oxidation states. In contrast, the heterolytic cleavage of H_2 requires metal center to be hard, high-valent and redox inactive. Not like homolytic cleavage of H_2 which are often seen in industrial process, nature usually adopts heterolytic cleavage process to utilize or produce H_2. This is because the homolytic route is associated with too high kinetic barriers for enzymes to access.[4] It is noteworthy that heterolytic route of H_2 activation is usually accompanied by strong π-acidic ligand, such as CO or CN^-, to prevent metal from oxidation, as well as Brønsted base to accept the proton from H_2.

One of the examples of heterolytic cleavage of H_2 in nature is [Fe]-hydrogenase.[5,6] The unique features of the enzyme—Fe(II) center, π-acidic CO ligation, basic pyridone-O atom—are consistent with a typical heterolytic H_2 activation catalyst. Indeed, two different computational studies have both proposed similar heterolytic cleavage mechanisms. Hall et al.[7], based on the truncated FeGP active site of Hmd (non-proteinaceous structure), performed the DFT calculation and suggested a stepwise H_2

* Adapted/Reproduced in part with the permission from Durgaprasad, G., Xie, Z.-L., Rose, M. J., *Inorg. Chem.*, **2016**, 55, 386-389. Copyright 2016 American Chemical Society.
Xie, Z.-L., Durgaprasad, G., Rose, Ali, A. K., Rose, M. J., *Dalton Trans.*, **2017**, 46, 10814-10829.
Rose, Xie and Gurgaprasad designed the research. Xie and Gurgaprasad performed the research and analyzed the data. Ali performed DFT calculation.

activation process, starting from i) a pentacoordinate Fe complex, ii) Fe–H_2 complex, iii) heterolytic splitting of H_2 forming Fe–H intermediate, iv) hydride transfer to methenyl-H_4MPT^+ regenerating the pentacoordinate complex. Meanwhile, Reiher et al.[8] and Hedegård et al.[9] carried out multiscale modeling of the full active site of Hmd (with the protein scaffold and substrate) and revealed a concerted pathway for heterolytic cleavage of H_2, which is reminiscent of frustrated Lewis-pair.

Although both mechanisms agree with the heterolytic route of H_2 activation, they vary in two major aspects. Firstly, the incorporation of protein scaffold and binding of the substrate is required in the second mechanism, whereas the first mechanism shows that the active site can split H_2 without the presence of protein or substrate. Secondly, Fe–H intermediate is identified in the stepwise mechanism, while the concerted mechanism suggests that the hydride is transferred to the substrate upon H_2 cleavage and no Fe–H intermediate is observed.

The investigations using synthetic models of Hmd by Hu et al.[10–12] seem to favor the concerted mechanism as their faithful pentacoordinate model complex lacked reactivity toward H_2 without the protein environment but was highly reactive after being reconstituted into Hmd. However, it is important to note that Hu's model complexes were extremely unstable at room temperature and in the dark (usually with half-life less than one hour). It is difficult to perform rigorous reactivity study with these model complexes.

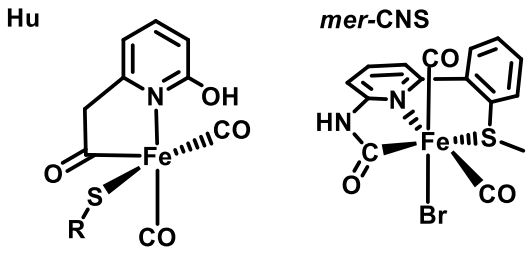

Scheme 2.1 Synthetic model complexes of [Fe]-hydrogenase of Hu et al.[10–12] and this work.

To shed light on the mechanism of H_2 activation in Hmd, it is imperative to develop stable model complexes that can tolerate rigorous reactivity study. We synthesized a new-type of *mer*-CNS complex with the tridentate CNS ligand and took advantage of its chelating effect to increase the stability of the model complex. The *mer-CNS* model complex contains a bio-relevant carbamoyl group, a thioether group and pyridine backbone, which shows some similarity to the FeGP cofactor. However, we do recognize the differences of this model complex from the native enzyme in that i) we used neutral thioether donor rather than the anionic thiolate donor, ii) the change of the acyl unit to slightly altered carbamoyl unit and iii) most importantly, the meridional arrangement of the *C, N, S* donors in the model complex, compared with the facial arrangement in the enzyme active site. It is an opportunity for us to compare the reactivity of the *mer*-CNS model with *fac*-CNS model[13], which was developed by our lab to obtain a reliable mechanistic insight into the enzymatic reactivity.

This chapter reports the synthesis and substitution reactions of the *mer*-CNS model complexes, the reactivity towards H_2 activation with the pentacoordinate complex that revealed one of the critical structural features that controls the H_2 activity of the model complex, and the reactivity of the Fe–H model complex.

2.2 THE BROMIDE-BOUND *MER*-CNS COMPLEX

2.2.1 Synthesis of the Ligand and Bromide Complex

The amino-appended N/S ligand $^{H2N}N^{py}S^{Me}$ was generated in good yield (89%) by a palladium catalyzed-Suzuki coupling reaction of unprotected 6-amino-2-bromopyridine with 2-methylthio(phenyl)boronic acid under standard coupling conditions (**Scheme 2.2**).[14] Metalation of the resulting $^{H2N}N^{py}S^{Me}$ ligand with $[Fe(CO)_4(Br)_2]$ in Et_2O at temperatures near −25 °C rapidly generated a copious yellow precipitate, which was accompanied by a vigorous evolution of gas (CO) and stoichiometric elimination of HBr. Due to the electrophilic nature of the Fe–C(δ^+)≡O(δ^-) unit in the starting salt,[15] nucleophilic addition of the free ortho-NH_2 (adjacent to the N^{py} binding site) results in the formation of the 'ferracyclic' carbamoyl unit. The resulting complex was purified via column chromatography over neutral Al_2O_3 using THF as an eluent, affording $[(^{O=}C^{NH}N^{py}S^{Me})Fe(CO)_2(Br)]$ (**1**) in moderate yield (40%). The crystallization conditions and structural details for **1** are discussed in the X-ray section (*vide infra*).

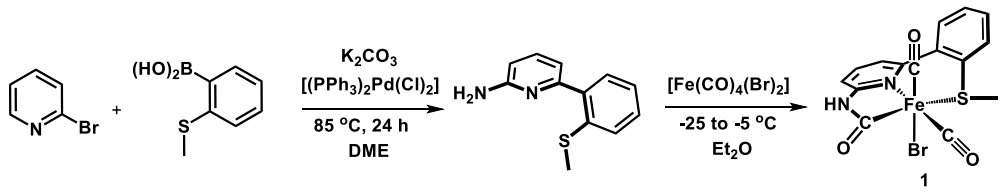

Scheme 2.2 Synthesis of the $^{H2N}N^{py}S^{Me}$ and $[(^{O=}C^{NH}N^{py}S^{Me})Fe(CO)_2(Br)]$ (**1**)

Remarkably, **1** is very stable under a variety of ambient conditions, and is insensitive to trace moisture, air, light and heat (up to ~50 °C). Given this highly stable platform, we utilized this model complex as a platform to investigate the reactivities towards auxiliary ligand substitution reactions, dihydrogen activation and reactions with hydride and base.

2.2.2 Structural and Spectroscopic Characterizations

The crystal structure of **1** was obtained by layering pentane over a THF solution of **1**. Complex **1** exhibits a pseudo-octahedral coordination environment (**Figure 2.1**). The selected bond lengths are shown in **Table 2.1**. It is apparent from the crystal structure of **1** that the pendant amine of the N/S ligand underwent a N–C(O) bond formation with a carbonyl ligand on $[Fe(CO)_4(Br)_2]$, affording the pseudo-biomimetic carbamoyl unit (the enzyme contains a methylene-bridged py-CH_2–C(=O)–Fe unit, instead of NH-linkage). The resulting tridentate CNS donor set chelates the Fe center in an equatorial motif, leaving the two carbonyls bound in *cis* fashion. Compared with the active site geometry wherein the solvato site is *trans* to the acyl moiety, the sixth coordination site in **1** is *trans* to one of the carbonyls and is occupied by bromide.

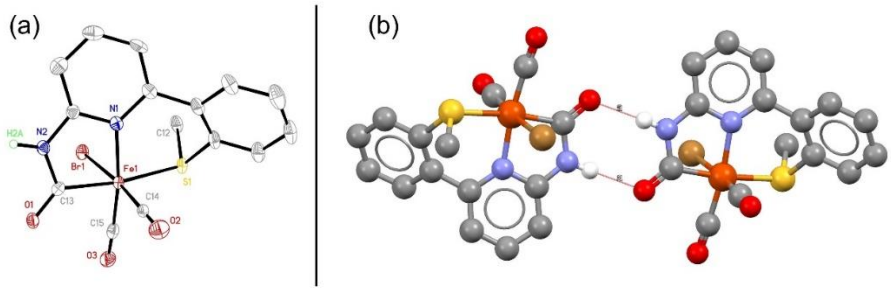

Figure 2.1 (a) ORTEP diagram (30% ellipsoids) of $[(^{O=}C^{NH}N^{py}S^{Me})Fe(CO)_2(Br)]$ (**1**), all hydrogen atoms except for NH have been omitted for clarity. (b) Hydrogen bonding between two enantiomers of **1** in crystal lattice.

Table 2.1 Selected bond lengths (Å) and angles (°) from X-ray structure of **1**.

Cmpd	**1**
N(1)–Fe(1)	2.003(7)
C(13)–Fe(1)	1.939(7)
C(14)–Fe(1)	1.808(10)
C(15)–Fe(1)	1.800(10)
S(1)–Fe(1)	2.329(2)
C(13)–N(2)	1.369(10)
C(13)–O(1)	1.222(10)
C(14)–O(2)	1.064(12)
C(15)–O(3)	1.116(11)
Br(1)–Fe(1)	2.4573(15)
O•••H–N	2.861(8)
C(14)–Fe–C(15)	92.6(4)°
pyridine-aryl dihedral angle	41.07

The carbamoyl C(13)–Fe(1) distance is 1.939(7) Å, which is slightly longer than the acyl–Fe bond in the enzyme active site (1.914 Å), but comparable to the $^{O=}$C–Fe bond (1.9390(19) Å) in the closely related carbamoyl-containing model complex [Fe($^{O=}C^{NH}N^{py}$)($Me_2C_6H_3S$)$(CO)_2$(MeCN)] reported by Pickett and coworkers.[16] The N(1)–Fe(1) bond distance [2.003(7) Å] is similar to those found in the enzyme (2.006 Å) and Pickett's complex [2.0000(17) Å]. The Fe(1)–S(1) bond length [2.329(2) Å] is within the typical range of Fe–SMe bonds found in low-spin Fe(II) complexes (2.22 Å to 2.33 Å).[17–19] The two carbonyls replicate the cis motif found in the active site with a C(14)–Fe–C(15) angle of 92.6(4)°. The Fe–C(O) bond distances are 1.808(10) Å and 1.800(10) Å for CO trans to Br and CO trans to pyridine, respectively, which are shorter than those found in the active site (1.829 Å, 1.858 Å). This is likely attributable to the more electron donating nature of the carbamoyl unit (as compared with acyl), thus resulting in stronger π back bonding to the carbonyls. On the contrary, the Fe–C(O) bonds are slightly longer

than those in [Fe($^{O=}$C^{NH}N^{py})($Me_2C_6H_3S$)$(CO)_2$(MeCN)][16] [1.766(2) Å and 1.776(2) Å]. This can be accounted for by the presence of an anionic thiolate ligand in [Fe($^{O=}$C^{NH}N^{py})($Me_2C_6H_3S$)$(CO)_2$(MeCN)], which increases the electron density of the Fe center. In addition, the pyridine and aryl(thioether) rings are not coplanar (py-Ar(S^{Me}) dihedral angle = 41.07°), and as a result the aryl ring tilts towards the CO side with the –$S(CH_3)$ group pointing towards bromide.

Interestingly, the crystal packing of **1** reveals that two enantiomers co-crystallized with Br and C(14)≡O(2) exchanging positions. The two enantiomers are linked by an intermolecular hydrogen bonding [O···H–N, 2.861(8) Å] between the carbamoyl units (**Figure 2.1**).

The solid infrared spectrum of **1** shows two absorption bands with nearly equivalent intensity for the two *cis*-oriented carbonyl ligands at 2034, 1974 cm^{-1} (**Table 2.2**), which are close to the features exhibited by the extracted FeGP cofactor in buffered H_2O (2031, 1972 cm^{-1}), but more blue-shifted with respect to the wild-type Hmd (2011, 1944 cm^{-1}).[20] The discrepancy in IR between **1** and the FeGP cofactor is likely derived from the lack of the more electron donating thiolate donor in **1**. The solution IR (in DCM) of **1** exhibits CO stretching frequencies slightly blue-shifted relative to the solid data and are the highest in frequency compared to the solution IR of the enzyme and cofactor (2011, 1944 cm^{-1} for the enzyme; 2031, 1972 cm^{-1} for the cofactor). This is attributed to that the protein environment to which the cofactor binds changes the electron density of the iron center likely through hydrogen bonding. The carbamoyl C=O vibration signal shows at 1619 cm^{-1}, which is comparable to the [Fe($^{O=}$C^{NH}N^{py})($Me_2C_6H_3S$)$(CO)_2$(MeCN)] (1620 cm^{-1}).[16]

Table 2.2 CO stretching frequencies in the IR spectra of **1**, Hmd and FeGP cofactor.

Complex (L)	ν(C≡O), cm^{-1} solid state	ν(C≡O), cm^{-1} Solution[e]	ν(C=O), cm^{-1} solid state
1	2034, 1974	2046, 1986	1619
[Fe]-hydrogenase	1996, 1928[a]	2011, 1944[b]	–
FeGP cofactor	2004, 1934[c]	2031, 1972[d]	–

[a] Spectrum of solid sample coordinated by dithiothreitol (DTT); data taken from ref [21]; [b] Spectrum of sample dissolved in water; data taken from ref [20]. [c] Spectrum of solid sample extracted with 2-mercaptoethanol; data taken from ref [22]. [d] Spectrum of sample extracted with 2-mercaptoethanol and dissolved in water; data taken from ref [20]. [e] DCM was used for IR analysis for **1**. The solution IR of enzyme was obtained in aqueous buffer solution.

The ^{1}H NMR spectrum of **1** was obtained in THF-d^8 and reveals the NH signal of carbamoyl at 9.96 ppm and S-CH_3 signal at 2.60 ppm. The resonances of two C≡Os and C=O in ^{13}C NMR are observed in 210.8, 210.7 and 208.4 ppm, respectively. While the peaks of C≡O resonance is comparable to the acyl-bound model complex [(6-MeO-C_5H_3N-2-CH_2CO)Fe(CO)$_2${S-(2,6-$Me_2C_6H_3$)}] (211.4 and 206.4 ppm),[11] the carbamoyl C=O signal is shifted to much higher field than the signal of acyl-bound complex (247.4 ppm). The lone pairs of the amide linkage form a conjugation π bond on NH–C=O which shielded the carbon and shifted the C=O signal to higher field.

2.3 Pentacoordinate Complexes Related to the Active Species of Hmd and Their Reactivity towards H_2 Activation

The pentacoordinate species of iron in [Fe]-hydrogenase has been proposed to be the active species in the catalytic cycle.[7,8,21] The dissociation of solvent molecule (H_2O) generates a vacant site for H_2 ligation, which leads to subsequent heterolytic cleavage of H_2 by metal-ligand cooperation. Since two separate computational proposals (pure DFT calculation and QM/MM calculation) provide contradictory arguments on whether the presence of the protein scaffold and substrate (H_4MPT^+) is necessary, it is imperative to

test the H_2 activation on stable small molecular model complex. Given the high stability of **1**, we proceeded to synthesize the pentacoordinate species and study its functionality towards H_2 activation.

2.3.1 Synthesis of the Pentacoordinate Complexes

The synthesis of pentacoordinate complex $[(^{O=}C^{NH}N^{py}S^{Me})Fe(CO)_2](BAr^F{}_4)$ (**2**) was achieved in the reaction of **1** with $TlBAr^F{}_4$, the bromide abstracting reagent, in non-coordinating solvent, 1,2-dichloroethane (DCE) or fluorobenzene (PhF) (**Scheme 2.3**). The bromide anion was readily abstracted by Tl^+ cation, which forms TlBr precipitate. Complex **2** was soluble and stable in DCE, PhF, Et_2O and toluene, and provided a better access to spectroscopic characterization. However, **2** rapidly decomposed in other "nominally non-coordinating solvents", such as CH_2Cl_2 and $CHCl_3$.

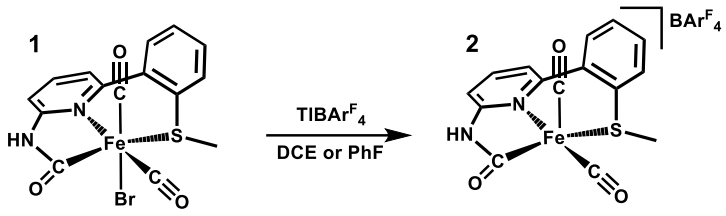

Scheme 2.3 Synthesis of the pentacoordinate complex $[(^{O=}C^{NH}N^{py}S^{Me})Fe(CO)_2](BAr^F{}_4)$ (**2**)

The attempts to obtain NMR spectrum of **2** were not fruitful as small quantity of paramagnetic decomposed iron product gave rise to a broadened spectrum which is difficult to interpret. Instead, IR spectroscopy provides clear evidence of the formation of **2**. In the solid IR spectrum, **2** shows a blue-shifted CO bands at 2008 and 2057 cm^{-1} (**Figure 2.2 left**) with respect to **1**, indicating the abstraction of Br^-. Similar blue-shifted

CO stretching frequencies—2046, 1986 cm^{-1} to 2057, 2006 cm^{-1}—are observed in the solution IR spectrum (**Figure 2.2 right**), suggesting its stability in DCE.

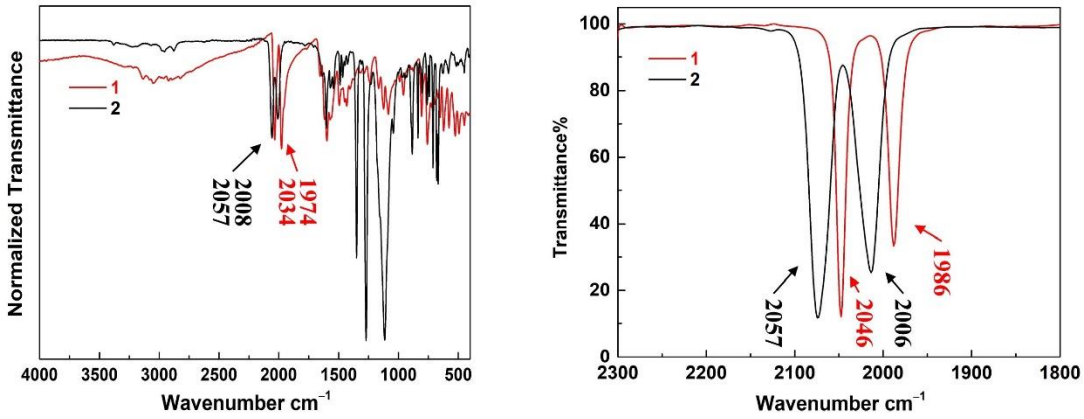

Figure 2.2 The comparison of the IR spectra of **2** and **1** in solid (left) and solution (right). The solution IR was measured by dissolving **1** in DCM and **2** in DCE.

To acquire more structural information of **2** from the IR spectra, we use Eq. 1 to calculate the bond angle of OC–Fe–CO in **2**:

$$\frac{I_{sym}}{I_{asym}} = \cot^2\theta \quad \text{(Eq. 1)}^{20}$$

The I_{sym} is the intensity of the symmetric vibration of CO ligands in IR spectrum, and I_{asym} is the intensity of the asymmetric vibration. The bond angle of OC–Fe–CO is represented by 2θ.[20] The calculated bond angle 2θ of **2** is 83.83°, which implies the iron center adopts a square pyramidal geometry, rather than a trigonal bipyramidal geometry. The result is consistent with the DFT-simulated structure of **2** (*vide infra*).

2.3.2 H_2 Activation of the Pentacoordinate Complex

The functional studies of pentacoordinate complex **2** were carried out to assess its ability of H_2 activation. The conditions have been tabulated in **Table 2.3**. The reactions were performed in high pressure NMR tubes (pressure limit: 150 psi) by first generating **2** in situ (mixing **1** and thallium salt in THF and filtering the solution), then treating **2** with the solution of substrate and base depending on the conditions, and finally adding D_2 gas to the NMR tube. The reactions were mixed on the mechanical rotator and monitored by NMR spectroscopy periodically.

We started from the reaction of **2** with D_2 gas (1 or 4 atm). Incubation of the NMR tube for 2 days resulted in no sign of cleavage of the D_2 gas (entry 1 and 2). The addition of exogenous base, sodium 2,6-di-*tert*-butyl-4-methoxyphenolate (NaDBHA), led to decomposition of the complex (entry 3 and 4), which was determined by the IR spectra after reaction. Changing to stronger base, KO^{t}Bu, also resulted in the complex decomposition (entry 5). On the other hand, the addition of weak organic base (entry 6),

DBU (1,8-diazabicyclo[5.4.0]undec-7-ene), could preserve the complex, but did not activate D_2. The experimental results and DFT study of Hmd showed that the H_2 activation requires the presence of substrate (H_4MPT^+).[23] Therefore, we investigate the effects on H_2 activation of a model substrate, 1,3-bis(2,6- difluorophenyl)-2-(4-tolyl)imidazolinium tetrakis[3,5-bis(trifluoromethyl)phenyl]borate ([TolIm][BAr^F_4]), which was synthesized based on the report by Meyer *et al*.[24] None of the tested reactions (entry 7-11) indicates heterolytic cleavage of D_2 molecule. Lastly, we studied the possibility of **2** acting as a hydride acceptor by treating it with silanes, weak hydride donors. Regardless of the addition of substrate (entry 12, 13 and 14), ^{2}H NMR showed no peak that can be assigned to new hydride-transferred products.

Table 2.3 Reaction conditions of the functional studies with the pentacoordinate complex.

Entry	**Fe**	Halide Abstracting Reagent	$P(D_2)$/ atm[a]	Silane	Substrate	Base	Sol.[d]	T/ °C
1	**1**	$TlBAr^F{}_4$	1	—	—		THF	RT
2	**1**	$TlBAr^F{}_4$	4	—	—		THF	RT
3	**1**	$TlBAr^F{}_4$	1	—	—	NaDBHA[b]	THF	RT
4	**1**	$TlBAr^F{}_4$	4	—	—	NaDBHA	THF	RT
5	**1**	$TlBAr^F{}_4$	4	—	—	KO^{t}Bu	THF	RT
6	**1**	$TlBAr^F{}_4$	4	—	—	DBU[c]	THF	RT
7	**1**	$TlBAr^F{}_4$	1	—	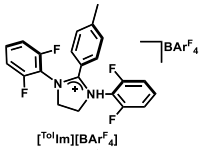 [^{Tol}Im][$BAr^F{}_4$]		THF	RT
8	**1**	$TlBAr^F{}_4$	1	—	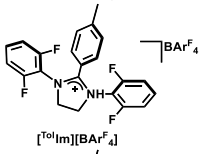 [^{Tol}Im][$BAr^F{}_4$]		THF	RT
9	**1**	$TlBAr^F{}_4$	1	—	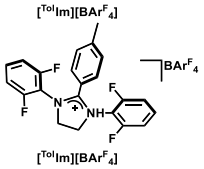 [^{Tol}Im][$BAr^F{}_4$]		THF	RT
10	**1**	—	1	—	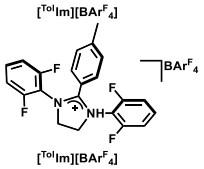 [^{Tol}Im][$BAr^F{}_4$]	NaDBHA	THF	RT
11	**1**	$TlBAr^F{}_4$	1	—	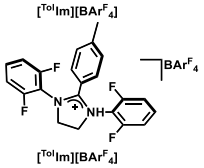 [^{Tol}Im][$BAr^F{}_4$]	DBU	THF	RT
12	**1**	$TlBF_6$	—	$PhSiH_3$	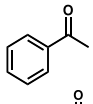		THF	RT
13	**1**	$TlBF_6$	—	$PhSiH_3$	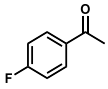		THF	–40
14	**1**	$TlBF_6$	—	$HexSiH_3$			THF	RT

[a] High pressure NMR tube was used for gas reactions. [b] NaDBHA = Sodium 2,6-di-*tert*-butyl-4-methoxyphenolate. [c] DBU = 1,8-diazabicyclo[5.4.0]undec-7-ene. [d] The total amount of THF solvent is 1 mL.

The inactivity of the *mer*-CNS complex in the H_2 cleavage reaction could be ascribed to several reasons: (1) the instability of complex **2** in basic condition. It is possible that the complex transforms to a $[Fe_2S_2]$ complex under the presence of strong base, as it is shown in the next section; (2) The use of thioether in lieu of thiolate as a mimic related to the cysteine thiolate in Hmd could change the electronic structure of the model, making it incompetent to H_2 activation; (3) the equatorial orientation of *C, N, S* donors decreases the reactivity of the model complex towards H_2 activation. It has been proposed that the acyl unit *trans* to H_2 binding site on Hmd could play a critical role in the enzymatic function.[22] To develop functional model of Hmd, the facial coordination arrangement of *C, N, S* donors could be the key to reactivity.

In separate works contributed by other group members[13], the anthracene-based synthetic model presents a platform with a facial *C, N, S* arrangement to test enzyme-related functions.[13] This model complex is active in D_2 heterolytic cleavage and deuteride transfer to proton source. The ^{1}H NMR spectrum of the reaction between THF-solvato complex and D_2, with 2,6-di-*tert*-butyl-4-methoxyphenol (dBPhOH), shows the increase of HD peak. Notably, the presence of a strong H_2 signal in the ^{1}H NMR spectrum indicates that the iron-mediated deuteride transfer is a catalytic process, rather than stoichiometric. The evidence of Fe-D intermediate is obtained by D NMR, in which the iron-bound deuteride nucleus resonates at –18 ppm. It is important to note that the deuteride resonance is only noticeable when deuterium-substituted 2,6-di-*tert*-butyl-4-methoxyphenol (dBPhOD) is used. Based on the different reactivity of the *mer*-CNS complex and *fac*-CNS complex, it indicates that the orientation of the CNS donors could be vital for the functionality of model complex.

2.3.3 DFT Calculation of the Bromide Complex and Pentacoordinate Complex: the Effects of the Facial-*C, N, S* Orientation on H_2 Activation

The theoretical insights to the physical properties and H_2 functionality of *mer*-CNS model complexes (**1**, $\mathbf{2}^+$) were obtained by DFT calculation, which is powerful in predicting structural parameters, energy and molecular properties. The calculations on bromide-bound complex **1** and pentacoordinate complex $\mathbf{2}^+$ were performed using PW91 functional and a combination of basis sets (denoted as 6-31G(d)-combo: m6-31G(d) on Fe, r6-311G on Br and 6-31G(d) on the rest of the atoms).

The geometry optimizations for **1** were calculated smoothly at $S = 0$ configuration. The optimized structure is shown in **Figure 2.3**. The calculation afforded the result that was closely matched (RMS error = 0.0543) to the experimentally found structure by X-ray analysis. However, there are some discrepancies shown in the in-silico structure, compared with the experimental structure. The Fe–Br bond length from calculation is longer than the experimental result (PW91/6-31G(d)-combo: $\Delta L = +0.014$ Å). As a result, the Fe–(C≡O) bond length is shortened and the C–O bond length is elongated (**Table 2.4**). This deviation is probably due to the excessively diffuse *d* orbital in the basis set applied in the computation. Thermodynamically, the anionic bromide has large binding affinity with the Fe(II) center (E_b = -5.51 eV, **Table 4**), which explains the fact that L-type ligands (i.e. PPh_3, MeCN, etc.) cannot replace bromide without halide abstracting reagents. The large binding affinity of anionic bromide is due to the presence of π-accepting *cis*-carbonyls, which diminishes electron density on the Fe(II) center and increases the Lewis acidity of metal.[25] Overall, it is evident that the B3LYP/6-31G(d) calculation reasonably reproduces the experimentally determined X-ray structure.

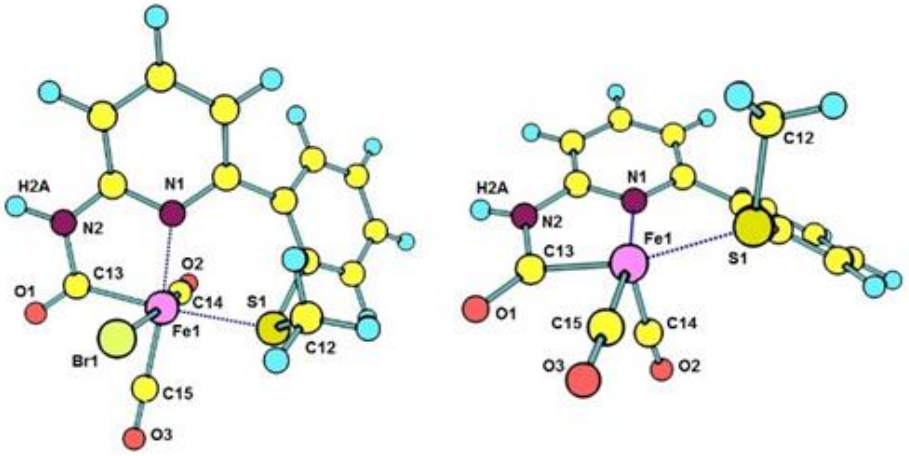

Figure 2.3 The optimized structures of **1** (left) and $\mathbf{2}^{+}$ (right) using B3LYP/6-31G(d).

Table 2.4 Selected bond lengths (Å) of the structures of wild-type Hmd, **1**, and the calculated $\mathbf{1}_{\mathbf{DFT}}$ and $\mathbf{2}^{+}$, and the binding energy E_b (eV) of Fe–Br.

Cmpd	**Hmd**[a]	**1**	$\mathbf{1}_{\mathbf{DFT}}$	$\mathbf{2}^{+}$
Npy−Fe (Å)	2.052(9)	2.003(7)	2.017	1.968
Cacyl−Fe (Å)	1.88(1)	1.939(7)	1.939	1.949
Ccarbonyl−Fe (Å)	1.769(5)	1.808(10) 1.800(10)	1.739 1.761	1.721 1.775
C≡O (Å)	1.170(8)	1.064(12) 1.116(11)	1.169 1.163	1.161 1.159
S−Fe (Å)	2.335(4)	2.329(2)	2.378	2.370
Br−Fe (Å)	-	2.4573(15)	2.523	-
E_b (eV)	-	-	-5.51[b]	-

[a] ref [26]. [b] E_b was calculated by the equation of $E_b = E(\mathbf{1}) - E(\mathbf{2}^{+}) - E(Br)$.

For the 5-coordinate complex $\mathbf{2}^{+}$, all the calculations were done implementing an $S = 0$ configuration (using higher $S = 1$ or 2 configurations led to >5 kcal/mol energies or non-convergence). The in-silico structure retains a square pyramidal geometry. While there is no substantial change in the bond lengths, some trends are noteworthy (**Table 2.4**). Comparing with the wild-type Hmd structure, the N_{py}–Fe bond distance of $\mathbf{2}^{+}$ is

compressed by 0.084 Å and the C_{acyl}–Fe bond length is elongated by 0.064 Å. Additionally, the C≡O bond lengths in the Hmd active site are longer than those found in $\mathbf{2}^{+}$, indicating less electron density on the Fe(II) in $\mathbf{2}^{+}$ and thus weaker back-bonding interactions between carbonyls and the iron center. The discrepancy is likely due to the presence of the neutral thioether ligand in $\mathbf{2}^{+}$, versus the anionic thiolate in the enzyme. It is notable that Fe–C(≡O) bond *trans* to the vacant site in $\mathbf{2}^{+}$ is shortened as compared to **1** (DFT and X-ray), due to loss of the anionic Br^{-} ligand.

Hessian calculations were undertaken for $\mathbf{2}^{+}$ using the same method and basis set, and none of the ground state structures obtained from structural optimization exhibited imaginary frequencies. All of the C≡O and C=O frequencies are tabulated in **Table 2.5**. The predicted data match with the experimental results with small error (calc: 2080, 2040 cm^{-1}; expt: 2057, 2008 cm^{-1}; $\Delta\nu$ = 27 ± 5 cm^{-1}), which suggests a high level of confidence for the PW91-predicted IR. In contrast to the reasonable deviations found for the C≡O ligands, both of the predicted carbamoyl C=O stretches show anomalously greater differences from the experimental data (more than 100 cm^{-1}). We ascribe this discrepancy to the presence of H-bonding found in the experimental crystal packing of **1** (*vide supra*, **Figure 2.1(b)**), wherein NH•••O=C contacts contribute to the lengthening of the C=O bond (i.e. lower ν values than predicted in vacuo).

Table 2.5 DFT-calculated IR frequencies of $\mathbf{2}^{+}$ and **Hmd**.

	CO-1 cm^{-1}	$\Delta\nu^{a}$ cm^{-1}	CO-2 cm^{-1}	$\Delta\nu^{a}$ cm^{-1}	(C=O)-NH- cm^{-1}	$\Delta\nu^{a}$ cm^{-1}
$\mathbf{2}^{+}$	2080	23	2040	32	1744	108
$\mathbf{2}_{exp}$	2057	—	2008	—	1636	—
Hmd	2011	—	1944	—	—	—

[a] $\Delta\nu$ is the difference in wavenumbers between DFT-calculated frequency and the experimental frequency for $\mathbf{2}^{+}$.

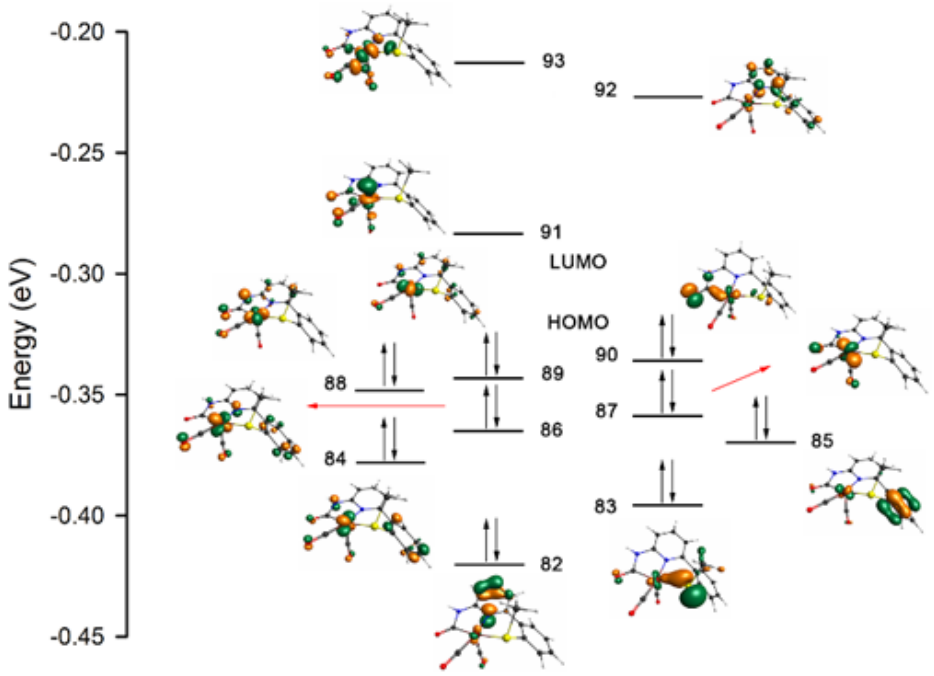

Figure 2.4 Molecular orbitals calculated for **2**$^{+}$ using PW91/6-31G(d)-combo.

The small differences between calculated and experimental results found in the structural studies and vibrational data provided confidence to continue the MO analysis using the PW91 functional (6-31G(d)-combo). The compilation of molecular orbitals for **2**$^{+}$ are shown in **Figure 2.4**. To study the orbital composition from atomic orbitals of Fe, natural bond orbital (NBO) calculations were undertaken, and the results are tabulated in **Table A13** in Appendix A. Interestingly, the *z*-axis for both structures are in line with the S–Fe–CO bonds, while the *y*-axis points towards the vacant site in **2**$^{+}$. The unoccupied orbitals of **2**$^{+}$ are largely metal-based (MO 93: Fe 35.69% and MO 91: Fe 39.36%; **Figure 2.4**) and include anti-bonding interactions between the Fe center and the chelate backbone and CO ligands. The largest atomic orbital contribution to MO 93 emanates from Fe d_{x2-y2} (16.69%). MO 91 is composed of Fe d_{x2-y2} and d_{yz} with nearly identical contributions (d_{x2-y2} 14.26% and d_{yz} 14.29%). The geometry of the 5-coordinate complex

and the orientation of MOs 91 and 93 benefit an incoming ligand (bromide or H_2) to form σ or π bonds with Fe center. Thus, major energy changes of d_{x2-y2} and d_{yz} can be envisioned upon coordination of the sixth ligand. For the occupied orbitals of $\mathbf{2}^+$, the HOMO 90 shows a bonding interaction with the carbamoyl carbon and consists almost exclusively of the d_{yz} orbital (14.87%; the total Fe contribution is 18.63%). The occupied MOs 89 and 86 have large contribution from d_{z2} and d_{xy}, respectively (28.30% and 15.05%). MOs 88 and 87 show the combination of a different group of *d* orbitals (MO 88 = d_{xy} 10.32% + d_{xz} 12.20%; MO 87 = d_{x2-y2} 15.37% + d_{z2} 20.48% + d_{xz} 23.17%). MO 84 is the lowest energy metal-based MO, which is mainly comprised of d_{xy} (23.99%). The remaining MO's, such as 92, 85, 83 and 82, are primarily ligand-based with only minor components of Fe atomic orbitals. Overall, the scenario that emerges is one where there are primarily three orbitals oriented properly to interact with the incoming sixth ligand: d_{x2-y2} and d_{yz} (unoccupied), and d_{xy} (occupied). However, the relatively low energy of d_{xy} precludes its participation as a frontier orbital for interacting with the incoming ligand. In contrast, the energies of the unoccupied and energetically accessible d_{x2-y2} and d_{yz} orbitals (i.e. the frontier orbitals) will be strongly modulated by the binding the sixth ligand.

Additionally, Dey has reported that the electronic structure of Hmd active site shows an extensive delocalization of electron density from metal *d*-orbitals to CO π*, pyridine/pyridone π* or acyl π* orbitals, as well as among the orbitals of ligands mediated by metal *d*-orbitals.[25] The delocalization is derived from the binding of strong π-acid ligands. As a result, the active site is fairly Lewis acidic and shows large affinity towards anionic ligands (H^- and CN^-). This presumably assists in the formation of a proposed hydride intermediate during catalysis. Likewise, the back-bonding between Fe orbitals and π-acid ligands is also present in the electronic structure of $\mathbf{2}^+$, as shown in MO 93, 92, 90. Indeed, the Lewis acidity of the Fe center in these *mer*-CNS pincer

complexes is considerable, as proven by the large binding energy for anionic ligand (Br^-). However, the equatorial orientation of the ligand backbone causes the sixth empty coordinating site to be *trans* to CO, a strong π-acceptor ligand which could make the incoming sixth ligand (Br^- for **1**) inert with the respect to substitution reaction.

Ultimately, the electron density at the metal center is *one* of the factors that allows the unique Fe(II) center found in [Fe]-hydrogenase to act as both a hydride abstractor (e.g. from H_2, or in the reverse reaction from H_4MPT) *and* as a hydride transfer agent (to H_4MPT^+). That is, a putative iron-hydride intermediate should not be so stable as to be unreactive for fast catalytic turnover. Thus, it is somewhat perplexing that the Hmd active site contains two strongly π-accepting CO ligands, while at the same time it also contains two extremely strong σ donors: the cysteinyl thiolate (pK_a ≈ 8-9, strong π donor) and the acyl carbanion (pK_a > 20, π acceptor). These donors might, upon first inspection, appear to mitigate one another's effects – and probably do to a certain extent. One may conclude, then, that the combination of strongly anionic and strongly π-accepting ligands provides some specific purpose for modulating or polarizing the electron density at the metal center.

Although the dicarbonyl and organometallic Fe–C(=O) bonding motifs in the present complex are thermally stable, reactivity studies of **2** with H_2 or D_2, and bases (KO^tBu, potassium 2,6-di-*tert*-butyl-4-methoxyphenolate) did not prove fruitful: neither H_2/D_2 splitting, H–D scrambling nor N*H*→N*D* exchange was observed. However, the MO analysis detailed above may provide critical insight into the lack of reactivity in this case. For example, if the interaction of an incoming H_2 molecule with $\mathbf{2}^+$ is considered, one can primarily focus on the interactions of H_2 with the HOMO and LUMO, i.e. the frontier orbitals. Specifically, it is apparent that in $\mathbf{2}^+$, the LUMO (MO 91: $d_{yz}|d_{x2-y2}$ admixture) is oriented in ideal fashion (pointed at the vacant site) to accept electron

density from the H–H σ bond (e.g. a Kubas M–(H–H) interaction[2,3]). Meanwhile, the primary character of the HOMO orbital in $\mathbf{2}^+$ (d_{yz}; MO 90) is an Fe–C(=O) σ bonding motif: only a small portion of the occupied d_{yz} is oriented towards the vacant site. Thus, the overall effect is that both metal-based components of the HOMO and LUMO orbitals are codirectional (**Figure 2.4**, MO 90 and 91).

As shown in **Scheme 2.4** below, the ideal arrangement of LUMO and HOMO to interact with σ(H–H) and σ*(H–H) involves *orthogonal* orientations of the frontier orbitals, so as to facilitate H_2 heterolytic splitting. In the present complex $\mathbf{2}^+$, we postulate that the *codirectional* nature of the HOMO and LUMO orbitals likely prevents any substantial interaction with H_2, let alone facilitating heterolytic cleavage.

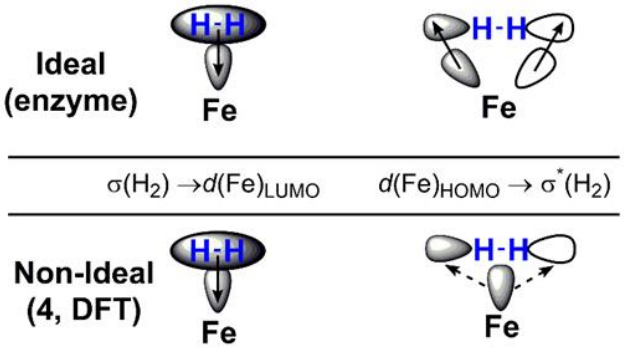

Scheme 2.4 Frontier orbital interactions between H_2 and Fe indicating ideal (top) and non-ideal (bottom) d orbital orientations for heterolytic H_2 cleavage.

Notably, another distinction of $\mathbf{2}^+$ from the enzyme active site is the equatorial CNS donor set of $\mathbf{2}^+$. This coordination forces a CO ligand to be *trans* to the H_2 binding site. Kubas[3] has indicated that, in order to increase the Fe–H_2 interaction and facilitate the H_2 activation, neither a strong π acceptor (CO) nor a strong σ donor (H^-) should be *trans* to H_2. A strong π acceptor *trans* to H_2 would compete with H_2 for π electron density, which could otherwise contribute to back-donation to the σ*(H–H) orbital (**Scheme 2.4**,

top). The overall effect is less weakening of the H–H bond. On the other hand, a strong σ donor – such as hydride – could exert a strong *trans*-effect to the H_2, which would lessen the σ donation from H_2 and thus decrease the Fe–H_2 interaction. Therefore, it is best that the ligand *trans* to H_2 is a weak π acceptor as well as a mediocre σ donor. The ligand *trans* to H_2 in the Hmd active site is acyl group, which is a π acceptor and strong σ donor. It is possible that this tunes the electron density and orbitals on the Fe center in such way that the Fe is primed to interact with H_2 molecule sufficiently and cleave H_2.

In contrast, separate work showed that the anthracene-based carbamoyl complex[13] that mimics the *facial* NCS orientation of [Fe]-hydrogenase was competent for heterolytic H_2/D_2 splitting to form an Fe–H/Fe–D species, which donates the hydride to proton, but not to imidazolium substrate. We concluded on this basis that the anthracene-scaffold based model is a good agent for hydride abstraction, but not good for hydride transfer. Considering that the most important difference between complex $\mathbf{2}^{+}$ and the anthracene-based compound is the *mer* vs *fac* coordination mode – and the fact that the Hmd active site also presents a *facial* CNS framework – these results in concert strongly suggest that the *facial* coordination mode (open site *trans* to anionic C donor) is imperative for H_2 binding and activation in the Hmd active site. We thus conclude that the lack of H_2 reactivity in the present case is attributable to the non-ideal orientations of the frontier orbitals and strong π acceptor ligand *trans* to the substrate binding site, resulting from the equatorial CNS donor set.

2.4 Ligand Substitution Reactions of *mer*-CNS Complexes

As is shown in the previous section, the bromide-bound complex **1** shows significant stability. The presence of a carbamoyl unit increases the electron density of the iron center which stabilizes the dicarbonyl core. To study the tunability of the iron

center by substituting the CO or Br^- ligand for other L-type ligands for developing new type of hydrogen catalysts, we synthesized a series of monocarbonyl and dicarbonyl complexes and studied their spectroscopic properties.

2.4.1 Synthesis

All of the ensuing substitution reactions are summarized in **Scheme 2.5**. The reagents $AgBF_4$ and $TlBAr^F_4$ readily abstracted bromide in most solvents (MeCN, THF, DCE – with or without strongly coordinating ligand), but treatment of **1** with $NaBAr^F_4$ removed Br^- only in the presence of a strongly coordinating ligand (i.e. PPh_3, pyridine – but not MeCN or THF). The acetonitrile-bound complex (**3d**) was synthesized using $AgBF_4$ in MeCN, leading to facile isolation of the solvated complex **3d**. The other bromide replaced complexes (**3a-c**, **3e** and **3f**) were obtained by using $NaBAr^F_4$ in the presence of strongly coordinating ligands in non-coordinating solvents, such as DCE or fluorobenzene (PhF). Substitution of bromide with PPh_3, for example, did not occur in the absence of halide abstracting agents. This suggests that the bromide in our model complex is fairly inert. Comparing this with the active site of the [Fe]-hydrogenase, the *trans*-influence of CO (to promote ligand substitution) is much weaker than that of the acyl group in the FeGP cofactor, wherein the substitutionally active solvent/substrate site is located *trans* to the acyl group. In the interest of modulating the electron density of Fe center, the reaction of **1** with $Na[S(2,6\text{-}Me_2C_6H_3)]$ in THF accessed the neutral dicarbonyl thiolate complex $[(^{O=}C^{NH}N^{py}S^{Me})Fe(CO)_2(S(2,6\text{-}Me_2C_6H_3))]$ (**3g**). Notably, complex **3g** is stable at room temperature under N_2 for days.

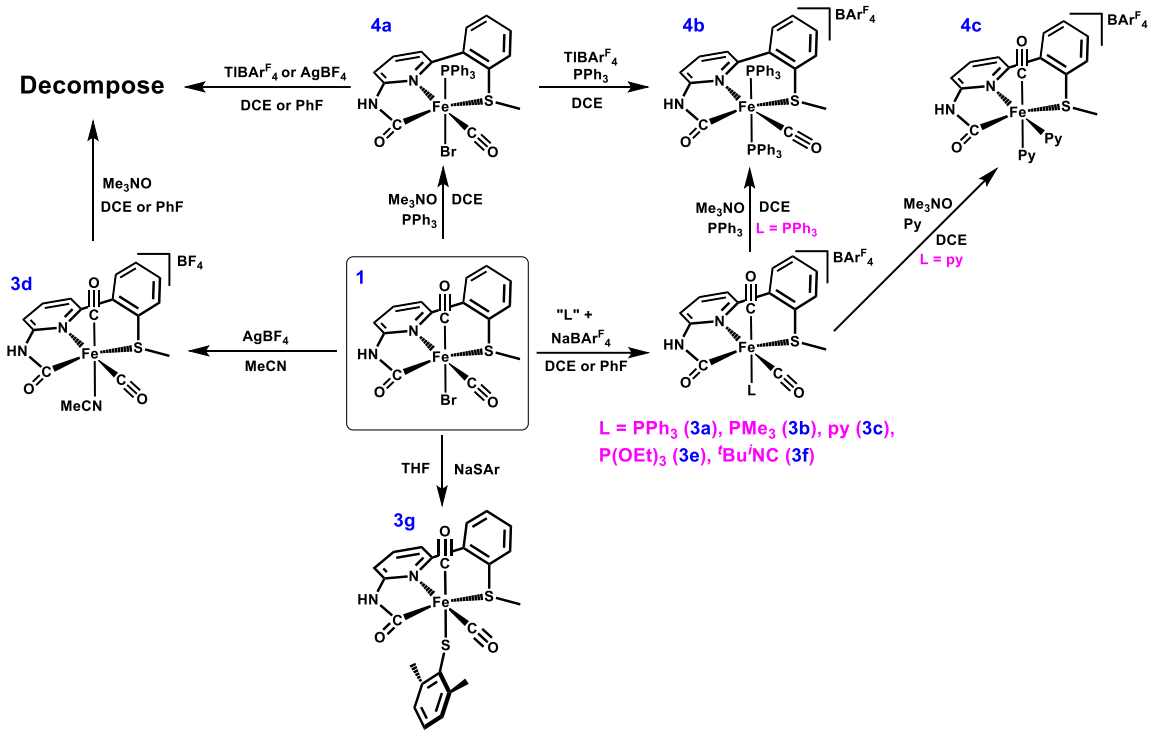

Scheme 2.5 Synthetic routes and interconversions for halide abstraction and CO rmoval in the present set of complexes.

The substitution reaction of one CO ligand was also investigated. Reaction of **1** with excess Me_3NO in presence of PPh_3 afforded the monocarbonyl species formulated as [($^{O=}C^{NH}N^{py}S^{Me}$)Fe(CO)(PPh_3)(Br)] (**4a**); the remaining CO ligand was unaffected by subsequent additions of Me_3NO at room temperature. Exposure of **4a** to $TlBAr^F_4$ in the presence of PPh_3 generated [($^{O=}C^{NH}N^{py}S^{Me}$)Fe(CO)(PPh_3)$_2$] (**4b**), which was alternately prepared directly by (*i*) halide replacement of **1** in presence of PPh_3, and (*ii*) CO replacement by PPh_3. The monocarbonyl complex [($^{O=}C^{NH}N^{py}S^{Me}$)Fe(CO)(py)$_2$] (**3c**) was synthesized by the similar method. The synthesis of monocarbonyl complexes revealed the trend of CO replacement. The decarbonylation of cationic complexes is more facile than the neutral complexes. The synthesis of **4a** from **1** requires adding Me_3NO as much as 2.3 equivalent to drive the reaction to completion, whereas the decarbonylation of **3a**

to afford **4b** can be achieved by 1.3 equivalent of Me_3NO. This can be rationalized by the higher electron density of the neutral complex **1** compared with the cation **3**. As a good σ-donor, bromide anion in neutral complex **1** stabilizes the CO ligand, making decarbonylation thermodynamically unfavorable. Therefore, the bisphosphine complex **4b** is much more accessible by first replacing the bromide ligand, and then the carbonyl ligand.

It is notable that the pentacoordinate *mono*carbonyl complexes rapidly decompose at room temperature (**4a** or **3d** to decomposition in **Scheme2.5**), yielding unidentifiable products. From these reactivity studies, some trends can be inferred in the context of the [Fe]-hydrogenase active site chemistry. Indeed, an authentic pentacoordinate intermediate has been structurally observed,[11] and it has been mechanistically invoked as the active species of H_2 activation, as well as for hydride abstraction from H_4MPT in the reverse reaction.[7,8] Therefore, the stability and structural viability of such a pentacoordinate species is a prerequisite for proper function of the enzyme. While many stable monocarbonyl complexes of Fe(II) exist, a select few can, in fact, exhibit an intermediate spin state.[27,28] The formation of such an intermediate spin species would (*i*) lead to lower binding affinity of the remaining CO ligand (via population of anti-bonding e_g* orbitals), and/or (*ii*) generate unpaired spins to promote radical chemistry (i.e., H• rather than H^-) that would derail the controlled, two-electron chemistry necessary for clean hydride transfer or abstraction. In contrast, there are no *cis*-dicarbonyl, Fe(II) species that exhibit unpaired spins. This could explain why the present set of *di*carbonyl, pentacoordinate species **2** (*vide supra*) are stable as authentic pentacoordinate species in many non-coordinating solvents (DCE, PhF; not DCM or $CHCl_3$), or as a solvato species in coordinating solvent (THF, MeCN, etc.). With regards to six-coordinate complexes, another trend is that isolation of a stable monocarbonyl species is dependent on the

premise of a strongly donating sixth ligand, such as Br^-, PPh_3 or pyridine. Attempts at isolating a variety of solvato species of *mono*carbonyls were not successful. All of the above observations indicate the critical importance of the *cis*-$\{Fe(CO)_2\}^{2+}$ motif in stabilizing the active site during catalysis.

2.4.2 Structural and Spectroscopic Characterization

The in-depth characterizations of the aforementioned dicarbonyl and monocarbonyl complexes are presented in this section, starting from the X-ray structures and followed by spectroscopic characterizations.

$[(^{O=}C^{NH}N^{py}S^{Me})Fe(CO)_2(PPh_3)](BAr^F_4)$ (3a) and $[(^{O=}C^{NH}N^{py}S^{Me})Fe(CO)_2(PMe_3)](BAr^F_4)$ (3b). These two complexes (**Figure 2.5**) crystallize as cationic species with the charge balance provided by BAr^F_4 anion. They are isostructural and exhibit the same coordination mode as **1**, except that PPh_3 or PMe_3 coordinates to the Fe center instead of bromide. The selected bond metrics are tabulated in **Table 2.6**. The change from an anionic bromide to neutral phosphine ligand results in shortening of the C(13)–Fe(1) bond distance of in both complexes [1.947(3) Å in **3a** and 1.944(6) Å in **3b**] as compared to **1** [1.939(7) Å]. This can be related to the decrease of electronic density in the Fe center and, as a result, weaker π back-bonding to the carbamoyl. The steric hindrance of PPh_3 and PMe_3 plays a critical role in controlling the structural features (cone angle θ = 145° and 118°, respectively).[29] This can be evidenced by the fact that the P(1)–Fe(1) bond distance in both complexes [2.3532(9) Å in **3a** and 2.2942(17) Å in **3b**] are slightly longer than typical low-spin, Fe(II)–P bonds (2.16 Å to 2.28 Å)[30,31]; the aryl ring is tilted towards the phosphine ligand, which results in the -$S(CH_3)$ group pointing towards the carbonyl. In particular, the ligand framework in **3a** is more planar than **3b**, with a pyridine-aryl dihedral angle of 35.65°, as compared with **3b**

(38.63°) and **1** (41.07°). This corresponds to the larger steric hindrance of PPh_3 versus PMe_3 (see cone angles) or Br^-. Interestingly, some weak interactions are present and non-trivial in **3a** and **3b**. The π···π stacking interaction is found in **3a** between one of the phenyl rings in PPh_3 [C(16)….C(21)] and the aryl ring on the CNS ligand backbone [C(6)….C(11)] (**Figure A5**, in Appendix A). In addition, an aliphatic CH···π interaction is found in **3b** (**Figure A6**). One of the C–H bonds on PMe_3 interacts with the aryl ring on the CNS backbone in a T-shape fashion Like **1**, the crystal structures of **3a** and **3b** consist of enantiomers that form a dimeric unit by hydrogen bond between the carbamoyl unit [O•••H–N, 2.801(4) Å in **3a**, 2.867(5) Å and 2.819(6) Å in **3b**] (**Figure A1**).

[($^{O=}C^{NH}N^{py}S^{Me}$)Fe(CO)$_2$(py)](BAr$^F_4$) (3c) and [($^{O=}C^{NH}N^{py}S^{Me}$)Fe(CO)$_2$(MeCN)](BF$_4$) (3d). The X-ray structure (**Figure 2.5**) of the py-bound cation, **3c**, and MeCN-bound cation, **3d**, reveal similar structural arrangements of the ligand frame as found in **1**. Both complexes are cationic with charge balance provided by $BAr^F_4^-$ and BF_4^-, respectively. The pyridine in **3c** and acetonitrile in **3d** have substituted for bromide and are coordinated to the iron center with Fe(1)–N(3) of 2.061(5) and 1.9667(18) Å, respectively. The Fe–N_{MeCN} bond in **3d** is typical for acetonitrile bound to low-spin Fe(II),[32,33] and the Fe–N_{py} bond in **3c** is within the typical iron-pyridine bond in low-spin Fe(II) complexes (1.94 Å to 2.07 Å).[34,35] This is probably due to the tilting of the py ligand to avoid the steric clash of its *ortho*-H with the *cis* carbonyl, wherein the pyridine slants about 37° with respect to Fe(1)–C(15) bond. Such a tilt results in a predominantly σ-only Fe–N_{py} bond, as the π-bonding $d_{xy,xz,yz}$ orbitals do not achieve substantial overlap with the π^*(py) orbitals, per the normal iron-pyridine bonding interaction. This effect is also evidenced by the compensating nature of the shorter C(14)–Fe(1) bond distance [1.769(7) Å] in **3c**, as compared to those in **1**, **3a**, **3b** and **3d** (≥ 1.80 Å).

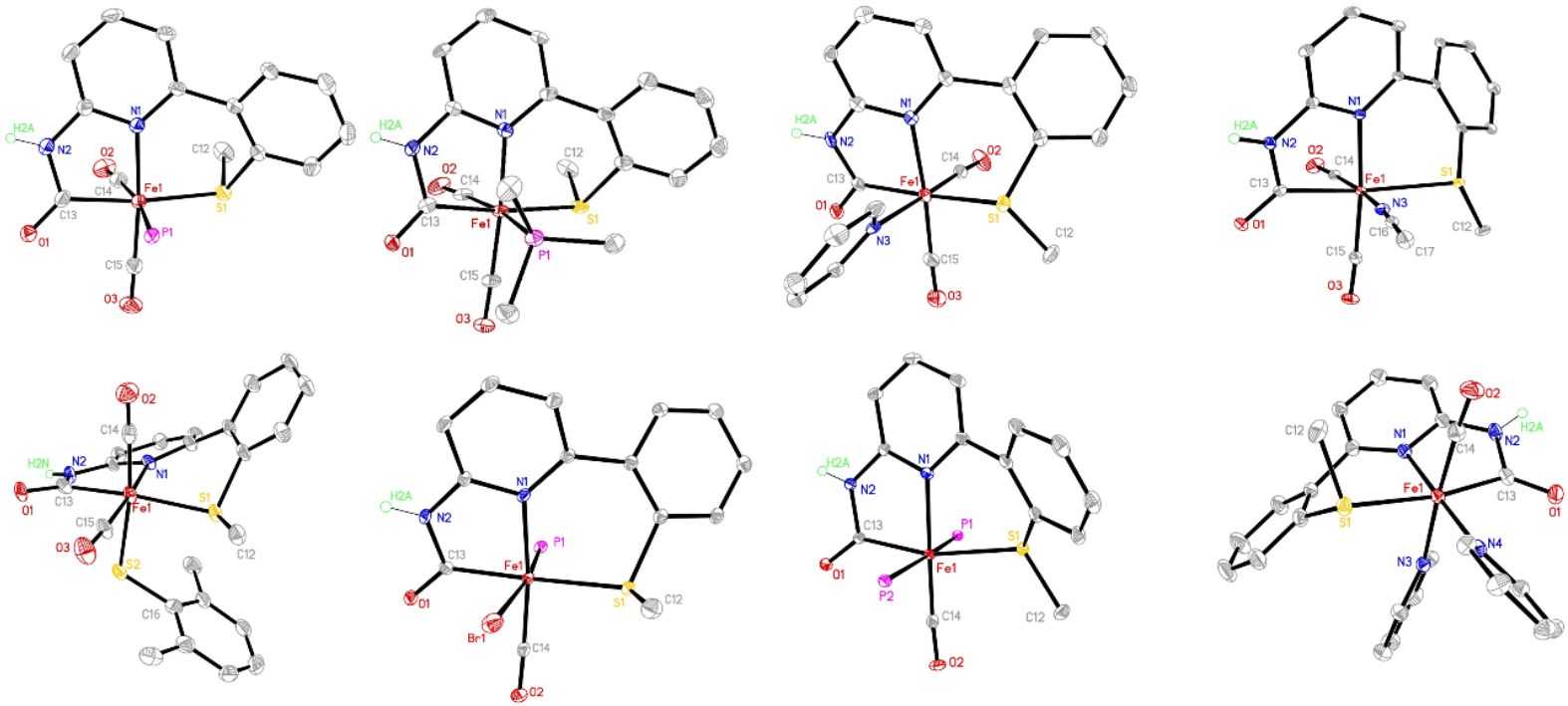

Figure 2.5 ORTEP diagrams (30% probability ellipsoids) of [($^{O=}C^{NH}N^{py}S^{Me}$)Fe(CO)$_2$(PPh$_3$)](BAr$^F_4$) (**3a**), [($^{O=}C^{NH}N^{py}S^{Me}$)Fe(CO)$_2$(PMe$_3$)](BAr$^F_4$) (**3b**), [($^{O=}C^{NH}$NpySMe)Fe(CO)$_2$(py)](BAr$^F_4$) (**3c**), [($^{O=}C^{NH}N^{py}S^{Me}$)Fe(CO)$_2$(MeCN)](BF$_4$) (**3d**), [($^{O=}C^{NH}N^{py}S^{Me}$)Fe(CO)$_2$(S(2,6-Me$_{3c6}$H$_3$))] (**3g**), [($^{O=}C^{NH}N^{py}S^{Me}$)Fe(CO)(Br)(PPh$_3$)] (**4a**), [($^{O=}C^{NH}N^{py}S^{Me}$)Fe(CO)(PPh$_3$)$_2$](BAr$^F_4$) (**4b**) and [($^{O=}C^{NH}N^{py}S^{Me}$)Fe(CO)(py)$_2$](BAr$^F_4$) (**4c**). All hydrogen atoms except for the N*H* have been omitted for clarity; PPh$_3$ phenyl units in **3a**, **4a** and **4b** have also been truncated.

Table 2.6 Selected bond lengths (Å) and angles (°) from the X-ray structures of **3a-d, 3g,** and **4a-c.**

Cmpd	**3a**	**3b**	**3c**	**3d**	**3g**	**4a**	**4b**	**4c**
L	PPh_3	PMe_3	py	MeCN	2,6-$Me_2C_6H_3$	Br, PPh_3	PPh_3	py
N(1)−Fe(1)	2.016(2)	2.007(4)	1.996(5)	2.0070(15)	2.012(4)	2.016(2)	2.0664(19)	1.987(3)
C(13)−Fe(1)	1.947(3)	1.944(6)	1.920(6)	1.951(2)	1.931(5)	1.922(3)	1.961(2)	1.932(3)
C(14)−Fe(1)	1.817(4)	1.817(6)	1.769(7)	1.794(2)	1.787(6)	1.757(3)	1.742(2)	1.772(3)
C(15)−Fe(1)	1.792(3)	1.767(6)	1.772(7)	1.799(2)	1.789(5)	—	—	—
S(1)−Fe(1)	2.3161(9)	2.3215(17)	2.3257(18)	2.3285(6)	2.3035(13)	2.3311(8)	2.300(6)	2.3551(9)
C(13)−N(2)	1.391(4)	1.394(7)	1.383(7)	1.3870(3)	1.394(6)	1.394(4)	1.395(3)	1.400(4)
C(13)−O(1)	1.223(4)	1.224(6)	1.249(7)	1.218(2)	1.237(6)	1.243(4)	1.226(3)	1.234(4)
C(14)−O(2)	1.130(4)	1.149(7)	1.146(7)	1.1310(3)	1.135(7)	1.145(4)	1.162(3)	1.147(4)
C(15)−O(3)	1.138(4)	1.149(7)	1.145(7)	1.136(2)	1.120(6)	—	—	—
Br(1)−Fe(1)	—	—	—	—	—	2.4965(6)	—	—
N(3)−Fe(1)	—	—	2.061(5)	1.9667(18)	—	—	—	2.042(3)
N(4)−Fe(1)	—	—	—	—	—	—	—	2.004(3)
P(1)−Fe(1)	2.3532(9)	2.2942(17)	—	—	—	2.2360(9)	2.3505(7)	—
P(2)−Fe(1)	—	—	—	—	—	—	2.3041(7)	—
S(2)−Fe(1)	—	—	—	—	2.4023(15)	—	—	—
O•••H–N	2.801(4)	2.867(5) 2.819(6)	2.800(7)	—	2.845(6)	2.810(3)	2.977(3)	2.845(4)
pyridine-aryl dihedral angle	35.65°	38.63°	36.92°	41.52°	41.81	37.24°	37.17°	39.59°

Another unique feature in **3c** and **3d** is that both the phenyl ring and -S(CH_3) group are directed towards the carbonyl *trans* to py/MeCN. This is distinct from **1**, **3a** and **3b** – wherein the aryl and -S(CH_3) units are positioned on opposite sides of the complexes. The lack of any intramolecular π interactions could likely account for this interesting phenomenon.

[($^{O=}C^{NH}N^{py}S^{Me}$)Fe(CO)$_2$(S(2,6-$Me_2C_6H_3$))] (3g). The crystal structure of neutral complex **3g** shows an octahedral geometry with (2,6-$Me_2C_6H_3$)S^- bound to Fe center in place of Br^- in **1** (**Figure 2.5**). The aryl plane of the thiolate tilts away from the axis of C(14)–Fe(1)–S(2) with a bond angle of C(16)–S(2)–Fe(1) = 111.48(17)°. The anionic nature of thiolate increases the electron density of the Fe center, as a result, the bond distances of C(13)–Fe(1), C(14)–Fe(1) and C(15)–Fe(1) are shortened, compared to complex **1** (C(13)–Fe(1) = 1.931(5), C(14)–Fe(1) = 1.787(6) and C(15)–Fe(1) = 1.789(5) Å). This is also evidenced by the lower wavenumber of the CO stretches of **3g** than those of complex **1** in IR (*vida infra*). The aryl ring of the ligand backbone inclines towards the carbonyl group and the methyl group of thioether points away from the exogenous thiolate aryl group because of the steric hindrance of the thiolate.

[($^{O=}C^{NH}N^{py}S^{Me}$)Fe(CO)(Br)(PPh_3)] (4a). The crystal structure of the neutral, CO-substituted complex **4a** (**Figure 2.5**) reveals an asymmetric pseudo-octahedral coordination environment with an Fe center coordinated to the CNS ligand in equatorial fashion, a carbonyl *trans* to pyridine, and Br^- and PPh_3 in *trans* fashion. The C(13)–Fe(1) bond length in **4a** [1.922(3) Å] is shorter than those in **1** [1.939(7) Å], due to the substitution of CO by PPh_3 and, thus, higher electron density on the Fe center. This also affects the C(14)–Fe(1) bond length [1.757(3) Å], which is shorter than all the previous dicarbonyl complexes. The P(1)–Fe(1) bond distance [2.2368(9) Å] is within the normal range of iron–phosphorous bond length (2.16 Å to 2.28 Å).[30,31] Again, a strong π···π

stacking interaction is observed (**Figure A7**) between the aryl ring on CNS ligand [C(6)–C(7)–C(8)–C(9)–C(10)–C(11)] and phenyl ring on PPh_3 [C(21)–C(22)–C(23)–C(24)–C(25)–C(26)]. This π···π stacking interaction facilitates the tilt of the ligand aryl unit towards PPh_3, thus leaving the –S(CH_3) unit pointing towards bromide. The 'choice' of the CO ligand to orient itself *trans* from the neutral py donor, rather than *trans* from the anionic bromide is a curious one. This orientation demonstrates the dominant effect of the aryl-PPh_3 π···π stacking in determining the molecular conformation of **4a**. In addition, this prevents the PPh_3 from clashing with -S(CH_3) group.

[($^{O=}C^{NH}N^{py}S^{Me}$)Fe(CO)(PPh_3)$_2$](BAr^F_4) (4b). The cationic complex **4b** exhibits a pseudo-octahedral geometry with similar structure as in **4a** except that the bromide in **4a** is substituted by a PPh_3 ligand. The crystal structure is shown in **Figure 2.5**. Unsurprisingly, the complex takes on the highest symmetry structure with *trans*-PPh_3 moieties. The two PPh_3 ligands significantly increase the electron density at the Fe center, and thus enhance the Fe–C(O) back-bonding interaction. As a result, the C(14)–Fe(1) bond distance [1.742(2) Å] is the shortest among all of the crystal structures reported herein. The aryl unit on the CNS ligand inclines towards P(2), while the –S(CH_3) group points towards P(1). The phenyl ring forms π···π stacking interaction (**Figure A8**) with one phenyl ring attached to P(2) [centroid-to-centroid distance = 3.9667(16) Å; interplanar spacing = 3.5146(10) Å; dihedral angle = 3.95(13)°]. Another π···π stacking interaction is also observed between the pyridine ring and a phenyl ring on P(1) [centroid-to-centroid distance = 3.5427(15) Å; interplanar spacing = 3.2231(10) Å; dihedral angle = 8.39(12)°].

[($^{O=}C^{NH}N^{py}S^{Me}$)Fe(CO)(py)$_2$](BAr^F_4) (4c). The cation of **4c** crystallizes with BAr^F_4 (**Figure 2.5**) and reveals a similar coordination environment as found in **4b**, except that the two pyridine ligands are bound in *cis* fashion. The N(3)–Fe(1) and N(4)–Fe(1)

bonds [2.042(3) Å and 2.004(3) Å] are slightly longer than the normal range for pyridine bound to low-spin Fe. The *cis*-orientation of the pyridine ligands and resulting orientation of the CO ligand (*trans* to exogenous CO) is attributable to steric issues emanating from the close proximity of the exo-pyridine *ortho*-H's. In this case, the alternate *trans*-L orientation (as found for PPh_3 in **4b**) would result in the CO ligand being sterically 'sandwiched' between two sets of *ortho*-H's, whereas in the experimentally observed structure the CO only interacts with a single py ligand.

IR Spectroscopy. The CO stretch is usually a reliable measure of electron density at the metal center, as the metal (d_π)(M)→CO(π^*) back-donation is influenced by the electron density of the metal. Substitutions of Br^- by any tested L-type ligands result in a blue-shift of ν(CO) to as high as 2093, 2046 cm^{-1} (**3e**; L = ^{t}BuNC) (**Table 2.7**). Based on the solid state ν(CO) of tested complexes (**1** to **3f**), the order of ligands with decreasing electron donating ability is Br^- (**1**) > PPh_3 (**3a**) ≈ $P(OEt)_3$ (**3e**) > PMe_3 (**3b**) > py (**3c**) > MeCN (**3d**) > ^{t}BuNC (**3f**). It is noteworthy that PR_3 (strong σ donor, weak π acceptor) presents higher electron donating effect than pyridine, MeCN (weaker σ donors, good π acceptors) and ^{t}BuNC (weak σ donor, strong π acceptor). Among the phosphine ligands, PMe_3 unexpectedly offers the smallest electronic donating effect among the three phosphine ligands. This is also unexpected based on the much shorter Fe–P bond found for PMe_3 (**3b**: 2.2942(17) Å) versus PPh_3 (**3a**: 2.3531(11) Å). Compared with the 5-coordinate **2** ($BAr^F{}_4$ salt), all the exogenous L-type ligands (except for ^{t}BuNC, py and MeCN) demonstrate an electron donating effect on the Fe center, since all of the CO stretching frequencies are lower energy than **2** (2057 and 2008 cm^{-1}). The ^{t}BuNC ligand exhibits the strongest electron withdrawing effect among all the L-type ligands, shifting the ν(CO) of **3f** to the highest frequencies (2093, 2046 cm^{-1}). The similar ν(CO) values between **3a** and **3b** (2057 and 2008 cm^{-1} for **3a** and 2061 and 2009 cm^{-1} for **3b**) indicate

that PMe_3 imparts almost equivalent electron donating and withdrawing effects, and, therefore exerts negligible change to the electron density at the Fe center.

Table 2.7 Selected ν(CO) in solid state and solution (DCE) IR measurements for the complexes, as well as both the Hmd active site and isolated FeGP cofactor.

Complex (L)	ν(C≡O), cm^{-1} solid state	ν (C≡O), cm^{-1} Solution[e]	ν(C=O), cm^{-1} solid state
3a (PPh_3)	2052, 2002	2051, 1996	1628
3b (PMe_3)	2061, 2009	2058, 2008	1631
3c (py)	2069, 2010	2061, 2012	1639
3d (MeCN)	2069, 2023	2071, 2020	1645
3e ($P(OEt)_3$)	2055, 2001	2051, 1994	1630
3f (^{t}BuNC)	2093, 2046	2058, 2006	1664
3g (S^{Ar})	2015, 1963	2029, 1975	1614
4a (Br, PPh_3)	1946	1958	1598
4b (PPh_3)	1919	1951	1609
4c (py)	1989	1975	1624
[Fe]-hydrogenase	1996, 1928[a]	2011, 1944[b]	–
FeGP cofactor	2004, 1934[c]	2031, 1972[d]	–

[a] Spectrum of solid sample coordinated by dithiothreitol (DTT); data taken from ref [21]; [b] Spectrum of sample dissolved in water; data taken from ref [20]. [c] Spectrum of solid sample extracted with 2-mercaptoethanol; data taken from ref [22]. [d] Spectrum of sample extracted with 2-mercaptoethanol and dissolved in water; data taken from ref [20]. [e] MeCN was used for IR analysis for **3d**. The solution IR of enzyme was obtained in aqueous buffer solution.

To further demonstrate the effect of σ donor strength on ν(CO), as well as to more accurately model the electron density on the Fe center found in the enzyme, we also prepared the thiolate substituted complex [($^{O=}C^{NH}N^{py}S^{Me}$)$Fe(CO)_2$($S(2,6\text{-}Me_2C_6H_3)$)] (**3g**; **Figure 2.5**, bottom left). Although the promiscuous thiolate tends to form bridged dimer,[36] the bulky *ortho*-dimethyl groups cleanly prevented dimerization in this case. The resulting red-shifted IR features observed for **3g** (2015, 1963 cm^{-1}) suggest that the

thiolate (strong σ donor, strong π donor) does, indeed, increase the electron density at the metal center.

The carbamoyl stretching frequency [ν(C=O)] follows the same trend as ν(C≡O) in reflecting the electron density on Fe center. That is, the greater the electron density on Fe, the lower the stretching frequency: complexes **1** and **3g** (where X = Br, $SMe_2C_6H_3$) show the lowest stretching frequencies (1619, 1614 cm^{-1}, respectively), while **3f** (L = ^{t}BuNC) displays the highest value (1664 cm^{-1}). Of course, the fact that the thiolate occupies the 'open site' in the coordination sphere in the present ligand system clearly limits the functional utility of **3g** to a structural/electronic model.

The solution IR of all the bromide-substituted complexes (**3a** to **3f**) are blue-shifted in terms of carbonyl stretching frequency in solution IR. The order of *ν*(CO) is comparable with the solid-state value [Br^- (**1**) > PPh_3 (**3a**) ≈ $P(OEt)_3$ (**3e**) > PMe_3 (**3b**) ≈ ^{t}BuNC (**3f**) > py (**3c**) > MeCN (**3d**)], except that **3f** is red-shifted and presents lower *ν*(CO) than **3c** and **3d**.

The ν(CO) features of the mono-carbonyl complexes (**4a**, **4b** and **4c**) are all – generally – substantially lower than the corresponding dicarbonyl species. For example, complex **4b** with two axial PPh_3 ligands exhibits a *ν*(CO) at 1919 cm^{-1}, which is significantly red-shifted compared to the *ν*(CO) features in the dicarbonyl species **4a** (2052, 2002 cm^{-1}). Indeed, the lowest *ν*(CO) is 1919 cm^{-1} in **4b** (L = PPh_3), while the dipyridine complex **4c** presents the highest *ν*(CO) among these three (1989 cm^{-1}) – most likely due to the lower electron donating ability (and π acceptor character) of pyridine. Ligand effects of one versus two PPh_3 ligands notwithstanding, the reasons for the significant red-shift are two-fold (yet intertwined): First, all of the $d_\pi(Fe) \rightarrow \pi^*(CO)$ back-bonding is now focused on a single carbonyl ligand. Second, in the case of the dicarbonyls, the 'second' CO ligand induces the same effect that is observed for

exogenous ^{t}BuNC – it serves as a strong π-acceptor to remove electron density from the metal center (and the other CO ligand).

2.5 Reactivity of the Bromide Complex with Hydride and Base

The proposed mechanism of H_2 cleavage of Hmd from DFT calculation indicates the existence of a hydride intermediate from which Methenyl-H_4MPT$^+$ accepts H^- to afford Methylene-H_4MPT. Whereas, the hydride intermediate has not been experimentally identified from the native enzyme study. Herein, we summarize the reactivity study of Fe–H species generated from our *mer*-CNS model complex, which infers the property of the hydride species in the native enzyme. In addition, the reaction of **1** with strong base has also been studied and reported in this section.

2.5.1 Reactivity of Bromide Complex with Hydride

To emulate an iron-hydride intermediate as proposed for the enzymatic mechanism, complex **1** was treated directly with a hydride source (**Figure 2.6a**). A pale yellow, THF-d^8 solution of **1** was mixed with ~1 equiv of $NaHBEt_3$ at –70 °C. The resulting ^{1}H NMR spectrum obtained at –70 °C (**Figure 2.6b**) exhibits a notable peak at –5.08 ppm, attributable to a Fe–*H* species. This resonance exhibits an intermediate value compared with other reported iron(II) carbonyl hydrides, such as $[(P^{NH}N^{NH}P)Fe(H)(CO)_2]^+$ (δ_{Fe-H} = –7.47 ppm) and [(PNNP)Fe(H)(CO)] (δ_{Fe-H} = –2.25 ppm).[37,38] The Fe–*H* resonance is accompanied by a downfield shift in the N*H* feature to 11.66 ppm (parent **1**, δ_{NH} = 8.26 ppm). The presence of the shifted (but not absent) N*H* resonance provides evidence that H_2 is not eliminated, precluding the formation of a dearomatized intermediate at low temperature. On this basis, we assign the structure of the iron-hydride intermediate as $[(^{O=}C^{NH}N^{Py}S^{Me})Fe(H)(CO)_2]$ (**5**).

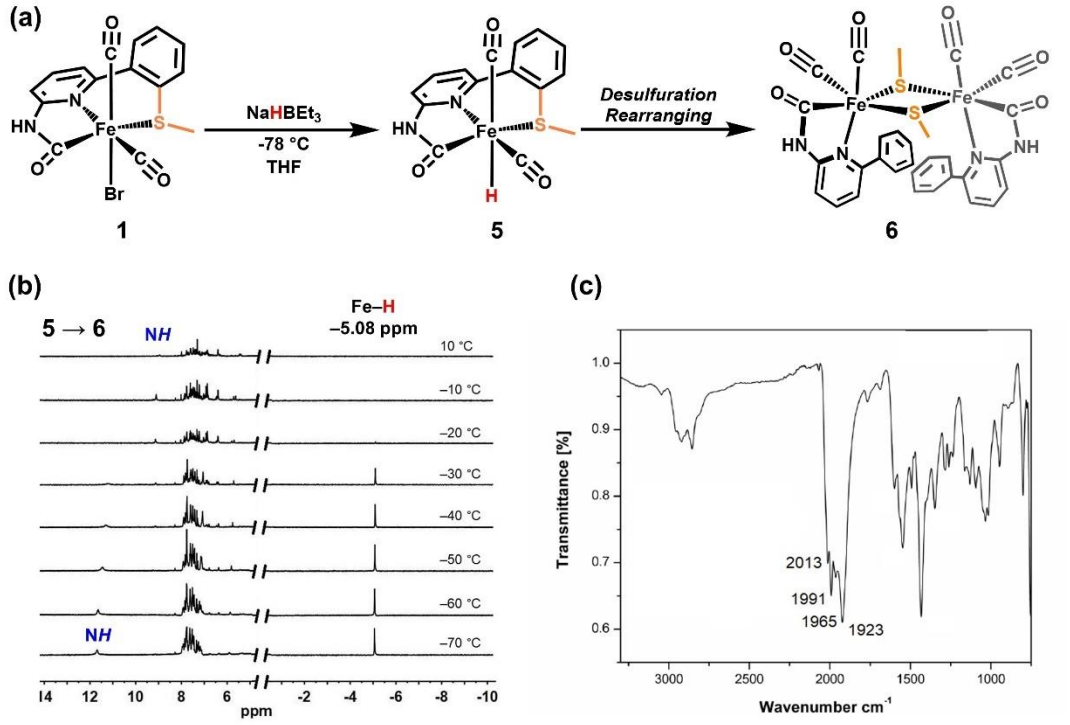

Figure 2.6 (a) Generation of [($^{O=}$C^{NH}N^{Py}S^{Me})Fe(H)(CO)$_2$] **5** from the reaction of **1** with NaHBEt$_3$, and the desulfuration rearrangement of **5** to μ_2-(CH$_3$S)$_2$-[($^{O=}$C^{NH}N^{Ph})Fe(CO)$_2$]$_2$ **6**. (b) VT ^{1}H NMR spectra (–70→–10 °C, 400 MHz) for the reaction of **1** in THF-d^8 with ~1 equiv NaHBEt$_3$ to form the iron-hydride species **5** and the conversion of **5** to **6** as temperature increases. (c) Infrared spectrum of **6** (neat). IR: 2013, 1991, 1965, 1923 cm^{-1}.

The variable temperature NMR study indicates that the hydride species **5** is stable between –70 °C and –40 °C. Above –40 °C, the Fe–*H* resonance decreases, indicating transformation to another species; this product was not readily identified by ^{1}H NMR spectroscopy. The solid-state IR exhibits four red-shifted ν(CO) features at 2015, 1995, 1965 and 1925 cm^{-1} (**Figure 2.6c**), indicating the formation of a species with more than two CO ligands. To structurally identify the product, a THF solution of **1** was treated with ~1 equiv NaHBEt$_3$ at RT. Following removal of THF and extraction into C$_6$D$_6$, the yellow product was re-dissolved in fluorobenzene/pentane to afford the dimeric species

μ_2-$(CH_3S)_2$-[($^{O=}C^{NH}N^{Ph}$)$Fe(CO)_2]_2$ (**6**) as a structurally characterized complex (**Figure 2.7**). In this complex, the C^{Ar}–S bond found in **1** has been cleaved, and the resulting (protonated) phenyl ring is twisted away from the core of the dimer. Notably, the Fe–$C(=O)^{NH}$ carbamoyl unit [Fe–C = 1.939(2) Å] and the *cis*-dicarbonyl fragments remain essentially undisturbed. The bridging methyl-thiolate units arrange the Fe–S distances at 2.3287(7) and 2.3679(7) Å, which fixes the two Fe(II) ions at a distance of ~3.544 Å within the Fe_2S_2 diamond core. It is important to note that the conversion from the hydride species **5** to dimeric **6** is completely stoichiometric, suggesting a controlled reaction pathway of intramolecular hydride transfer, followed by dimerization.

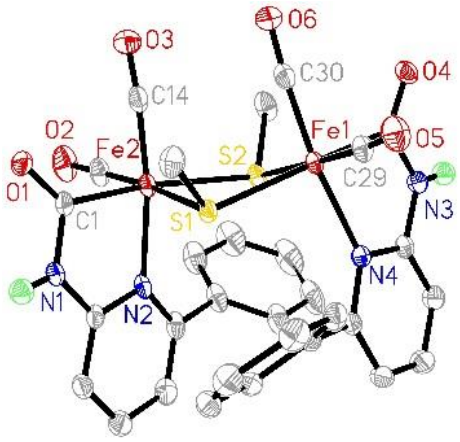

Figure 2.7 ORTEP diagram (30% ellipsoids) of μ_2-$(CH_3S)_2$-[($^{O=}C^{NH}N^{Ph}$)$Fe(CO)_2]_2$ (**6**); H atoms except N*H* are omitted for clarity. Selected bond distances (Å) and angles (°): Fe2–C1 = 1.939(2), Fe2–N2 = 2.083(2), Fe2–S1 = 2.3287(7), Fe2–S2 = 2.3679(7), Fe2–C14 = 1.751(3), Fe–C13 = 1.763(3); N1–C1–O1 = 119.0(2), Fe2–C1–N1 = 109.90(17), Fe2–C1–O1 = 130.9(2).

2.5.2 Reactivity of Bromide Complex with Base

To investigate the possibility of the hydride acting as a base (N*H*-activating agent) in the reaction, complex **1** was treated with a strong base (no hydride source). Reaction of a yellow solution of **1** in THF with ^{t}BuOK at room temperature rapidly generates a dark

red solution and a beige precipitate (KBr). Subsequently, extraction of the product into C_6D_6 affords a ^{1}H NMR spectrum (**Figure 2.8**, inset) indicative of a single species in solution. The resulting stable, yellow solid exhibits a red-shifted IR spectrum consistent with *cis*-dicarbonyl ligation, evidenced by ν(CO) = 2003 and 1940 cm^{-1} (**Figure 2.8**). The observation of an N*H* proton in the ^{1}H NMR spectrum of this isolated species shifted upfield to 7.35 ppm (for **1**, δ_{NH} = 9.96 ppm in d_8-THF), as well as the lack of a thioether resonance near $\delta_{CH3} \approx$ 2.60 ppm and the aforementioned desulfurization, led to formulation of this species as the putative five-coordinate CNC pincer [($^{O=}$C^{NH}NC^{Ph})Fe(CO)$_2$] (**8**) (**Scheme 2.6**).

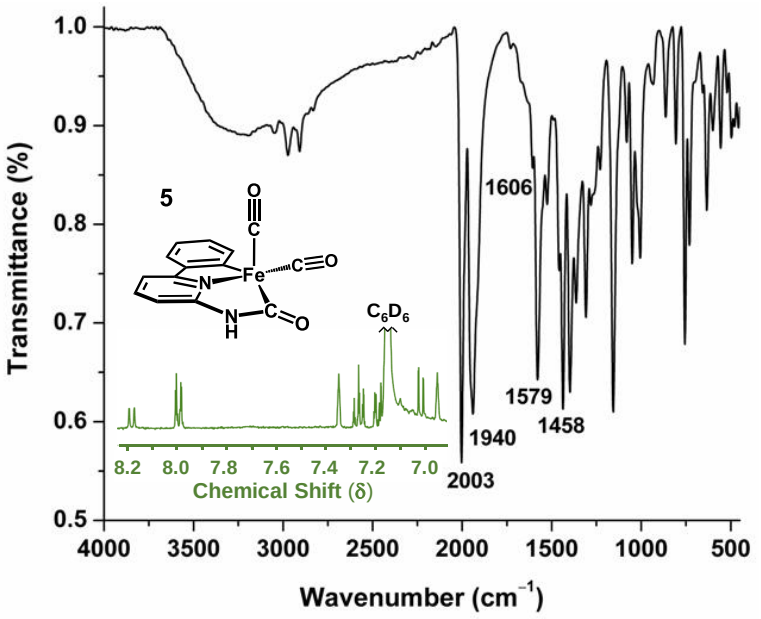

Figure 2.8 Infrared spectrum and ^{1}H NMR spectrum (*inset*) [($^{O=}$C^{NH}NC^{Ph})Fe(CO)$_2$] (**8**) in the aromatic region. IR: 2003 ν(C≡O), 1940 ν(C≡O), 1606 ν(^{HN}C=O), 1579 ν(C=N^{py}).

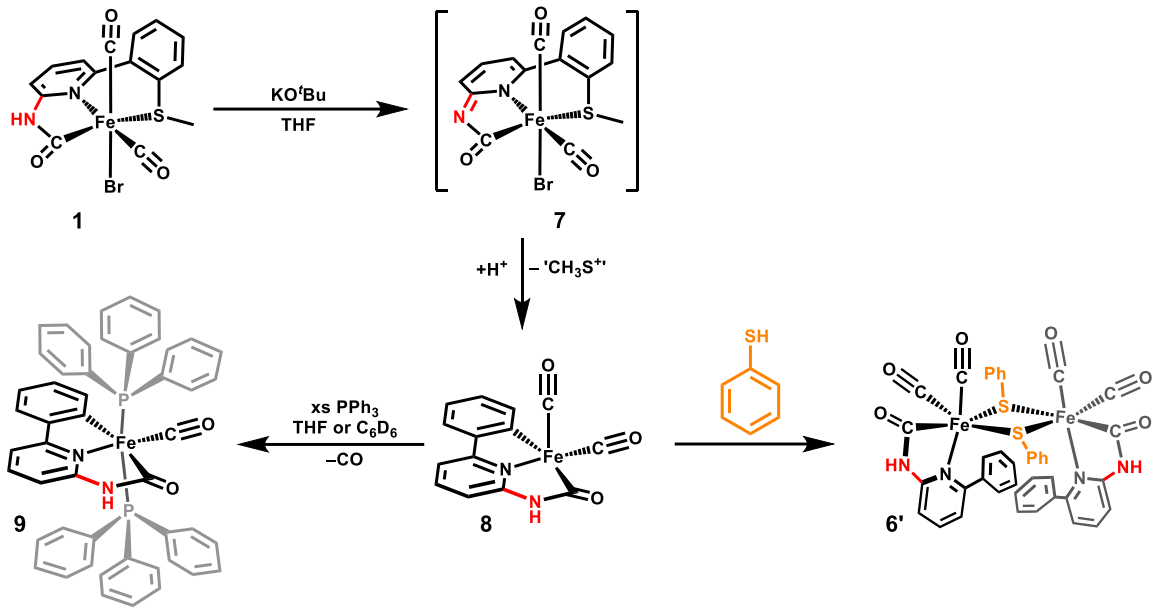

Scheme 2.6 Reactivity of **1** with strong base and the proposed intermediate.

To confirm the ligand binding mode of the putative cyclometalate, **8**, the complex was derivatized with PPh_3 for structural characterization. Reaction of **8** with excess PPh_3 in benzene followed by layering with pentane afforded yellow X-ray quality crystals of [($^{O=}C^{NH}NC$)Fe(CO)(PPh_3)$_2$] (**9**, **Figure 2.9**). The crystallographic analysis confirms *i*) desulfurization of the ligand framework, and *ii*) concomitant cyclometalation of the former *C*–S(CH_3) carbon directly to the Fe(II) center. Pseudo-octahedral **9** again retains the Fe–C(=O)NH carbamoyl unit, as well as one carbonyl; the remaining axial sites are occupied by PPh_3. To determine the fate of the extruded sulfur unit, an analogous reaction was performed in the presence of PMe_3 as a [S] scavenger. Extraction of the mixture into $CDCl_3$ afforded a ^{31}P NMR resonance at 30.3 ppm (Me_3P=S) (**Figure A9**), as well as a GC-MS peak at *m*/*z* = 109 [M+H$^+$] and a HR-MS peak at *m*/*z* = 108.0163 [M$^+$] (**Figure A10-A11**). Thus, we conclude that the base-assisted extrusion product is elemental sulfur.

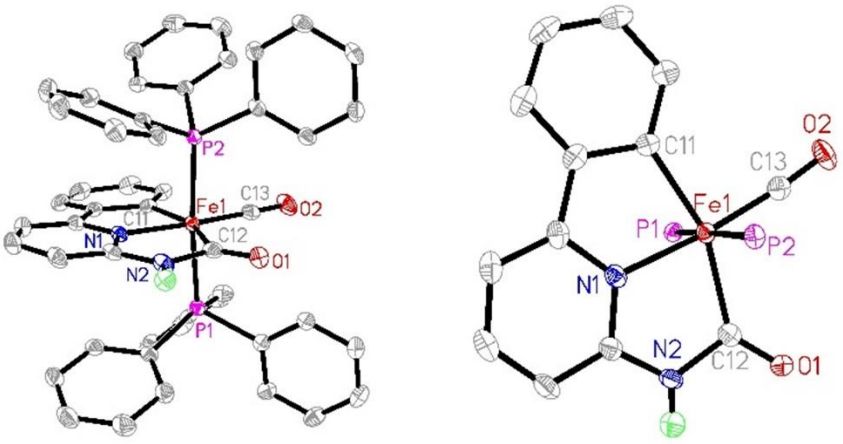

Figure 2.9 Two ORTEP views (50% ellipsoids) of [($^{O=}$C^{NH}NC)Fe(CO)(PPh$_3$)$_2$] (**9**); PPh$_3$ is truncated for clarity; all H-atoms except N*H* are omitted for clarity. Selected bond distances (Å) and angles (°): Fe–C11 = 2.009(2), Fe–C12 = 2.008(2), Fe–C13 = 1.725(2), Fe–N1 = 1.9540(18), Fe–P1 = 2.2531(6), Fe–P2 = 2.2525(6); C11–Fe–C12 = 159.36(9), N1–Fe–C13 = 174.36(9), P1–Fe–P2 = 174.92(3).

We thus postulate the formation the dearomatized species [($^{O=}$C$^{N=}$NS)Fe(CO)$_2$] ([**7**] in **Scheme 2.6**). Recent work has shown the feasibility of dearomatized iron complexes such as [**7**] involving metal/ligand cooperativity during catalysis with pincer complexes. For example, Kirchner and coworkers reported that the dearomatized pincer complex [($^{i\text{Pr}2}$P$^{N=}$N^{NH}P$^{i\text{Pr}2}$)Fe(CO)$_2$]$^+$ is formed upon treatment of the precursor [($^{i\text{Pr}2}$P^{NH}N^{NH}P$^{i\text{Pr}2}$)Fe(CO)$_2$]$^+$ with zinc dust.[37] Also, Milstein and Huang individually reported the isolation of dearomatized complexes of type [(PNP)M(CO)(H)(L)]$^+$ (M = Fe, Ru) by analogous treatment with base.[39–44]

It was desirable to prove that the five-coordinate cyclometallate **8** served as a common intermediate for both structurally characterized products (**6** and **9**). As such, a THF solution of **8** was treated with ~1 equiv of thiophenol (PhSH) at room temperature.

Following solvent exchange to C_6D_6, the ^1H NMR spectrum (**Figure A12**) and the characteristic 4-peak IR spectrum [ν(CO) = 2018, 1999, 1965, 1933 cm^{-1}] (**Figure A13**) were similar to the structurally characterized **6**, indicating the formation of μ_2-$(PhS)_2$-$[(^{O=}C^{NH}N^{Ph})Fe(CO)_2]_2$ (**6'**). This reaction confirms **8** as the common intermediate along each pathway of desulfurization (^{t}BuOK or $NaHBEt_3$).

2.6 CONCLUSION

(1) A synthetic model of [Fe] hydrogenase has been prepared in a simple one-step metalation using an ortho-aminopyridine/thioether pincer ligand and iron tetracarbonyl bromide. The organometallic Fe–C(=O) σ bond, dicarbonyl motif and NCS chelate donor set provide a reasonably biomimetic donor set. This biomimetic model is somewhat limited on two fronts: (i) by the inclusion of thioether-S in place of thiolato-S, and (ii) by the equatorial CNS donor set of the pincer ligand (the enzyme is facial CNS). The pyridine/carbamoyl unit (with basic amide-N) serves as a facsimile for the endogenous pyridone.

(2) Functional study of the pentacoordinate complex revealed that it lacks the reactivity towards H_2 activation. DFT MO analysis of the pentacoordinate species **2** indicates that the codirectional orientation of the HOMO and LUMO orbitals is detrimental for H_2 activation, possibly explaining the lack of H_2 reactivity with the equatorial CNS donor set (facial CNS donor set is in the enzyme). We postulate that for biomimetic H_2 activation, a *fac*-CNS donor set is likely an important factor, due to (*a*) a *cis*/*trans* effect of orienting the vacant site to the Fe–C(=O) σ bond, and (*b*) the resultant orthogonal orientation of the HOMO/LUMO frontier orbitals for polarizing the H–H bond into $H(\delta^+)$–H (δ^+) along the pathway to heterolysis.

(3) substitution studies indicate that the organometallic Fe–C(=O) σ bond imparts an exceptional extent of stability to both dicarbonyl and monocarbonyl six-coordinate adducts of the chelate (where exogenous **L** = PPh_3, py, MeCN, etc.) The organometallic *cis*-$\{Fe(CO)_2\}^{2+}$ unit imparts an unusual extent of stability to the diamagnetic *five-coordinate* dicarbonyl species, which is most relevant to the 'pre' H_2 activation state of the enzyme. No decomposition was observed in most solvents (MeCN, THF; DCE, FPh), and higher spin-states were not observed.

(4) We studied the reactivity of an iron-hydride intermediate (**5**) in a synthetic model of [Fe]-hydrogenase. This Fe–H species promotes $C–S_{thioether}$ bond cleavage and formation of a Fe_2S_2 complex. The reaction of the bromide-bound complex with strong base KO^{t}Bu also led to $C–S_{thioether}$ bond cleavage and formation of a cyclometalated complex (**8**). The generation of $Fe_2S^{Ph}_2$ complex from the cyclometalated complex indicates that **8** could be the intermediate in the reaction of Fe–H species decomposition. However, the equatorial arrangement of the present CNS donor set is distinct from the facial CNS motif found in the active site.[8] Incorporation of the biomimetic thiolate and methylene-acyl unit would be important to develop a more accurate model of the active site.

2.7 EXPERIMENTAL PROCUDURES

2.7.1 General Information

All manipulations involving metal complexes were carried out under N_2 using either a Schlenk line or an inert atmosphere (N_2) drybox. All organic starting materials were purchased from Acros Organics or Sigma-Aldrich and used without further purification. The iron(II) carbonyl starting salt $[Fe(CO)_4(Br)_2]$ was prepared by reaction of $[Fe(CO)_5]$ (Strem) with Br_2 according to the published procedure,[16] and purified by re-

crystallization from CH_2Cl_2 at –20 °C. HPLC grade solvents were purchased from EMD, Fisher, Macron or J.T. Baker, and dried through an alumina column system (Pure Process Technology). Deuterated solvents (CD_2Cl_2, CD_3CN, C_6D_6 and THF-d^8) were purchased from Cambridge Isotopes or Across Organics and used as received.

2.7.2 Physical Measurements

The ^1H, ^{13}C and ^{31}P NMR spectra were collected on Varian DirecDrive 400 MHz spectrometer and chemical shifts were referenced to solvent TMS, $CDCl_3$/THF-d^8/CD_3CN/CD_2Cl_2 and H_3PO_4, respectively. Solid state infrared spectra were recorded on a Bruker Alpha spectrometer equipped with a diamond ATR crystal. Solution IR data were obtained on the same instrument equipped with a 0.1 cm path length cell with CaF_2 windows. Micro-analytical (C, H, N) data were obtained with a FLASH EA 1112 Series CHNS Analyzer or by Midwest Microlabs.

The X-ray diffraction data for **3b**, **3c**, **3d**, **4b** and **9** were collected on either a Rigaku AFC12 diffractometer with a Saturn 724+ CCD using a graphite monochromator with Mo Kα radiation and data reduction was performed using Rigaku Crystal Clear version 1.4.0.[45] The datasets for complexes **1**, **3a**, **3g**, **4a**, **4b**, **4c** and **6** were collected at an Agilent Technologies SuperNova Dual Source diffractometer using a μ-focus Cu Kα radiation source (λ = 1.5418Å) with collimating mirror monochromators and data reduction were performed using Agilent Technologies CrysAlisPro V 1.171.37.31.[46] The structure was solved by direct methods using SuperFlip[47] and refined by full-matrix least-squares on F^2 with anisotropic displacement parameters for the non-H atoms using SHELXL-2013.[48] A region of disordered solvent which could not be modeled in **4b** was squeezed, using SQUEEZE.[49] The formula is calculated without the masked solvent. Structure analysis was aided by use of the programs PLATON98[50] and WinGX[51]. The

hydrogen atoms were calculated in ideal positions with isotropic displacement parameters set to 1.2 × U_{eq} of the attached atom (1.5 × U_{eq} for methyl hydrogen atoms). The data were checked for secondary extinction effects, but no correction was necessary. Neutral atom scattering factors and values used to calculate the linear absorption coefficient are from the International Tables for X–ray Crystallography.

2.7.3 DFT calculations

Geometry optimizations of the structures of **1** and $\mathbf{2}^{+}$ were performed with the Firefly software package[52], which is partially based on the GAMESS (US)[53] source code, with combinations of 6-31G(d)-combo and the functional PW91[54,55]. The structures were visualized with MacMolPlt.[56] The 6-31G(d)-combo basis set is a hybrid basis set consisting of the Pople 6- 31G(d) basis set obtained from the EMSL Basis Set Exchange[57,58] with diffuse functions on all heteroatoms and the ligating carbonyl carbon atoms, the modified basis set (m6-31G) of Mitin et al. used for iron,[59] and the revised basis set (r6-311G) of McGrath used for bromine.[60] Hessian calculations were performed at the same level of theory as the optimizations. All Hessian calculations showed no imaginary frequencies, and rotations/translations showed energies of less than 5 cm^{-1}. Graphical manipulations were performed with ChemCraft.[61] The orbital calculation was performed with PW91/6-31G(d)-combo and visualized with MacMolPlt. The localized electron density and molecular orbital components were calculated by Natural Bond Orbital (NBO) analysis using NBO 6.0 program.[62]

2.7.4 Synthetic Procedures

6-(2-(methylthio)phenyl)pyridin-2-amine ($^{H2N}N^{py}S^{Me}$). A batch of *trans*-dichlorobis(triphenylphosphine)palladium(II) (1.630 g, 0.0023 mol) was placed in a 500

mL thick-walled glass flask fitted with a teflon bushing, and dissolved in 100 mL of 1,2-dimethoxyethane. To this mixture was added 2-(methylthio)phenylboronic acid (5.796 g, 0.0353 mol) and 2-amino,6-bromopyridine (4.00 g, 0.0234 mol). Potassium carbonate (6.910 g, 0.0500 mol) was dissolved in 50 mL of water and added to the solution. The flask was sealed and heated to 85 °C for 24 h. The resulting orange solution was filtered, and evaporation of the solvent afforded a brown tar. Subsequent purification by column chromatography (98/2, DCM/methanol) afforded the ligand as an off-white solid. Yield: 4.43 g (89%). ^{1}H NMR (400 MHz, $CDCl_3$), δ in ppm from TMS: 7.53 (dd, *J* = 8.2, 7.4 Hz, 1H), 7.40 (ddd, *J* = 7.5, 1.6, 0.5 Hz, 1H), 7.35 (ddd, *J* = 8.0, 7.1, 1.5 Hz, 1H), 7.30 (dd, *J* = 8.0, 1.5 Hz, 1H), 7.21 (ddd, *J* = 7.6, 7.1, 1.5 Hz, 1H), 6.88 (dd, *J* = 7.4, 0.8 Hz, 1H), 6.51 (dd, *J* = 8.2, 0.8 Hz, 1H), 4.70 (s, 2H, N*H*$_2$), 2.41 (s, 3H, S–C*H*$_3$) ppm. ^{13}C NMR (101 MHz, $CDCl_3$) *δ*: 157.9, 157.0, 139.9, 138.0, 137.4, 129.6, 128.7, 125.6, 124.7, 114.3, 107.2, 16.4 ppm. Selected IR peaks (*v*, cm^{-1}): 3462 (s), 3306 (s), 1627 (vs), 1594 (s), 1584 (s), 1560 (s), 1458 (vs), 1430 (vs), 1352 (m), 1289 (m), 1255 (w), 1241 (w), 1167 (s), 1124 (s), 1042 (m). HR–MS: *m/z* 217.0794 $[M+H]^+$. Anal. calcd. for $C_{12}H_{12}N_2S$: C 66.63, H 5.59, N 12.95%; found: C 66.72, H 5.51, N, 12.86%.

[($^{O=}$C^{NH}N^{py}S^{Me})Fe(CO)$_2$(Br)] (1). A solid sample of $[Fe(CO)_4(Br)_2]$ (1.40 g, 4.27 mmol) was added to a stirred solution of ^{NH2}N^{py}S^{Me} ligand (0.912 g, 4.160 mmol) in Et_2O (50 mL) at –25 °C. Immediately the evolution of gas (presumably CO) was observed, and the temperature was slowly allowed to increase to –5 °C over the course of 20 min, during which time a yellow precipitate was formed. The solid was collected by filtration and washed with pentane (30 mL). The solid residue was purified by column chromatography over neutral alumina. Elution of the desired product was achieved with THF, which eluted a yellow band that was collected and the solvent removed in vacuo. The resulting residue was washed thoroughly with Et_2O, which afforded an analytically

pure sample of **1** as a yellow powder. Yield: 0.365 g (20%). X-ray quality crystals of **1** were obtained by layering pentane over a THF solution of **1** at –25 °C. ^{1}H NMR (400 MHz, THF-d^8), δ in ppm from TMS: δ 9.96 (s 1H), 7.84 (t, J = 7.9 Hz, 1H), 7.79 (dd, J = 5.6, 3.4 Hz, 1H), 7.62 (dd, J = 5.8, 3.4 Hz, 1H), 7.53 (dd, J = 5.8, 3.4 Hz, 2H), 7.39 (d, J = 7.6 Hz, 1H), 6.94 (d, J = 8.2 Hz, 1H) 2.60 (s 3H). ^{13}C NMR (101 MHz, THF-d^8) δ: 210.8(C≡O), 210.7 (C≡O), 208.4 (C=O), 161.4, 156.6, 140.6, 135.1, 132.7, 132.2, 131.0, 129.2, 129.0, 116.7, 109.7, 17.2 ppm. Solid state IR (v, cm^{-1}): 2034 (vs), 1974 (vs) (C≡O), 1619 (s) ($_{HN}$C=O), 1598 (s), 1565 (s), 1493 (m), 1448 (m), 1405 (w), 1242 (w), 1168 (m), 1088 (m), 806 (m), 756 (s). Solution IR (v, cm^{-1} CH_2Cl_2): 2046 (vs), 1986 (vs) (C≡O). HR–MS (ESI$^+$): *m/z* 456.8917 [M+Na]$^+$. Anal. calcd for $C_{15}H_{11}N_2O_3SFeBr$: C 41.41, H 2.55, N 6.44%; found: C 41.58, H 2.51, N 6.36%.

[($^{O=}$C^{NH}N^{py}S^{Me})Fe(CO)$_2$](BAr$^F_4$) (2). Under a N_2 atmosphere, a small amount of TlBAr$^F_4$ (0.050 g, 0.047 mmol) was added into a clear yellow solution of **1** (0.020 g, 0.046 mmol) in DCE (6 mL). The resulting small amount of precipitate was removed by filtration after stirring 5 minutes through Celite, and the solvent was removed in *vacuo*. This residue was washed with pentane (10 mL) and dried under vacuum to afford **2** as a bright yellow solid. Yield: 0.048 g (85%). IR (v, cm^{-1} solid): 2057 (s), 2008 (s) (C≡O), 1636 (w) ($_{HN}$C=O), 1569 (s), 1541 (s), 1350 (vs), 1270 (s), 1115 (vs), 884 (m), 836 (w), 759 (w), 710 (m), 679 (m). Solution IR (v in cm^{-1}, DCE): 2057 (vs), 2006 (vs) (C≡O). Anal. calcd for $C_{47}H_{23}BF24FeN_2O_3S$: C 46.33, H 1.90, N 2.30%; found: C 43.73, H 2.04, N 2.43%.

[($^{O=}$C^{NH}N^{py}S^{Me})Fe(CO)$_2$(PPh$_3$)](BAr$^F_4$) (3a). Under a N_2 atmosphere, a small amount of NaBAr$^F_4$ (0.050 g, 0.055 mmol) was added into a clear yellow solution of **1** (0.020 g, 0.046 mmol) in 1,2-dichloroethane (DCE, 6 mL) containing ~1 equiv of triphenylphosphine (0.013 g, 0.046 mmol). The resulting small amount of precipitate was

removed by filtration after stirring 5 minutes through Celite, and the solvent was removed in *vacuo*. This residue was washed with pentane (10 mL) and dried under vacuum to afford **3a** as a bright yellow solid. Yield: 0.050 g (73%). X-ray quality crystals of **3a** were obtained by layering pentane over a DCE solution of **3a** at –25 °C. ^{1}H NMR (400 MHz, CD_2Cl_2), δ from TMS in ppm: 8.33 (s, 1H, N*H*), 7.75 (t, 8H), 7.68 (t, 1H), 7.58 (s, 4H), 7.47 (m, 2H), 7.36 (m, 2H), 7.29 (m, 15H), 7.15 (m, 1H), 6.50 (dd, 1H) 2.55 (s, 3H). ^{31}P NMR (162 MHz, CD_2Cl_2), δ from H_3PO_4: 37.97 ppm. Solid state IR (v, cm^{-1}): 2052 (vs), 2002 (vs) (C≡O), 1628 (s) ($_{HN}$C=O), 1605 (s), 1571 (w), 1434 (w), 1352 (w), 1352 (s), 1272 (s), 1114 (br),998 (w), 931 (w), 885 (s), 838 (m), 803 (m), 711(m). Solution IR (v, cm^{-1} DCE): 2051 (vs), 1996 (vs) (C≡O). Anal. calcd for $C_{65}H_{38}BFeN_2O_3SF_{24}P$: C 52.73, H 2.59, N 1.89%; found: C 52.49, H 2.63, N 1.81%.

[($^{O=}$C^{NH}N^{py}S^{Me})Fe(CO)$_2$(PMe$_3$)](BAr$^{F}_4$) (3b). Complex **3b** was prepared by the same procedure as **3a**, except that ~1 equiv of PMe_3 (0.0035 g, 0.046 mmol) was used in place of PPh_3, leading to isolation of **3b** as a yellow solid. X-ray quality crystals of **3b** were obtained by layering pentane over a DCE solution of **3b** at –25 °C. Yield: 0.046 g (78%). ^{1}H NMR (400 MHz, CD_2Cl_2), δ from solvent in ppm: 8.87 (s,1H, N*H*), 7.95 (t, J = 6.8 Hz, 1H), 7.80 (d, J = 6.8 Hz, 1H), 7.73 (t, J = 8.0 Hz, 8H), 7.64 (s, 4H), 7.56 (s, 4H), 7.09 (dd, J = 7.8 Hz, 1H), 2.74 (s, 3H, S–CH_3), 1.10 (d, 9H, P(CH_3)$_3$). ^{31}P NMR (162 MHz, CD_2Cl_2), δ from H_3PO_4: 12.02 ppm. Solid state IR (v in cm^{-1}): 2061 (vs), 2009 (vs) (C≡O), 1631 (s) ($_{HN}$C=O), 1605 (s), 1571 (m), 1494 (w), 1470 (vw), 1426 (w), 1352 (vs), 1272 (vs), 1114 (br), 950 (m), 886 (m), 856 (m), 837 (m), 806 (m), 763 (m), 743 (m) 711 (w), 668 (m). Solution IR (v in cm^{-1}, DCE): 2058 (vs), 2008 (vs) (C≡O). HR–MS (ESI^{+}): *m/z* 431.0278 [M]$^{+}$. Anal. calcd for $C_{50}H_{32}BFeN_2O_3SF_{24}P$: C 46.39, H 2.49, N 2.16%; found: C 46.30, H 2.52, N 2.21%.

[($^{O=}C^{NH}N^{py}S^{Me}$)Fe(CO)$_2$(py)](BAr$^F_4$) (3c). Complex **3c** was prepared according to the same procedure for **3a**, except that pyridine (0.004 g, 0.045 mmol) was used in place of PPh_3. Complex **3c** was obtained as a bright yellow solid. X-ray quality crystals of **3c** were obtained by layering pentane over a DCE solution of **3c** at –25 °C. Yield: 83% (0.049 g, 0.038 mmol). ^{1}H NMR (400 MHz, CD_2Cl_2), δ from solvent in ppm: 8.13 (t, 3H), 7.96 (t, 1H), 7.84 (m, 1H), 7.72 (s, 8H), 7.63 (q, 1H), 7.61 (s, 1H), 7.59 (d, 1H), 7.57 (m, 2H), 7.55 (s, 4H), 7.34 (m, 2H), 6.90(q, 1H), 3.00 (s, 3H, S–C*H*$_3$). IR (*v*, cm^{-1} solid): 2069 (vs), 2010 (vs) (C≡O), 1639 (s) ($_{HN}$C=O), 1609 (s), 1572 (m), 1565 (w), 1492 (w), 1470 (w), 1443 (w), 1353 (vs), 1273 (vs), 1115 (br), 886 (m), 838 (m). Solution IR (*v*, cm^{-1} DCE): 2061 (vs), 2012 (vs) (C≡O). HR–MS (ESI$^+$): *m/z* 434.0260 [M]$^+$. Anal. calcd for $C_{52}H_{28}BFeN_3O_3SF_{24}$: C 48.14, H 2.18, N 3.24%; found: C 48.06, H 2.23, N 3.32%.

[($^{O=}C^{NH}N^{py}S^{Me}$)Fe(CO)$_2$(MeCN)](BF$_4$) (3d). Under a N_2 atmosphere, a small amount of $AgBF_4$ (0.030 g, 0.154 mmol) was added into a solution of **1** (0.050 g, 0.115 mmol) in a mixture of CH_3CN/THF (1:1, 5 mL). An off-white precipitate was formed immediately, and after stirring 5 minutes the mixture was filtered through Celite. The solvent was removed in vacuo, and the yellow residue was washed with pentane (10 mL) and dried under vacuum to afford **3d** as a bright yellow solid. X-ray quality crystals of **3d** were obtained by layering pentane over a MeCN solution of **3d** at –25 °C. Yield: 0.053 g (95%). ^{1}H NMR (400 MHz, CD_3CN), δ from TMS in ppm: 9.22 (1H, s, N*H*), 8.01 (t, *J* = 6.8 Hz, 1H), 7.82 (d, *J* = 6.8 Hz, 1H), 7.56 (s, 4H), 7.19 (d, *J* = 7.8 Hz, 1H), 2.60 (s, 3H, S–C*H*$_3$), 1.96 (MeCN). Solid state IR (*v*, cm^{-1}): 2311 (vs), 2282 (vs), 2069 (vs), 2023 (vs) (C≡O), 1645 (s) ($_{HN}$C=O), 1647 (s), 1605 (s), 1574 (w), 1493 (s), 1433 (m), 1368 (m), 1282 (w), 1231 (m), 1023 (m), 929 (m), 811 (m), 764 (s), 575 (s). Solution IR (*v* in cm^{-1}, DCE): 2071, 2020 (C≡O). Solution IR (*v* in cm^{-1}, CH_3CN): 2068, 2018 (C≡O). Anal.

calcd for $C_{17}H_{14}FeN_3O_3SBF_4$: C 42.27, H 2.92, N 8.70%; found: C 42.15, H 2.96, N 8.83%.

[($^{O=}C^{NH}N^{py}S^{Me}$)Fe(CO)$_2$(P(OEt)$_3$)](BAr$^F_4$) (3e). Complex **3e** was prepared by the same procedure as **3a**, except that ~1 equiv of $P(OEt)_3$ (0.076 g, 0.046 mmol) was used in place of PPh_3. This resulted in isolation of **3e** as a yellow solid. Yield: 0.052 g (82%). ^{1}H NMR (400 MHz, CD_2Cl_2) δ from TMS: 8.50 (1H, s, N*H*), 8.02 (dd, 1H), 7.86 (d, 2H), 7.74 (d, J = 8.0 Hz, 8H), 7.62 (s, 3H), 7.58 (s, 4H), 7.05 (d, J = 8.0 Hz, 1H), 3.91 (q, J = 20.0 Hz, 6H), 2.69 (s, 3H, S–C*H*$_3$), 1.20 (d, J = 20.0 Hz, 9H, 3 C*H*$_3$) ppm. ^{31}P NMR (162 MHz, CD_2Cl_2), δ from H_3PO_4: 128.7 ppm. IR (υ, cm^{-1} solid): 2054 (vs), 2001 (vs) (C≡O), 1630 (s) ($_{HN}$C=O), 1608 (s), 1569 (m), 1493 (m), 1470 (vw), 1449 (vw), 1353 (s), 1272 (vs), 1114 (br), 1016 (m), 886 (m), 838 (m), 803 (m), 761 (s). Solution IR (υ in cm^{-1}, DCE): 2051 (vs), 1994 (vs) (C≡O). HR–MS (ESI$^+$): *m/z* 521.0593 [M]$^+$. Anal. calcd for $C_{53}H_{38}BFeN_2O_6PSF_{24}$: C 45.98, H 2.77, N 2.02%; found: C 45.81, H 2.71, N 2.07%.

[($^{O=}C^{NH}N^{py}S^{Me}$)Fe(CO)$_2$(^{t}Bu^{i}NC)](BAr$^F_4$) (3f). Complex **3f** was prepared by the same procedure as **3a**, except that ~1 equiv. of ^{t}Bu^{i}NC (0.038 g, 0.05 mmol) was used instead of PPh_3. Compound **3e** was obtained as a bright yellow solid. Yield: 0.015 g (70%). ^{1}H NMR (400 MHz, CD_2Cl_2) δ from TMS: 8.52 (s, N*H*, 1H), 7.94 (dd, J = 6.8 Hz, 1H), 7.84 (d, J = 6.8 Hz, 1H), 7.74 (d, J = 8.0 Hz, 8H), 7.64 (s, 2H), 7.57 (s, 6H), 7.09 (dd, J = 8.0 Hz, 1H), 2.55 (s, 3H, S–C*H*$_3$), 1.26 (s, 9H, C(C*H*$_3$)$_3$). Solid state IR (υ in cm^{-1}): 2223 (s) (C≡N–), 2093 (vs), 2046 (vs) (C≡O), 1664 (s) ($_{HN}$C=O), 1604 (s), 1571 (s), 1496 (s), 1470 (m), 1452 (m), 1428 (m), 1375 (w), 1285 (w), 1236 (w), 1115 (br), 983 (w), 876 (w). Solution IR (υ in cm^{-1}, DCE): 2058 (vs), 2006 (vs) (C≡O). HR–MS (ESI$^+$): *m/z* 438.0575 [M]$^+$. Anal. calcd for $C_{52}H_{32}BFeN_3O_3SF_{24}$: C 47.99, H 2.48, N 3.23%; found: C 47.85, H 2.41, N 3.36%.

[($^{O=}C^{NH}N^{py}S^{Me}$)Fe(CO)$_2$(S(2,6-Me$_2$C$_6$H$_3$))] (3g). Under a N_2 atmosphere, a small amount of NaS(2,6-$Me_2C_6H_3$) (0.005 g, 0.031 mmol) in 2 mL of THF was added into a clear yellow solution of **1** (0.010 g, 0.023 mmol) in 3 mL of THF, which turned orange gradually. The reaction was stirred for 10 min and filtered through Celite. The solvent was removed in vacuo, and the orange residue was purified by column chromatography over neutral alumina. Elution of the desired product was achieved with THF. The solvent was removed in vacuo. The resulting residue was washed thoroughly with pentane, which afforded an analytically pure sample of **3g** as a yellow powder. Yield: 0.075g (66%). The residue was recrystallized from a solution of DCE layered with pentane at –25 ˚C, which provided yellow crystals suitable for X–ray diffraction. ^{1}H NMR (400 MHz, CD_2Cl_2) δ: 8.71 (s, 1H), 7.81 (m, 1H), 7.56 (m, 5H), 7.38 (d, 1H), 6.90 (m, 3H), 2.62 (s, 3H), 2.25 (s, 6H) ppm. Solid state IR (υ, cm^{-1}): 2015 (s), 1963 (s) (C≡O), 1614 (m), 1594 (s), 1562 (s), 1490 (m), 1430 (m), 1330 (w), 1239 (w), 1119 (m), 1054 (m), 803 (m), 756 (s), 742 (m), 650 (m), 625 (m), 579 (m). IR (υ, cm^{-1}, DCE): 2029 (vs), 1973 (vs) (C≡O). HR–MS (ESI$^+$): *m/z* 515.0158 [M+Na]$^+$. Anal. calcd for $C_{23}H_{20}FeN_2O_3S_2$: C 56.10, H 4.09, N 5.69%; found: C 54.15, H 3.99, N 5.40%.

[($^{O=}C^{NH}N^{py}S^{Me}$)Fe(CO)(PPh$_3$)Br] (4a). Under a N_2 atmosphere, a small amount of Me_3NO (0.0159 g, 0.211 mmol) in 3 mL DCE was added into a clear yellow solution of **1** (0.040 g, 0.092 mmol) in 6 mL DCE containing ~1 equiv of PPh_3 (0.024 mg, 0.092 mmol), which turned red immediately. The reaction was stirred for 10 min and filtered through Celite. The solvent was removed in *vacuo*, and the orange residue was washed with pentane (10 mL) and dried under vacuum to afford **4a** as an orange solid. Yield: 0.045g (67%). The residue was recrystallized from a solution of PhF (2 drops) and Et_2O (1 mL) layered by pentane at –25 ˚C, which provided red crystals suitable for X–ray diffraction. Solid state IR (υ, cm^{-1}): 1946 (vs), 1604 (m), 1598 (vs), 1557 (s), 1486 (s),

1407 (m), 1124 (s), 1086 (s), 812 (m), 693 (s), 577 (m), 478 (m). Solution IR (υ in cm^{-1}, DCE): 1958 (vs) (C≡O). Anal. calcd for $C_{35}H_{33}BrFeN_3O_2PS$: C 57.42, H 3.92, N 4.19%; found: C 56.85, H 3.48, N 4.32%.

[($^{O=}C^{NH}N^{py}S^{Me}$)Fe(CO)(PPh_3)$_2$](BAr^F_4) (4b). Under a N_2 atmosphere, a small amount of $NaBAr^F_4$ (0.106 g, 0.120 mmol) was added into a clear yellow solution of **1** (0.040 g, 0.092 mmol) in 4 mL DCE containing ~1 equiv of PPh_3 (0.024 g, 0.092 mmol). The resulting small amount of precipitate after stirring 5 minutes was removed by filtration through Celite, and the solvent was removed in vacuo. This residue was washed with pentane (10 mL) and dried under vacuum to afford **3a** as a bright yellow solid. In the next step, PPh_3 (0.024 mg, 0.092 mmol) were added into the solid in 4 mL DCE, followed by the addition of Me_3NO (0.018 g, 0.234 mmol) in 2 mL DCE. The reaction was stirred for 10 min and filtered through Celite. The solvent was removed in vacuo, and the yellow residue was washed with pentane (10 mL) and dried under vacuum to afford **4b** as an orange solid. X-ray quality crystals of **4b** were obtained by layering pentane over an Et_2O solution of **4b** at –25 °C. Yield: 0.063 g (40%). ^{1}H NMR (400 MHz, CD_2Cl_2) δ: 7.74 (t, 8H), 7.57 (s, 4H), 7.54 (d, 1H), 7.42 (m, 20), 7.25 (t, 13H), 7.19 (t, 1H), 7.06 (s, 1H), 7.00 (t, 1H), 6.33 (d, 1H), 1.90 (s, 3H) ppm. ^{31}P NMR (162 MHz, CD_2Cl_2), δ from H_3PO_4: 43.9 ppm. IR (υ, cm^{-1}, crystal): 1919 (s) (C≡O), 1609 (s), 1591 (w), 1485 (w), 1434 (w), 1354 (vs), 1276 (vs), 1113 (br), 1088 (vs), 884 (m), 838 (m), 804 (m), 708 (s), 510 (s). Solution IR (υ, cm^{-1}, DCE): 1951 (vs) (C≡O). Anal. calcd for $C_{82}H_{53}BF_{24}FeN_2O_2P_2S$: C 57.43, H 3.12, N 1.63%; found: C 56.76, H 2.91, N 1.00%.

[($^{O=}C^{NH}N^{py}S^{Me}$)Fe(CO)(py)$_2$](BAr^F_4) (4c). Under a N_2 atmosphere, a small amount of $NaBAr^F_4$ (0.106 g, 0.120 mmol) was added into a clear yellow solution of **1** (0.040 g, 0.092 mmol) in 4 mL DCE containing ~1 equiv of pyridine (7.4 μL, 7.27 mg, 0.092 mmol). The resulting precipitate was removed by filtration through Celite after

stirring 5 minutes, and the solvent was removed in vacuo. This residue was washed with pentane (10 mL) and dried under vacuum to afford **3c** as a bright yellow solid. In the next step, a 4 mL solution of DCE containing pyridine (7.4 μL, 7.27 mg, 0.092 mmol) was used to dissolve the solid, followed by the addition of Me_3NO (0.010 g, 0.138 mmol) in 2 mL DCE. The reaction was stirred for 10 min and filtered through Celite. The solvent was removed in vacuo, and the yellow residue was washed with pentane (10 mL) and dried under vacuum to afford **4c** as an orange solid. X-ray quality crystals of **4c** were obtained by layering pentane over a fluorobenzene solution of **4c** at –25 °C. Yield: 0.082 g (66%). ^{1}H NMR (400 MHz, CD_2Cl_2) δ: 8.38 (s, 1H), 8.23 (d, 1H), 7.80 (m, 2H), 7.72 (s, 8H), 7.64 (t, 1H), 7.55 (s, 4H), 7.37 (m, 4H), 7.26 (m, 4H), 7.15 (t, 1H), 7.06 (m, 3H), 6.86 (d, 1H), 2.82 (s, 3H) ppm. IR (v, cm^{-1}, crystal): 1989 (s) (C≡O), 1624 (w), 1601 (w), 1563 (w), 1491 (w), 1353 (vs), 1274 (vs), 1116 (br), 999 (w), 946 (w), 886 (s), 837 (m), 804 (m), 714 (m). Solution IR (v, cm^{-1}, DCE): 1975 (vs) (C≡O). Anal. calcd for $C_{56}H_{33}BF_{24}FeN_4O_2S$: C 49.88, H 2.47, N 4.15%; found: C 48.99, H 2.57, N 3.61%.

Low temperature NMR preparation of [($^{O=}$C^{NH}N^{Py}S^{Me})Fe(CO)$_2$(H)] (5): the iron(II) hydride species. A small batch of [($^{O=}$C^{NH}N^{py}S^{Me})Fe(CO)$_2$(Br)] (**1**) (0.013 g, 0.032 mmol) was placed in a J–Young NMR tube and suspended in THF-d^8 (0.75 mL). The suspension was frozen in the cold well (liquid N_2) and degassed by a freeze-pump-thaw cycle. Next, an aliquot of the $NaHBEt_3$ solution (1 M in THF, 38 μL, 1.3 equiv) was transferred by syringe into the tube, and also frozen; the headspace of the NMR tube was again degassed by several vacuum/N_2 cycles. The NMR tube containing the frozen mixture was then placed directly in the NMR instrument pre-cooled to –70 °C. After several minutes to allow the mixture to slowly thaw to –70 °C, the sample was ready for data collection in the VT-NMR experiment. ^{1}H NMR (400 MHz, C_6D_6 at –70 °C), δ in

ppm from TMS: 11.66 s *br* (1H, N*H*), 7.84 t br (1H), 7.77-7.71 m (2H), 7.60 t (1H), 7.51 t (1H), 7.45 d (1H), 7.24 d *br* (1H), 2.21 s (3H, S-CH_3), –5.08 s (1H, Fe-H).

μ_2-$(CH_3S)_2$–[($^{O=}C^{NH}N^{Ph}$)$Fe(CO)_2]_2$ (6). The parent complex **1** (0.021 g, 0.048 mmol) was dissolved in 5 mL of THF at room temperature to generate a yellow solution. A volume of 0.056 mL of a $NaHBEt_3$ solution (1 M in THF; 0.0626 mmol, 63 μL, 1.3 equiv) was slowly added, immediately causing a color change from yellow to red. After stirring at room temperature for 15 min, the solvent was removed in vacuo. The resulting red solid was washed with pentane and extracted with C_6D_6. The resulting turbid solution (NaBr + insoluble impurities) was filtered through a Celite pad, and the solution reduced to dryness in vacuo, which produced **6** as an analytically pure yellow solid. Yield: 0.022 g (0.032 mmol, 60%). X-ray quality crystals of **6** were obtained by layering pentane over a fluorobenzene solution of **6**. Solid state IR (υ, cm^{-1} solid): 2013 s, 1991 vs, 1965 s, 1923 vs (C≡O); 1598 w ($_{HN}$C=O); 1547 m, 1493 w, 1433 s, 1349 m, 1289 w, 1237 w, 1162 w, 1133 w, 1094 w, 1044 w, 948 w, 800 m, 755 vs, 693 m, 665 m. ^{1}H NMR (400 MHz, C_6D_6), δ in ppm from TMS: 8.04 d (1H), 7.56 d (1H), 7.35 s (1H, N*H*), 7.28 q (2H), 7.07 m (1H), 6.95 m (1H), 6.69 d (1H), 5.84 d (1H), 1.94 s (3H). Elem. Anal. (%) calcd. for $C_{30}H_{24}N_4O_6S_2Fe_2$: C 50.58, H 3.40, N 7.87; found: C 50.48, H 3.45, N 7.76.

μ_2-$(PhS)_2$–[($^{O=}C^{NH}N^{Ph}$)$Fe(CO)_2]_2$ (6'). A small portion of ^{t}BuOK (0.010 g, 0.092 mmol) was added to a solution of the parent complex **1** (0.040 g, 0.046 mmol) in THF (5 mL) at room temperature under N_2 atmosphere. This clear yellow solution slowly turns to turbid orange solution over 25 min, and then the solution was passed through a Celite filter. Next, 1 equiv of thiophenol (0.04 g, 0.046 mmol) was added slowly to the reaction mixture, which turned the orange solution to a dark red color. After stirring for 0.5 h at room temperature, the solvent was evaporated under vacuum, and the resulting red residue was washed with pentane. The residue was extracted with a small portion of C_6H_6

(2-3 mL) to generate a turbid yellow-orange solution. After filtration through a cotton plug, the solvent was removed to afford the thiophenol analogue dimer, namely **6'** as orange solid. Yield: 12.5 mg (0.015 mmol, 33%). Solid state IR (υ, cm^{-1} solid): 2017s, 1998 s, 1964 s, 1932 s (C≡O); 1601 m ($_{HN}$C=O); 1571 s, 1491 w, 1470 s, 1433 m, 1366 w, 1312 m, 1236 m, 1152 s, 1081 w, 1053 s, 1022 s, 802 w, 738 s, 693 s. ^{1}H NMR (400 MHz, C_6D_6), δ in ppm from TMS: 8.18 d (2H), 7.99 d (2H), 7.35 s (1H), 7.27 t (2H), 7.01 d (2H), 6.94 d (1H), 6.80 m (2H), 5.84 d (1H). Elem. Anal. (%) calcd. for $C_{40}H_{28}N_4O_6S_2Fe_2$: C 57.43, H 3.37, N 6.70; found: C 57.32, H 3.42, N 6.63.

[($^{O=}C^{NH}NC^{Ph}$)Fe(CO)$_2$] (8). A small batch of ^{t}BuOK (0.010 g, 0.092 mmol) was added to a solution of the parent complex **1** (0.02 g, 0.046 mmol) in THF (5 mL) at room temperature under N_2 atmosphere. Over the course of 25 min, the yellow solution slowly turned to orange, and the solution was filtered through a Celite pad (removes KBr) to afford a clear orange solution. Evaporation of the solvent to dryness generated an orange solid. This crude product was extracted into C_6D_6 and filtered through a cotton plug to afford analytically pure sample of **8**. Yield: 0.010 g, (70% yield). IR (υ, cm^{-1} solid): 2003 vs, 1940 vs (C≡O); 1606 w ($_{HN}$C=O); 1579 s, 1525 w, 1458 s, 1436 s, 1398 m, 1363 w, 1308 m, 1281 w, 1229 w, 1156 s, 1081 w, 1050 m, 1005 m, 806 w, 756 s, 730 m. ^{1}H NMR (400 MHz, C_6D_6), δ in ppm from TMS: 8.18 d (1H), 7.99 d (1H), 7.35 s (1H, N*H*), 7.27 m (1H), 7.20 m (1H), 7.02 d (1H), 7.01 d (1H), 6.95 s (1H). Elem. Anal. (%) calcd. for $C_{14}H_8FeN_2O_3$: C 54.58, H 2.62, N 9.09; found: C 54.43, H 2.68, N 9.17.

[($^{O=}C^{NH}NC$)Fe(CO)(PPh$_3$)$_2$] (9). A solution of the parent complex **1** (0.020 g, 0.046 mmol) was prepared in THF (5 mL) at room temperature in presence of PPh_3 (0.024 g, 0.092 mmol, 2 equiv); no immediate reaction was observed. Upon addition of a small portion of ^{t}BuOK (0.008 g, 0.069 mmol), a color change from clear yellow to turbid orange was observed. After 25 min stirring, the same work-up procedure as

described for **8** was followed. The resulting yellow C_6D_6 solution afforded an orange solid upon evaporating the sample to dryness, resulting in the isolation of **9** as an orange solid. Yield: 0.023 g (0.028 mmol, 62% yield). X-ray quality crystals of **9** were obtained by layering pentane over a benzene solution of **9**. IR (υ, cm^{-1} solid): 1881 s (C≡O), 1587 m ($_{HN}$C=O), 1557 w, 1495 s, 1480 m, 1431 m, 1335 w, 1287 m, 1186 w, 1166 w, 1130 w, 1088 w, 1011 w, 997 s, 949 m, 804 m, 763 m, 691 m, 595 s, 568 s. ^{1}H NMR (400 MHz, C_6D_6), δ in ppm from TMS: 7.76 q (2H), 7.63 s (1H), 7.51 s (1H), 7.39 m (6H, *p*-PPh_3), 7.04 m (24H, *o,m*-PPh_3), 6.90 m (1H), 6.82 m (1H), 6.59 dd (1H), 6.39 d (1H). ^{31}P NMR (162 MHz, C_6D_6), δ in ppm from H_3PO_4: 24.8. Elem. Anal. (%) calcd. for $C_{49}H_{38}FeN_2O_2P_2$: C 73.14, H 4.76, N 3.48; found: C 73.06, H 4.71, N 3.48.

Detection of elemental sulfur from reaction of [($^{O=}$C^{NH}N^{Py}S^{Me})Fe(CO)$_2$(Br)] with ^{t}BuOK. In an N_2 drybox, the parent complex **1** (20 mg, 0.046 mmol) and ^{t}BuOK (7.6 mg, 0.068 mmol) were dissolved in 6 mL of THF, and stirred for 20 min. Then, PMe_3 (14 μL, 0.14 mmol) was added to the reaction and stirred for 1.5 h. The solvent was removed *in vacuo*. The mixture was extracted by $CDCl_3$ and filtered through Celite. The existence of S=PMe_3 was determined by ^{31}P NMR and GC-MS (CI^+) and HR-MS (CI^+). ^{31}P NMR (162 MHz, $CDCl_3$), δ in ppm from H_3PO_4: 30.3. GC-MS (CI+): retention time = 6.36 min, *m/z* = 93 $[M\text{-}CH_3]^+$, 109 $[M+H]^+$, 137 $[M+C_2H_5]^+$, 149 $[M+C_3H_5]^+$. HR-MS (CI^+), *m/z* = 108.0163 $[M]^+$.

Chapter 3: Schiff-Base Thiolate Complexes Derived from NNSH Ligands as Synthetic Models for Mono-Iron Hydrogenase: Synthesis, Stability and Understanding of the effects of thiolate ligation in Mono-Iron Hydrogenase*

3.1 INTRODUCTION

The structure of the active site of Hmd was determined crystallographically by Shima and coworkers.[1,2] As shown in **Scheme 3.1**, the active site contains an Fe(II) ion ligated by a bidentate acyl-pyridone/pyridinol ligand, two terminal CO's in *cis* orientation, and a cysteinyl sulfur (Cys176). The coordination site *trans* to the acyl unit is occupied by solvent (H_2O) in its resting state, and is the putative binding and activation site for H_2. Although the exact mechanism of H_2 activation remains unknown, researchers agree that either the pyridone oxygen or cysteine sulfur serves as the 'pendant base' in cooperating with the Lewis acidic Fe(II) ion.[3–5] As a result, the kinetic barrier of H_2 cleavage has been calculated to be drastically lowered ($\Delta G^{\ddagger} \approx 2$ kcal/mol).[5]

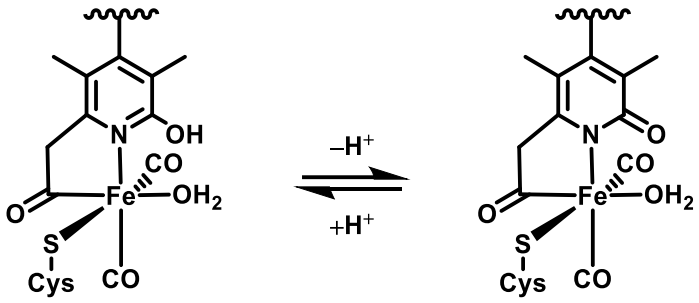

Scheme 3.1 Active site of mono-[Fe] Hydrogenase (Hmd) detailing the two possible protonation states: pyridinol (*left*) versus pyridone (*right*).

* Adapted/Reproduced in part with the permission from Xie, Z.-L., Pennington, D. L., Boucher, D. G., Lo, J., Rose, M. J., *Inorg. Chem.*, **2018**, 57, 10028-10039. Copyright 2018 American Chemical Society. Rose and Xie designed the research. Xie, Pennington, Boucher and Lo performed the research and analyzed the data.

One seemingly innocuous feature of the active site warrants some discussion: the *cis*-$\{Fe(CO)_2\}^{2+}$ motif. While hundreds of examples of structurally characterized iron(II) carbonyl complexes can be found in the CCDC, there are relatively few *phosphine-free* coordination complexes containing *cis*-$\{Fe(CO)_2\}^{2+}$ motif.

More specific to the enzyme, synthetic models of [Fe]-hydrogenase have been developed to understand the mechanistic details, reactivity and bonding of the active site. Previously, Hu and coworkers reported a series of methylene-acyl containing iron complexes exhibiting structural relevance to the Hmd active site (**Scheme 3.2**).[6] Pickett and coworkers synthesized a series of 'carbamoyl' (amide-acyl) iron complexes that mimicked the active site. And while the aforementioned models replicated most features of the first coordination sphere, none exhibited the enzyme-like functionality of H_2 cleavage in the absence of the protein environment.[7]

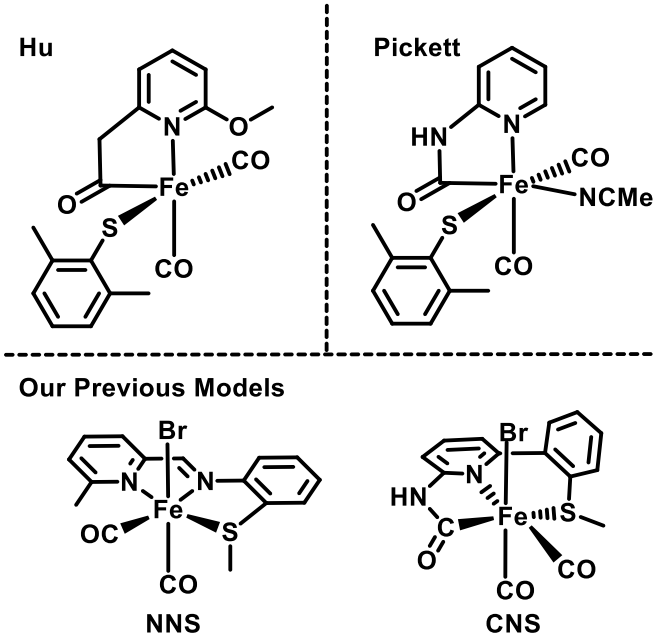

Scheme 3.2 Synthetic models for [Fe]-hydrogenase

Previously, we have utilized Schiff base (NNS) and carbamoyl-pincer (CNS) ligands bearing thioether moieties to generate mononuclear iron(II) carbonyl species resembling the active site to lesser or greater extents, respectively (**Scheme 3.2**).[8–10] While both systems replicated the *cis*-$\{Fe(CO)_2\}^{2+}$ motif, the Schiff base ligand did not provide thermal stability (decarbonylation occurred above –20 °C in coordinating solvent), and the pincer-CNS complex – while stable up to 60 °C in coordinating solvents – did not exhibit any reactivity with H_2 or model substrates. In fact, in the latter case (pincer), CO dissociation was only observed when using a strong decarbonylation reagent such as Me_3NO.[10] Overall, on these premises, it was not clear whether the inclusion of a thiolate donor (in the absence of an acyl-C donor) would provide (*i*) thermal stability to the *cis*-$\{Fe(CO)_2\}^{2+}$ unit, or (*ii*) promote reactivity with H_2 and model substrates. Therefore, in this work we have incorporated a thiolate into the donor set to evaluate its exclusive structural preferences and thermal stability.

One possible outcome of thiolate metalation ligands is the formation of dimeric or multinuclear complexes due to the bridging tendency of thiolato-S (**Scheme 3.3**). By increasing the bulkiness of the thiolate, we attempted to avoid the bridging thiolate motif and thus afford mono-iron complex, as we have demonstrated in our anthracene-base CNS(thiolate) model.[11] Herein, we report the synthesis of Schiff base thiolate iron complexes and, ultimately, the control of nuclearity of these complexes by changing the steric hindrance of the thiolate ligands.

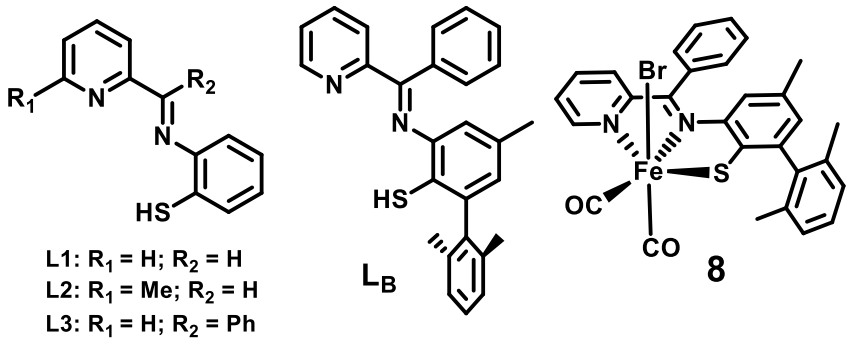

Scheme 3.3 Targeted ligands and dicarbonyl complex.

3.2 SCHIFF-BASE NON-BULKY THIOLATE COMPLEXES

We started with the syntheses and characterizations of the Schiff-base non-bulky thiolate ligands and their complexes. Despite of the hope for the non-bulky thiolate ligands to stabilize the iron dicarbonyl complexes, the bridging promiscuity of thiolate ligand presented a variety of diiron complexes, with which, surprisingly, we could build a jigsaw of the decomposition of iron dicarbonyl complexes to bis-ligated iron complexes.

3.2.1 Syntheses

Non-Bulky Ligands. The non-bulky ligands were derived from the condensation of the substituted pyridine carboxaldehyde or ketone with 2-aminobenzenethiol, based on the literature report (**Scheme 3.4**).[12,13] The thermodynamically more favorable benzothiazoline products were obtained as a result of cyclization after condensation (**Scheme 3.4**), wherein the benzothiazoline features an S/N heterocyclic 5-membered ring that can be easily opened by metal ions or organic bases.[14] The formation of the benzothiazoline was demonstrated by NMR and IR spectroscopies as follows. The ^{1}H NMR spectra for **L1**-**L3** in $CDCl_3$ showed a single product isolated from each reaction. The benzothiazoline methine –C*H*– proton of **L1** and **L2** are identified at 6.41 and 6.38

ppm, respectively, which fall within the expected range of methine resonances, rather than the C*H*=N resonance (pyridine-imines ≈ 8.0 ppm).[12,13] The two ligands exhibit amine N*H* protons at 5.06 and 5.12 ppm, and the methyl proton of **L2** resonates at 2.55 ppm as expected for 2-methylpyridine. Although **L3** does not have a C*H* proton, its existence was indicated by N*H* resonance at 6.17 ppm. None of the ligands exhibit a thiol S*H* resonance, usually observed at ~3 ppm.[15] The ^{13}C NMR spectra in $CDCl_3$ for the three ligands are also consistent with the benzothiazoline structures. For example, all three ligands show the hallmark features for methine carbon (*C*H) near 70 ppm (70.08 ppm for **L1**, 70.26 ppm for **L2**, 82.24 ppm for **L3**).[16] It has been speculated that an equilibrium of benzothiazoline and imine may be present in the solution.[14] However, in the present study no such equilibrium was evident in the ^{1}H or ^{13}C NMR spectra. This result is consistent with the study of Tyler and coworkers, who also proposed the formation of benzothiazoline as the only product in both solid and solution.[12,13] Lastly, none of the IR spectra of the three ligands exhibit a feature typical for the *ν*(S–H) stretch (generally ~2500 cm^{-1}).[17] All of the above characterization data support the benzothiazoline formation for **L1**, **L2** and **L3**.

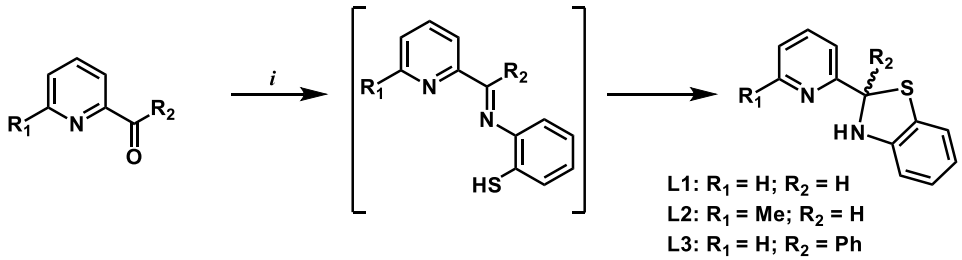

Scheme 3.4 Synthetic pathways for non-bulky benzothiazoline ligands.

Metal Complexes of Non-bulky Ligands. The syntheses of the iron carbonyl complexes of the non-bulky ligands **L1**-**L3** are summarized in **Scheme 3.5**. The

metalation of **L1**-**L3** with $[Fe(CO)_4(I)_2]$ was pursued in MeCN at –30 °C to thermally stabilize the CO ligands bound to the iron center. The bridging promiscuity of the thiolate donor promotes dimerization of the iron complexes in all three cases, which yielded the dimeric dicarbonyl complexes $[(NNS)_2Fe_2(CO)_2(I)_2]$ (**1**), $[(N^{Ph}NS)_2Fe_2(CO)_2(I)_2]$ (**2**) and $[(^{Me}NNS)_2Fe_2(CO)_2(I)_2]$ (**3**). These dark green products are stable for weeks in solid state at –30 °C under inert atmosphere, and when dissolved in weakly coordinating solvents such as MeCN or THF, these products are stable for days at –30 °C. At room temperature, the dimeric dicarbonyl complexes in MeCN are rapidly transformed to the dinuclear *mono*carbonyl complex, $[(NNS)_3Fe_2(CO)]I$ (**4**), $[(N^{Ph}NS)_3Fe_2(CO)]I$ (**6**) and $[(^{Me}NNS)_3Fe_2(CO)]I$ (**7**), as evidenced by UV/vis, X-ray diffraction (*vide infra*). Complex **4** can be independently synthesized by first treatment of **L1** with $[Fe(CO)_4(I)_2]$ at –30 °C, followed by crystallization with a trace amount of DMF in MeCN. The green crystals of **4** are stable in solid state under inert atmosphere, and a MeCN solution of **4** can be stored under light at ambient temperature without loss of CO. The sharp contrast of stability between **1** and **4** indicates that the NNS ligand — specifically, inclusion of the thiolate moiety — does not generate a stable iron dicarbonyl core. Additionally, as indicated by the **1**→**4** conversion in trace DMF, strongly coordinating solvents easily replace one of the CO ligands, generating the thermodynamically more favorable monocarbonyl complexes, e.g. $[(NNS)_3Fe_2(CO)]I$ (**4**). In terms of the stoichiometry of the **1**→**4** conversion, complex **1** likely first loses one CO ligand. Then $^2/_3$ of the decarbonylated intermediate obtains a third ligand, provided by the other $^1/_3$ of the intermediate, thus forming complex **4**. The $^1/_3$ equivalent of Fe_2I_2 core (plus two released I^-) then forms two equiv of an unrecovered $Fe(I)_2(solv)$ species:

$$3\ L_2Fe_2I_2(CO)_2 \rightarrow 2\ [L_3Fe_2(CO)]I + 2\ FeI_2 + 4\ CO \quad \text{(Eq. 1)}$$

Attempts to further decarbonylate **4** to prepare the bis-ligated Fe(II) complex $[(NNS)_2Fe]$ with UV light were unsuccessful (for comparison, $[(NNS)_2Fe]$ was synthesized separately); the single CO is tightly bound to the Fe center. On the other hand, an MeCN solution of **4** is oxidized by air within seconds, turning the dark green solution to gray. Crystallization of this species afforded green crystals of the bis-ligated Fe(III) complex $[(NNS)_2Fe]I$ (**5**), whose BPh_4 salt was previously reported by Mascharak.[18] Complex **5** can be also directly accessed from **1** when exposed to air.

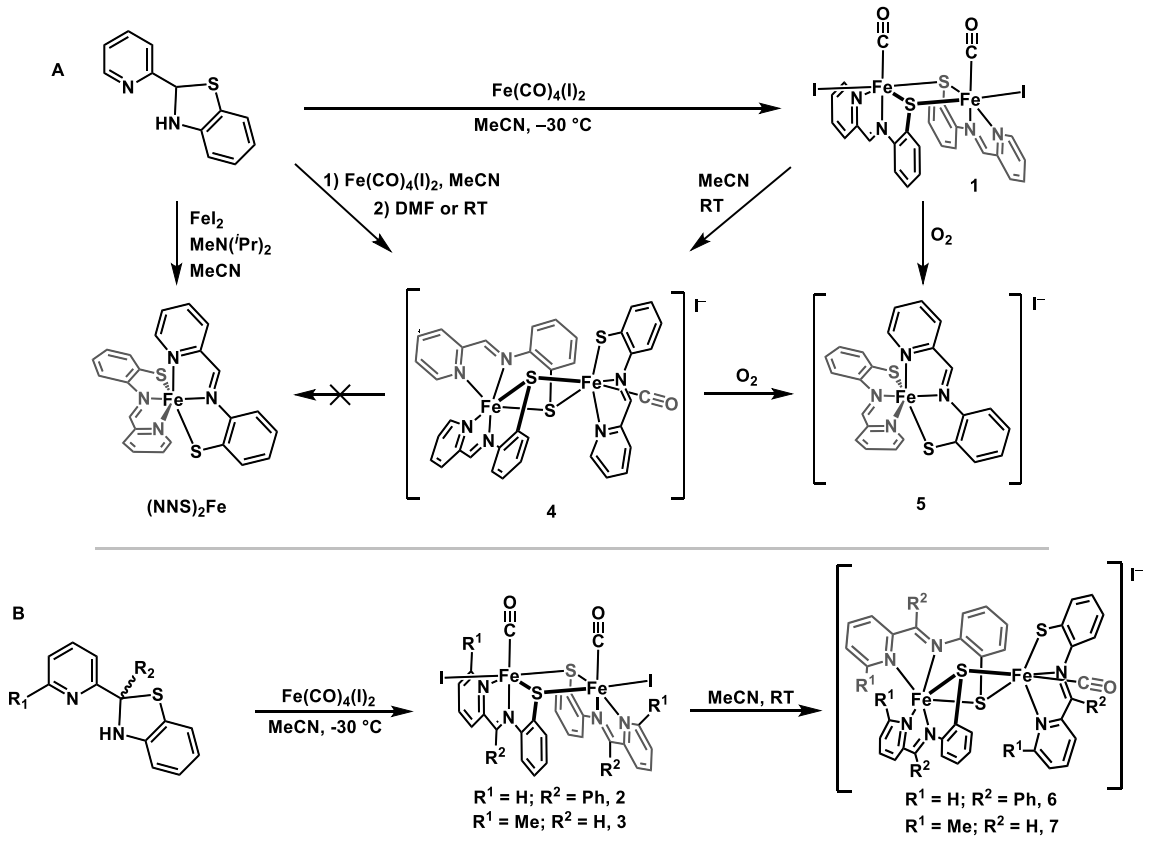

Scheme 3.5 Synthetic pathways for iron complexes derived from non-bulky benzothiazoline (A for **L1**; B for **L2** and **L3**). See text above for discussion of **1**→**4** conversion stoichiometry.

3.2.2 Structural and Spectroscopic Characterization of Non-Bulky Thiolate Complexes

X-ray Structures. The complex $[(NNS)_2Fe_2(CO)_2(I)_2]$ (**1**) (**Figure 3.1**) crystallized in monoclinic *C*2/c. The structure is a neutral dimeric complex with a $[Fe_2(S_{thiolate})_2]$ core. The two monomers are symmetric to each other with respect to a C_2 axis. Each Fe(II) ion exhibits pseudo-octahedral geometry, consisting of a NNS ligand coordinated in meridional fashion, a carbonyl, an iodide ion and another (bridging) thiolate sulfur. The N_{py}–Fe, Fe–C(O) and C≡O distances are 1.979(5), 1.789(8), 1.114(8) Å, respectively, which are within the normal range for a low-spin Fe(II) ion.[8,10,19] In addition, there are two unique Fe–S distances: the primary NNS thiolate bound to Fe (2.2889(17) Å), and the S-donor from the neighboring NNS ligand (2.3276(18) Å).

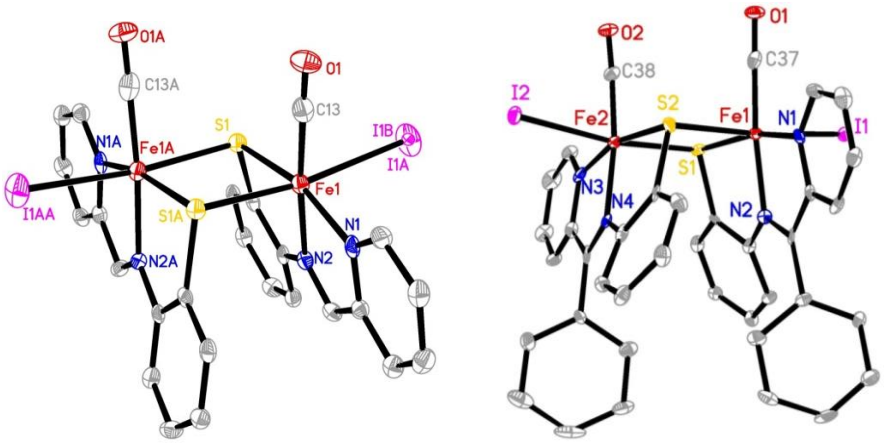

Figure 3.1 ORTEP diagrams (30% thermal ellipsoids) for $[(NNS)_2Fe_2(CO)_2(I)_2]$ (**1**) and $[(N^{Ph}NS)_2Fe_2(CO)_2(I)_2]$ (**2**). H atoms are omitted for clarity.

The structure of $[(N^{Ph}NS)_2Fe_2(CO)_2(I)_2]$ (**2**) (**Figure 3.1**) is also dimeric and the Fe(II) centers exhibit pseudo-octahedral geometry. The coordination environment of the complex is the same as that of **1** and the bond lengths (Appendix B, **Table B1**) are within the expected range for low-spin Fe(II) center.[8,10,19] However, the phenyl ring on the

Schiff base linkage slightly changes the structure of the complex, compared with **1**. The Schiff base phenyl rings are tilted away from the plane of ligand backbone, with dihedral angles of 63.52° and 67.68°. Notably, because of the steric hindrance of Schiff base phenyl rings, the planes of two ligand backbones are not parallel, and the dihedral angle between them in **2** (34.93°) is larger than that of **1** (21.29°). Another subtle difference between **2** and **1** is the 'bite angle' provided by the NNS chelate. In unsubstituted **2**, the N_{py}–Fe–S 'bite angle' of 98.5° is more acute versus that for **1** (101.5°). Correspondingly, the spatial distance between the N_{py} and S donors in **2** (4.169 Å) is notably shorter than that for **1** (4.229 Å). Thus, the phenyl substituent in **2** causes a slight 'pinching' effect in the ligand frame that is not evident in **1**. As a result, the Fe–N_{py} and Fe–S distances in **2** are shorter than those of **1** (Fe–N_{py}: 1.963(11) and 1.945(11) Å in **2**, versus 1.979(5) Å in **1**; Fe–S: 2.259(4) Å and 2.306(4) Å, versus 2.2889(17) Å); the Fe–N_{SB} bonds follow the opposite trend (1.994(10) in Å **2** versus 1.982(5) Å in **1**).

Complex $[(NNS)_3Fe_2(CO)]I$ (**4**) (**Figure 3.2**) crystallized in monoclinic $P2_1/c$ and is a cationic di-iron monocarbonyl complex with charge balance provided by an outer sphere iodide. Unlike **1**, the two Fe ions in **4** are in different coordination environments. One of the Fe ions is bis-ligated by two NNS ligands. The other Fe center is bridged by the thiolates from the bis-ligation unit, as well as coordinated by a third NNS ligand (the only non-bridging thiolate observed in this series). The coordination geometry is completed by CO. All of the Fe ions exhibit pseudo-octahedral geometry. Notably, **4** can be regarded as an intermediate in the transformation from **1** to **5**. The N_{py}–Fe distances are within the expected range for low-spin Fe(II) (N1–Fe1=1.961(3) Å, N3–Fe1=1.964(3) Å, N5–Fe2=1.988(3) Å).[8,10,19] The Fe–C(O) distance (1.774(5) Å) is slightly shorter than that of **1**, but still within the normal range for low-spin Fe(II). The C≡O distance

(1.115(5) Å) in **4** is comparatively longer, due to increased π back-bonding from the Fe center (compared to **1**) due to the additional ligation of the *non-bridging* thiolate donor.

The Fe–S bonds in **4** can be categorized into three types: Fe1–$S_{bridging}$, Fe2–$S_{bridging}$, Fe2–$S_{non\text{-}bridging}$. The Fe2–$S_{non\text{-}bridging}$ distance is the shortest [2.2733(10) Å], followed by Fe1–$S_{bridging}$ [2.2888(11) and 2.2972(10) Å], and finally the longest, Fe2–$S_{bridging}$ [2.3061(10) and 2.4026(11) Å].

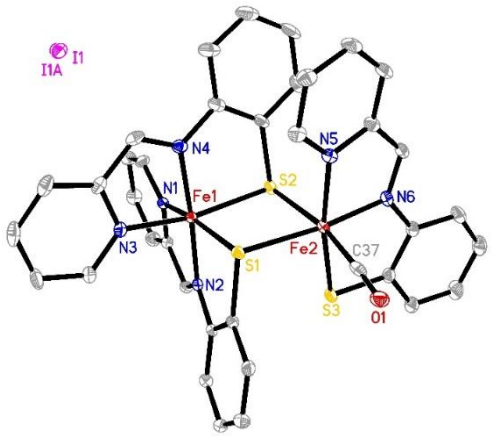

Figure 3.2 ORTEP diagram (30% thermal ellipsoids) for $[(NNS)_3Fe_2(CO)]I$ (**4**). H atoms are omitted for clarity.

Complex $[(NNS)_2Fe]I$ (**5**) (**Figure 3.3**) was crystallized in $P2_1/n$ and consists of two NNS units ligated to a single Fe(III) ion in pseudo-octahedral geometry; an outer sphere iodide provides charge balance, and a molecule of I_2 was also present as solvate. The Fe–N_{py} distances are 2.015(8) and 2.016(8) Å, and the Fe–S distances are 2.212(3) and 2.222(3) Å, which are comparable with the analogous structure of $[(NNS)_2Fe]BPh_4$ obtained by Mascharak and coworkers,[18] with Fe–N_{py} = 2.015, 1.977 Å and Fe–S = 2.223, 2.211 Å. For comparison, the Fe(II) bis-ligated complex $[(NNS)_2Fe]$ was synthesized and crystallized independently in $Pna2_1$. The Fe–N_{py} distances are shorter

than those of **5** (1.973(9) and 1.961(10) Å) and Fe–S distances are longer than **5** (2.290(3) and 2.294(3) Å). The different change in bond distances are likely due to the higher oxidation state, which facilitates the bonding between anionic-*S* donor with the cationic Fe(III).

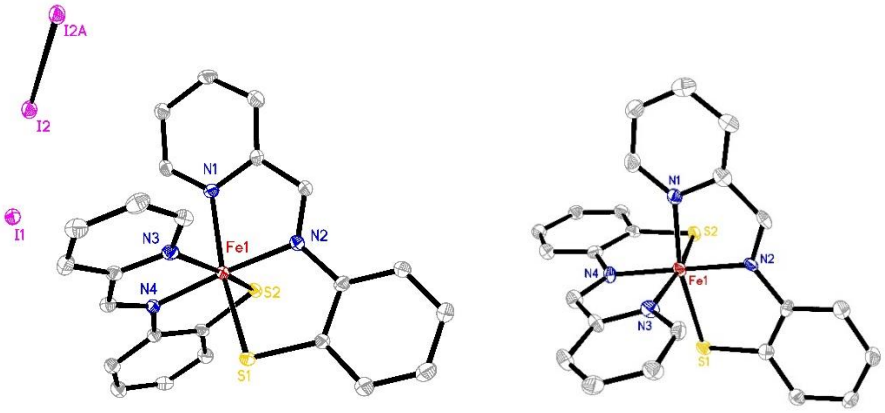

Figure 3.3 ORTEP diagram (30% thermal ellipsoids) for $[(NNS)_2Fe]I•I_2$ (**5•I$_2$**) and $[(NNS)_2Fe]$. H atoms are omitted for clarity.

IR Spectroscopy. The solid-state IR spectra of the non-bullky thiolate complexes were recorded under N_2 atmosphere and are shown in the Appendix B (**Figure B16**-**B20**); the values are tabulated in **Table 3.1**. The CO peaks for **1**, **2** and **3** are observed below 2000 cm^{-1}, which correspond to the symmetric (higher wavenumber) and asymmetric stretches of the two CO ligands. The similar wavenumbers of CO peaks in **1**, **2** and **3** show negligible change of the electron density at the metal center. Whereas modification of the ligand backbone (i.e. adding methyl group on the *ortho*-position of pyridine or phenyl group on the imine carbon) decreases the intensity of the asymmetric stretching of CO (1932 cm^{-1} for **2** and 1927 cm^{-1} for **3**). Small $\Delta\nu$ (<50 cm^{-1}) and different intensity between symmetric and asymmetric CO stretches suggest that the CO ligands do not bind

to Fe center in a *cis* orientation.[20] For **4**, a single CO vibration is observed at 1940 cm^{-1}, which is consistent with the X-ray structure of **4** as a monocarbonyl complex.

Table 3.1 Selected *ν*(CO) IR features for the non-bulky and bulky thiolate complexes.

Cmpd	**1**	**2**	**3**	**4**
Experimental	1941, 1926	1955, 1932	1951, 1927	1940
Calculated	2028, 2005			2023

the UV/Vis spectra of **4** and **5** were acquired in MeCN (**Figure 3.4**), to study the electronic structure of the non-bulky thiolate complex. The thermal instability of **1** prevented us from measuring the UV/vis spectrum with an isolated sample. Instead, **1** was generated in-situ at low temperature and immediately used for measurement. Complex **1** exhibits a strong charge transfer (CT) band at 245 nm, a shoulder at 309 nm and a very weak absorption feature at 465 nm, a medium band at 309 nm and an intense absorption at 245 nm. Complex **4** shows two intense bands at 244 and 317 nm (ε = 42000 and 25500 M^{-1} cm^{-1}), which are assigned as metal-ligand-charge-transfer (MLCT) transitions. Three weaker and low-energy transitions are also observed in the spectrum of **4** at 424 nm, 627 nm and 727 nm with molar absorptivity of ε = 8470 M^{-1} cm^{-1}, 3790 M^{-1} cm^{-1} and 4360 M^{-1} cm^{-1}, respectively. The UV/vis spectra for oxidized complex **5** shows similar shape of absorbance and comparable molar absorptivity: 245 nm (32500 M^{-1} cm^{-1}), 292 nm (27800 M^{-1} cm^{-1}), 340 nm (15400 M^{-1} cm^{-1}), 413 nm (5230 M^{-1} cm^{-1}), 563 nm (3730 M^{-1} cm^{-1}). As a comparison, the UV/vis spectrum of separately synthesized $[(NNS)_2Fe]$ shows four bands with two intense peaks at 281 nm (15300 M^{-1} cm^{-1}) and 319 nm (12600 M^{-1} cm^{-1}), which can be attributed to the metal-ligand-charge-transfer (MLCT) transitions, and two weak bands at 441 nm (5000 M^{-1} cm^{-1}) and 614 nm (2210 M^{-1} cm^{-1}).

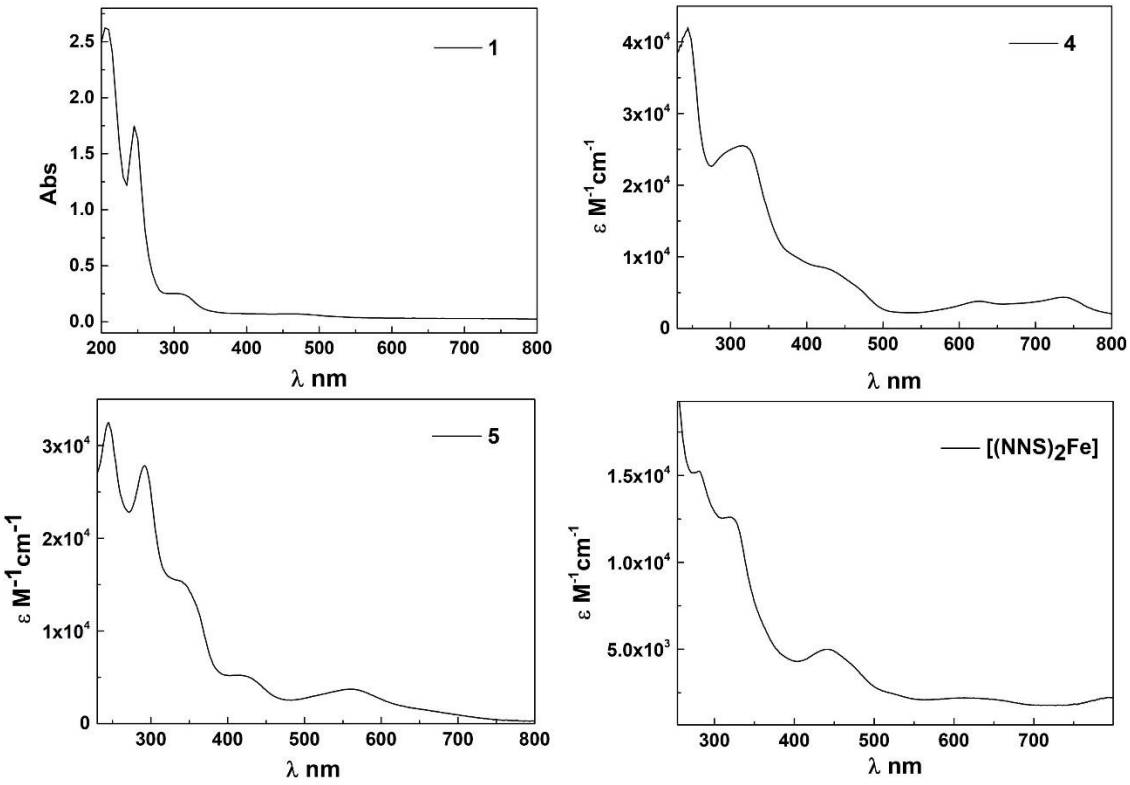

Figure 3.4 UV/vis spectra of $[(NNS)_2Fe_2(CO)_2(I)_2]$ (**1**), $[(NNS)_3Fe_2(CO)]I$ (**4**), $[(NNS)_2Fe]I$ (**5**) and $[(NNS)_2Fe]$. Complexes **4**, **5** and $[(NNS)_2Fe]$ were dissolved in MeCN and complex **1** was synthesized in-situ.

3.2.3 DFT Simulation of the Non-Bulky Complexes

To study the electronic property and rationalize the spectroscopic characterization of the non-bulky complexes, density functional theory (DFT) calculations were performed for **1**, $\mathbf{4}^+$ and $\mathbf{5}^+$. Geometry optimizations were first carried out with crystallographic data employing B3LYP as the functional, and using SDD basis set for Fe, LanL2DZ for I and 6-311G(d,p) for C, H, N, O, S. The optimized structures are shown in the appendix B (**Figure B25**, **B28** and **B31**) and the selected bond lengths and angles are tabulated in **Table B1**. Although the bond lengths and angles of in-silico structures are similar to the crystallographic data, but it is notable that all the bond

metrics are slightly longer than the experimental data. The difference of bond lengths between experimental and in-silico data for complex **1** is mostly 0.02-0.04 Å. But the bond distances for Fe–S and Fe–I differ more substantially (0.08 Å). Indeed, it is normal for Pople-type basis sets to afford overestimated bond lengths, especially for polar bonds.[21] For $\mathbf{4}^{+}$, the average bond length differences between the experimental and calculated structures are slightly larger (0.04 Å). Complex $\mathbf{5}^{+}$ shows similar extend of difference in bond length (average: 0.01 Å). Therefore, the calculated structures of the three complexes closely match the experimental data with acceptable deviations.

The frequency calculations for **1** and $\mathbf{4}^{+}$ show no imaginary frequency, confirming the nature of the stationery points to be minima. The calculated CO stretch frequencies for **1** and $\mathbf{4}^{+}$ are tabulated in **Table 3.1**. The CO region of the calculated IR spectra are shown in the appendix B (**Figure B26** and **B29**). The simulated CO bands for **1** are blue-shifted to 2028 and 2005 cm^{-1}, compared with the experimental wavenumber (1941 and 1926 cm^{-1}). It is important to note that the symmetric vibration of CO (2028 cm^{-1}) gives rise to an intense peak in the CO region, whereas the asymmetric vibration of CO (2005 cm^{-1}) exhibits much weaker absorption, which is consistent with the experimental results (**Figure B16**). The sharp contrast in the intensity between the two CO bands can be related to the CO ligand binding with two different iron centers.[20] The calculated IR spectra of $\mathbf{4}^{+}$ shows a single CO band at 2023 cm^{-1}, which is also blue-shifted with respect to the experimental data (1940 cm^{-1}). The calculated CO frequency of $\mathbf{4}^{+}$ is slightly smaller than the symmetric CO stretching frequency of the calculated **1**. The small discrepancy is in line with the experimental data (1 cm^{-1} difference for **1** and **4**). This indicates that from dicarbonyl complex **1** to monocarbonyl complex $\mathbf{4}^{+}$, there is no drastic change in the electron density on the iron center.

Next, we carried out the Time-dependent density functional theory (TDDFT) calculation to study the excited states and simulate the UV/vis spectra of complex **1**, $\mathbf{4}^{+}$ and $\mathbf{5}^{+}$. All the calculated spectra were shown in **Figure 3.5**. For **1**, the calculated absorptions show at 266, 320 and 455 nm, and is in close agreement with the experimental spectrum (245, 309 and 465 nm). By examining the molecular orbitals involved in a specific transition, we can understand the nature of the absorption attributed to that transition. The MOs associated with each transition are shown in **Figure 3.6a**. The intense peak at 266 nm can be assigned to ligand-to-ligand charge transfer (LLCT) since the ground state shows major contribution from the p orbital from iodine and the excited state has major contribution from the π* orbital of the ligand backbone. The two bands at 320 and 465 nm are derived from a mixture of charge transfers of *d*(Fe) → π*(L) and p(I) → π*(L), which therefore can be assigned as a mixture of MLCT and LLCT. The participation of iodine in all the transition indicates that the energy difference between MOs are small and the electrons in I are allowed to be excited to various states.

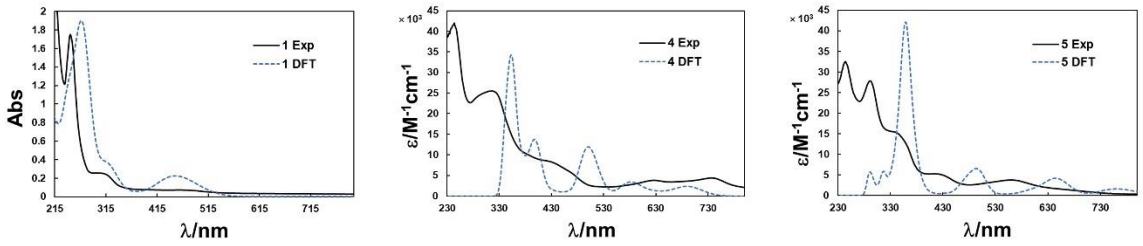

Figure 3.5 The comparison between experimental and DFT simulated UV/vis spectra of **1**, **4** and **5**.

The simulated UV/vis spectrum of complex $\mathbf{4}^{+}$ is in less agreement with the experimental data than is complex **1**. The lower energy peaks are blue-shifted (584 and 690 nm) and the higher energy peaks are red-shifted (351, 396 and 500 nm) comparing to

the experimental data (244, 317, 424, 627 and 727 nm; **Figure 3.5**). The absorption at 351 nm can be attributed to the transition from the metal to ligand backbone (MLCT). The ground state MO consists of $d_{xz/yz}$ orbital in iron and π orbital in the ligand backbone (**Figure 3.6b)**. The excited state involves the orbital that is primarily π* orbital of the ligand backbone. The bands at 396, 500 and 584 nm are contributed by the charge transfer from the $[Fe_2S_2]$ core to the ligand backbone and can be categorized into MLCT band, as well. The absorption at 690 nm can be assigned as a mixture of LLCT and MMCT, as the transition are composed by p(S) → π*(L) and $d(Fe^1)$ → $d(Fe^2)$.

Although the calculated UV/vis spectrum of $\mathbf{5}^+$ deviates from the experimental spectrum, the shape of the trace agrees with the experimental data. The peaks at 295 and 314 nm in the in-silico data are much weaker than the counterparts with a slight shift in the wavelength. The low energy absorptions (491, 644 and 757 nm) appear at the longer wavelength than the experimental spectrum. The nature of the transitions can be determined as MLCT (295, 314 nm), d-d transfer (491 nm), intra-ligand charge transfer (361, 644 nm) and LMCT (757 nm), by examining the MO diagram of each transition (**Figure 3.6c**).

The DFT calculation shows the variety and complexity of electron transitions under UV/vis illumination, which indicates the small energy difference between each MO in these complexes. This can be explained by the π conjugation of ligand backbone, multi-nuclearity and the available p electrons in the anionic sulfur donor, which provides different pathways for electrons to move after excitation.

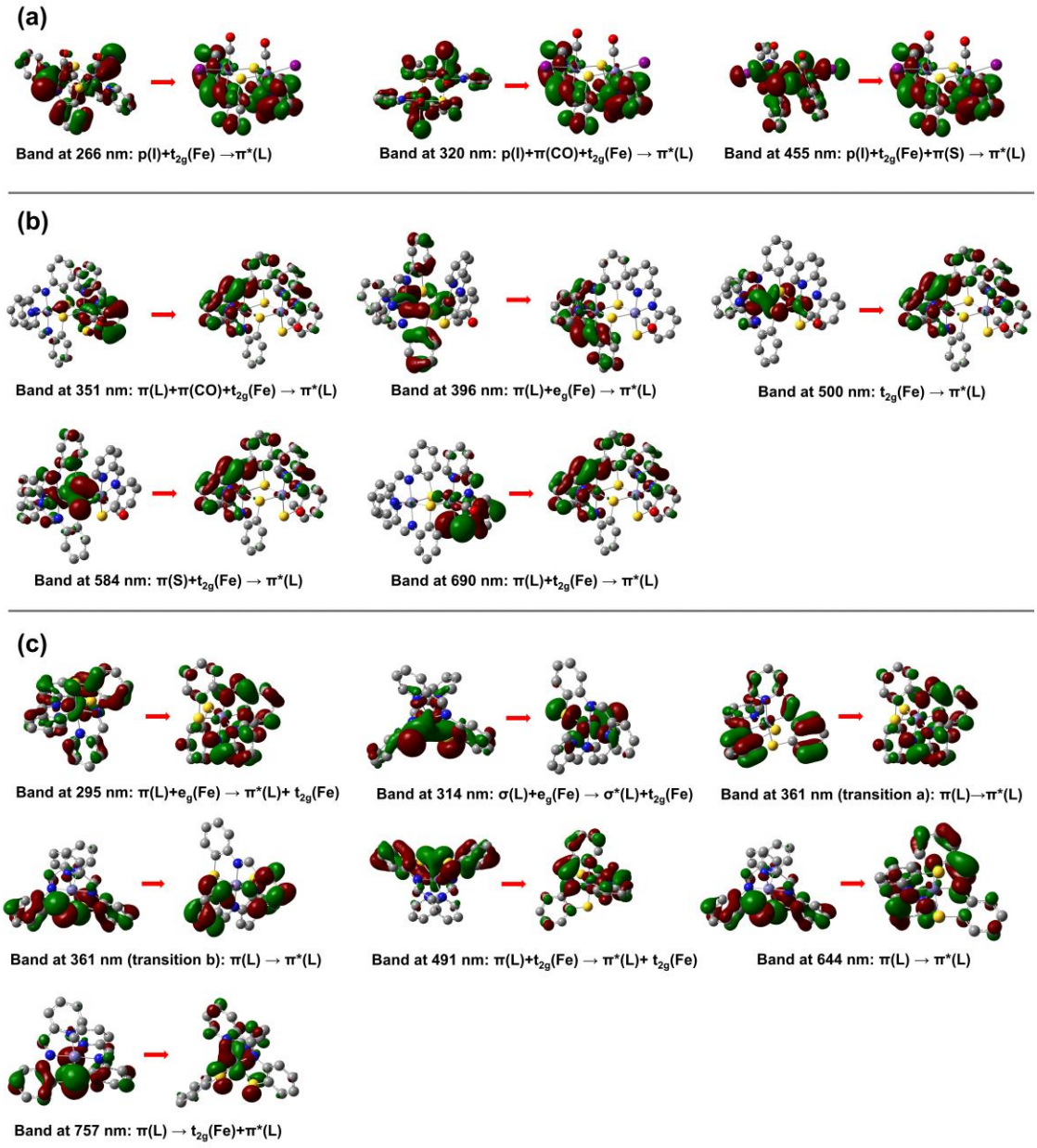

Figure 3.6 Molecular orbitals involved in different transitions leading to specific absorptions. (a) Transitions from **1**. (b) Transitions from $\mathbf{4}^{+}$. (c) Transitions from $\mathbf{5}^{+}$.

3.3 SCHIFF-BASE BULKY THIOLATE COMPLEXES

3.3.1 Syntheses of Bulky Ligand and its Metal Complexes

The dimerization issue encountered above prompted us to increase the steric bulk of the thiolate to facilitate the formation of mononuclear thiolate complexes. In this strategy, a bulky substituent (2,6-dimethylphenyl) was installed *ortho* to the thiolate donor. The synthetic pathway is represented in **Scheme 3.6**. Starting with 4-methyl-2-nitroaniline, bromination at the 6-position was performed in acetic acid using NH_4Br/H_2O_2 as a bromine source. The purpose of starting with 4-methyl-2-nitroaniline, rather than 2-nitroaniline, was to prevent the bromination at the 4-position, which otherwise decreased the yield and prevented clean separation. Subsequently, Suzuki coupling of ***a*** with 2,6-dimethylphenyl boronic acid afforded the dimethylphenyl-appended nitroaniline ***b***; the reaction proceeded with good yields only with $Pd(dba)_2$/XPhos as catalyst. The preparation of ***c*** was carried out via diazotization (acetone/H_2O, 0 °C, $NaNO_2$, H_2SO_4) followed by the addition of KSCN and CuSCN. The one-pot reduction of the nitro and thiocyanate groups was achieved with $LiAlH_4$ in dry THF, producing the expected product ***d***. Finally, the condensation reaction of ***d*** with 2-benzoylpyridine in acetic acid afforded the target ligand $\mathbf{L_B}$ in its 'apo-form' as the benzothiazoline, as evidenced by ^{1}H NMR (N-*H* = 6.17 ppm) and ^{13}C NMR (methine *C*-H = 83.70 ppm).

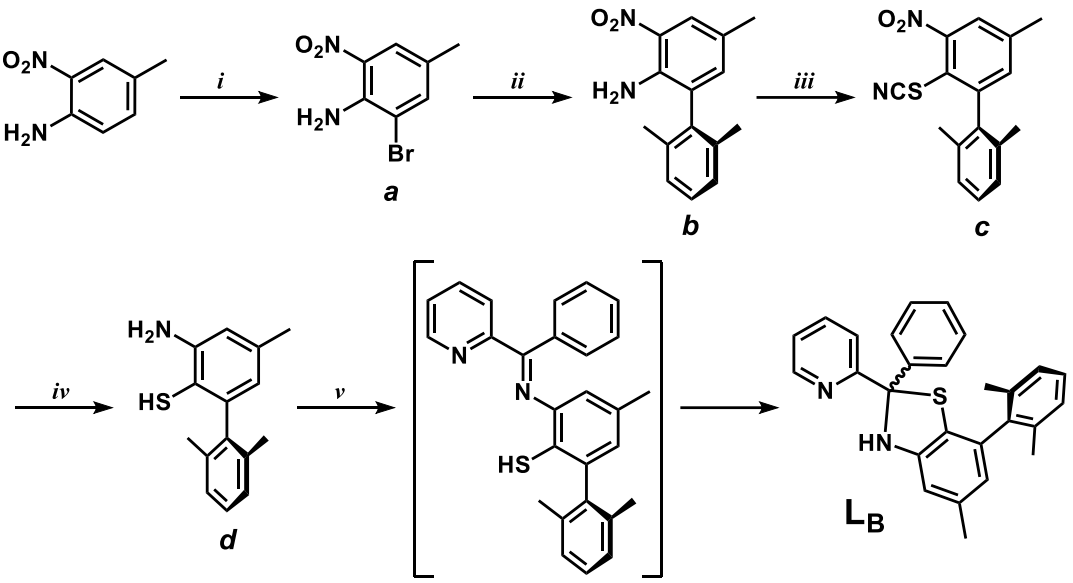

Scheme 3.6 Synthesis of bulky ligand, $\mathbf{L_B}$, ultimately derived from isomerization of the intended Schiff base ligand. Reaction condition: *i*) NH_4Br, 30 wt% H_2O_2, AcOH, r.t.; *ii*) 2,6-dimethyl boronic acid, K_2CO_3, $Pd(dba)_2$, XPhos, THF/H_2O (5:1, *v/v*), reflux; *iii*) H_2SO_4, $NaNO_2$, H_2O/acetone, 0 °C; KSCN, CuSCN, r.t.; *iv*) $LiAlH_4$, THF, reflux; *v*) 2-benzoylpyridine, AcOH, r.t.

Similar to the method described above, metalation of the bulky ligand $\mathbf{L_B}$ with $[Fe(CO)_4(Br)_2]$/$[Fe(CO)_4(I)_2]$ (**Scheme 3.7**) in THF at –30 °C was attempted. However, these conditions resulted in crude products with an ν(CO) stretches exclusively above 2000 cm^{-1}; this is distinct from complexes **1**-**4** which exhibit ν(CO) features in the 1950 cm^{-1} region. Such high energy ν(CO) features are consistent with the ligation of a neutral thioether donor[8] (e.g. benzothiazoline), rather than the intended thiolate. We thus inferred that for the bulky ligand, base might be necessary to promote the desired ring-opening reaction *prior to* rather than *during* metalation. We subsequently found that, when using $[Fe(CO)_4(Br)_2]$ as a metal source, anionic bases such as acetate (K^+ or NEt_4^+ salt) resulted in decarbonylation of the iron starting salt, whereas bulky and neutral nitrogen bases such as Hünig's base and proton sponge successfully promoted ring-opening and thiolate

ligation, vis a vis retention of ν(CO) features (below 2000 cm^{-1}). Ultimately, it was determined that 1,8-diazabicyclo[5.4.0]undec-7-ene (DBU) provided the cleanest product, as evidenced by two ν(CO) features in the IR. These set of ν(CO) features – one above and one below 2000 cm^{-1} – is consistent with the formulation of a mononuclear dicarbonyl species ligated by an anionic ligand frame.[4,6,20,22] By comparison, iron(II) dicarbonyls ligated by neutral NNS ligands (with methylthioether donor) exhibit *both* ν(CO) stretches above 2000 cm^{-1}.[8] Thus, the product was postulated as the target complex, [($N^{Ph}NS^{DMPh}$)$Fe(CO)_2Br$] (**8**); further spectroscopic evidence for **8** is provided below. Comparatively, the reactions of $[Fe(CO)_4(I)_2]$ with the bulky ligand only afforded product with ν(CO) stretches above 2000 cm^{-1}, regardless of the addition of bases. This may indicate that in the presence of $[Fe(CO)_4(I)_2]$, the pK_a of NH is not decreased as with $[Fe(CO)_4(Br)_2]$, and stronger base may be required in order to convert the ligand into Schiff base; such conditions were not pursued upon obtaining the successful result of metalation with $[Fe(CO)_4(Br)_2]$.

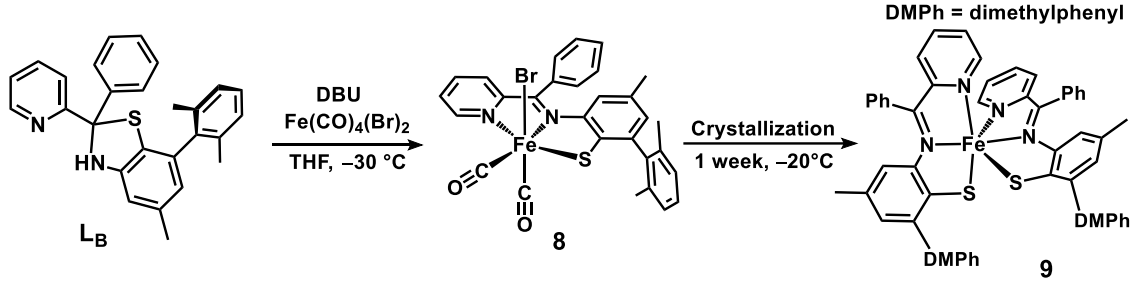

Scheme 3.7 Synthesis of the iron complexes **8** and **9** derived from the bulky thiolate ligand.

Concerning the above observations, the use of a base in the reaction proved imperative to generate the desired bulky ring-opened Schiff base ligand. In contrast to the non-bulky ligands (no base required), the base-specificity when metalating with the bulky

$\mathbf{L_B}$ is likely due to its large steric hindrance which prevents the metal source from pre-emptively binding to either the N or S moiety, thus precluding a decrease in NH pK_a that would be expected upon such 'pre'-complexation. The importance of choosing the proper solvent for metalation was also noticed in this reaction. THF evidently provided a suitable 'middle ground' in terms of coordinating ability. The same reactions in MeCN or DCM afforded products with multiple or no ν(CO) features, respectively.

Upon crystallization in THF at –30 °C, the complex **8** gradually decomposed, affording a diamagnetic bis-ligated Fe(II) complex, [($N^{Ph}NS^{DMPh}$)$_2$Fe] (**9**). The structure is shown in **Figure B24** and the selected bond distances and angles are tabulated in the supporting information (**Table B1**). The monocarbonyl intermediate was not isolated, nor was spectroscopically identified (*vice infra*).

3.3.2 Spectroscopic Characterization

Although the instability of the complex **8** prevented its crystallization, the formation of the mononuclear dicarbonyl complex [($N^{Ph}NS^{DMPh}$)Fe(CO)$_2$Br] (**8**) was evidenced by spectroscopic data (IR and ^{13}C NMR) and DFT calculation. The IR spectrum (**Figure 3.7**) of **8** shows two carbonyl peaks at 2036 and 1985 cm^{-1}, which are blue-shifted about 90 cm^{-1} compared with those of the dimer complexes (**1**, **2** and **3**). The equal intensity and Δν of the two CO frequencies is about 51 cm^{-1}, larger than those of the dimers. Both of the above features suggest that the two COs are bound to one iron center in a *cis* fashion.[20] Compared with the CO stretch of FeGP cofactor (solid[23]: 2004 and 1934 cm^{-1}, solution[20]: 2031 and 1972 cm^{-1}), the CO frequencies are blue-shifted, indicating that the electron density of the Fe center in the NNS complex is less than that of the enzyme active site.

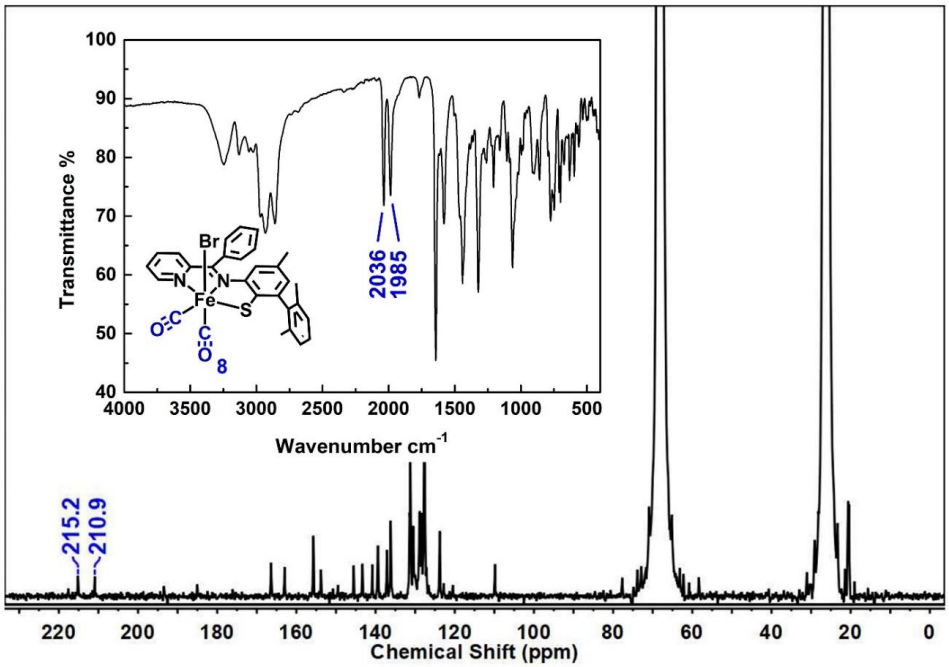

Figure 3.7 Low temperature (–30 °C) ^{13}C NMR spectrum of **8** (solvent: THF. The complex was generated in situ at –30 °C under CO atmosphere); Inset: solid-state IR spectrum of **8**.

The ^{13}C NMR spectrum of **8** was obtained at –30 °C with the in situ prepared complex in THF. The NMR tube was charged with CO gas (1 atm) to prevent decomposition. The ^{13}C NMR exhibits two resonances in the far downfield region at 215.2 and 211.9 ppm, which are assigned as the two chemically inequivalent terminal COs. The chemical shift of the COs is comparable with other reported complexes with *cis*-$\{Fe(CO)_2\}^{2+}$ motif (195-220 ppm).[6,24] The possibility of the presence of **8** as a dinuclear dicaronyl complex can be excluded, as in those cases the two terminal COs are chemically equivalent and will only display a single resonance in the ^{13}C NMR spectrum.

Attempts of observing **8** in mass spectrometry was unsuccessful, as the dicarbonyl complex decomposed during ionization process (ESI or CI). Instead, the ESI-MS analysis

shows two peaks with *m/z* = 463.0944 and 565.0036, consistent with the formulations of monomeric $[(N^{Ph}NS^{DMPh})Fe]^+$ and $[(N^{Ph}NS^{DMPh})FeBr+Na]^+$, respectively.

3.3.3 DFT Characterization of the Bulky Thiolate Monomer

To further postulate the formation of the mononuclear iron(II) dicarbonyl complex **8**, DFT calculations were performed at the level of B3LYP/6-311G** for C, H, O, N, S, Br and B3LYP/SDD for Fe. Geometry optimization provided a converged mononuclear diamagnetic Fe(II) structure featuring *cis* terminal carbonyls (**Figure 3.8**). The selected bond lengths and angles are shown in the supporting information (**Table B1**). The calculated IR of **8** (**Figure 3.8**) also exhibits two CO stretching features at 2044 and 2020 cm^{-1}, corresponding to the symmetric and asymmetric vibrations, respectively. Notably, the two CO vibrations are almost equally intense, which is in contrast to the calculated CO intensities for $[(NNS)_2Fe_2(CO)_2I_2]$ (**1**), where the CO symmetric vibrations are significantly more intense than the asymmetric vibration (**Figure B26-B27**). In addition, the wavenumber of CO vibrations for **8** is blue-shifted by 20 cm^{-1}, compared to the calculated value of **1**. The same trend is evident in the experimental data.

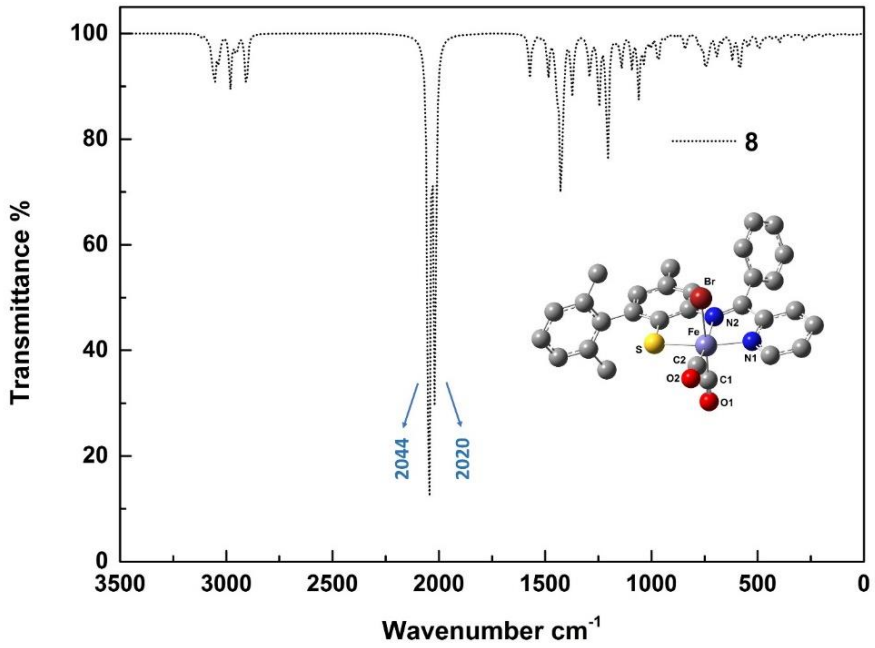

Figure 3.8 DFT-calculated structure and IR spectrum of **8**.

Based on the above data, the increase of the steric hindrance of the NNS ligand considerably affects the product afforded from the metalation. The bulky aryl substituent (DMPh = 2,6-dimethylphenyl) facilitates the formation of a mononuclear *cis*-dicarbonyl complex **8**.

3.4 Thermal Stability of the Dicarbonyl Complexes

We have demonstrated the different ligation properties of the non-bulky and bulky NNS ligands. The thermal instability of the dicarbonyl complexes (**1**, **2**, **3** and **8**) are also observed qualitatively in the synthesis. To quantitatively compare the ability of the NNS ligands to stabilize the carbonyl complexes, time-dependent UV/vis and IR experiments were performed.

The dimeric dicarbonyl complexes **1**–**3** were synthesized in situ in MeCN at low temperature (–30 °C) with a concentration of ~0.5 mM. The solutions were quickly

transferred to an air-free cuvette and the change in UV/vis absorption spectra were monitored at room temperature in the dark (**Figure B33**). All the samples gradually converted to the corresponding monocarbonyl complexes; the conversions are plotted in **Figure 3.9**. The variation of the ligand backbone gave rise to different $t_{½}$. Complex **2** shows the shortest $t_{½}$ (30 min), whereas complexes **3** and **1** exhibit similar stabilities ($t_{½}$: 75 min for **3**, 80 min for **1**). The difference in $t_{½}$ can be attributed to the structural distortion evident in the crystal structures. As the structure of **2** shows, the phenyl moiety on the imine carbon prevents ligand backbone ideal planarity in the crystal structure (see X-ray structure section), which decreases the stability of **2**. In contrast, in **3** the methyl group at the *ortho*-position of pyridine does not twist the ligand backbone, thus rendering a similar $t_{½}$ as **1**. The monocarbonyl complexes (**4**, **6** and **7**) show decent stability at room temperature in the inert atmosphere; no change in the UV/vis spectra was observed at room temperature over the course of several days.

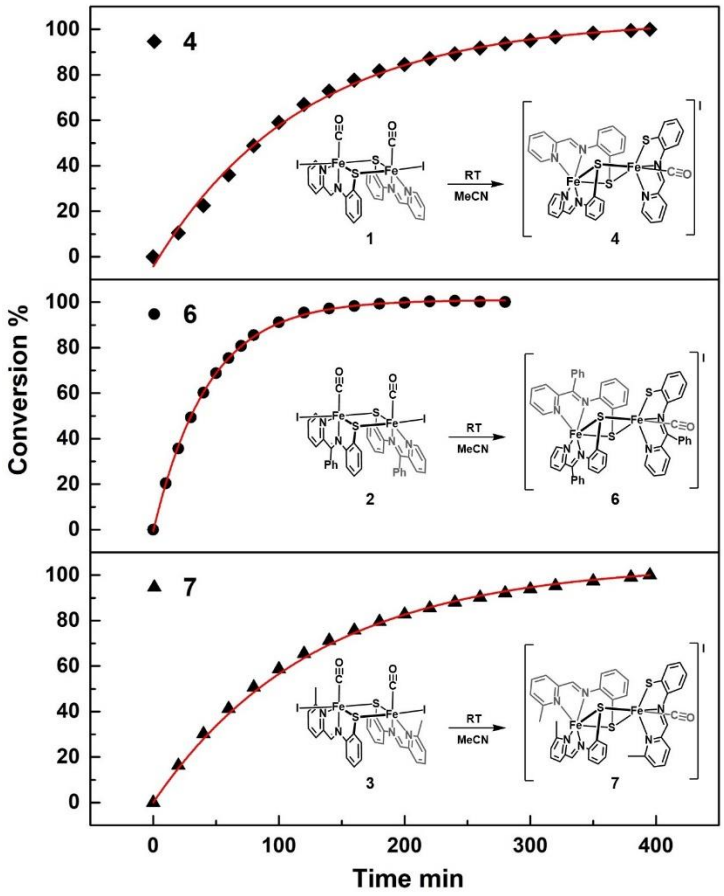

Figure 3.9 Conversion of **1**, **2** and **3** to the corresponding Fe^{II} monocarbonyls **4**, **6** and **7**, respectively, as determined by changes in the UV/vis spectra (changes of absorbance were monitored at the wavelength of 731 nm for **1**, 766 nm for **2** and 430 nm for **3**).

The attempts to monitor the decomposition of the mononuclear dicarbonyl complex [($N^{Ph}NS^{DMPh}$)$Fe(CO)_2Br$] (**8**) by UV/vis were proven unsuccessful, as **8** is unstable at room temperature and the absorption spectrum of the bis-ligated complex **9** completely obscures the trace of **8** (**Figure B34**). Thus, we instead proceeded to monitor the solution IR of **8** to study its thermal stability. A THF solution of **8** was incubated in dark at room temperature and an IR spectrum was taken every minute. As shown in

Figure 3.10, the thermal stability of **8** is considerably shorter than those dimeric dicarbonyl complexes. The conversion of **8** to **9** is complete within 15 min, with $t_{½}$ = 2 min. During the decomposition, complex **8** loses two CO ligands simultaneously and the dimeric dicarbonyl complex was not observed (**Figure 3.10 inset**).

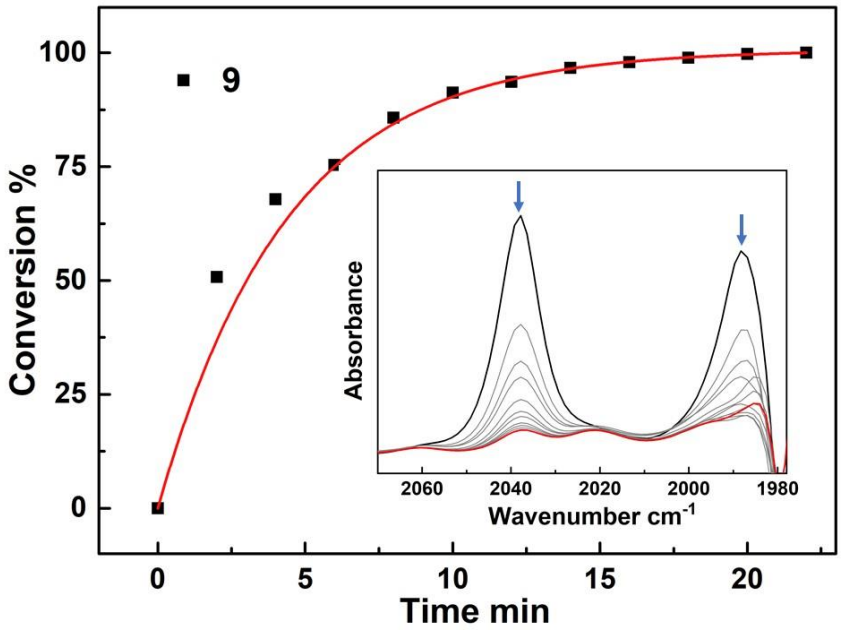

Figure 3.10 Conversion of **8** to the bis-ligated Fe^{II} complex **9** as determined by changes in the solution IR spectra in THF (*inset*).

Overall, it is evident that the NNS(thiolate) ligand frame is unable to stabilize the *cis*-dicarbonyl motif – regardless of mono- or dinuclearity – leading to decarbonylation and the (half)bisligated complexes. This suggests that one of the critical roles of the organometallic Fe–C(acyl) moiety in the Hmd enzyme active site is to prevent thermalization of the CO ligands under biological temperature and conditions. The same effect is also observed in our previous research.[8,10] The incorporation of carbamoyl unit

to the Fe center resulted in a series of stable organometallic complexes, $[(^{O=}C^{NH}N^{py}S^{Me})Fe(CO)_2L]$.[9,10]

3.5 CONCLUSION

(1) This series of iron carbonyl complexes featuring Schiff-base pyridine/(NNS) thiolate have been prepared via one-step metalation using benzothiazoline ligands and iron tetracarbonyl halides.

(2) Upon metalation, the non-bulky NNS thiolate ligands produce diiron dicarbonyl complexes due to the thiolate bridging effect. The products of stepwise transformation of diiron dicarbonyl complexes to diiron monocarbonyl complexes; finally, the oxidized iron(III) bis-ligated complexes were isolated.

(3) A bulky thiolate ligand with a 2,6-dimethylphenyl group *ortho* to the (aryl)thiolate was developed. This functional group prevents the dimerization across the thiolate, thereby affording a mononuclear dicarbonyl complex. This strategy could be applied to the synthesis of future structural and functional model of [Fe]-hydrogenase.

(4) The stability study has shown that the thiolate (without the acyl unit) is not sufficient to stabilize the *cis*-$\{Fe(CO)_2\}^{2+}$ core, and that ensuing decarbonylation leads to the formation of a bis-ligated complex. This indicates that one of functions of the acyl unit in the active site of [Fe]-hydrogenase is to prevent thermalization of the CO ligands bound to the Fe center.

3.6 EXPERIMENTAL PROCUDURES

3.6.1 General Information

All organic starting materials were purchased from Acros Organics or Sigma-Aldrich and used without further purification. The Fe(II) starting salt $[Fe(CO)_4(I)_2]$ was prepared by reaction of $[Fe(CO)_5]$ (Strem) with I_2 according to the published procedure.[25] The Fe(II) starting salt $[Fe(CO)_4(Br)_2]$ was prepared by reaction of $[Fe(CO)_5]$ (Strem) with Br_2 according to the published procedure,[22] and purified by re-crystallization from CH_2Cl_2 at –20 °C instead of sublimation. All iron complexes were prepared inside the glove box under dinitrogen atmosphere in the dark, unless otherwise indicated. HPLC grade solvents were purchased from EMD, Fisher, Macron or J.T. Baker, and dried through an alumina column system (Pure Process Technology). Deuterated solvent ($CDCl_3$) was purchased from Cambridge Isotopes and used as received.

3.6.2 Physical Measurements

NMR spectra were collected on Varian 400 MHz spectrometer and chemical shifts were referenced to $CDCl_3$. Solid state infrared spectra were recorded on a Bruker Alpha spectrometer equipped with a diamond ATR crystal. Mass spectra (MS) were acquired on either Thermo Scientific TSQ (CI) or Thermo Finnigan TSQ with Dionex Ultimate 3000 LC (ESI). The UV/vis absorption spectra were obtained at 298 K with an Agilent Cary 60 spectrophotometer. Micro-analytical (C, H, N) data were obtained by Midwest Microlabs.

The X-ray structure data for **1**, **2** and **4** were collected on a Rigaku AFC12 diffractometer with a Saturn 724+ CCD using a Mo Kα radiation with graphite monochromator. Reduced temperatures were maintained using an Oxford Cryostream low temperature device. Data reduction were performed using Rigaku CrystalClear

version 1.4.0.[26] The data for **5**, **9** and [Fe(NNS)$_2$] were collected on an Agilent Technologies SuperNova Dual Source diffractometer using a μ-focus CuKα radiation (λ = 1.5418Å) with collimating mirror monochromators. Data reduction was performed using Agilent Technologies CrysAlisPro 1.171.37.31.[27] Reduced temperatures were maintained using an Oxford Cryostream low temperature device. Structures were solved by direct methods using SuperFlip[28] and refined by full-matrix least-squares on F^2 with anisotropic displacement parameters for the non-H atoms using SHELXL-2013[29]. Structure analysis was aided by PLATON98[30] and WinGX[31]. The hydrogen atoms on carbon were calculated in ideal positions with isotropic displacement parameters set to 1.2 × U_{eq} of the attached atom (1.5 × U_{eq} for methyl hydrogen atoms). The data were checked for secondary extinction effects but no correction was necessary. Neutral atom scattering factors and values used to calculate the linear absorption coefficient are from the International Tables for X-ray Crystallography.

3.6.3 DFT Calculations

DFT calculations were carried out for **1**, **4**, **5** and **8** in the Gaussian 09[32]. Geometry optimizations and energy calculations employed B3LYP[33,34] functional; SDD[35] basis set for Fe; LanL2DZ[36,37] basis set for iodine; and 6-311G(d,p)[38,39] basis set for C, H, N, O, S. Frequency calculations were performed for **1**, **4** and **8** at the same level of theory as the optimizations. All frequency calculations showed no imaginary frequencies and the wavenumbers were scaled by 0.964.[40] Time-dependent density functional theory (TDDFT[41,42]) calculations were executed for **1**, **4** and **5** to study their excited states at the same level of theory as the optimizations. The effect of solvation was considered by performing polarizable continuum model (PCM),[43] MeCN as solvent, ε = 35.688. GaussView[44] was used for visualization and data analysis.

3.6.4 Synthetic Procedures

NNS 2-(Pyridin-2'-yl)benzothiazoline (L1). The synthesis of **L1** was a modified version of a published procedure.[45] Under dinitrogen atmosphere, the 2-pyridinecarboxaldehyde (1.000 g, 9.337 mmol) was mixed with 2-aminobenzenethiol (1.167 g, 9.337 mmol), upon the addition of which a pale yellow precipitate formed immediately. Then, 2 mL of methanol was added and the reaction was stirred for 10 min. The methanol was decanted and the residue was washed with pentane. The product was collected as a pale yellow solid. Yield: 1.930 g (96.5%). IR (neat, cm^{-1}) 3185 m, 3166 m, 3067 w, 3015 w, 2953 w, 1589 m, 1577 m, 1467 s, 1434 m, 1421m, 1348 m, 1306 m, 1268 w, 1250 m, 1158 m, 1146 m, 1120 m, 1098 m, 1071 m, 1048 m, 1017 m, 996 w, 957 w, 911 m, 905 w, 794 m, 768 m, 745 s, 733 s, 716 s, 685 s, 646 m, 620 s, 572 w, 562 w, 529 m,478 s; ^{1}H NMR (400 MHz, $CDCl_3$) δ = 8.56 (ddd, *J* = 4.9, 1.8, 1.0 Hz, 1H), 7.69 (ddd, *J* = 7.4, 1.8, 0.4 Hz, 1H), 7.58 (dtd, *J* = 7.9, 1.1, 0.5 Hz, 1H), 7.22 (dddd, *J* = 7.5, 4.8, 1.2, 0.4 Hz, 1H), 7.12 – 7.02 (m, 1H), 7.01 – 6.91 (m, 1H), 6.86 – 6.75 (m, 2H), 6.41 (s, 1H), 5.06 (s, 1H); ^{13}C NMR (100 MHz, $CDCl_3$) δ = 160.4, 149.2, 146.7, 137.4, 127.7, 125.6, 123.3, 121.9, 121.6, 121.1, 111.7, 70.1; MS (ESI, *m*/*z*): 215 $[MH]^+$, 237 $[MNa]^+$.

^{Me}NNS 2-(6'-Methyl-pyridin-2'yl)benzothiazoline (L2). Under dinitrogen atmosphere, the 6-methyl-2-pyridinecarboxaldehyde (0.985 mg, 8.131 mmol) was mixed with 2-aminobenzenethiol (1.017 g, 8.131 mmol), upon the addition of which a pale yellow precipitate formed immediately. Then, 1 mL of methanol was added and the reaction was stirred for 10 min. The methanol was removed *in vacuo*. The resulting orange oil was triturated with Et_2O/pentane (*v*/*v* = 1/4, 5 mL) and washed with pentane (3 mL), which afforded the product as a pale yellow solid. Yield: 1.429 g (76%). IR (neat, cm^{-1}) 3136 br, 3066 m, 3007 w, 2935 w, 2884 m, 1591 s, 1571 s, 1498 w, 1446 s, 1374

w, 1305 w, 1275 w, 1251 w, 1149 m, 1114 w, 1085 m 1056 m, 1032 w, 1018 m, 989 m, 808 m, 731 s, 690 m, 421 w; ^{1}H NMR (400 MHz, $CDCl_3$) δ = 7.58 (t, *J* = 7.7 Hz, 1H), 7.37 (d, *J* = 7.7 Hz, 1H), 7.11 – 7.05 (m, 2H), 6.99 – 6.93 (m, 1H), 6.80 (d, *J* = 7.8 Hz, 2H), 6.38 (s, 1H), 5.12 (s, 1H), 2.55 (s, 3H); ^{13}C NMR (100 MHz, $CDCl_3$) δ = 159.4, 158.04, 146.9, 137.5, 128.2, 125.5, 122.9, 121.8, 121.6, 118.1, 111.9, 70.3, 24.5; MS (ESI, *m*/*z*): 229 $[MH]^+$, 251 $[MNa]^+$.

$N^{Ph}NS$ 2-(Pyridin-2'-yl)-2-phenyl-benzothiazoline (L3). Under dinitrogen atmosphere, the 2-benzoylpyridine (1.000 g, 5.460 mmol) was mixed with 2-aminobenzenethiol (0.750 g, 6.000 mmol), and 10 mL of acetic acid was added. The reaction was stirred at *room temperature* for 24 h. The acetic acid was removed *in vacuo*. The resulting oil was triturated with ethanol (3 × 3 mL), Et_2O (3 mL) and pentane (3 mL), which afforded the product as a pale yellow solid. Yield: 1.130 g (71%). IR (neat, cm^{-1}) 3258 m, 3058 w, 2979 m, 2875 w, 1607 w, 1582 m, 1474 w, 1458 m, 1446 m, 1275 m, 1212 w, 1119 w, 1032 w, 904 w, 763 s, 749 s, 730 m, 714 m, 576 w, 454 w; ^{1}H NMR (400 MHz, $CDCl_3$) δ =8.67 – 8.51 (m, 1H), 7.84 (d, *J* = 7.9 Hz, 1H), 7.69 (td, *J* = 7.7, 1.8 Hz, 1H), 7.65 – 7.50 (m, 2H), 7.47 – 7.27 (m, 2H), 7.25 (d, *J* = 7.3 Hz, 1H), 7.22 – 7.12 (m, 1H), 7.06 (dd, *J* = 7.6, 1.3 Hz, 1H), 6.95 (td, *J* = 7.6, 1.3 Hz, 1H), 6.83 (dd, *J* = 7.9, 1.2 Hz, 1H), 6.77 (td, *J* = 7.5, 1.2 Hz, 1H), 6.17 (s, 1H); ^{13}C NMR (100 MHz, $CDCl_3$) δ = 163.0, 148.8, 146.1, 144.5, 136.8, 128.3, 127.8, 127.1, 125.6, 122.5, 121.8, 121.3, 121.2, 111.8, 84.2; MS (ESI, *m*/*z*): 291 $[MH]^+$, 313 $[MNa]^+$.

2-Bromo-4-methyl-6-nitrobenzenamine (a). 4-Methyl-2-nitroaniline (5.00 g, 32.90 mmol) was dissolved in acetic acid (50 mL). Finely ground ammonium bromide (5.16 g, 52.60 mmol) and 30 wt% solution of hydrogen peroxide (in H_2O) (5.25 mL, 52.60 mmol) were added consecutively to reaction mixture, which then was stirred for 68 hours. The mixture was poured into an aqueous solution of 1 M sodium carbonate and the

precipitate was collected by filtration and dried *in vacuo* to afford **a** as a pure, bright orange powder. Yield: 7.132 g (93.8%). IR (neat, cm^{-1}) 3481 m, 3466 m, 3367 s, 3355 s, 1621 m, 1573 s, 1551 s, 1504 s, 1445 m, 1395 m, 1344 s, 1323 s, 1251 s, 1237 s, 1201 s, 1086 s, 935 s, 865 s, 791 m, 761 s, 727 s, 551 s, 458 m; ^{1}H NMR (400 MHz, $CDCl_3$) δ = 7.93 (s, 1H), 7.55 (d, *J* = 2.0 Hz,1H), 6.46 (s, 2H), 2.27 (s, 3H);^{13}C NMR (100 MHz, $CDCl_3$) δ = 140.3, 140.1, 132.7, 126.6, 125.6, 112.0, 20.0; MS (ESI, *m*/*z*): 291 $[MH]^+$, 313 $[MNa]^+$.

2-(2',6'-Dimethylphenyl)-4-methyl-6-nitroaniline (b). Under dinitrogen atmosphere, **a** (5.00 g, 21.64 mmol), 2,6-dimethylphenyl boronic acid (4.00 g, 26.67 mmol), potassium carbonate (4.00 g, 28.94 mmol), 2-dicyclohexylphosphino-2′,4′,6′-triisopropylbiphenyl (*Xphos*) (309 mg, 0.649 mmol), and $Pd(dba)_2$ (373 mg, 0.649 mmol) were mixed in 120 mL of degassed THF and 24 mL of degassed water. The reaction was refluxed for 24 h, after which an additional amount of 2,6-dimethyl boronic acid (2.00 g, 13.34 mmol) and potassium carbonate (2.00 g, 14.47 mmol) were added and refluxed for another 24 h. After cooling to *room temperature*, THF was removed *in vacuo* and the mixture was extracted with ethyl acetate (50 mL × 3). The combined organic phase was washed with brine and dried over Na_2SO_4. The product was purified by column chromatography (silica gel, EtOAc/Hexane = 1/8) to afford **b** as an orange oil. Yield: 4.33 g (78%). IR (neat, cm^{-1}): 1716 m, 1629 m, 1567 s, 1517 m, 1442 m, 1253 m, 1230 s, 1083 w, 1031 w, 935 m, 872 m, 768 s, 709 m; ^{1}H NMR (400 MHz, $CDCl_3$): δ 7.97 (d, *J* = 1.2 Hz, 1H), 7.25 – 7.21 (m, 1H), 7.17 (d, *J* = 7.3 Hz, 2H), 7.02 (d, *J* = 2.1 Hz, 1H), 5.81 (s, 2H), 2.60 (s, 3H), 2.04 (s, 6H); ^{13}C NMR (100 MHz, $CDCl_3$): δ = 140.3, 137.5, 137.3, 135.1, 132.2, 129.7, 128.5, 128.1, 126.0, 124.5, 20.2, 20.0; MS (ESI, *m*/*z*): 257 $[MH]^+$, 279 $[MNa]^+$.

2-(2',6'-Dimethylphenyl)-4-methyl-6-nitrobenzenethiocyanate (c). To a solution of **b** (4.33 g, 16.89 mmol) in 300 mL of acetone was added 10.7 mL of sulfuric acid (202.59 mmol). $NaNO_2$ (5.82 g, 84.47 mmol) in 150 mL of water was added dropwise to the mixture at 0 °C. The reaction was stired at 0 °C for 30 minutes. Then, copper thiocyante (5.34 g, 43.92 mmol) and potassium thiocyanate (16.42 g, 168.9 mmol) in 150 mL of water were added to the reaction at 0 °C. The reaction was stirred at 0 °C for 1 h and at *room temperature* for 4 h. NaOH aqueous solution was added dropwise to adjust the pH to ~7 and acetone was removed under reduced pressure. The mixture was filtered and the filtrate was extracted by ethyl acetate (20 mL × 3). The combined organic phase was washed by brine and dried over Na_2SO_4. The product was purified by column chromatography (silica gel, EtOAc/Hexane = 1/8) to afford **c** as an orange solid. Yield: 1.92 g (38%). IR (neat, cm^{-1}): 2170 m (SCN), 1531 s, 1463 s, 1379 m, 1355 s, 1081 w, 770 s, 710 m; ^1H NMR (400 MHz, $CDCl_3$): δ 7.82 (s, 1H), 7.35 (m, 1H), 7.30 (m, 1H), 7.19 (d, *J* = 7.9 Hz, 2H), 2.53 (s 3H), 2.04 (s 6H); ^{13}C NMR (101 MHz, $CDCl_3$): δ = 152.5, 147.5, 143.3, 137.1, 136.5, 136.0, 129.2, 128.3, 125.4, 114.9, 108.1, 21.3, 20.8; MS (CI, *m*/*z*): 272 [M^+ without CN], 279 $[MNa]^+$.

2-Mercapto-3-(2',6'-dimethylphenyl)-5-methyl-aniline (d). Under dinitrogen atmosphere, **c** (500 mg, 1.676 mmol) in 15 mL of dry THF was added $LiAlH_4$ (508 mg, 13.407 mmol) slowly at 0 °C and then refluxed for 16 hours. After cooling to 0 °C, the reaction was quenched with degassed water and filtered under dinitrogen. The residue was washed by degassed THF (5 mL) and water (2 × 5 mL). $NaHSO_4$ aqueous solution was added to the filtrate until the pH was about 3. THF was removed *in vacuo* and the compound **d** precipitated as a yellow solid, which was washed by water (3 × 10 mL) and pentane (3 × 5 mL), and used for the next step without further purification. Yield: 257 mg (63%). IR (neat, cm^{-1}): 3383 w, 3309 w, 2961 w, 2584 w (S-H), 2558 w (S-H), 1620 s,

1566 s, 1453 s, 1408 m, 1375 m, 1329 m, 1259 s, 1084 s, 1027 s, 798 m, 768 m, 567 w; ^{1}H NMR (400 MHz, $CDCl_3$): δ = 7.18 (dd, *J* = 8.6, 6.5 Hz, 1H), 7.13 – 7.08 (m, 2H), 6.58 (dd, *J* = 1.8, 0.7 Hz, 1H), 6.39 (dd, *J* = 1.8, 0.7 Hz, 1H), 4.02 (s, 2H), 2.61 (s, 1H), 2.26 (s, 3H), 2.00 (s, 6H); MS (CI, *m*/*z*): 244 $[MH]^+$.

$N^{Ph}NS^{DMPh}$ 2-(Pyridin-2'-yl)-2-phenyl-4-(2",6"-dimethylphenyl)-6-methylbenzothiazoline (L_B). Under dinitrogen atmosphere, **d** (257 mg, 1.056 mmol) and 2-benzoylpyridine (174 mg, 0.950 mmol) were mixed in 5 mL of acetic acid. The reaction was stirred at *room temperature* for 24 h, and large amount of off-white precipitate was observed. The acetic acid was removed *in vacuo*. The resulting oil was treated with pentane (30 mL), which afforded the product as an off-white solid. Yield: 233 mg (54%). IR (neat, cm^{-1}): 1577 m 1464 m 1435 m 1409 m 1287 w 1210 w, 995 w, 839 m, 760 s, 701 s, 595 m, 551 m; ^{1}H NMR (400 MHz, $CDCl_3$, 25 °C): δ = 8.53 (d, *J* = 4.6 Hz, 1H), 7.80 (d, *J* = 8.0 Hz, 1H), 7.65 (td, *J* = 7.6, 1.6 Hz, 1H), 7.50 (dd, *J* = 8.2, 1.0 Hz, 2H), 7.26 (s, *J* = 15.0 Hz, 1H), 7.20 (d, *J* = 7.0 Hz, 1H), 7.18 – 7.11 (m, 2H), 7.07 (d, *J* = 7.7 Hz, 2H), 6.64 (s, 1H), 6.36 (s, 1H), 6.29 (s, 1H), 4.71 (s, 1H), 2.26 (s, 3H), 2.04 (s, 3H), 1.97 (s, 3H);^{13}C NMR (101 MHz, $CDCl_3$, 25 °C): δ = 163.3, 148.7, 146.5, 144.6, 140.0, 136.6, 136.2, 136.0, 135.8, 134.3, 128.2, 127.5, 127.4, 127.3, 127.2, 126.7, 123.5, 122.3, 122.0, 121.7, 111.0, 83.7, 21.3, 20.2, 20.2. MS (ESI, *m*/*z*): 408 $[MH]^+$, 431 $[MNa]^+$.

$[(NNS)_2Fe_2(CO)_2(I)_2]$ (1). Under dinitrogen atmosphere, 0.099 g (0.234 mmol) of $[Fe(CO)_4(I)_2]$ in a vial was dissolved in 4 mL of acetonitrile as a dark red solution. In a separate vial, 0.050 g (0.234 mmol) of **L1** was dissolved in another 4 mL of acetonitrile to generate a yellow solution. At –30 °C, the addition of $[Fe(CO)_4(I)_2]$/acetonitrile solution to the ligand solution immediately generated a dark green solution, which was stirred at –30 °C for 4 h. The resulting solution was filtered and the filtrate was subjected

to vapor diffusion of diethyl ether at -30 °C, which resulted in small dark brown crystals suitable for X-ray diffraction. Yield: 52 mg (53%). IR (neat, cm^{-1}): 1941 s, 1926 s, 1601 m, 1469 m, 1456 m, 1432 m, 1149 m, 777 s, 757 s, 743 s, 580 s. UV/vis in MeCN, λ_{max} in nm: 465, 309, 245.

[($N^{Ph}NS)_2Fe_2(CO)_2(I)_2$] (2). This complex was prepared according to the procedure for **[$(NNS)_2Fe_2(CO)_2(I)_2$] (1)**: **L3** (0.050 g, 0.172 mmol) in 4 mL of acetonitrile, $[Fe(CO)_4(I)_2]$ (0.073 g, 0.172 mmol) in 4 mL of acetonitrile. The dark brown crystals suitable for X-ray diffraction were obtained from acetonitrile solution subjected to diethyl ether vapor diffusion at –30 °C. Yield: 17 mg (21%). IR (neat, cm^{-1}): 1955 s, 1932 m, 1588 m, 1573 s, 1458 m, 1442 m, 1327 m, 1017 w, 745 s, 714 s, 617 s, 580 s, 568 s, 440 m. UV/vis in MeCN, λ_{max} in nm = 465, 309, 245.

[($^{Me}NNS)_2Fe_2(CO)_2(I)_2$] (3). This complex was prepared according to the procedure for **[$(NNS)_2Fe_2(CO)_2(I)_2$] (1)**: **L2** (0.050 g, 0.219 mmol) in 4 mL of acetonitrile, $[Fe(CO)_4(I)_2]$ (0.092 g, 0.219 mmol) in 4 mL of acetonitrile. The resulting acetonitrile solution was subjected to diethyl ether vapor diffusion at –30 °C, which afforded black powder. Yield: 36 mg (38%). IR (neat, cm^{-1}): 1951 s, 1927 m, 1605 m, 1471 s, 1375 m, 1329 m, 1098 m, 794 m, 766 s, 736 s, 567 s, 424 m. UV/vis in MeCN: λ_{max} in nm: 465, 309, 245.

[$(NNS)_3Fe_2(CO)$]I (4). Method A. This complex was prepared according to the procedure for **[$(NNS)_2Fe_2(CO)_2(I)_2$]**, except that, after the reaction, the filtrate was subjected to vapor diffusion of diethyl ether at *room temperature*, which resulted in small dark green crystals suitable for X-ray diffraction. Yield: 48 mg (69%). IR (neat, cm^{-1}): 1940 s, 1661 s, 1651 s, 1596 m, 1504 m, 1467 m, 1434 m, 1384 m, 1297m, 1287 m, 1151 s, 764 m, 712 m, 572 m. UV/vis in MeCN, λ_{max} in nm (ε in M^{-1} cm^{-1}): 727 (4360), 627 (3790), 424 (8470), 317 (25500), 244 (42000). Note: Elemental analysis for bulk

crystalline material of **4** indicated the presence of **5** (~25%), which immediately forms from solutions of **4** exposed to oxygen. Although samples of **4** were synthesized and crystallized in a drybox, we attribute the presence of **5** (estimated ~25%) to two factors: first, residual O_2 in the drybox, and second, with the identical charge (monocation) and counterion (I^-) of the two complexes. Anal. calcd for $C_{37}H_{27}Fe_2N_6OS_3I$ (**4**, 75%) plus $C_{24}H_{18}FeIN_4S_2$ (**5**, 25%): C 48.75, H 3.00, N 9.25%; found: C 46.50, H 3.73, N 9.76%. **Method B.** The **[(NNS)$_3$Fe$_2$(CO)]I** was prepared according to the procedure for **[(NNS)$_2$Fe$_2$(CO)$_2$(I)$_2$]**, except that, after the reaction, the filtrate was treated with several drops of DMF and subjected to vapor diffusion of diethyl ether at –30 °C, which resulted in small dark green crystals suitable for X-ray diffraction.

[(NNS)$_2$Fe]I·0.25I$_2$ (5). This complex was prepared according to the procedure for **[(NNS)$_3$Fe$_2$(CO)]I (4)**, except that after the reaction, the filtrate was subjected to vapor diffusion of diethyl ether at room temperature in air, which resulted in small dark green crystals suitable for X-ray diffraction. Yield: 23 mg (32%). IR (neat, cm^{-1}): 1599 s, 1577 s, 1472 s, 1454 m, 1437 m, 1352 m, 1256 m, 1151 m, 1063 m, 896 w, 763 s, 709 m, 590 s, 433 m. High-resolution mass spectrometry (HR-MS) (ESI+): m/z 482.0328 $[M]^+$. UV/Vis in MeCN, λ_{max} (in nm) (ε in M^{-1} cm^{-1}): 563 (3730), 413 (5230), 340 (15 400), 292 (27 800), 245 (32 500). Anal. calcd for $C_{24}H_{18}FeIN_4S_2$•0.25I_2: C 42.85, H 2.70, N 8.33%; found: C 43.14, H 2.92, N 8.41%.

[(NNS)$_2$Fe]. Under dinitrogen atmosphere, 50 mg (0.23 mmol) of **L1** was dissolved in 2 mL of MeCN, and 40 µL (0.23 mmol) of N,N-diisopropylethylamine was added. The mixture was stirred for 10 min. In a separate vial, FeI_2 (36 mg, 0.12 mmol) was dissolved in 2 mL of MeCN and then added to the solution. The resultant solution was stirred for 30 min at *room temperature*. The solvent was removed in vacuo and the residue was washed with Et_2O, which afforded a dark green powder. Yield: 43 mg (76%).

The dark green crystal suitable for X-ray diffraction was obtained from MeCN solution subjected to diethyl ether vapor diffusion. IR (neat, cm^{-1}): 1657 m, 1587 s, 1568 s, 1481 s, 1438 m, 1421 m, 1250 s, 1144 s, 1062 s, 1024 m, 909 m, 834 s, 759 s, 735 s, 654 s, 600 m, 439 s. UV/vis in MeCN, λ_{max} in nm (ε in M^{-1} cm^{-1}): 614 (2210), 441 (5000), 319 (12600), 281 (15300).

[($N^{Ph}NS^{DMPh}$)$Fe(CO)_2(Br)$] (8). Under dinitrogen atmosphere, 0.010 g (0.0245 mmol) of $\mathbf{L_B}$ was dissolved in 1 mL of THF as a pale yellow solution in a vial. Then, 3.65 μL (0.0245 mmol) of 1,8-diazabicyclo[5.4.0]undec-7-ene *(DBU)* was added to the same vial and stirred for 20 min. In a separate vial, 0.008 g (0.0245 mmol) of $[Fe(CO)_4(Br)_2]$ was dissolved in another 1 mL of THF to generate a dark red solution. At –30 °C, the addition of $[Fe(CO)_4(Br)_2]$ solution to the ligand solution immediately generated a dark green solution, which was stirred at –40 °C for 2 h. The resulting product was not stable. After the product was subjected to vapor diffusion of ether at –30 °C, dark green crystals suitable for X-ray diffraction were isolated which were proved to be **[($N_{Ph}NS_{DMPh}$)$_2$Fe] (9)**. The ^{13}C NMR spectrum was taken with in situ synthesized product and the J-Y tube was charged with CO gas and kept at –30 °C to avoid product decomposition (**CAUTION!** Decomposition could lead to explosion, handle with care!). IR for **8** (neat, cm^{-1}): 2036 m, 1985 m, 1643 s, 1581 m, 1441 m, 1321 m, 1206 w, 1063 m, 858 m, 775 m, 699 w. ^{13}C NMR (126 MHz, THF, –30 °C): δ = 215.2, 210.9, 166.4, 163.0, 155.7, 153.8, 145.5, 143.3, 140.8, 139.4, 137.1, 136.2, 131.4, 131.2, 130.5, 128.9, 128.8, 128.4, 127.8, 127.6, 127.1, 123.8, 109.9, 20.7, 20.4.

[($N^{Ph}NS^{DMPh}$)$_2$Fe] (9) (Method B). Under dinitrogen atmosphere, $\mathbf{L_B}$ (30 mg, 0.074 mmol) in 1 mL of PhF was mixed with N,N-diisopropylethylamine (7.0 μL, 0.040 mmol). In a separate vial, $FeBr_2$ (8.7 mg, 0.040 mmol) was dissolved in 1 mL of PhF and then was added to $\mathbf{L_B}$. The solution turned dark green immediately and was stirred for 1

h. The solvent was removed *in vacuo* and the residue was washed with diethyl ether and pentane. The dark green crystals suitable for X-ray diffraction were obtained from PhF solution subjected to diethyl ether vapor diffusion at –30 °C. Yield: 21 mg (68%) IR (neat, cm^{-1}): 1582 m, 1471 m, 1436 s, 1422 m, 1324 m, 1308 m, 1275 m, 1228 m, 1153 w, 1128 w, 937 m, 743 s, 686 s, 643 s, 593 m. MS (ESI, *m*/*z*): 870 $[M]^+$.

Stability Studies. *Non-bulky Complexes*. In two separate vials, $[Fe(CO)_4(I)_2]$ and the specific NNS ligand were dissolved in MeCN, respectively. The solutions were cooled down to –30 °C, and then mixed together in the dark (the concentrations of product were about 0.5 mM). The resultant solution was immediately transferred to an air free cuvette and UV/vis spectra were taken every five minutes.

Bulky Complexes. In two separate vials, $[Fe(CO)_4(Br)_2]$ and $\mathbf{L_B}$ ligand were dissolved in THF, respectively (*DBU* was added to the ligand). The solutions were cooled down to –30 °C, and then mixed together in the dark (the concentrations of product were about 0.5 mM). The resultant solutions were immediately transferred to an air free cell, and IR spectra were obtained one per minute.

Chapter 4: Bio-inspired CNP Iron(II) Pincer Relevant to [Fe]-Hydrogenase: Effect of Dicarbonyl versus Monocarbonyl Motifs in H_2 Activation and Transfer Hydrogenation*

4.1 INTRODUCTION

As the availability and environmental cost of fossil fuels make their extraction increasingly difficult, the world's energy sources are slowly shifting from traditional energies to renewable energies.[1–3] One promising alternative renewable energy source is dihydrogen (H_2), which has many advantages: zero carbon emission, high mass energy density (120 MJ/kg) and high energy efficiency in combustion.[4] Despite of the benefits of dihydrogen, its generation limits its applications because 95% of H_2 production is derived from carbon intensive methods, such as steam reforming and water-gas shift.[5] Although methods like biomass fermentation and direct water-splitting have drawn substantial attention from researchers, the efficiency of H_2 generation remains an issue.[6] This motivates the development of more efficient catalysts for both H_2 generation and utilization derived from earth abundant elements.

In nature, H_2 is both generated and utilized by hydrogenases. To date, three types of hydrogenases have been discovered: [NiFe]-hydrogenase, [FeFe]-hydrogenase and [Fe]-hydrogenase.[7] In contrast to the thorough understanding of the bimetallic hydrogenases, studies of [Fe]-hydrogenase remain relatively nascent. The enzyme [Fe]-hydrogenase catalyzes the non-redox hydride transfer from H_2 to the substrate methenyl-tetrahydromethanopterin (H_4MPT^+), which serves as a C_1 carrier in methanogenic carbon dioxide (CO_2) reduction (**Scheme 4.1**).[7–9] This metalloenzyme (also called Hmd: $\underline{H}_2$-forming $H_4\underline{m}$ethylene-PT $\underline{d}$ehydrogenase) plays an obligate role in the 'nickel-free'

* Unpublished work. Rose and Xie designed the research. Xie performed the research. Wenrui performed the DFT calculation. Xie and Wenrui analyzed the data.

$CO_2 \rightarrow CH_4$ metabolism in the absence of bio-available nickel (and thereby, [NiFe] hydrogenase).[7–9] The active site of [Fe]-hydrogenase (FeGP cofactor) exhibits a unique array of non-proteinaceous ligands (except for Cys_{176}), including a *cis*-dicarbonyl motif, a bidentate pyridone-acyl unit that presents a unique (to biology) organometallic Fe–C bond, and a substrate binding site occupied by a weakly bound H_2O in the resting state.[10,11]

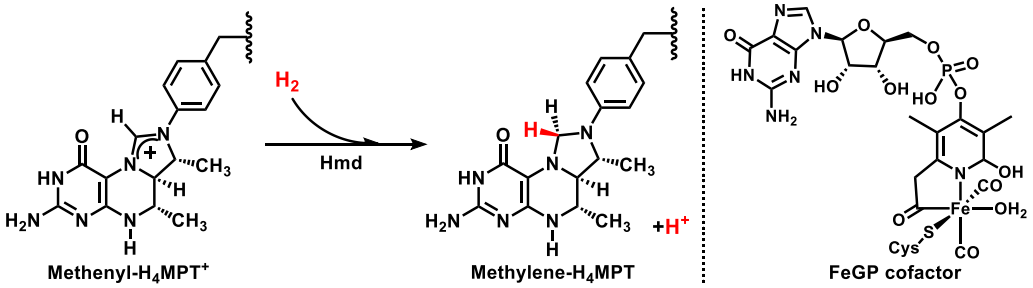

Scheme 4.1 Reaction of methenyl-H_4MPT^+ to Methylene-H4MPT by [Fe]-hydrogenase and the structure of FeGP cofactor.

Computational studies of [Fe]-hydrogenase have evaluated several plausible mechanisms of H_2 splitting. Hall and coworkers[12] performed DFT calculations on a simplified active site. This study suggested that the active site binds and activates H_2 in stepwise fashion without the participation of substrate (H_4MPT^+). The coordination site *trans* to the acyl unit is ideal for binding and cleavage of H_2, as it requires the minimum structural change on the ligand backbone during the catalytic circle. The main pathway of H_2 heterolytic splitting utilized metal-ligand bifunction between iron(II) and the (deprotonated) pyridone-oxygen. The resulting iron-hydride intermediate was calculated along the reaction trajectory and provides hydride transfer to H_4MPT^+ with an accessible activation barrier (15.2 kcal/mol). In 2014, Reiher and coworkers[13] reported a theoretical study based on the full protein structure using a multiscale modeling method (QM/MM).

In contrast to the previously proposed mechanism, Reiher suggested that the protein scaffold where the FeGP cofactor harbors provides the necessary conformation change for the substrate to approach the active site. As such, the coordinated H_2 can be cleaved by the orbital push-pull effect between the pyridone oxygen and the cationic carbon on the substrate imidazolium ring (ΔE_a = 1.0 kcal/mol). As a result, no formal iron-hydride intermediate was suggested.

In a *non-biomimetic* synthetic system (**Scheme 4.2**), Kirchner[14] reported $P^{NH}N^{NH}P$ iron(II) carbonyl complexes, in which the dicarbonyl complex $[(P^{NH}N^{=N}P)Fe(CO)_2]^+$ is able to cleave H_2 via metal-ligand bifunctional mechanism, leading to the hydride complex $[(P^{NH}N^{NH}P)Fe(CO)_2(H)]$. Later, Kirchner[15] reported the monocarbonyl complexes $[(P^{NH}N^{NH}P)Fe(CO)(L)(H)]$, with labile ligands (L = Br^-, MeCN, BH_4^-) *trans* to the hydride, are efficient catalysts for hydrogenation of ketones and aldehydes to alcohols. In parallel, methylene-spaced PNP iron monocarbonyl complexes developed by Milstein have been applied to hydrogenation of CO_2[16], ketones[17,18] and trifluoroacetic esters[19] with high efficiency. Hu synthesized a third type of PNP iron complexes with oxygen spacer which can carry out methanol-assisted H/D scrambling and hydrogenation and transfer hydrogenation of aldehydes.[20]

Returning to [Fe]-hydrogenase, the DFT proposed mechanisms warrant researchers to experimental investigation by synthesizing model complexes that faithfully mimic the active site. In this vein, Hu[21–23] and (separately) Pickett[24,25] reported a series structural models containing acyl-methylpyridine and 'carbamoyl'-pyridine ligands (**Scheme 4.2**). Later, Hu and Shima[26] reported semisynthetic [Fe]-hydrogenases comprised of apo-enzyme reconstituted with pyridine- and pyridinol-containing iron complexes. The construct containing 2-hydroxypyridine (conjugate base: pyridone) exhibited detectable turnover frequencies in the forward and reverse reactions of [Fe]-

hydrogenase (2 s^{-1} and 1 s^{-1}, respectively). In contrast, the methoxy analogue exhibited catalytic reactivity below the detection limit. These results revealed the importance of the 2-hydroxy group — presumably as a pendant base that accepts H^+ during H_2 cleavage. The above reports also supported the second mechanism[13] (proposed by QM/MM) in which the protein scaffold is imperative for the catalytic activity.

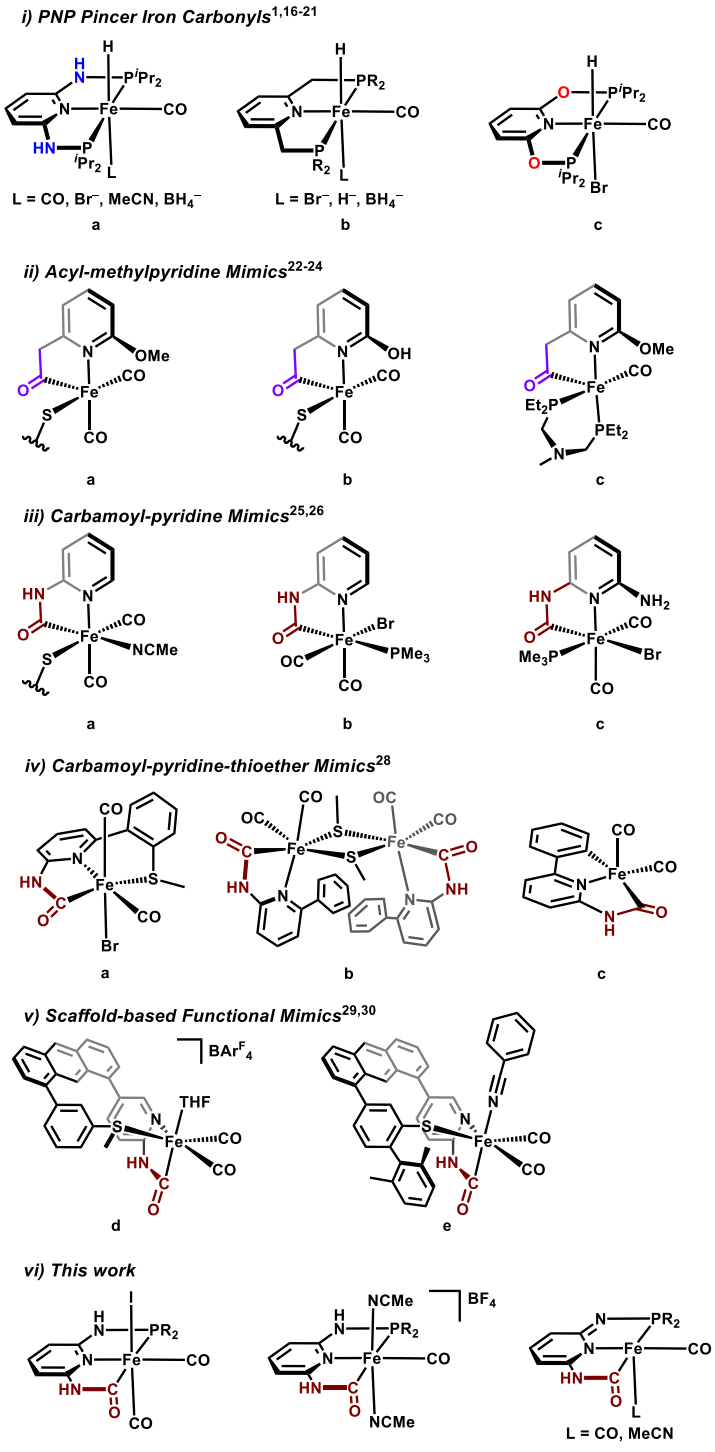

Scheme 4.2 Non-biomimetic and biomimetic iron carbonyls for hydrogen reactivity.

Our own foray into this area started with the development of carbamoyl-pyridine-thioether (CNS) iron carbonyl complexes (**Scheme 4.2**).[27] The dicarbonyl bromide species bears a tridentate ligand backbone with C, N, S ligating in meridional mode. With this pincer-type mimic, we observed the first Fe–H species relevant to [Fe]-hydrogenase by treating the bromide salt with $KHBEt_3$. The thermal instability of the hydride species resulted in the isolation of desulfurized complex with $[Fe_2S^{Me}_2]$ core derived from C–S bond cleavage. Similarly, treating the bromide complex with strong base, KO^tBu, led to C–S bond cleavage, forming a CNC pentacoordinate Fe complex. It is likely that KO^tBu generated a putative deprotonated carbamoyl intermediate $[(^{O=}C^{N=}NS^{Me})Fe(CO)_2]$ which triggered the desulfurization process. Furthermore, we also reported several model systems based on an 'anthracene scaffold'.[28,29] The implementation of the anthracene scaffold tethers the C, N, S donors to form a unique tridentate ligand which not only increases the stability of the synthetic model through chelating effect, but also restricts the chelation to a facial motif. Reactivity studies showed that the thioether complexes $[(Anth•C^{NH}NS^{Me})Fe(CO)_2(THF)]^+$ and $[(Anth•C^{NH}NS)Fe(CO)_2(PhCN)]$ functional towards H_2 activation.

The success of our model complexes motivated us to develop a hybrid system that contains both elements of the biological motif (iron-acyl bonding) and of proven catalytic platforms (phosphine pincer), while maintaining a pendant base at the pyridine *ortho* position. Previously, a bioinspired complex with an acyl ligation and a PNP ligand ($Et_2PCH_2NMeCH_2PEt_2$) has been reported (complex **c** in **Scheme 4.2**).[23] In this system, the amine group functions as pendant base, activating H_2 through a metal-ligand bifunctional mechanism. Herein, we report a bioinspired CNP pincer complex with a biomimetic pendant base and carbamoyl group. The experimental and computational

studies were performed regarding the synthesis, dearomatization, H_2 activation, and transfer hydrogenation within this model system.

4.2 Synthesis of the Ligand and Bromide Complex

The CNP pincer complexes herein are derived from monosubstituted phosphine ligands (**L$_{Ph}$** and **L$_{iPr}$**; **Scheme 4.3**), which were synthesized by a nucleophilic substitution reaction of 2,6-diaminopyridine and chlorodiphenylphosphine or chlorodiisopropylphosphine (1 eq.) by modification of a reported procedure.[30–32] The metalation of **L$_{Ph}$** and **L$_{iPr}$** proceeded at room temperature with $[Fe(CO)_4(I)_2]$ in DCM, which generated the dicarbonyl complexes (**1** and **2**) with a bio-inspired carbamoyl unit related to Hmd. Complexes **1** and **2** were characterized by ^{1}H NMR, ^{31}P{^{1}H} NMR and IR. The ^{1}H NMR spectrum of **1** exhibits features at 9.64 and 8.74 ppm that correspond to carbamoyl-N*H* and phosphino-N*H*, respectively. For **2**, the resonances of NH protons are shifted upfield (8.70 ppm for carbamoyl-N*H*, 6.93 ppm for phosphino-N*H*), indicating the increased electronic density at the iron center in **2** resulting from the electron donating isopropyl substituents. In the ^{31}P{H} NMR spectra, complex **1** displays a singlet at 90.8 ppm, whereas complex **2** gives rise to a singlet at 121.2 ppm. The IR spectrum of **1** shows two carbonyl stretches at 2032 and 1976 cm^{-1}, and for **2** the carbonyl peaks are red-shifted to 2019 and 1967 cm^{-1} due to the stronger (^{i}Pr)$_2$P donor. The CO stretching frequencies are slightly blue-shifted relative to the native enzyme data (Hmd: 1996, 1928 cm^{-1}; FeGP cofactor: 2004, 1934 cm^{-1}) and comparable for the anthracene-based model complexes ([(Anth•C^{NH}NS^{Me})Fe(CO)$_2$I]: 2031, 1981 cm^{-1}; [(Anth•C^{NH}NS)Fe(CO)$_2$(PhCN)]: 2016, 1956 cm^{-1}).

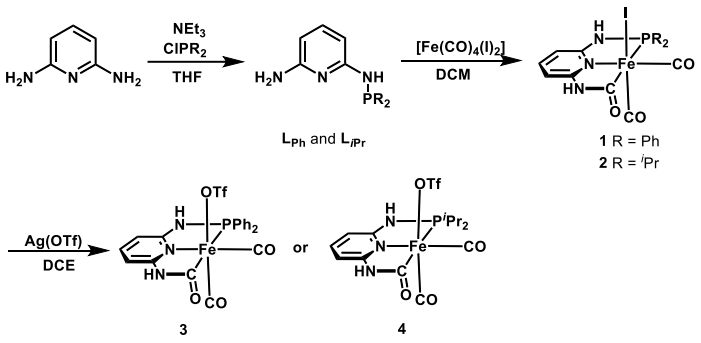

Scheme 4.3 Synthesis of monosubstituted phosphine ligands (**L$_{Ph}$** and **L$_{iPr}$**) and dicarbonyl iron(II) complexes (**1**, **2**, **3** and **4**).

To provide structural characterization and provide a more labile coordinate site for reactivity studies, the thermodynamically formed dicarbonyl complexes were derivatized by halide abstraction reaction with silver triflate, forming the triflate-bound complex and AgI precipitate. Treatment of a 1,2-dicholoroethane (DCE) solution of complex **1** or **2** with Ag(OTf) resulted in the formation of either the adduct [($C^{NH}N^{NH}P^{Ph2}$)Fe(CO)$_2$(OTf)] (**3**) or the triflate salt [($C^{NH}N^{NH}P^{iPr2}$)Fe(CO)$_2$(OTf)] (**4**), depending on the R group (R = Ph or ^{i}Pr, respectively). The IR spectra exhibited the two carbonyl peaks at higher wavenumber (2049, 1993 cm^{-1} for **3**; 2045, 1994 cm^{-1} for **4**) and the ^{31}P resonance of **4** was observed as a singlet at 122.8 ppm. However, the ^{31}P NMR of **3** showed no resonance due to paramagnetic impurity possibly derived from decarbonylation. The crystal structures of the trilafte salts were obtained upon recrystallization of the products (vapor diffusion of cyclohexane into the THF solution of complexes). Surprisingly, complex **4** underwent ligand exchange of OTf$^-$ by ambient H$_2$O during crystallization (the crystallization was set up outside the N$_2$ box), generating H$_2$O-bound complex [($C^{NH}N^{NH}P^{iPr2}$)Fe(CO)$_2$(H$_2$O)](OTf) (**4-H$_2$O**). Selected bond parameters and crystal information are tabulated in the **Table 4.1** and **Table C1**. Complex **3** crystallized as a neutral complex (**Figure 4.1**), wherein the iron center is

coordinated with a carbamoyl C, pyridine-N and diphenyl-P in the conventional 'pincer' equatorial fashion. The CO ligands are arranged in *cis* fashion, and the sixth coordination site is occupied by triflate ligand. The bond distances are unremarkable except that the Fe–P bond distance (2.3037(14) Å) is longer than typical range of bond length for iron(II) carbonyl phosphine complexes (2.16-2.25 Å).[14,15,17,18,33–36] This is attributed to the *trans* influence of the strongly σ-donating carbamoyl unit.[21] Complex **4** crystallized as a cationic complex, wherein the iron center is coordinated to the CNP ligand, *cis* CO ligands and a water molecule — with the charge balance provided by the outer-sphere triflate anion. Presumably, the stronger σ-donating effect of isopropyl substituted phosphine ligand than diphenylphospine[37,38] gives rise to (*i*) the more labile triflate anion due to increased electronic density at the Fe center, and (*ii*) the Fe–P bond of **4** is slightly shortened (2.288(3) Å) compared with **3** (2.3037(14) Å). Two types of Fe–CO bond are presented in the dicarbonyl complexes; the in-plane CO is further from the iron center than the axial CO ligand (1.792(5) Å vs 1.751(7) Å in **3**; 1.809(12) Å vs 1.722(13) Å in **4**), which can be ascribed to the stronger *trans* influence of pyridine versus halide. This is comparable to the Fe–CO bond length in *cis*-[Fe(PNP-^{i}Pr)$(CO)_2$(Br)]$^{+}$, where the CO in the plane of ligand backbone has longer distance to the iron center comparing with the CO perpendicular to the plane (1.772(1) Å vs 1.758(2) Å).[39] Both complexes display an intermolecular hydrogen bonding motif on the amide proton linkers in the solid state (**Figure C37-C38**). The N*H*–P proton interacts with carbamoyl oxygen with bond metrics of O•••H = 1.93 Å, O•••N = 2.781(7) Å, bond angle = 163° for **3,** and O•••H = 1.98 Å, O•••N = 2.854(10) Å, bond angle = 174° for **4**. In **4**, the outer sphere triflate anion displays hydrogen bonding with the N*H*–carbamoyl proton with O•••H = 2.07 Å, O•••N = 2.932(7) Å, bond angle = 168° for **1**, and O•••H = 2.10 Å, O•••N = 2.913(15) Å, bond angle = 154°.

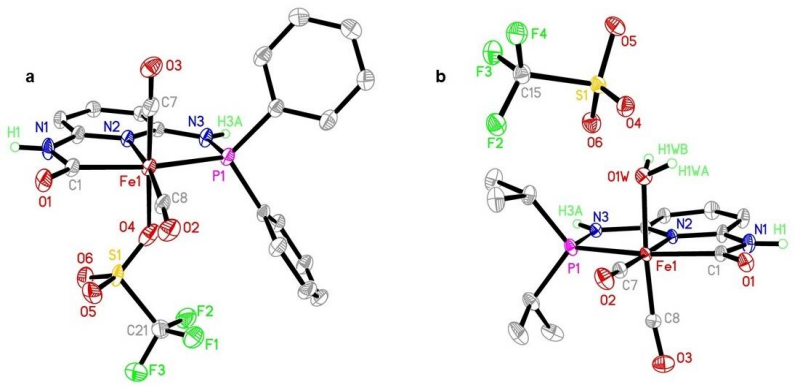

Figure 4.1 ORTEP diagrams for (a) [($C^{NH}N^{NH}P^{Ph2}$)Fe(CO)$_2$(OTf)] (**3**) (30% thermal ellipsoids) and (b) [($C^{NH}N^{NH}P^{iPr2}$)Fe(CO)$_2$(H_2O)](OTf) (**4-H_2O**) (50% thermal ellipsoids). The H atoms except for the N*H* protons are omitted for clarity.

Table 4.1 Selected bond lengths (Å) and angles (°).

Complex	**3**	**4-H_2O**	**7**	***cis*-8**	***trans*-8**	***cis*-9**
Fe–(C)carbamoyl	1.969(5)	1.962(10)	1.972(7)	1.959(4)	1.955(4)	1.963(2)
Fe–P	2.3037(14)	2.288(3)	2.2729(18)	2.2769(10)	2.2930(11)	2.2976(5)
Fe–N^{Py}	1.947(4)	1.940(8)	1.957(5)	1.937(3)	1.963(3)	1.9456(16)
N(–P)–C^{Py}	1.372(6)	1.377(14)	1.343(9)	1.372(5)	1.366(6)	1.362(3)
N–P	1.690(4)	1.711(9)	1.658(6)	1.701(4)	1.696(4)	1.7012(17)
Fe–C(≡O)$^{in\text{-}plane}$	1.792(5)	1.809(12)	1.778(7)		1.793(4)	
Fe–C(≡O)$^{out\text{-}of\text{-}plane}$	1.751(7)	1.722(13)	1.831(8) 1.793(7)[a]	1.770(5)		1.765(2)
C≡O$^{in\text{-}plane}$	1.149(6)	1.109(14)	1.089(9)		1.139(5)	
C≡O$^{out\text{-}of\text{-}plane}$	1.146(7)	1.150(17)	1.118(8) 1.198(7)[a]	1.143(5)		1.147(3)
Fe–I			2.4984(15) 2.4929(14)[a]			
Fe–NCMe				1.974(4)[b] 1.932(4)	1.916(3) 1.908(4)	1.9717(17) 1.9291(17)
Fe–OH_2		2.001(9)				
Fe–OTf	2.064(5)					
(O=)C–Fe–P	163.60(16)	165.0(3)	161.3(2)	164.94(14)	164.01(13)	164.29(6)
N^{Py}–Fe–P	81.86(12)	82.4(2)	79.74(17)	82.23(9)	81.81(10)	82.24(5)
MeCN–Fe–NCMe				86.11	175.76	87.15(7)

a. substitutional disorder of CO and I. *b*. *trans* to CO.

4.3 Activation via Deprotonation/Dearomatization of Dicarbonyl Complexes

The treatment of dicarbonyl complex **1** in THF with one equivalent of the bulky phenolate, Sodium 2,6-di-*tert*-butyl-4-methoxyphenolate (NaDBHA), yielded an orange solution containing the deprotonated/dearomatized product formulated as [($C^{NH}N^{N=}P^{Ph2}$)Fe(CO)$_2$] (**5**) (**Scheme 4.4**). The *ν*(CO) peaks were shifted to lower energy at 2006 and 1952 cm^{-1}, indicating deprotonation of the ligand backbone. While the precursor **1** possesses two acidic N*H* protons on the sidearms, the ^{1}H NMR spectrum after deprotonation provides no information on determining the deprotonation site, as the spectrum shows the disappearance of both N*H* resonances. The ^{31}P{^{1}H} NMR spectrum of **5** exhibits a singlet at 90.6 ppm, which is a trivial shift compared to that of **1** (90.8 ppm). These results may be ascribed to a fast proton exchange process the N*H* proton with protic species. Similarly, Kirchner et al. reported a fast proton exchange process between the two N-sites of deprotonated [Fe(PNP-BIPOL)(CH_3CN)$_3$]BF_4 in MeCN, giving rise to a singlet in ^{31}P{^{1}H} NMR.[40] Since NMR results were ambiguous in determining the exact deprotonation site of **1**, DFT calculations of P–N*H*-deprotonated **5** and carbamoyl N*H*-deprotonated **5'** were performed at PBE0/opt theory level. The P–N*H*-deprotonated **5$_{DFT}$** shows 12.3 kcal/mol lower than **5'$_{DFT}$** in energy (Appendix C, **Table C2**), indicating that the N*H* on the phosphine side arm is likely the first to be deprotonated. The reversibility of the deprotonation was demonstrated by treating **5** with pyridinium bromide in THF, as ^{1}H NMR and IR spectroscopies revealed the regeneration of complex **1^{Br}** (Br-bound). For complex **2**, similar deprotonation was observed upon the treatment of NaDBHA and the IR spectrum of the deprotonated complex **6** demonstrated analogously red-shifted CO bands at 2001 and 1942 cm^{-1}, again consistent with

deprotonation of the ligand backbone. The $^{31}P\{^{1}H\}$ NMR spectrum exhibits a singlet at 116.3 ppm.

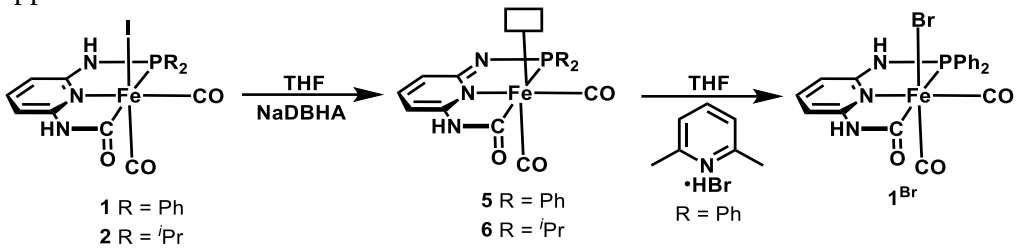

Scheme 4.4 Synthesis of dearomatized complexes (**5**, **6**).

To verify the dissociation of iodide from the iron center in complex **5** (lost as NaI), we substituted NaDBHA with other bases and compared the changes of CO stretches in the solid-state IR spectra recorded by drop-cast method. As shown in **Figure 4.2**, treatment of **1** with the corresponding ammonium salt, tetraethylammonium 2,6-di-*tert*-butyl-4-methoxyphenolate ([NEt_4][DBHA]) and the halide abstracting reagent, thallium tetrakis(3,5-bis(trifluoromethyl)phenyl)borate ($TlBAr^F$) affords IR spectra that displays two CO bands at 2004 and 1949 cm^{-1} — similar to those of **5**. The means that in the reaction of NaDBHA and **1**, iodide dissociates from the iron center, forming a pentacoordinate/deprotonated species **5**. Interestingly, the addition of reagent, [(18-crown-6)Na][DBHA] (**Figure 4.2d**) or [NEt_4][DBHA] (**Figure 4.2e**) to complex **1** gave rise to two CO peaks red-shifted much further in the solid IR (1992, 1936 cm^{-1} and 1991, 1934 cm^{-1}, respectively). The difference in the CO region can be explained by the formation of an iodide-bound deprotonated species **7**, as evidenced by the crystal structure (*vide infra*). It is noteworthy that the IR spectra in **Figure 4.2** were obtained by the means of drop-casting the sample solution directly taken from the reaction. These results indicate that the iodide is so tightly bound to the iron center that in solid state,

without Tl^+ or Na^+ cation, it ligates the iron regardless of the deprotonation of the ligand backbone.

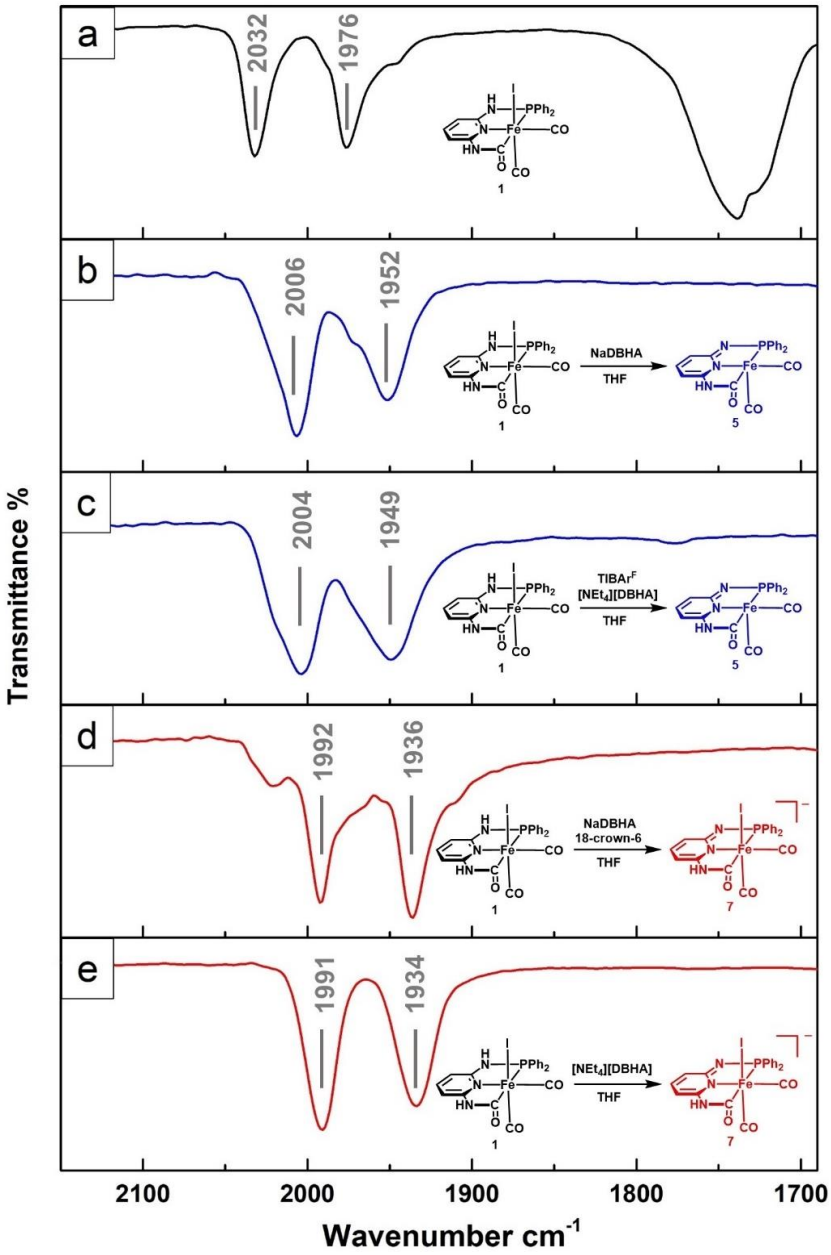

Figure 4.2 The CO region in the IR spectra (drop-cast) of (a) **1** only, (b) reaction of **1** + NaDBHA producing **5**, (c) reaction of **1** + [NEt_4][DBHA] + TlBArF producing **5**, (d) reaction of **1** + NaDBHA + 18-crown-6 ether producing **7**, (e) reaction of **1** + [NEt_4][DBHA] producing **7**.

While attempts to obtain the X-ray structure of the dearomatized species **5** or **6** were not fruitful, the reaction of **1** with NaDBHA and one equivalent of 18-crown-6 (**Figure 4.2d**) did afford [(18-crown-6)Na][($C^{NH}N^{N=}P^{Ph2}$)Fe$(CO)_2$(I)] (**7**) as orange crystals. The structure of complex **7** exhibits an iron center coordinate to the CNP ligand, two *cis*-COs and I^- anion, displaying a pseudo-octohedral geometry (**Figure 4.3**). Interestingly, the iodide anion shows substitutional disorder due to its coordination from both sides of the CNP plane (Appendix C, **Figure C39**). The occupations of the two isomers are around 50% for each. The 18-crown-6–encapsulated sodium cation binds with carbamoyl-O with a distance of 2.309(5) Å. *Notably, the NH on the phosphine sidearm was verifiably deprotonated*. As a result, the N(–P)–C^{Py} and N–P distances are shortened to 1.343(9) Å and 1.658(6) Å, respectively (~1.37 Å and ~1. 70 Å for **3** and **4**). The Fe–P bond length also decreases (2.2729(18) Å) with respect to **3** (2.3037(14) Å) and **4** (2.288(3) Å). The bond angle of P–N–C in **7** is more acute (114°) than those of **3** and **4** (120° and 119°). In addition, hydrogen bonding is observed between carbamoyl-NH and crown-O (O•••H = 2.24 Å, O•••N = 3.028(9) Å, bond angle = 153°). Importantly, *no sign of hydrogen bonding is observed on the phosphine sidearm*, consistent with the deprotonation state of the phosphine-NH linker.

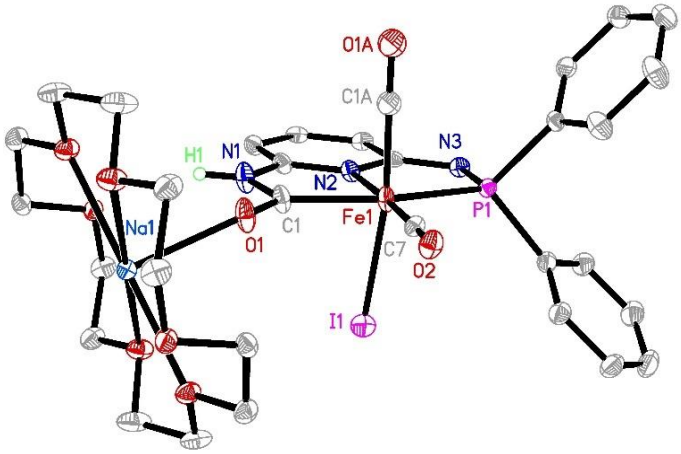

Figure 4.3 ORTEP diagram (30% thermal ellipsoids) for [Na(18-crown-6)][($C^{NH}N^{N=}P^{Ph2}$)$Fe(CO)_2I$] (**7**). H atoms except for the N*H* proton are omitted for clarity.

Surprisingly, dissolution of **7** in d^8-THF gives rise to a ^{1}H NMR spectrum equivalent to that of **5** (**Figure 4.4**), and the $^{31}P\{^1H\}$ NMR spectrum of **7** displays a singlet peak at 91.4 ppm, almost the same to the ^{31}P resonance of **5** (90.6 ppm). These suggest that in solution complex **7** loses iodide and converts to the pentacoordinate complex **5**. Similar dehydrohalogenation has been observed or proposed in PNP iron complexes; the deprotonation/dearomatization of the ligand backbone promotes halide dissociation from the iron center.[14,17] Importantly, such dearomatized and dehalogenated intermediate has been proposed to be the active species to cleave H_2 by the fashion of metal-ligand cooperation.[41] It is promising that the CNP pincer complex could also function as a H_2 activation complex, however, with an anionic carbamoyl unit, the reactivity might be different from the neutral PNP complexes. Since the iodide anion is still dissolved in the solution, upon crystallization, it binds with the iron center, forming **7**. While the ^{1}H NMR spectrum of complex **7** matches that of **5**, the ^{1}H NMR spectrum of **7** exhibits the N*H* resonance at 8.90 ppm, which was not seen in the original spectrum of

5. This can be attributed to the lack of protic solvent to facilitate proton exchange of N*H*, whereas in **5**, phenol is present, leading to the extinction of the NH peak.

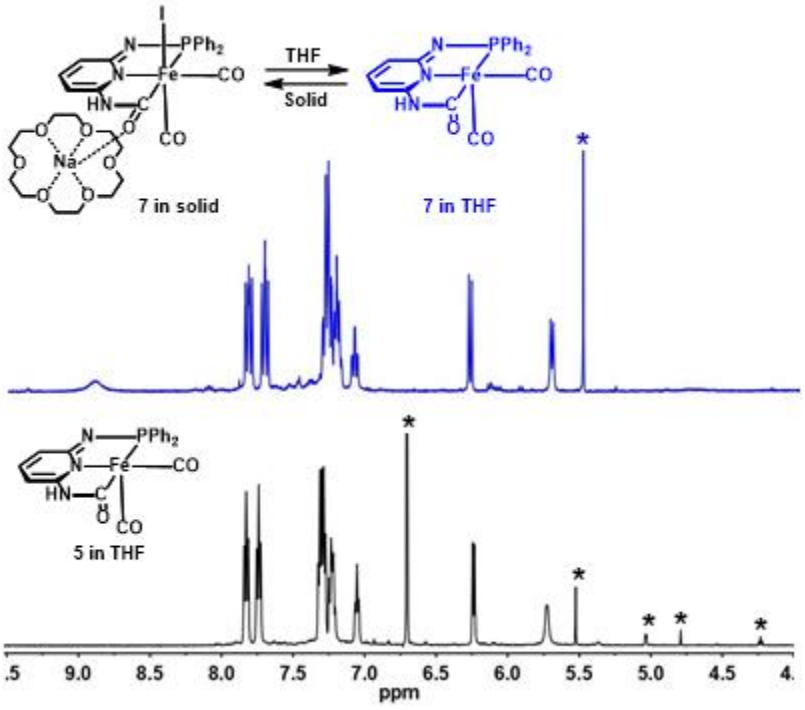

Figure 4.4 The comparison of ^{1}H NMR spectra of **7** and **5** in THF-d^{8}. Peaks corresponding to residual solvent impurity and phenol are labeled (*****).

4.4 Synthesis of Monocarbonyl Complexes

To study the effect of the number of CO ligands on tuning hydrogen activation reactivity, we synthesized the corresponding monocarbonyl CNP complexes. Direct addition of stoichiometric amounts of the decarbonylating reagent trimethyl ammonium *N*-oxide (Me_3NO) to **1** resulted in no reaction, as no change in the CO bands was observed in the IR spectroscopy. Meanwhile, treatment of **1** with excessive Me_3NO led only to complete decarbonylation of both CO ligands. The high electron density on the Fe center renders strong backbonding from Fe to CO, which stabilizes CO ligands on Fe. Previously, we have reported that decarbonylation can be facilitated by replacing the

anionic halide with neutral L-type ligand.[42] Therefore, to attain the monocarbonyl complex **8** we utilized a two-step synthesis shown in **Scheme 4.5**. Starting with **1**, the halide abstracting reagent $AgBF_4$ was added to the acetonitrile solution of **1**, generating the acetonitrile-bound dicarbonyl species. Then, Me_3NO was used to selectively eliminate one CO ligand, affording the monocarbonyl species with two acetonitrile molecules bound in *trans* or *cis* fashion, ***trans*-8** and ***cis*-8**. The IR spectrum (drop cast) of **8** exhibits a single CO band at 1987 cm^{-1}. In ^1H NMR, the *cis* and *trans* isomers can be readily identified at a ratio of ~3:5. The assignments for each feature were based on the ^1H-^{31}P HMBC NMR on the isolated product in MeCN-d_3 (**Figure C32**). The *cis* isomer exhibits two singlets at 8.85 and 7.88 ppm, which correspond to the carbamoyl-NH and phosphino-NH, respectively. The *trans* isomer displays the specific NH signals at 8.80 and 8.05 ppm. The protons at 5- and 3-positions on pyridine ring give rise to two doublets at 6.47, 6.34 ppm for ***cis*-8** and 6.72, 6.52 ppm for ***trans*-8**. In the aliphatic region, two singlets resonating at 2.31 and 1.74 ppm are attributed to the methyl protons of the coordinated acetonitrile of ***cis*-8**, and the singlet observed at 1.56 ppm correspond to the methyl protons of ***trans*-8**. In $^{31}P\{^1H\}$ NMR, a singlet is observed at 89.4 ppm for ***cis*-8**, and ***trans*-8** gives rise to a singlet at 100.5 ppm.

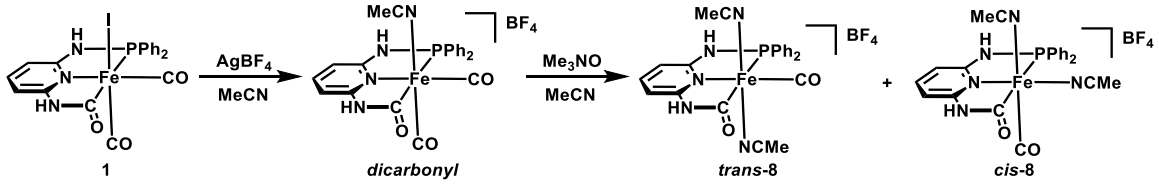

Scheme 4.5 Synthesis of monocarbonyl complexes (***trans*-8** and ***cis*-8**).

The crystal structure of **8** was obtained upon diffusion of diethyl ether to the acetonitrile solution, and, interestingly, ***trans*-8** and ***cis*-8** *co-crystallized* in the crystal

lattice. The structure is shown in **Figure 4.5** and the selected bond parameters are tabulated in **Table 4.1**. Both Fe atoms exhibit pseudo-octahedral geometry and coordinate with the CNP ligand, one CO ligand and two acetonitrile molecules. The charge of the complex is balanced by BF_4^- anion. The Fe–C(=O) bond distances are shortened (1.959(4) Å for ***cis*-8** and 1.955(4) Å for ***trans*-8**), compared with dicarbonyl complexes. It is noteworthy that in ***cis*-8**, the orientation of acetonitrile applies the weakest trans-influence on pyridine, leading to the shortest Fe–N^{py} bond length (1.937(3) Å) among all the structures. The Fe–NCMe bond distances are among comparable range of iron(II) acetonitrile bond distance,[40,43–45] except for the longest Fe(2)–N(9) bond (1.974(4) Å).

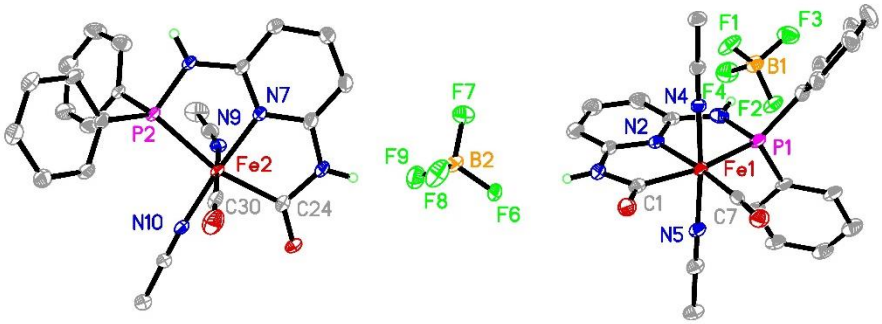

Figure 4.5 (*Entire image*) Asymmetric part of the unit cell for **8**: ORTEP diagrams (30% thermal ellipsoids) for *cis*-[($C^{NH}N^{NH}P^{Ph2}$)Fe(CO)$(MeCN)_2$](BF_4) (***cis*-8**) and *trans*-[($C^{NH}N^{NH}P^{Ph2}$)Fe(CO)$(MeCN)_2$](BF_4) (***trans*-8**). Both complexes were found co-crystallized in the same unit cell. H atoms except for the N*H* proton are omitted for clarity.

While room-temperature synthesis of the monocarbonyl complexes afforded ***trans*-8** as the major product, conversion of ***trans*-8** to ***cis*-8** was observed at elevated temperature. The solution of **8** in MeCN-d_3 was heated at 55 °C and NMR spectra were recorded along with the reaction. As shown in **Figure 4.6**, the ^{1}H NMR resonances

derived from ***trans*-8** gradually decreased, as those of ***cis*-8** increased; the same trend was observed in the ^{31}P NMR spectrum. These results indicate that ***trans*-8** is the kinetic product and ***cis*-8** is the thermodynamic product.

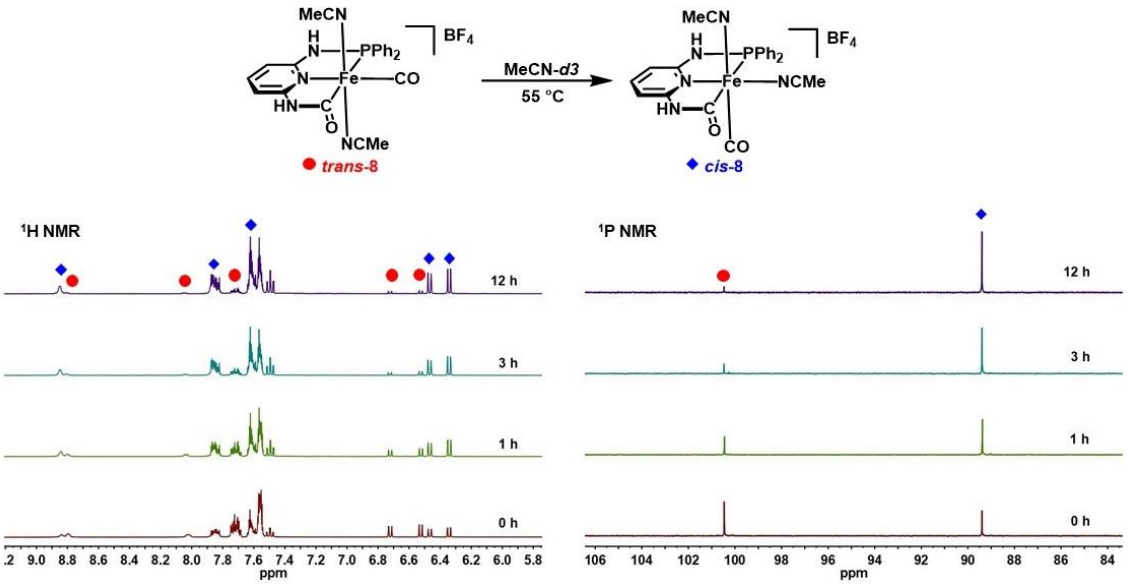

Figure 4.6 ^{1}H NMR and $^{31}P\{^{1}H\}$ NMR spectra showing interconversion of *trans*-$[(C^{NH}N^{NH}P^{Ph2})Fe(CO)(MeCN)_2](BF_4)$ (*trans*-**8**) to *cis*-$[(C^{NH}N^{NH}P^{Ph2})Fe(CO)(MeCN)_2](BF_4)$ (*cis*-**8**) in MeCN-*d3* solution incubated at 55 °C.

The energy difference between ***cis*-8** and ***tran*-8** was obtained through DFT calculation by geometry optimization at PBE0/opt (see experimental for details of the basis set) level of theory. The converged structures (**Figure C44** and **Figure C45**) precisely simulated the structural characteristics of **8**, indicating the accuracy of PBE0 in structural calculation with transition metal complex. Importantly, the electronic energy of ***cis*-8** is lower than ***tran*-8** by ~1.5 kcal/mol (**Table C2**). This result is consistent with the NMR study of conversion of the *trans* isomer to the *cis* isomer.

The isopropyl analogue complex **9** was synthesized by the similar method, in which we only isolated the ***cis*-9** in 75% yield. Small amount (~8%) of ***trans*-9** complex could be observed from the crude NMR (**Figure C33**). The ^{1}H NMR displays the N*H* protons at 8.75 and 6.86 ppm, which are assignable to carbamoyl NH and phosphine NH, respectively. The signals of isopropyl protons exhibit in an asymmetric pattern as the *cis* acetonitrile ligands make the two isopropyl groups chemical inequivalent (methine: 2.82, 2.69 ppm; methyl: 1.46-1.27 ppm). The ^{31}P NMR shows a singlet at 110.6 ppm, lower than ***cis*-8**. The CO stretching frequency of ***cis*-9** appears at 1969 cm^{-1}, red-shifted relative to **8**, indicating higher electron density on the Fe of ***cis*-9**. The crystal structure of ***cis*-9** is shown in **Figure 4.7** and the selected bond parameters are tabulated in **Table 4.1**. The Fe atom coordinates with the CNP ligand, one CO ligand and two *cis*-acetonitrile molecules in a pseudo-octahedral geometry. The Fe–C(=O) bond distance is comparable with **4** (1.963(2) Å for ***cis*-9** and 1.962(10) Å for **4**). It is noteworthy that in ***cis*-9**, Fe–P bond length (2.2976(5) Å) is the longest among all the structures.

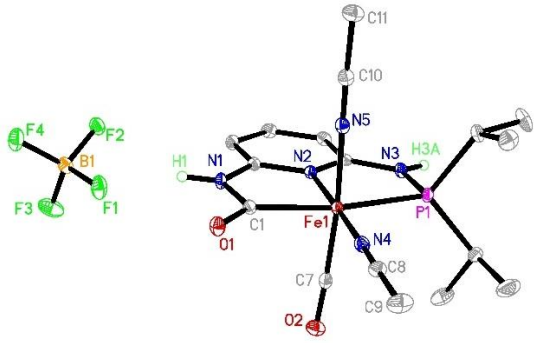

Figure 4.7 ORTEP diagrams (30% thermal ellipsoids) for *cis*-$[(C^{NH}N^{NH}P^{iPr2})Fe(CO)(MeCN)_2](BF_4)$ (***cis*-9**). H atoms except for the N*H* proton are omitted for clarity.

4.5 H_2 REACTIVITY

As we have proven that the ***phosphor***amide NH of CNP complexes can be deprotonated, we considered the possibility that the CNP complexes could perform H_2 cleavage using the anionic amide as a pendant base. This would be consistent with numerous literature examples of organometallic iron pincer complexes. Kirchner *et al.*, reported the dearomatized $P^{NH}N^{NH}P$-Fe pincer complex cleaves H_2, the proton of which protonates the ligand backbone and the hydride binds to the iron center.[14] Milstein *et al.*, synthesized a series of methylene-derived $P^{CH2}N^{CH2}P$-Fe complexes which carry out hydrogenations of aldehydes, ketones and trifluoroacetic esters with high efficiency.[17,19,46] The active species of methylene-deprotonated intermediate is also proven spectroscopically and computationally to be critical for hydrogen splitting and hydride transfer. It is noted that the organometallic pincer complexes are mostly constructed via neutral phosphine tridentate ligands. It is likely that in our CNP complexes the increase of the negative charge of the ligand backbone from neutral to –1 would increase the reactivity in H_2 activation. Moreover, in relation to the bio-inspiration for Hmd — we hypothesized that the non-biomimetic monocarbonyl motif would provide a reactivity advantage over the dicarbonyl motif found in the enzyme due to higher electron density on the iron center.

To test these hypotheses, we performed the H_2 activation studies using D_2 and ^2H NMR spectroscopy. To a high-pressure NMR tube were charged the THF solution of complexes (**1** or **8**, dicarbonyl and monocarbonyl complexes, respectively), base (bulky phenolate NaDBHA or KO^{t}Bu) and D_2 gas (4-7 atm); after a determined time period, ^2H NMR spectra were obtained to identify the formation of products. As shown in **Figure 4.8**, treatment with D_2 and 1 equiv of either NaDBHA (weaker phenolate base) or KO^{t}Bu (stronger alkoxide base) did not result in any product peak as evidenced by the ^2H NMR

spectrum. However, inclusion of 2 equiv of KO^{t}Bu resulted in a new feature at 3.16 ppm assigned to the *tert*-butanol O*D* resonance (**Figure 4.8**), indicating heterolytic H_2 cleavage. The ^{t}BuOD formation suggests that the H_2 is cleaved by the exogenous bulky phenolate base. It is evident that the deprotonated ligand backbone does not directly participate in the reaction because of the absence of N*D* signal in ^{2}H NMR. In addition, a resonance for Fe–D intermediates was not observed.

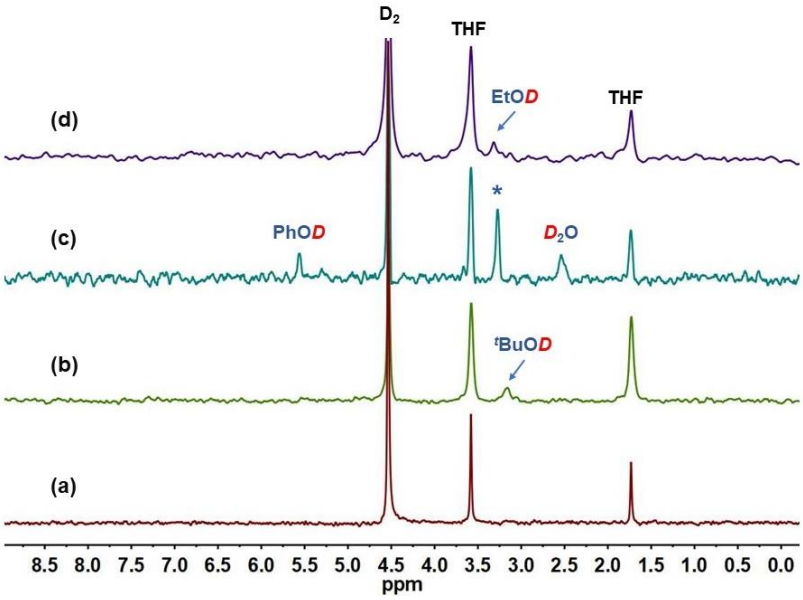

Figure 4.8 ^{2}H NMR spectra of D_2 activations with dicarbonyl complex **1** or monocarbonyl complex **8**. Reaction conditions: (*a*) **1** + D_2 (7 atm) + KO^{t}Bu (1 equiv), THF, RT, 1 d; (*b*) **1** + D_2 (7 atm) + KO^{t}Bu (2 equiv), THF, RT, 1 d; (*c*) **8** + D_2 (4 atm) + NaDBHA (1 equiv), THF, RT, 2 d; (*d*) **8** + D_2 (4 atm) + NaDBHA (1 equiv) + EtOH, THF, RT, 2 d. The identity of the asterisk (*) feature in *c* remains unknown.

By comparison, complex **8** was found to readily activate D_2 gas (4 atm) in the presence of only 1 equiv of the weaker base NaDBHA. The ^{2}H NMR spectrum exhibited two product peaks at 5.56 and 2.56 ppm, assigned to deuterated 2,6-di-*tert*-butyl-4-methoxyphenol (PhO*D*) and D_2O, respectively, as well as a feature at 3.27 ppm —

derived from an as yet unidentifiable alcohol -O*D* resonance. Previously, it has been proposed that ethanol is able to promote the hydrogen cleavage catalyzed by a $P^{NH}N^{NH}P$ iron complex by forming a proton shuttle between the ligand-backbone pendant base and the iron-bound dihydrogen molecule, thus decreasing the reaction barrier for H_2 splitting.[15,47] To examine this possibility, 20 μL of ethanol (~65 equiv) was added to the reaction containing **8** (same conditions as **Figure 4.8c**). Surprisingly, ethanol quenched the reactivity of **8**, and the ^{2}H NMR spectrum only showed a tiny peak attributed to EtO*D* signal. The effect of ethanol may be explained by coordination of ethanol to Fe center, which blocks the binding of H_2.

The aforementioned reactions were also investigated in MeCN as solvent in lieu of THF. The ^{2}H NMR spectra display no resonances for deuterated species except for those derived from solvent and D_2. This result indicates that in THF D_2 is activated upon directly binding to the Fe center; with MeCN as solvent, the vacant site of Fe center is occupied by MeCN, which precludes the reactivity of D_2.

Next, we investigated the D_2/hydride transfer reactivity of **1** and **8** to assess the possibility of CNP complexes to perform the complete Hmd-relevant process. Complexes **1** or **8** were treated with D_2, base and a hydride acceptor — such as an imidazolium cation (1,3-bis(2,6-difluorophenyl)-2-(*p*-tolyl)imidazolium, Im^+), or the more strongly hydride-accepting acridinium cation (9-phenyl-10-methylacridinium, Ac^+).[48] However, neither ^{2}H NMR spectroscopy nor mass spectrometry could detect the corresponding hydride-transferred product, Im–H or Ac–H. The lack of hydride transfer could be attributed to the high Lewis acidity of the Fe center. Bound with only one anionic donor, carbamoyl unit, as well as strong π-accepting CO ligands, the iron center functions more as a hydride acceptor, rather than a hydride donor.

4.6 Summary of DFT Study of H_2 Activation (In collaboration with Dr Wenrui Chai[49] and Prof. Graeme A. Henkelman)

Based on the above reactivity study, it is evident that the monocarbonyl complex exhibits higher reactivity in H_2 activation than the dicarbonyl complex. To obtain theoretical insight, DFT was used to investigate H_2 binding and activation. The calculations were performed by Dr Wenrui Chai and more detailed discussions of the calculations can be found in Dr Wenrui Chai's dissertation.[49] The key discoveries can be summarized as follows.

Three putative pentacoordinate active species were considered (**Figure 4.9A**): the dicarbonyl complex ($\mathbf{A_{diCO}}$), the monocarbonyl complex with MeCN *trans* to the vacant site ($\mathbf{A_{MeCN}}$), and the monocarbonyl complex with CO *trans* to the vacant site ($\mathbf{A_{CO}}$). First, the H_2 binding affinities were quantified by $\Delta G_{\mathbf{A\rightarrow B}}$, which are all exergonic. $\mathbf{A_{MeCN}}$ shows the highest affinity for H_2 ($\Delta G_{\mathbf{A\rightarrow B}}$ = –16.6 kcal/mol) and $\mathbf{A_{CO}}$ has the lowest affinity for H_2 ($\Delta G_{\mathbf{A\rightarrow B}}$ = –8.4 kcal/mol) with $\mathbf{A_{diCO}}$ exhibiting a value only slightly higher than $\mathbf{A_{CO}}$ ($\Delta G_{\mathbf{A\rightarrow B}}$ = –9.1 kcal/mol) (**Figure 4.9B**). The prominently strong affinity for H_2 by $\mathbf{A_{MeCN}}$ is likely due to the influence of the *trans* ligand. The weak π-accepting ligand MeCN *trans* to the vacant site is less competitive (versus *trans* CO) with H_2 for back-donation from d_{xz}(Fe) – an orbital which the two *trans* ligands (H_2 and MeCN/CO) must share.[50] The trans MeCN case thus gives rise to the strongest Fe–H_2 bonding interaction in the set.

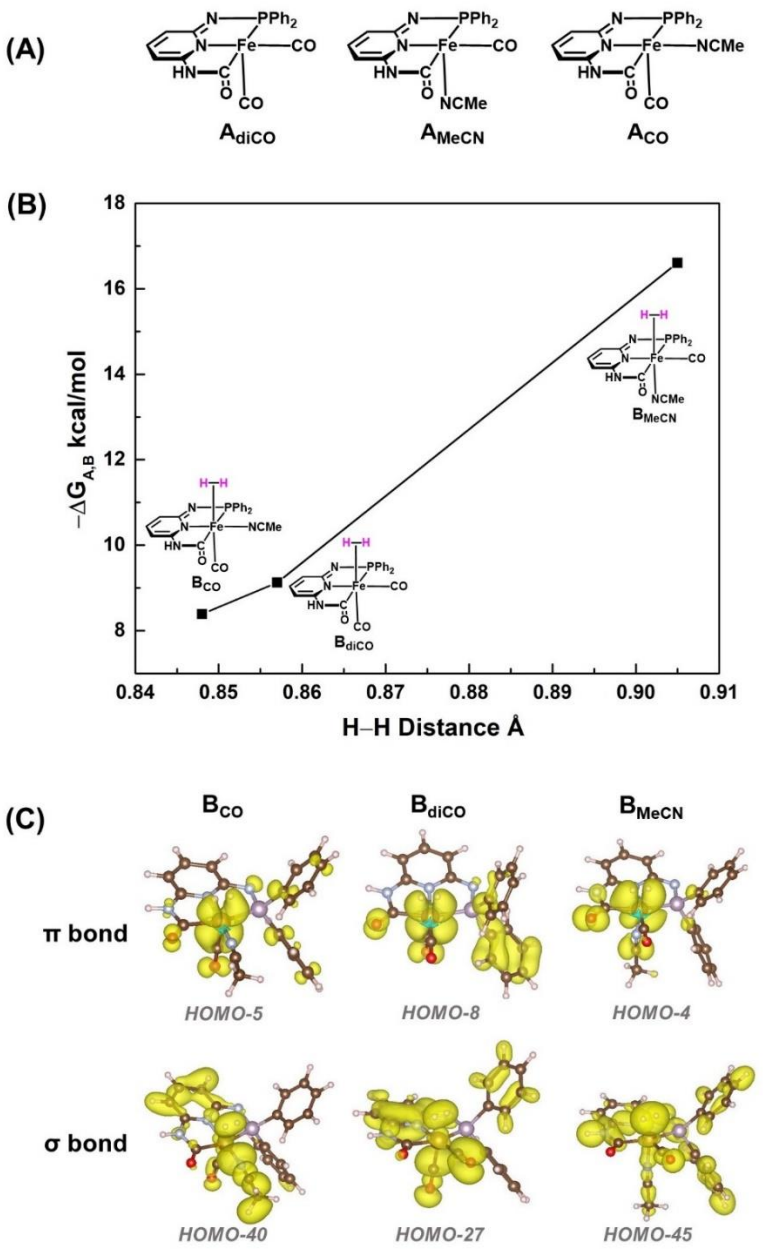

Figure 4.9 DFT calculation of H_2 binding by pentacoordinate complexes: (A) The dearomatized pentacoordinate complexes considered; (B) correlation between $-\Delta G_{\mathbf{A}\rightarrow\mathbf{B}}$ (kcal/mol) of H_2 binding and H–H bond elongation; (C) σ and π interactions stabilizing the Fe–H_2 Kubas adduct.

The more negative $\Delta G_{\mathbf{A\rightarrow B}}$ values are highly correlated with longer H–H bond lengths (**Figure 4.9C**): the most elongated H–H bond distance (0.905 Å) is found in $\mathbf{B_{MeCN}}$ ($\Delta G_{\mathbf{A\rightarrow B}}$ = –16.6 kcal/mol), and the least activated H–H bond (0.848 Å) is observed in $\mathbf{B_{CO}}$ ($\Delta G_{\mathbf{A\rightarrow B}}$ = –8.4 kcal/mol). The dicarbonyl complex $\mathbf{B_{diCO}}$ exhibits an intermediate H–H bond (0.857 Å) with $\Delta G_{\mathbf{A\rightarrow B}}$ = –9.1 kcal/mol. By examining the calculated MO diagram, we identified the MOs contributing to the Fe–H_2 interaction. The σ bonding orbital of Fe–H_2 for the complexes are found to be very low in energy. The π interaction emerging from back-donation are closer to the frontier orbitals. Thus, the MO diagrams of the bonding orbitals for Fe–H_2 are consistent with a strong bonding interaction.

The energy change of the H_2 cleavage step was determined by calculating the enthalpies of the transition states ($\mathbf{TS_{diCO}}$, $\mathbf{TS_{MeCN}}$ and $\mathbf{TS_{CO}}$) and the final Fe–H products ($\mathbf{C_{diCO}}$, $\mathbf{C_{MeCN}}$ and $\mathbf{C_{CO}}$) resulting from heterolytic H_2 cleavage via metal-ligand cooperation is illustrated by the energy profiles of the H_2 cleavage in **Figure 4.10**. The activation energies (ΔE_a) of H_2 cleavage for all three complexes are quite high (>23 kcal/mol), and the enthalpy differences between **B** and **C** ($\Delta H_{\mathbf{B\rightarrow C}}$) are around –15 kcal/mol. The high ΔE_a and low $\Delta H_{\mathbf{B\rightarrow C}}$ suggest the H_2 cleavage is a kinetically slow but thermodynamically favorable reaction for all three complexes. Interestingly, the dicarbonyl complex exhibits the lowest ΔE_a (23.2 kcal/mol) and most negative $\Delta H_{\mathbf{B\rightarrow C}}$ (–17.2 kcal/mol), indicating that — once the Fe–H_2 adduct is formed — the dicarbonyl complex is most reactive towards H_2 cleavage and produces the most stable hydride intermediate ($\mathbf{C_{diCO}}$) provided the metal-ligand cooperativity mechanism is operable. In the case of the single carbonyl species, while $\mathbf{B_{CO}}$ has lower ΔE_a (28.0 kcal/mol) than $\mathbf{B_{MeCN}}$ (30.5 kcal/mol), it has the less negative $\Delta H_{\mathbf{B\rightarrow C}}$ (–13.7 kcal/mol) than $\mathbf{B_{MeCN}}$ (–

15.6). Given that this is a kinetically limited reaction, the DFT-revealed order of reactivity for H_2 cleavage is **diCO** > **CO** > **MeCN**.

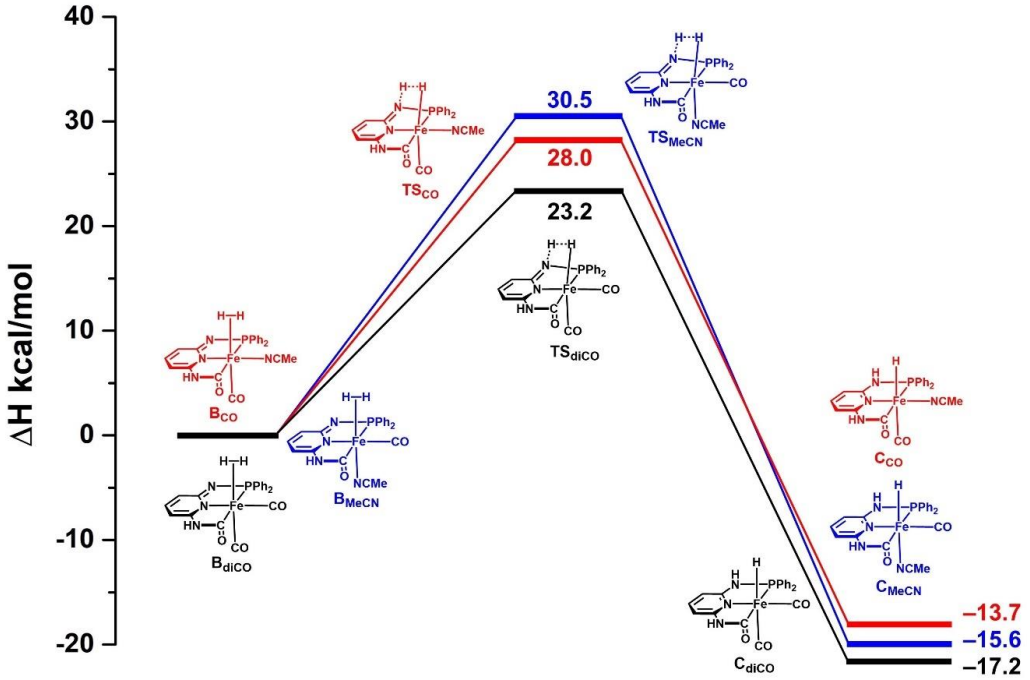

Figure 4.10 Calculated relative enthalpies in the H_2 cleavage reaction via metal-ligand cooperation of $\mathbf{B_{CO}}$ (red), $\mathbf{B_{MeCN}}$ (blue) and $\mathbf{B_{diCO}}$ (black) proceeding from the corrected iso-energetic state **B** through **TS** and forming **C**.

Paradoxically, the experimental results of H_2 activation disclosed that the monocarbonyl complex (**8**) is more reactive than the dicarbonyl complex (**1**) (*vide supra*). To rationalize this discrepancy, we note that the high ΔE_a for the metal-ligand cooperativity mechanism and the *complete absence* of P–N*D* signal in the ^{2}H NMR spectra during the reaction indicate that strict metal-ligand bifunction is not a favorable mechanism for this system; indeed, it is experimentally proven that an external base (e.g. NaDBHA) must be used to drive H_2 cleavage. Several previous examples reported that H_2 cleavage by Fe and external bases affords lower ΔE_a values than the metal-ligand

bifunctional mechanism.[15,18] Furthermore, it is reasonable to argue that the longest H–H bond in $\mathbf{B_{MeCN}}$ implies a more weakened bond that is easier for H_2 to be deprotonated by external bases, leading to a more facile H_2 activation as shown experimentally. As the H–H bond distance is shorter in $\mathbf{B_{diCO}}$, the deprotonation of H_2 requires a stronger and higher equivalent of base (KO^tBu, 2 eq.). In total, the important H_2 activation observed in the CNP system should be achieved with Fe and external bases, whose efficiency is determined by the pK_a of the bases and the degree of H–H bond being elongation in the transient Kubas-type intermediate.

4.7 TRANSFER HYDROGENATION

The affinity of CNP complexes to alcohol (*vide supra*) prompted us to test their function as transfer hydrogenation (TH) catalysts to explore the reactivity of the CNP system. The reaction we investigated was transfer hydrogenation of benzylaldehyde using ^{i}PrOH as hydrogen source. A complete screening of the base, temperature, solvent and catalysts was carried out (**Table 4.2**). Starting with the monocarbonyl complex **8** and NaDBHA as base at 60 ℃, increasing the amount of NaDBHA to 3 equiv leads to higher reactivity with 87% of conversion of benzylaldehyde (entry 3). However, GC-MS results revealed the major product to be the dienone **b** (53%) with the minor product as enone **c** (6%). The desired hydrogen-transferred product benzyl alcohol **a** formed with yield of only 22%. Lowering the temperature provided lower amounts of side products (entry 4 and 5), but with decreased the yield of benzyl alcohol, as well. Screening of different bases revealed that the nitrogen-based neutral base, 1,8-diazabicyclo[5.4.0]undec-7-ene (DBU), is not suitable to promote the reaction, most likely due to its weaker basicity (entry 6). Instead, using the strong inorganic base KOH (entry 8) afforded higher yield of benzyl alcohol and lower formation of side products, compared with other organic bases

(NaDBHA, DBU and KO^{t}Bu). The optimal temperature with KOH was determined to be 60 ℃ with highest yield of **a** at 35% (entry 9 and 10). Water has also been reported to benefit the TH reaction with PNP complexes due to its formation of proton bridge which facilitates the proton transfer between pendant base and substrate.[47] However, addition of ~10% water (V_{H2O}:V_{iPrOH} = 1:9) to the reaction mixture suppressed the reaction regardless of the of base identity (entry 11-13). The shortening reaction time from 20 h to 1 h (entry 14) resulted in a slightly lower yield of **a** (29%), indicating benzylaldehyde was reduced within the first hour of reaction. Last, we investigated the effects of changing complexes on TH reaction. Switching the monocarbonyl complex **8** to the dicarbonyl complex **1** led to decrease of the yield of **a** to only 18% (entry 15), indicating much lower catalytic activity of the dicarbonyl system. It is noteworthy that in the absence of Fe complex, the TH reaction still occurred, with benzyl alcohol formed at 13% yield (entry 16). Indeed, it has been reported that quantitative reduction of acetophenone to phenylethanol was observed in a concentrated NaOH solution.[51] Surprisingly, substituting the isopropyl monocarbonyl analogue complex **9** for **8** again gave lower yield (21%, entry 17). This is comparable to the reaction with **1**, indicating the isopropyl substitution would not promote the TH reactivity for CNP complex.

Table 4.2 Reaction optimization of transfer hydrogenation of iPrOH to benzylaldehyde.[a]

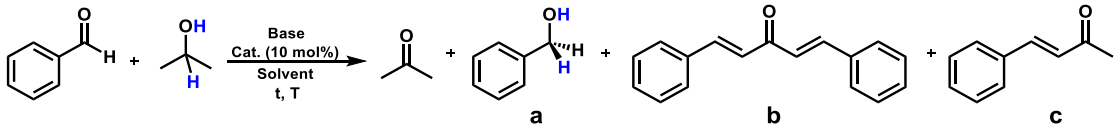

Entry	Cat. 10 mol%	t /h	Base	Base eq.	T /°C	Solvent	Conv.%	Yield%[c]			TON[d]
								a	**b**	**c**	
1	**8**	20	NaDBHA	1	60	^{i}PrOH	0	0	0	0	
2	**8**	20	NaDBHA	2	60	^{i}PrOH	3	1	0	0	
3	**8**	20	NaDBHA	3	60	^{i}PrOH	87	22	53	6	2
4	**8**	20	NaDBHA	3	40	^{i}PrOH	33	21	3	7	2
5	**8**	20	NaDBHA	3	RT	^{i}PrOH	4	2	0	2	
6	**8**	20	DBU	3	40	^{i}PrOH	0	0	0	0	
7	**8**	20	KO^{t}Bu	3	40	^{i}PrOH	38	17	11	9	2
8	**8**	20	KOH	3	40	^{i}PrOH	34	18	7	8	2
9	**8**	20	KOH	3	60	^{i}PrOH	53	35	7	11	3
10	**8**	20	KOH	3	80	^{i}PrOH	84	31	51	2	3
11	**8**	20	NaDBHA	3	40	^{i}PrOH+H_2O[b]	3	3	0	0	
12	**8**	20	KO^{t}Bu	3	40	^{i}PrOH+H_2O	26	8	11	6	
13	**8**	20	KOH	3	40	^{i}PrOH+H_2O	2	2	0	0	
14	**8**	1	KOH	3	80	^{i}PrOH	83	29	47	7	3
15	**1**	20	KOH	3	80	^{i}PrOH	40	18	22	1	2
16	-	20	KOH	3	80	^{i}PrOH	37	13	23	1	1
17	**9**	20	KOH	3	80	^{i}PrOH	58	21	32	5	2

[a]General reaction conditions: 0.0157 mmol of base, 0.0523 mmol of benzylaldehyde, 10 mol% of catalyst, 1 mL of solvent. [b]0.9 mL ^{i}PrOH + 0.1 mL H_2O. [c]Yields calculated from the integration of GC-MS data. [d]TON = (mmol of benzyl alcohol)/(mmol of catalyst).

Although some catalytic activity was observed by our CNP complexes, the overall performance of the catalysts do not compare favorably with other well-established catalysts.[52] Such low TH activity could be due to the low hydricity of the hydride species (thermodynamically hydride donating ability).[53] The active species in TH is usually hydride bound complexes.[52] For example, Hu reported the [Fe(H)(Br)(^{i}Pr$_2$PONOP ^{i}Pr$_2$)] catalyzes the TH reaction to aldehydes using formate as the hydride source, in which the dihydride species [Fe(H)$_2$(^{i}Pr$_2$PONOP ^{i}Pr$_2$)] was proposed to be the active species.[20] Although we have not yet observed the hydride intermediate in the present set of CNP

complexes, it is reasonable to hypothesize that the catalytic cycle involves the formation of hydride species. In the previous section, we have established the energy profile of H_2 cleavage with the CNP complexes. The DFT calculations suggest high stability of the hydride species (**B**), which likely results in weak hydricity and thus TH activity. In the same manner, the dicarbonyl complex **1** and isopropyl complex **9** yielded lower activity than **8**, as their hydride species are more stabilized.

4.8 CONCLUSION

The main conclusions of this work can be summarized as follows:

(1) Bio-inspired iron(II) carbonyl pincers are synthetically accessible via metalation of the apo-ligand with a ferrous carbonyl salt, which forms the Fe–C(carbamoyl) bond in situ.

(2) Base addition results in deprotonation of the phosphoramide unit (analogous to the Kirchner system), rather than the carbamoyl unit.

(3) Incubation of the pentacoordinate dearomatized/deprotonated complexes in D_2 gas leads to the appearance of the PhO*D* or ^{t}BuO*D* signals in ^{2}H NMR spectroscopy, indicating the heterolytic cleavage of D_2 with the CNP complexes. Conditions for reactions (1 eq. of PhONa for **8** and 2 eq. of KO^{t}Bu for **1**) show that monocarbonyl complex **8** have higher reactivity for H_2 activation than dicarbonyl complex **1**.

(4) DFT calculations show that H_2 binding is better facilitated by the monocarbonyl motif (with MeCN rather than CO trans to the H_2 binding site) than the dicarbonyl motif. This is driven by the greater extent of electron density at the iron center with MeCN *trans* to the H_2 activaing site, which improves $d_\pi(M)\rightarrow\sigma^*(H_2)$ back-bonding via Kubas interaction. Experimentally,

H_2 splitting is only achieved by the cooperation of Fe center and external bases, rather than metal-ligand bifunctional mechanism proposed for the Hmd chemistry. Its efficiency is related to the pK_a of the base and the extent of H–H weakening in the Kubas intermediate, which are consistent with the experimental results.

(5) Biologically, the counterintuitive use of the less H_2-reactive *dicarbonyl* motif likely serves to restrain the reactivity of the Fe–H_2/H intermediate, thus providing more selectivity for hydride transfer only to the imidazolium unit of the H_4MPT^+.

(6) The catalytic activity of the monocarbonyl CNP complex (**8**) towards transfer hydrogenation of benzylaldehyde is observed, whereas the dicarbonyl complex (**1**) and –P^{i}Pr$_2$-substituted complex (**9**) exhibit lower to no reactivity. This could be ascribed to the latter species' more stable hydride species, leading to low hydricity and hydride transfer.

(7) These results highlight two key items regarding the [Fe]-hydrogenase enzyme: (*i*) The methylene-acyl carbanion present in the active site occurs *0* to the site of H_2 activation; this strong σ donor and weak π acceptor likely drives significant H–H elongation in the putative Kubas intermediate. (*ii*) The pyridone/pyridonate-O atom directly adjacent to the H_2 binding site in the enzyme likely provides both the optimum *basicity and orientation* that promotes H_2 heterolysis ($\Delta E_a \approx 1$ kcal/mol estimated by QM/MM method).[13]

(8) Future bio-inspired catalysts (with or without phosphine) should aspire to achieve such a second-coordination sphere feature. Additionally, new catalysts and complexes with strong σ-donating and weak π-accepting ligand

trans to the hydride (e.g. H^-, phosphine and cyclopentadiene) would increase reactivities towards both H_2 splitting and hydride transfer.

4.9 EXPERIMENTAL PROCUDURES

4.9.1 General Information

All organic starting materials were purchased from Acros Organics or Sigma-Aldrich and used without further purification. The Fe(II) starting salt $[Fe(CO)_4(I)_2]$ was prepared by reaction of $[Fe(CO)_5]$ (Strem) with I_2 according to the published procedure.[25] All the complexes were prepared inside the glove box under dinitrogen atmosphere, unless otherwise indicated. HPLC grade solvents were purchased from EMD, Fisher, Macron or J.T. Baker, and dried through an alumina column system (Pure Process Technology). Deuterated solvents ($CDCl_3$) was purchased from Cambridge Isotopes and used as received.

4.9.2 Physical Measurements

NMR spectra were collected on Varian 400 MHz spectrometer and chemical shifts were referenced to the solvent peaks. Solid state infrared spectra were recorded on a Bruker Alpha spectrometer equipped with a diamond ATR crystal. Mass spectra (MS) were acquired on either Thermo Scientific TSQ (CI) or Thermo Finnigan TSQ with Dionex Ultimate 3000 LC (ESI). GC-MS measurements were performed on Agilent Technologies 5977E Single Quadrupole GC-MS instrument using electron imparct (EI) ionization method.

The X-ray structure data for **3**, **4-H_2O**, **7**, **8** and **9** were collected on an Agilent Technologies SuperNova Dual Source diffractometer using a μ-focus Cu Kα radiation (λ = 1.5418 Å) with collimating mirror monochromators. Data reduction was performed

using Agilent Technologies CrysAlisPro 1.171.37.31.[54] Reduced temperatures were maintained using an Oxford Cryostream low temperature device. Structures were solved by direct methods using SuperFlip[55] and refined by full-matrix least-squares on F2 with anisotropic displacement parameters for the non-H atoms using SHELXL-2013[56]. Structure analysis was aided by PLATON98[57] and WinGX[58]. The hydrogen atoms on carbon were calculated in ideal positions with isotropic displacement parameters set to 1.2 × U_{eq} of the attached atom (1.5 × U_{eq} for methyl hydrogen atoms). The data were checked for secondary extinction effects, but no correction was necessary. Neutral atom scattering factors and values used to calculate the linear absorption coefficient are from the International Tables for X-ray Crystallography.

4.9.3 DFT Calculations Details

Calculations of **5**, **5'**, ***cis*-8$_{DFT}^{+}$** and ***trans*-8$_{DFT}^{+}$** were performed using the Gaussian 09 software package.[59] Geometry optimization was achieved with PBE0 functional, which was derived from a pure PBE functional in combination of HF exchange with predefined coefficients and has shown a wide application and a good accuracy in molecular structure and properties.[60,61] The basis set for geometry optimization (basis opt) was composed by the Stuttgart/Dresden ECP (SDD) basis set[62,63] used for iron and the 6-31G(d,p) basis set[64–66] for all other atoms. Frequency calculations were performed at the same level of theory (BPE0/opt) to confirm the nature of stationary points with none imaginary points for the minima.

Ab initio calculations were carried out to study H_2 absorption and activation by CNP pentacoordinate complexes. Geometry optimization and energy calculation of molecular orbitals used DFT as implemented in the Vienna Ab-Initio Package. Optimization cut-off force was chosen to be 0.01 eV/Å. Core electrons were described

within the projected augmented wave framework; valence electrons were described with a plane wave basis set up to an energy cutoff of 400 eV[67]. The generalized gradient approximation in the form of the Perdew, Burke and Ernzehof (PBE) functional was used to model electronic exchange and correlation.[68] Spin polarization is used for all calculations. Reaction pathways were calculated using the climbing image nudged elastic band method (CI-NEB)[69] with double nudging.[70] Reaction energies were converted to free energies under standard conditions first by adding +5.5 kcal/mol.[71] Then, the free energies were modified to match the experimental conditions where the H_2 concentration was 7 atm in gas phase and 2 mM in solution, and the solution was set to pH = 12. The resulting free energy for H_2 adsorption can be calculated in the following equation:

$$\Delta G_{H^*} = \Delta E_{H^*} + 4.96\ kcal/mol$$

Where the 0.54 kcal/mol difference to literature comes from the decreased entropy of H_2 at elevated pressure.

4.9.4 Synthetic Procedures

***N*-Diphenylphosphino-2,6-diaminopyridine ($\mathbf{L_{Ph}}$).** Under dinitrogen atmosphere, a solution of 2,6-diaminopyridine (500 mg, 4.58 mmol) and freeze-pump-thawed triethylamine (0.64 mL, 4.6 mmol) in 8 mL of THF was cooled to –70 °C, and $ClPPh_2$ (0.85 mL, 4.6 mmol) was added dropwise. The temperature was allowed to gradually increase to room temperature. After the reaction was stirred overnight, the solvent was removed in vacuo and the product was purified by column chromatography (silica gel, EtOAc/Hexane = 1/1) to afford **$\mathbf{L_{Ph}}$** as an off-white powder. Yield: 740 mg (55%). ^{1}H NMR (400 MHz, $CDCl_3$) δ = 7.47-7.43 (m, 4H, $Ph^{2,5}$), 7.37-7.34 (m, 6H, $Ph^{3,4,5}$), 7.27 (t, *J* = 7.9 Hz, 1H, py^4), 6.40 (ddd, *J* = 7.9, 1.6, 0.6 Hz, 1H), 5.95 (d, *J* = 7.8 Hz, 1H), 4.98 (d, *J* = 8.8 Hz, 1H, -N*H*-), 4.21 (s, 2H, NH_2). ^{31}P{^{1}H} NMR (162 MHz,

$CDCl_3$) δ = 25.5. ^{13}C NMR (126 MHz, $CDCl_3$) δ = 157.4, 140.1, 140.1, 139.8, 139.7, 131.5, 131.3, 129.4, 128.7, 128.7, 99.1, 98.1, 97.9. HR-MS (ESI^+): *m/z* 294.1163 $[M+H]^+$.

***N*-Diisopropylphosphino-2,6-diaminopyridine (L_{iPr})**. Under dinitrogen atmosphere, a solution of 2,6-diaminopyridine (1.00 g, 9.16 mmol) and freeze-pump-thawed triethylamine (1.28 mL, 9.16 mmol) in 50 mL of THF was cooled to –78 °C, and ClP^iPr_2 (1.46 mL, 9.16 mmol) was added dropwise. The temperature was allowed to gradually increase to room temperature. After the reaction was stirred overnight, the solvent was removed in vacuo and the product was purified by column chromatography (silica gel, EtOAc/Hexane = 1:2) to afford **L_{iPr}** as an off-white powder. Yield: 767 mg (37%). ^1H NMR (500 MHz, $CDCl_3$) δ = 7.24 (t, *J* = 7.9 Hz, 1H, py^4), 6.45 (dd, *J* = 8.0, 2.2 Hz, 1H, py^3), 5.88 (d, *J* = 7.7 Hz, 1H), 4.42 (d, *J* = 10.7 Hz, 1H, –N*H*–), 4.17 (s, 2H, NH_2), 1.75 (dtd, *J* = 14.0, 7.0, 2.1 Hz, 2H, –C*H*$(CH_3)_2$), 1.14 – 0.98 (m, 12H, –CH(C$H_3)_2$). $^{31}P\{^1H\}$ NMR (202 MHz, $CDCl_3$) δ = 47.5. ^{13}C NMR (126 MHz, $CDCl_3$) δ = 160.1, 160.0, 157.5, 139.5, 98.2, 98.1, 98.1, 26.6, 26.5, 18.9, 18.8, 17.2, 17.2. HR-MS (CI^+): *m/z* 225.1397.

[($^{O=}C^{NH}N^{NH}P^{Ph2}$)$Fe(CO)_2(I)$] (1). Under dinitrogen atmosphere, a solution of **L_{Ph}** (260 mg, 0.886 mmol) in 4 mL of DCM was treated dropwise by a solution of $[Fe(CO)_4(I)_2]$ (375 mg, 0.886 mmol) in 2 mL of DCM at room temperature with CO bubbles generated. The mixture was stirred for 1 h, during which time yellow precipitate formed. The solid was separated by filtration and the product was purified by column chromatography over neutral alumina. Elution of the desired product was achieved with THF, which eluted a yellow band that was collected. The solvent was removed *in vacuo* and the residue was washed thoroughly by Et_2O, which afforded **1** as a yellow powder. Yield: 92 mg (19%). ^1H NMR (400 MHz, THF-d_8) δ = 9.64 (d, *J* = 3.9 Hz, 1H, -C(=O)-

N*H*-), 8.74 (d, *J* = 5.8 Hz, 1H, -P-N*H*-), 7.75 – 7.67 (m, 1H, Ph), 7.64 – 7.55 (m, 2H, Ph), 7.55 – 7.40 (m, 7H), 6.41 (d, *J* = 7.9 Hz, 1H, py^5), 6.30 (d, *J* = 8.0 Hz, 1H, py^3). $^{31}P\{^1H\}$ NMR (162 MHz, THF-d_8) δ = 90.8. IR (cm^{-1}): 2032, 1976. HR-MS (ESI$^+$): *m/z* 581.9131 $[M+Na]^+$.

[($^{O=}$C^{NH}N^{NH}P^{iPr2})Fe(CO)$_2$(I)] (2). Under dinitrogen atmosphere, a solution of **L$_{iPr}$** (200 mg, 0.888 mmol) in 4 mL of DCM was treated dropwise by a solution of $[Fe(CO)_4(I)_2]$ (375 mg, 0.888 mmol) in 2 mL of DCM at room temperature with CO bubbles generated. The mixture was stirred for 1 h, during which time yellow precipitate formed. The solid was separated by filtration and the product was purified by column chromatography over neutral alumina. The elution of the desired product was achieved with THF, which eluted a yellow band. The solvent was removed *in vacuo* and the residue was washed thoroughly by Et_2O, which afforded **5** as a yellow powder. Yield: 150 mg (34%). ^{1}H NMR (400 MHz, CD_3CN) δ = 8.70 (s, 1H, -C(=O)-N*H*-), 7.49 (td, *J* = 8.0, 1.4 Hz, 1H), 6.93 (s, 1H, -P-N*H*-), 6.36 (ddd, *J* = 10.0, 8.0, 0.9 Hz, 2H), 3.24 (dp, *J* = 11.3, 7.3 Hz, 1H, –C*H*$(CH_3)_2$), 2.81 – 2.66 (m, 1H, –C*H*$(CH_3)_2$), 1.51 – 1.06 (m, 13H, –CH(C*H*$_3)_2$). $^{31}P\{^1H\}$ NMR (162 MHz, CD_3CN) δ = 121.2. IR (cm^{-1}): 2019, 1967. HR-MS (ESI$^+$): *m/z* 491.9625 $[M+H]^+$.

[($^{O=}$C^{NH}N^{NH}P^{Ph2})Fe(CO)$_2$(OTf)] (3). Under dinitrogen atmosphere, a solution of **1** (20 mg, 0.036 mmol) in 4 mL of 1,2-dichloroethane (DCE) was mixed with silver trifluoromethanesulfonate (AgOTf) (9.2 mg, 0.036 mmol). The reaction was stirred for 30 min, during which time a beige precipitate formed. The precipitate was removed by Celite filtration and the solvent was evaporated in reduced pressure. The resulting residue was washed thoroughly with Et_2O, which afforded the product as a yellow powder. Single crystals suitable for X-ray diffraction to were obtained by vapor diffusion of cyclohexane into the THF solution to afford yellow blocks. Yield: 7.4 mg (4%). ^{1}H NMR

(400 MHz, DCM-d_2) δ = 9.69 (s, 1H), 7.75 (d, J = 26.0 Hz, 4H), 7.58 (s, 7H), 7.15 (td, J = 7.3, 1.2 Hz, 1H), 7.09 – 7.03 (m, 2H). ^{19}F NMR (376 MHz, DCM-d_2) δ = –75.30. IR (cm^{-1}): 2049, 1993.

[($^{O=}$C^{NH}N^{NH}P^{iPr2})Fe(CO)$_2$(OTf)] (4). Under dinitrogen atmosphere, a solution of **2** (10 mg, 0.020 mmol) in 2 mL of 1,2-dichloroethane (DCE) was mixed with silver trifluoromethanesulfonate (AgOTf) (5.2 mg, 0.020 mmol). The reaction was stirred for 30 min, during which time a beige precipitate formed. The precipitate was removed by Celite filtration and the solvent was evaporated in reduced pressure. The resulting residue was washed thoroughly with Et_2O, which afforded the product as a yellow powder. Single crystals suitable for X-ray diffraction to were obtained by vapor diffusion of cyclohexane into the THF solution to afford yellow blocks. Yield: 5.1 mg (48%). ^{1}H NMR (400 MHz, DCM-d_2) δ = 8.84 (s, 1H), 7.69 – 7.49 (m, 2H), 6.58 (dd, J = 8.2, 0.9 Hz, 1H), 6.45 (dd, J = 7.9, 0.9 Hz, 1H), 2.72 (s, 1H), 2.51 (s, 1H), 1.58 – 1.16 (m, 12H). ^{31}P{^{1}H} NMR (162 MHz, DCM-d_2) δ = 122.8. ^{19}F NMR (376 MHz, DCM-d_2) δ = –79.2. IR (cm^{-1}): 2045, 1994.

Deprotonated [($^{O=}$C^{NH}N$^{=N}$P^{Ph2})Fe(CO)$_2$] (5). Under dinitrogen atmosphere, a yellow solution of **1** (5.0 mg, 0.0087 mmol) in 1 mL of THF was treated with sodium 2,6-di-*tert*-butyl-4-methoxyphenolate (2.3 mg, 0.009 mmol) in 1 mL of THF, generating an orange solution. The reaction was stirred at room temperature for 5 min and was filtered through Celite. The solvent was removed *in vacuo* and the resulting residue was washed thoroughly with Et_2O, affording the desired product as an orange powder. Due to the instability of the product, complex **5** has only been observed spectroscopically and, thus, the calculation of yield is hampered. ^{1}H NMR (600 MHz, the NMR was measured in the normal THF with the instrument unlocked, referenced by THF peak at 1.79 ppm) δ = 7.81 (t, *J* = 9.0 Hz, 2H, Ph), 7.73 (t, *J* = 8.9 Hz, 2H, Ph), 7.29 (dt, *J* = 15.7, 7.5 Hz, 4H,

Ph), 7.24 – 7.17 (m, 2H, Ph), 7.04 (t, J = 7.7 Hz, 1H, py^4), 6.22 (d, J = 8.3 Hz, 1H, py^5), 5.71 (s, 1H, py^3). ^{31}P{^{1}H} NMR (243 MHz, THF) δ = 90.6. IR (cm^{-1}): 2006, 1952. HR-MS (ESI$^+$): *m/z* 348.0355 [M+H–3CO]$^+$.

Deprotonated [($^{O=}$C^{NH}N$^{=N}$P^{iPr2})Fe(CO)$_2$] (6). Under dinitrogen atmosphere, a yellow solution of **5** (5.0 mg, 0.010 mmol) in 1 mL of THF was treated with sodium 2,6-di-*tert*-butyl-4-methoxyphenolate (2.6 mg, 0.010 mmol) in 1 mL of THF, generating an orange solution. The reaction was stirred at room temperature for 5 min and was filtered through Celite. The solvent was removed *in vacuo* and the resulting residue was washed thoroughly by Et_2O, affording the desired product as an orange powder. Due to the instability of the product, complex **6** has only been observed spectroscopically and, thus, the calculation of yield is hampered. ^{1}H NMR (600 MHz, the NMR was measured in the normal THF with the instrument unlocked, referenced by THF peak at 1.79 ppm) δ = δ 7.15 (s, 1H, py^4), 6.10 (s, 1H, py^5), 5.95 (s, 1H, py^3). ^{31}P{^{1}H} NMR (243 MHz, THF) δ = 116.3. IR (cm^{-1}): 2001, 1942. HR-MS (ESI$^+$): *m/z* 280.0667 [M+H–3CO]$^+$.

Deprotonated [Na(18-crown-6)][($^{O=}$C^{NH}N$^{=N}$P^{Ph2})Fe(CO)$_2$I] (7). Under dinitrogen atmosphere, a yellow solution of **1** (5 mg, 0.009 mmol) in 1 mL of THF was treated with 1 mL of THF solution of sodium 2,6-di-*tert*-butyl-4-methoxyphenolate (2.3 mg, 0.009 mmol) and 18-crown-6 (2.4 mg, 0.009 mmol), generating an orange solution. The reaction was stirred at room temperature for 5 min and was filtered through Celite. The solvent was removed *in vacuo* and the resulting residue was washed thoroughly with Et_2O, affording the desired product as orange powder. Single crystals suitable for X-ray diffraction were obtained by vapor diffusion of Et_2O into the THF solution to afford red prisms. Yield: 2.5 mg (33%). ^{1}H NMR (400 MHz, THF-d_8) δ = 8.90 (s, 1H, -C(=O)-N*H*-), 7.89 – 7.79 (m, 2H, Ph), 7.77 – 7.68 (m, 2H, Ph), 7.31 – 7.19 (m, 6H, Ph), 7.09 (t, J = 7.8 Hz, 1H, py^4), 6.29 (d, J = 8.3 Hz, 1H, py^5), 5.73 (d, J = 7.7 Hz, 1H, py^3), 3.64 (s,

24H). $^{31}P\{^{1}H\}$ NMR (162 MHz, THF-d_8) δ = 91.4. IR (cm^{-1}): 1984, 1930. HR-MS (ESI^-): *m/z* 557.9170 $[M]^-$.

Cis/Trans-[($^{O=}C^{NH}N^{NH}P^{Ph2}$)Fe(CO)(MeCN)$_2$][BF_4] (8). Under dinitrogen atmosphere, a yellow solution of **1** (100 mg, 0.179 mmol) in 4 mL of MeCN was treated with 2 mL of MeCN solution of $AgBF_4$ (34.8 mg, 0.179 mmol). The reaction was stirred at room temperature for 10 min. Then, trimethylamine N-oxide (18.8 mg, 0.250 mmol) in 2 mL of MeCN was added to the reaction. After stirring for 1 h, the solvent was removed *in vacuo* and the resulting residue was washed thoroughly with Et_2O. The product was recrystallized as orange crystals using vapor diffusion of Et_2O into the MeCN solution. X-ray structure and spectroscopic characterizations show that both the *cis* and *trans* acetonitrile-bound products formed in approximately equal amounts. Yield: 64 mg (62%). ^1H NMR (400 MHz, Acetonitrile-d_3). ***cis-isomer*** δ = 8.85 (s, 1H), 7.88 (s, 1H), 7.87 – 7.81 (m, 2H), 7.66 – 7.58 (m, 6H), 7.57 (m, 2H), 7.49 (td, *J* = 8.0, 1.5 Hz, 1H, py^4), 6.47 (dt, *J* = 8.1, 0.8 Hz, 1H, py^5), 6.34 (dd, *J* = 8.0, 0.9 Hz, 1H, py^3), 2.31 (d, *J* = 1.6 Hz, 3H, CH_3CN), 1.74 (d, *J* = 2.6 Hz, 3H, CH_3CN). ***trans*-isomer** δ = 8.80 (d, *J* = 4.2 Hz, 1H), 8.05 (d, *J* = 6.4 Hz, 1H), 7.76 – 7.67 (m, 4H), 7.57 – 7.55 (m, 7H), 6.72 (d, *J* = 8.0 Hz, 1H, py^5), 6.52 (dd, *J* = 8.0, 0.8 Hz, 1H, py^3), 1.56 (d, *J* = 2.2 Hz, 6H, CH_3CN). $^{31}P\{^{1}H\}$ NMR (162 MHz, Acetonitrile-d_3) δ = 89.4 (***cis-isomer***), 100.5 (***trans-isomer***). IR (cm^{-1}): 1987. HR-MS (ESI^+): *m/z* 486.0765 $[M]^+$.

Cis-[($^{O=}C^{NH}N^{NH}P^{iPr2}$)Fe(CO)(MeCN)$_2$][$BF_4$] (*cis*-9). Under dinitrogen atmosphere, a yellow solution of **2** (100 mg, 0.204 mmol) in 7 mL of MeCN was treated with 2 mL of MeCN solution of $AgBF_4$ (39.6 mg, 0.204 mmol). After stirring for 20 min at room temperature, the solution was filtered through Celite, followed by pumping off MeCN and washing the residue with Et_2O. Then, trimethylamine N-oxide (16.8 mg, 0.224 mmol, 1.1 eq.) in 4 mL of MeCN was added to the reaction. After stirring for 3 h,

the solvent was removed *in vacuo* and the resulting residue was washed thoroughly with Et_2O. The product was recrystallized as orange crystals using vapor diffusion of Et_2O into the MeCN solution. Yield: 78 mg (75%). ^{1}H NMR (400 MHz, Acetonitrile-d_3) δ = 8.75 (s, 1H), 7.39 (td, *J* = 8.0, 1.3 Hz, 1H), 6.86 (d, *J* = 4.7 Hz, 1H), 6.28 – 6.20 (m, 2H), 2.91 – 2.77 (m, 1H), 2.69 (dt, *J* = 10.1, 7.3 Hz, 1H), 2.24 (d, *J* = 1.4 Hz, 3H), 1.46 – 1.27 (m, 15H). ^{31}P{^{1}H} NMR (162 MHz, Acetonitrile-d_3) δ =110.6. IR (cm^{-1}): 1969.

H_2 Activation. A THF (1 mL) solution of pincer iron complex (5 μmol) was treated with base (sodium 2,6-di-*tert*-butyl-4-methoxyphenolate or ^{t}BuOK). The mixture was stirred at room temperature for 1 min. The solution was filtered through Celite and transferred to a high-pressure NMR tube. The solution was incubated with D_2 (4-7 atm). At various time-points, the reaction was monitored ^{1}H and ^{2}H NMR spectroscopy.

Transfer Hydrogenation. To a THF (1 mL) solution of pincer iron complex (5 μmol) was added base. The mixture was stirred for 1 min, followed by adding benzyl aldehyde (5.34 μL, 50 μmol). The reaction was stirred at specific conditions and was monitored by GC-MS.

Appendices

APPENDIX A SUPPORTING INFORMATION FOR CHAPTER 2

Table A1 Crystal data and refinement parameters for **1**

Cmpd **L**	**1** **Br**
CCDC number	1547030
Formula	$C_{15}H_{11}BrFeN_2O_3S$
FW	435.08
T (K)	153(2)
size (mm^{-3})	0.10 × 0.05 × 0.04
system	Monoclinic
space group	$P2_1/n$
Z	4
λ (Å)	1.54184
a (Å)	9.7866 (12)
b (Å)	16.118(3)
c (Å)	10.6175(17)
α (°)	90.0
β (°)	102.42(13)
γ (°)	90.0
V ($Å^3$)	1635.6(4)
d_{calc} (mg/cm^3)	1.767
μ (mm^{-1})	11.588
R(int)	0.0675
GOF on F^2	1.014
R_1/wR_2 [I>2σ(I)]	0.069 0.1577
R_1/wR_2 (all data)	0.1093 0.1863

Table A2 Crystal data and refinement parameters for **3a**

Cmpd **L**	**3a** **PPh_3**
CCDC number	1547031
Formula	$C_{65}H_{38}BF_{24}FeN_2O_3PS$
FW	1480.66
T (K)	153(2)
size (mm^{-3})	0.12 × 0.08 × 0.06
system	Triclinic
space group	P-1
Z	2
λ (Å)	1.54184
a (Å)	12.3336(6)
b (Å)	13.7435(6)
c (Å)	19.1836(8)
α (°)	82.35(4)
β (°)	76.41(4)
γ (°)	86.56(4)
V ($Å^3$)	3131.2(3)
d_{calc} (mg/cm^3)	1.570
μ (mm^{-1})	3.575
R(int)	0.0454
GOF on F^2	1.030
R_1/wR_2 [I>2σ(I)]	0.0505 0.1190
R_1/wR_2 (all data)	0.0720 0.1344

Table A3 Crystal data and refinement parameters for **3b**

Cmpd **L**	**3b** **PMe_3**
CCDC number	1547032
Formula	$C_{101}H_{66}B_2Cl_2F_{48}Fe_2N_4O_6P_2S_2$
FW	2673.86
T (K)	153(2)
size (mm^{-3})	0.15 × 0.13 × 0.09
system	Triclinic
space group	P-1
Z	2
λ (Å)	0.71073
a (Å)	12.2647(13)
b (Å)	18.6289(19)
c (Å)	24.731(3)
α (°)	90.896(3)
β (°)	95.597(2)
γ (°)	95.427(3)
V ($Å^3$)	5596.6(10)
d_{calc} (mg/cm^3)	1.587
μ (mm^{-1})	0.507
R(int)	0.1102
GOF on F^2	1.055
R_1/wR_2 [I>2σ(I)]	0.0831 0.1697
R_1/wR_2 (all data)	0.1265 0.1917

Table A4 Crystal data and refinement parameters for **3c**

Cmpd **L**	**3c** **py**
CCDC number	1547033
Formula	$C_{55}H_{34}BCl_3F_{24}FeN_3O_3S$
FW	1445.92
T (K)	153(2)
size (mm^{-3})	0.14 × 0.12 × 0.10
system	Triclinic
space group	P-1
Z	2
λ (Å)	0.71073
a (Å)	13.038(10)
b (Å)	14.2685(11)
c (Å)	16.8688(13)
α (°)	89.575(2)
β (°)	71.762(2)
γ (°)	79.118(2)
V ($Å^3$)	2922.4(4)
d_{calc} (mg/cm^3)	1.643
μ (mm^{-1})	0.555
R(int)	0.1512
GOF on F^2	1.029
R_1/wR_2 [I>2σ(I)]	0.0838 0.1446
R_1/wR_2 (all data)	0.1600 0.1761

Table A5 Crystal data and refinement parameters for **3d**

Cmpd **L**	**3d** **MeCN**
CCDC number	1547034
Formula	$C_{17}H_{14}FeN_3O_3SBF_4$
FW	483.03
T (K)	173(2)
size (mm^{-3})	0.11 × 0.10 × 0.05
system	Orthorhombi
space group	$P2_1\ 2_1\ 2_1$
Z	4
λ (Å)	0.71073
a (Å)	7.8618(7)
b (Å)	13.0402(11)
c (Å)	19.3301(15)
α (°)	90.0
β (°)	90.0
γ (°)	90.0
V ($Å^3$)	1981.7(3)
d_{calc} (mg/cm^3)	1.619
μ (mm^{-1})	0.928
R(int)	0.0351
GOF on F^2	1.124
R_1/wR_2 [I>2σ(I)]	0.0219 0.0539
R_1/wR_2 (all data)	0.0226 0.0542

Table A6 Crystal data and refinement parameters for **3g**

Cmpd **L**	**3g** **2,6-$Me_2C_6H_3$**
CCDC number	1547035
Formula	$C_{25}H_{24}N_2FeCl_4O_3S_2$
FW	659.93
T (K)	100(2)
size (mm^{-3})	0.51 × 0.05 × 0.03
system	Monoclinic
space group	$I2/a$
Z	12
λ (Å)	1.54184
a (Å)	17.0361
b (Å)	14.2521
c (Å)	26.0871
α (°)	90
β (°)	90.091(3)
γ (°)	90
V ($Å^3$)	6333.9(4)
d_{calc} (mg/cm^3)	1.300
μ (mm^{-1})	7.595
R(int)	0.0855
GOF on F^2	0.989
R_1/wR_2 [$I>2\sigma(I)$]	0.0719 0.1838
R_1/wR_2 (all data)	0.0960 0.2048

Table A7 Crystal data and refinement parameters for **4a**

Cmpd **L**	**4a** **Br, PPh_3**
CCDC number	1547036
Formula	$C_{36}H_{34}BrCl_4FeN_2O_2PS$
FW	867.24
T (K)	100(2)
size (mm^{-3})	0.20 × 0.12 × 0.07
system	Monoclinic
space group	$P2/n$
Z	4
λ (Å)	1.54184
a (Å)	14.1110(9)
b (Å)	13.7420(8)
c (Å)	19.9776(12)
α (°)	90.0
β (°)	104.537(6)
γ (°)	90.0
V ($Å^3$)	3749.9(4)
d_{calc} (mg/cm^3)	1.536
μ (mm^{-1})	8.301
R(int)	0.0296
GOF on F^2	1.035
R_1/wR_2 [$I>2\sigma(I)$]	0.0474 0.1255
R_1/wR_2 (all data)	0.0500 0.1280

Table A8 Crystal data and refinement parameters for **4b**

Cmpd **L**	**4b** **PPh_3**
CCDC number	1547037
Formula	$C_{82}H_{53}BF_{24}FeN_2O_2P_2S$[a]
FW	1714.92
T (K)	100(2)
size (mm^{-3})	0.40 × 0.34 × 0.20
system	Triclinic
space group	P-1
Z	2
λ (Å)	0.71073
a (Å)	14.5766(10)
b (Å)	17.7215(13)
c (Å)	18.8505(13)
α (°)	87.007(2)
β (°)	70.413(2)
γ (°)	68.967(2)
V ($Å^3$)	4269.1(5)
d_{calc} (mg/cm^3)	1.334
μ (mm^{-1})	0.336
R(int)	0.0430
GOF on F^2	1.050
R_1/wR_2 [I>2σ(I)]	0.0537 0.1320
R_1/wR_2 (all data)	0.0716 0.1423

[a] In **4b**, SQUEEZE was used to eliminate the electron density of the masked solvent that was unable to model, so the formula is calculated without the masked solvent.

Table A9 Crystal data and refinement parameters for **4c**

Cmpd **L**	**4c** **Py**
CCDC number	1547038
Formula	$C_{62}H_{38}BF_{25}FeN_4O_2S$
FW	1444.68
T (K)	100(2)
size (mm^{-3})	0.50 × 0.30 × 0.20
system	Triclinic
space group	P-1
Z	2
λ (Å)	1.54184
a (Å)	12.6230(4)
b (Å)	13.1564(3)
c (Å)	19.2160(4)
α (°)	98.635(2)
β (°)	98.815(2)
γ (°)	99.964(2)
V ($Å^3$)	3054.41(14)
d_{calc} (mg/cm^3)	1.571
μ (mm^{-1})	3.428
R(int)	0.0388
GOF on F^2	1.024
R_1/wR_2 [I>2σ(I)]	0.0524 0.1317
R_1/wR_2 (all data)	0.0790 0.1442

Table A10 Crystal data and refinement parameters for **4c**

Cmpd **L**	**4c** **Py**
CCDC number	1547038
Formula	$C_{62}H_{38}BF_{25}FeN_4O_2S$
FW	1444.68
T (K)	100(2)
size (mm^{-3})	0.50 × 0.30 × 0.20
system	Triclinic
space group	P-1
Z	2
λ (Å)	1.54184
a (Å)	12.6230(4)
b (Å)	13.1564(3)
c (Å)	19.2160(4)
α (°)	98.635(2)
β (°)	98.815(2)
γ (°)	99.964(2)
V ($Å^3$)	3054.41(14)
d_{calc} (mg/cm^3)	1.571
μ (mm^{-1})	3.428
R(int)	0.0388
GOF on F^2	1.024
R_1/wR_2 [I>2σ(I)]	0.0524 0.1317
R_1/wR_2 (all data)	0.0790 0.1442

Table A11 Crystal data and refinement parameters for **6**

Cmpd L	**6**
CCDC number	1031886
Formula	$C_{39}H_{31.50}F_{1.50}Fe_2N_4O_6S_2$
FW	856.50
T (K)	173(2)
size (mm^{-3})	0.21 × 0.13 × 0.05
system	Monoclinic
space group	*C*2/c
Z	8
λ (Å)	1.54184
a (Å)	22.9479(6)
b (Å)	18.8950(6)
c (Å)	18.6299(5)
α (°)	90
β (°)	90.928(2)
γ (°)	90
V ($Å^3$)	8076.9(4)
d_{calc} (mg/cm^3)	1.409
μ (mm^{-1})	7.204
R(int)	0.0387
GOF on F^2	1.193
R_1/wR_2 [$I>2\sigma(I)$]	0.0414 0.1002
R_1/wR_2 (all data)	0.0550 0.1056

Table A12 Crystal data and refinement parameters for **9**

Cmpd L	**9**
CCDC number	1031885
Formula	$C_{61}H_{50}FeN_2O_2P_2$
FW	960.82
T (K)	100(2)
size (mm^{-3})	0.18 × 0.13 × 0.09
system	Monoclinic
space group	$P2_1/n$
Z	4
λ (Å)	0.71073
a (Å)	14.1826(6)
b (Å)	20.0251(8)
c (Å)	17.0084(8)
α (°)	90
β (°)	98.3580(10)
γ (°)	90
V ($Å^3$)	4779.2(4)
d_{calc} (mg/cm^3)	1.335
μ (mm^{-1})	0.431
R(int)	0.0355
GOF on F^2	1.045
R_1/wR_2 [I>2σ(I)]	0.0399 0.0849
R_1/wR_2 (all data)	0.0518 0.0902

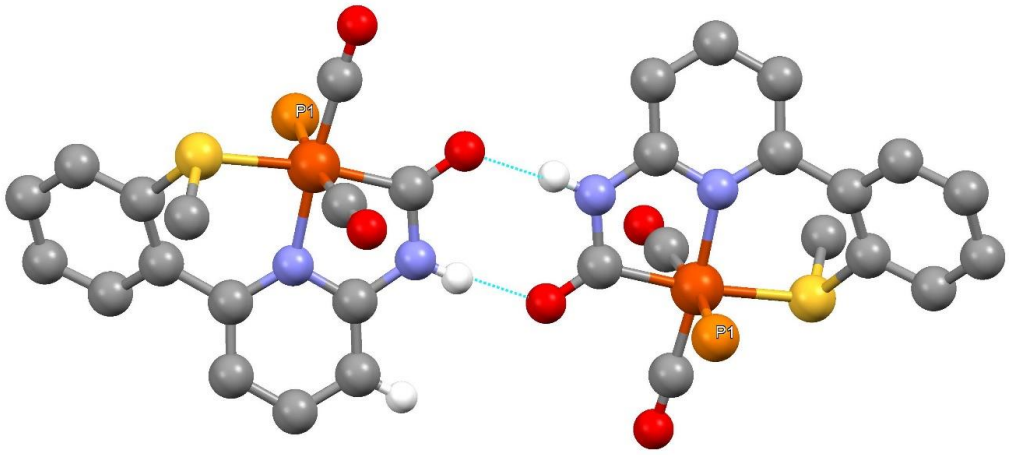

(b)

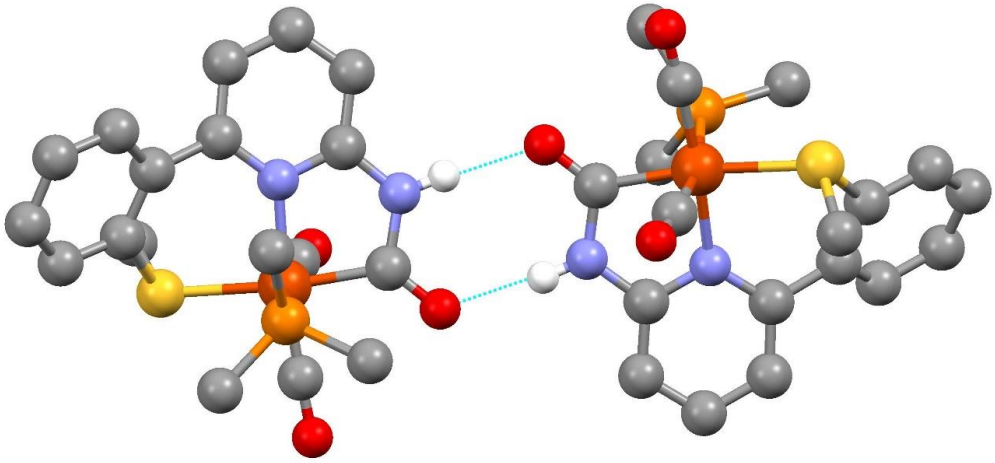

Figure A1 Hydrogen bond of **3a** (a) and **3b** (b). The phenyl rings on **3a** and all hydrogens have been omitted except for the N*H* hydrogen.

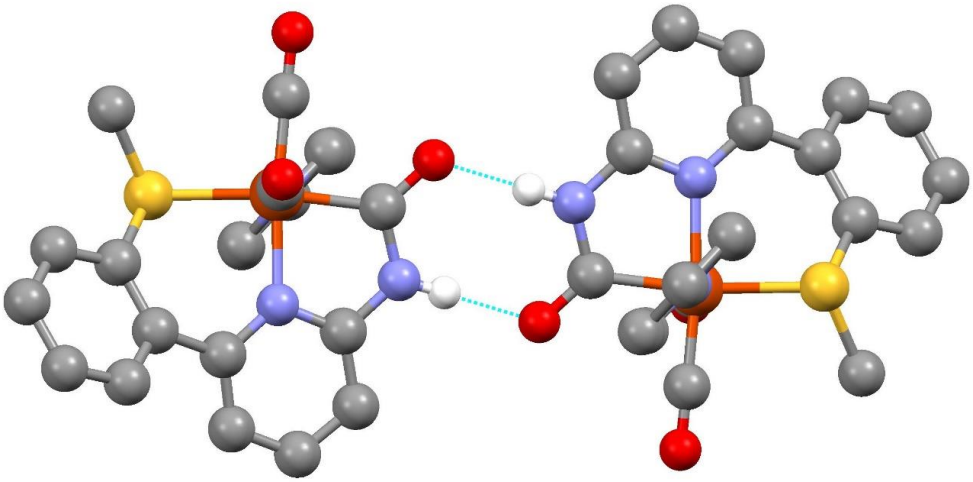

Figure A2 Hydrogen bond of **3c**. All hydrogens have been omitted except for the N*H* hydrogen.

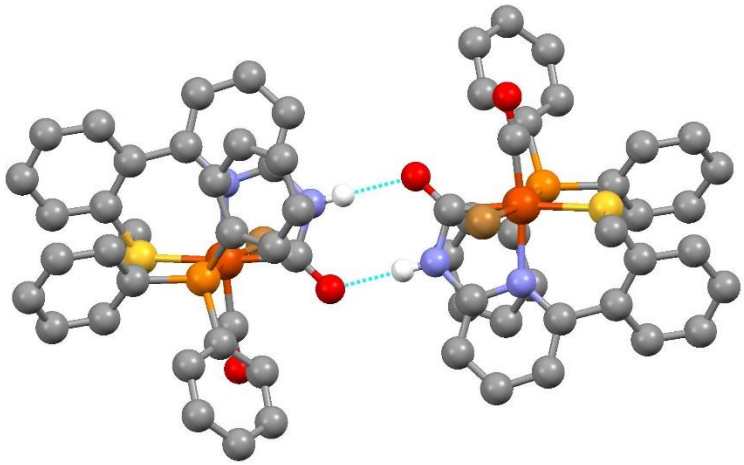

(a)

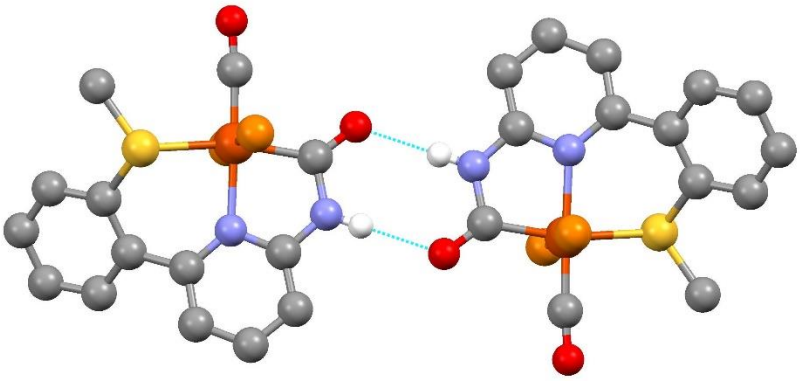

(b)

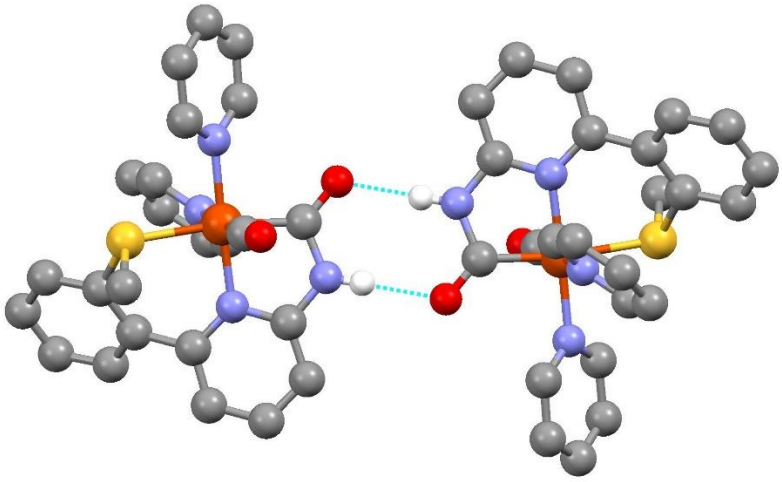

(c)

Figure A3 Hydrogen bond of **4a** (a), **4b** (b) and **4c** (c). The phenyl rings on **4b** and all hydrogens have been omitted except for the N*H* hydrogen.

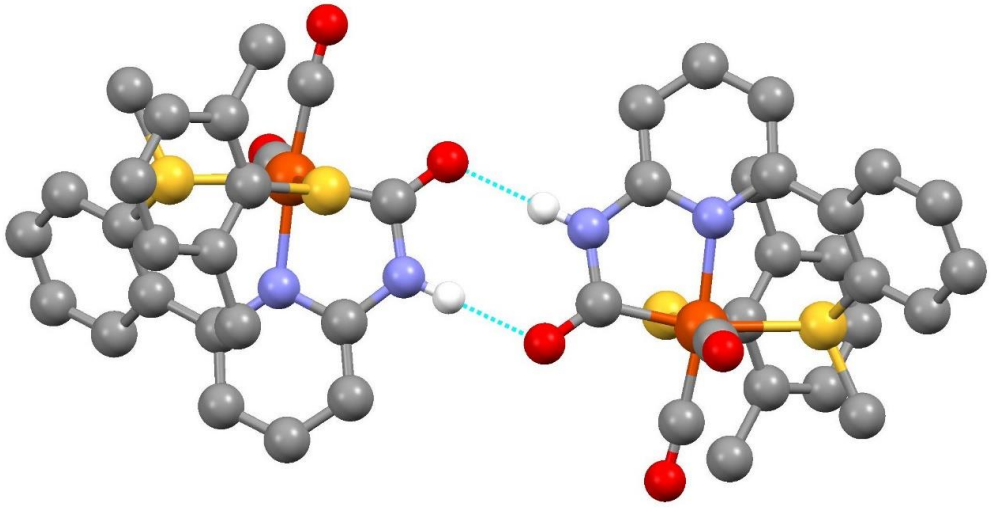

Figure A4 Hydrogen bond of **3g**. All hydrogens have been omitted except for the N*H* hydrogen

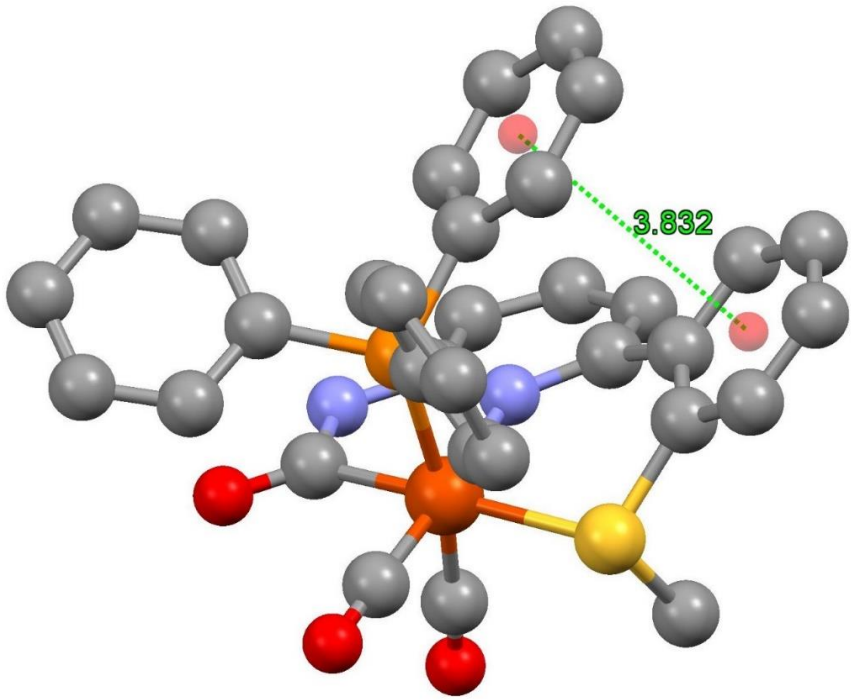

Figure A5 Intramolecular π···π interaction within **3a**.

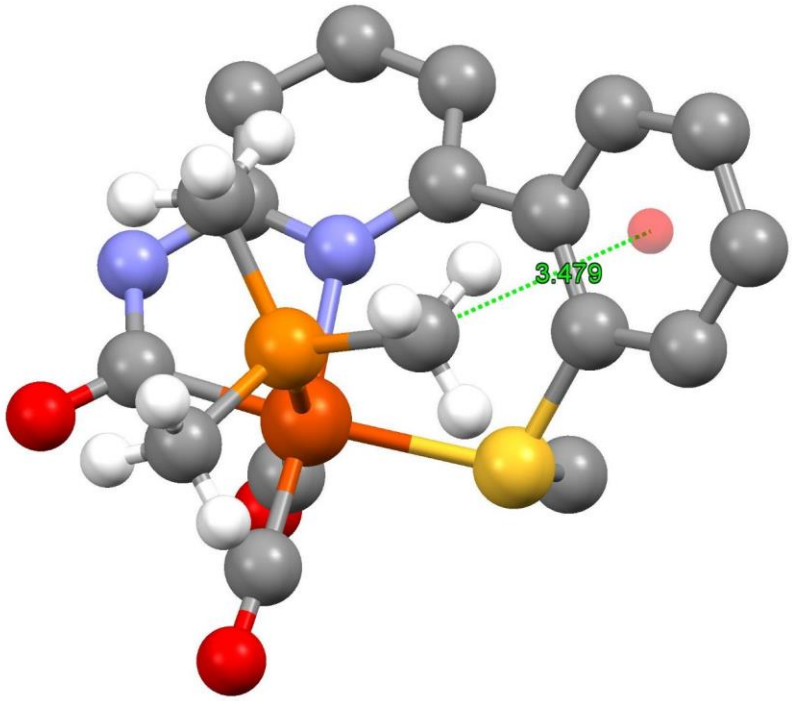

Figure A6 Intramolecular CH···π interaction in **3b**.

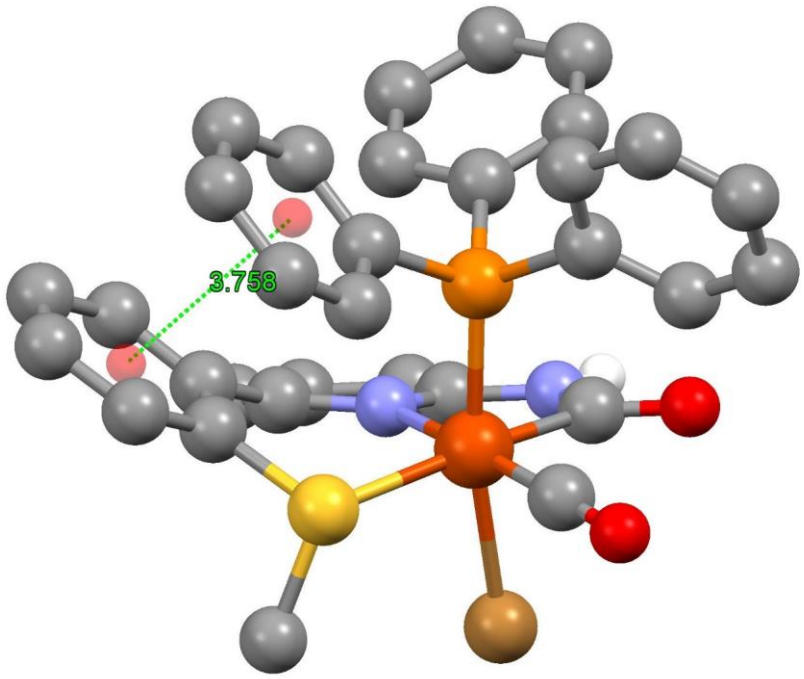

Figure A7 Intramolecular π···π interaction in **4a**.

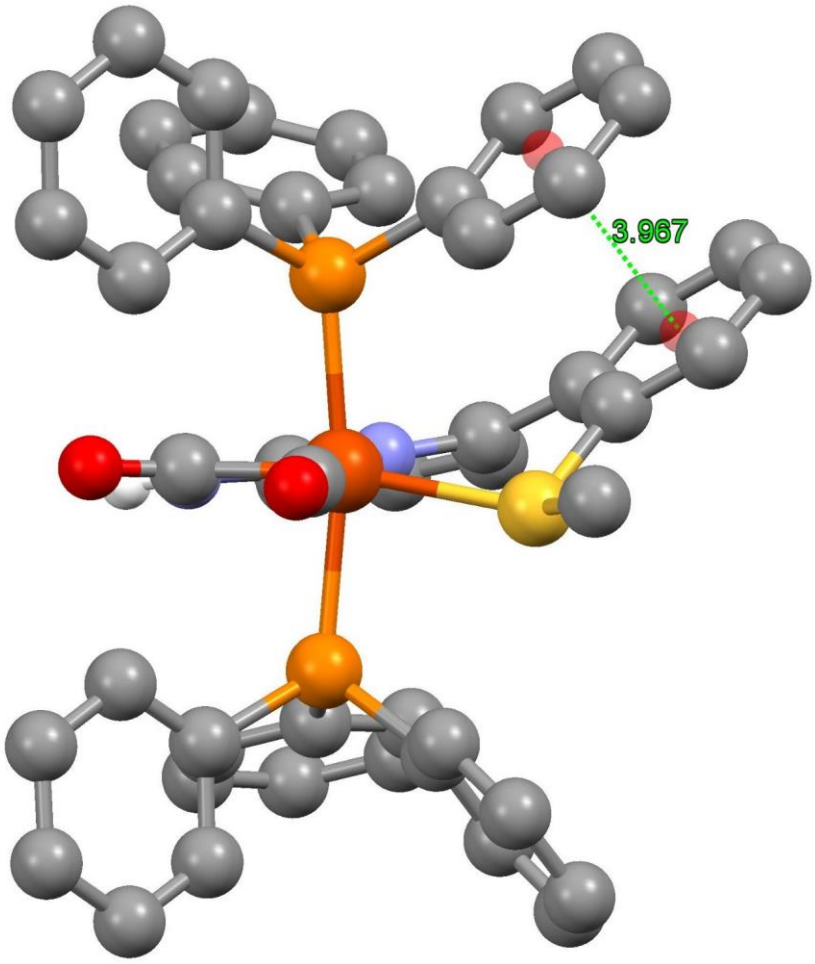

Figure A8 Intramolecular π···π interaction in **4b**.

Table A13 The total contribution of Fe and contribution of valent atomic orbitals of Fe to the molecular orbitals in $\mathbf{2}^{+}$.

Orbital Number		**Fe %**	**Br %**	d_{x2-y2} **%**	d_{z2} **%**	d_{xy} **%**	d_{xz} **%**	d_{yz} **%**	***4s* %**	$3p_x$ **%**	$3p_y$ **%**	$3p_z$ **%**
93	LUMO+2	35.69	0.00	16.69	1.74	6.07	4.70	6.31	0.14	0.02	0.01	0.02
92	LUMO+1	5.48	0.00	1.24	0.18	1.33	0.81	1.89	0.02	0.00	0.00	0.01
91	LUMO	39.36	0.00	14.26	1.36	3.35	3.15	14.29	2.68	0.01	0.09	0.15
90	HOMO	18.63	0.00	0.91	1.40	1.17	0.00	14.87	0.12	0.01	0.08	0.05
89	HOMO-1	44.85	0.00	2.13	28.30	8.84	5.18	0.29	0.11	0.00	0.00	0.00
88	HOMO-2	35.83	0.00	5.64	5.13	10.32	12.20	2.52	0.03	0.00	0.00	0.00
87	HOMO-3	62.41	0.00	15.37	20.48	0.67	23.17	2.07	0.59	0.00	0.00	0.00
86	HOMO-4	39.62	0.00	0.09	9.04	15.05	6.12	9.17	0.13	0.01	0.01	0.00
85	HOMO-5	13.14	0.00	1.15	8.00	0.60	0.80	2.49	0.09	0.00	0.00	0.00
84	HOMO-6	30.98	0.00	0.51	0.91	23.99	3.97	1.48	0.11	0.00	0.00	0.00
83	HOMO-7	14.74	0.00	6.64	0.07	0.31	0.61	6.47	0.53	0.02	0.03	0.01
82	HOMO-8	6.84	0.00	0.71	0.14	5.18	0.68	0.10	0.01	0.02	0.00	0.01

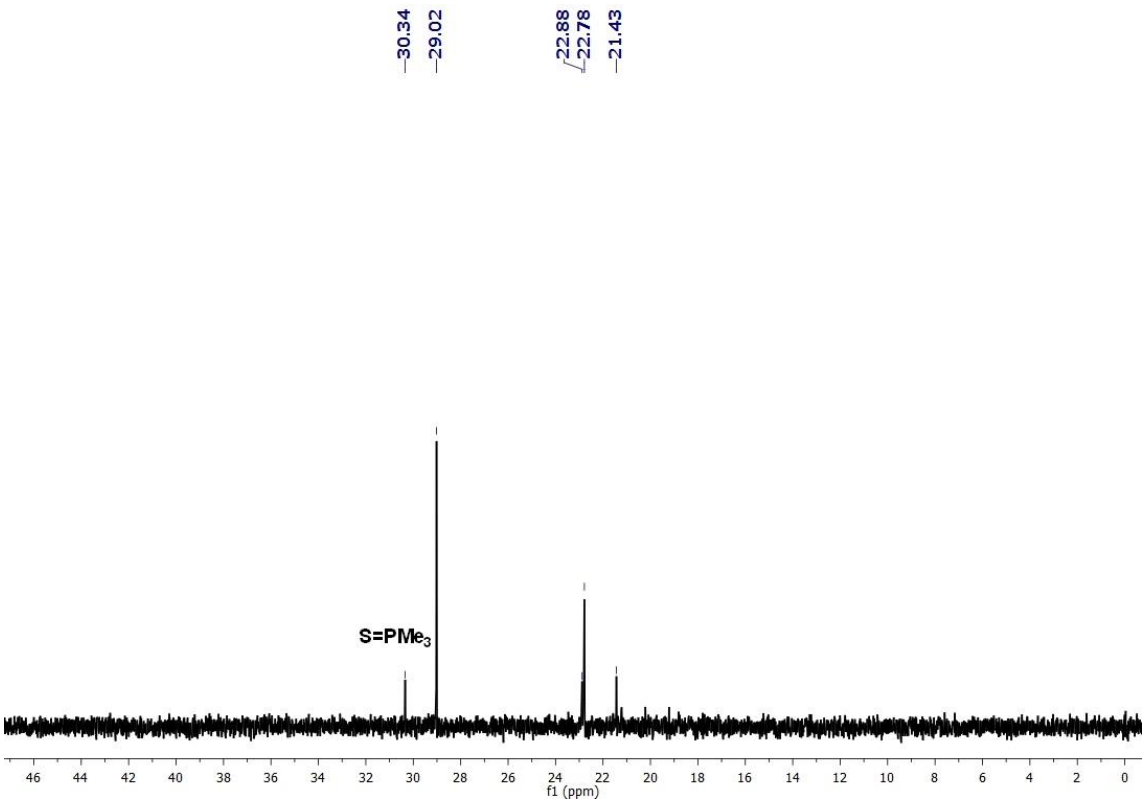

Figure A9 ^{31}P NMR of S=PMe$_3$ in the mixture of reaction of [($^{O=}$C^{NH}N^{Py}S^{Me})Fe(CO)$_2$(Br)] (**1**) with ^{t}BuOK and PMe$_3$.

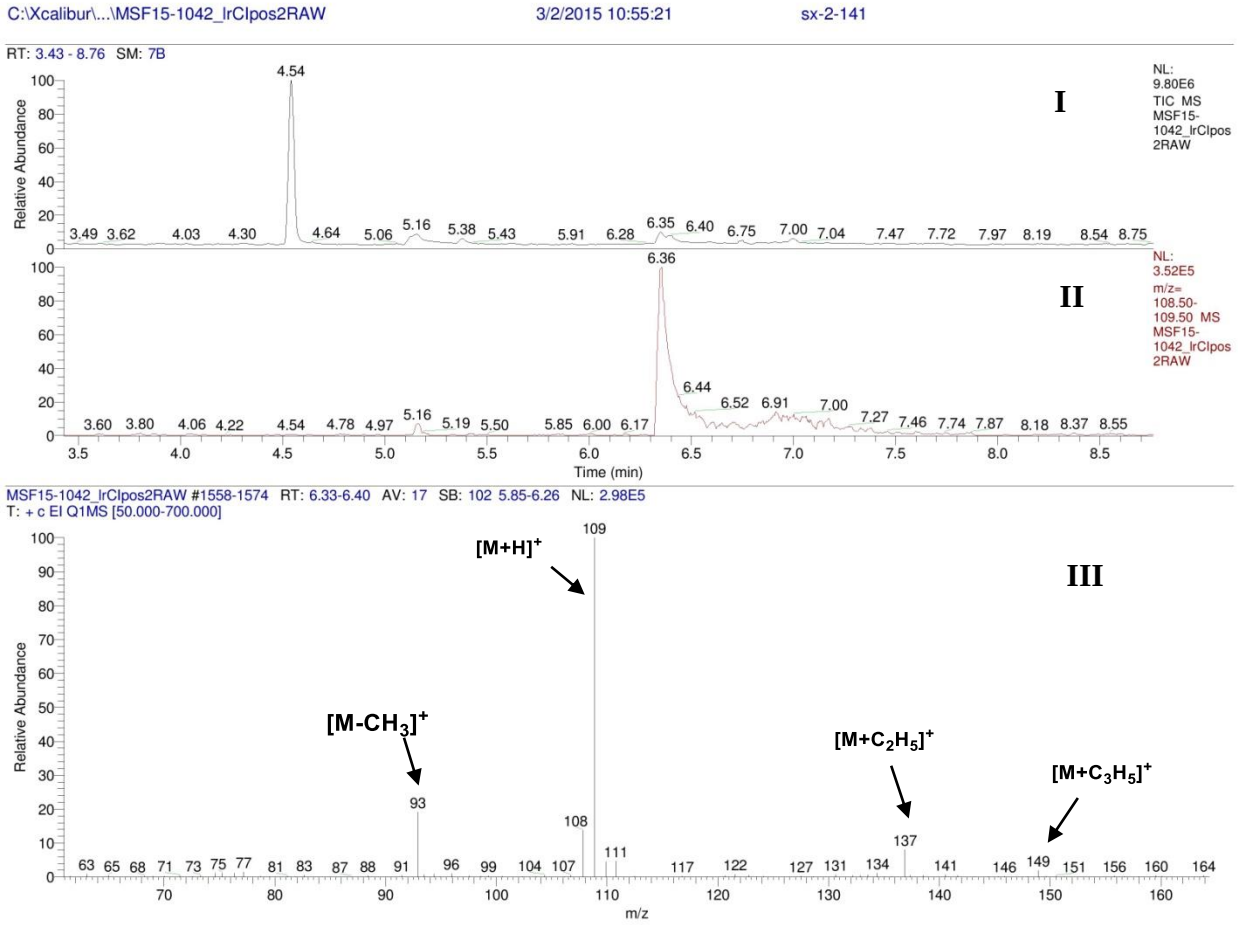

Figure A10 GC-MS analysis of $S{=}PMe_3$. (II) The total chromatogram of the reaction mixture. (II) The chromatogram of the species with *m*/*z* from 108.50 to 109.50. The eluted $S{=}PMe_3$ was observed at 6.36 min. (III) The MS (CI^+) of $S{=}PMe_3$ showing at 6.36 min.

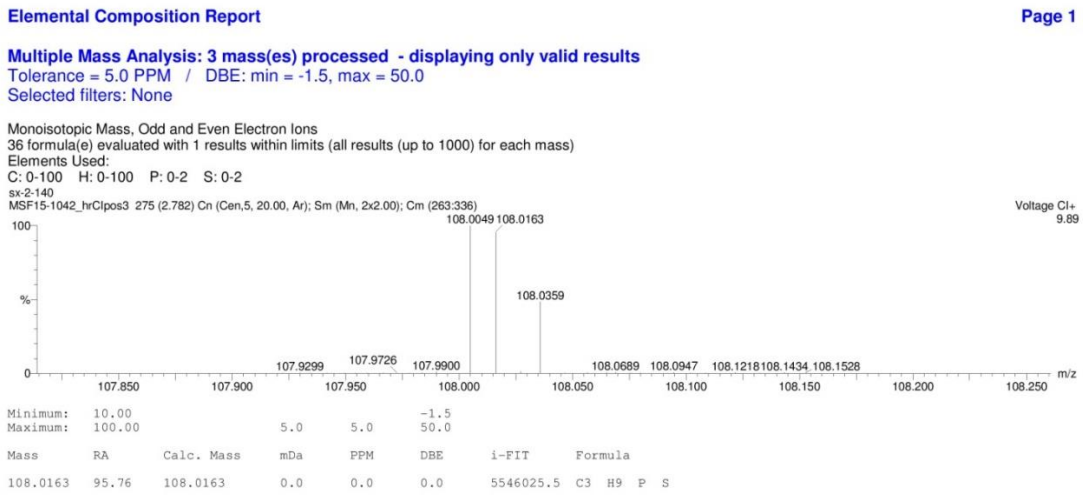

Figure A11 HR-MS analysis of $S{=}PMe_3$ (CI^+). [M+] with *m*/*z* = 108.0163.

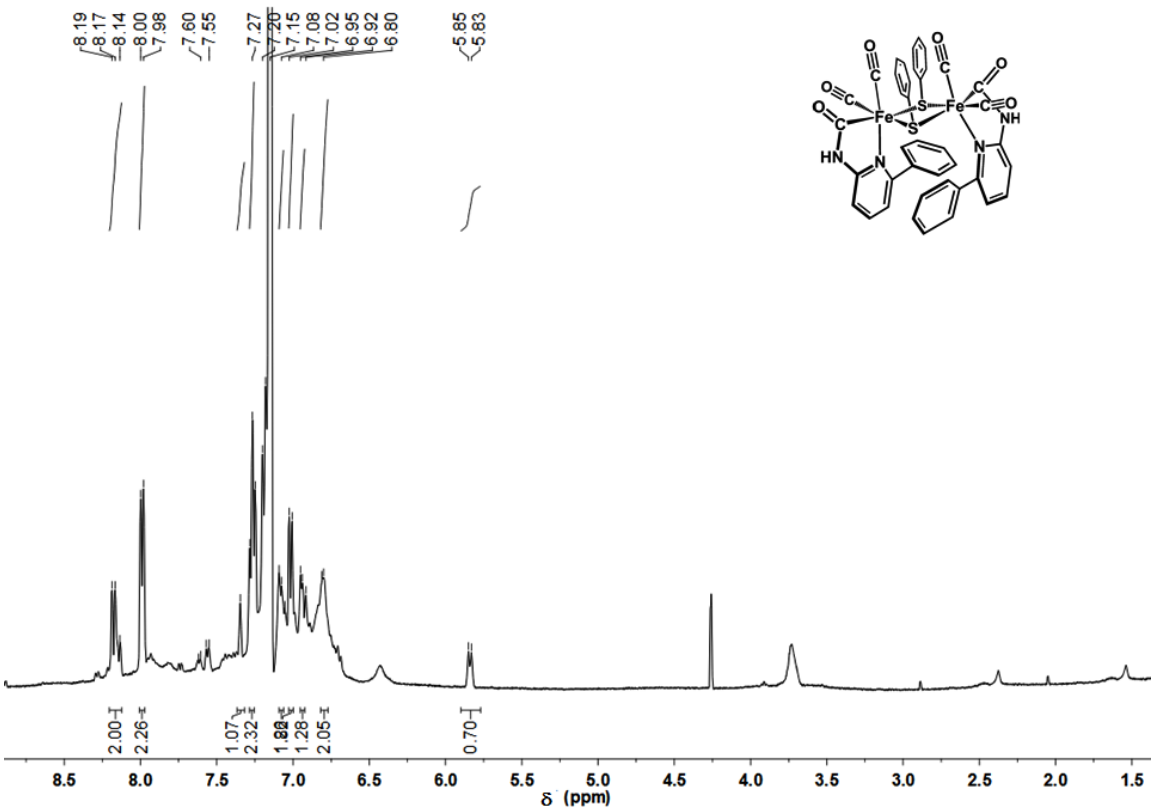

Figure A12 ^{1}H NMR (400 MHz) spectrum of μ_2-$(PhS)_2$–$[(^{O=}C^{NH}N^{Ph})Fe(CO)_2]_2$ (**6'**) in C_6D_6 at 298 K.

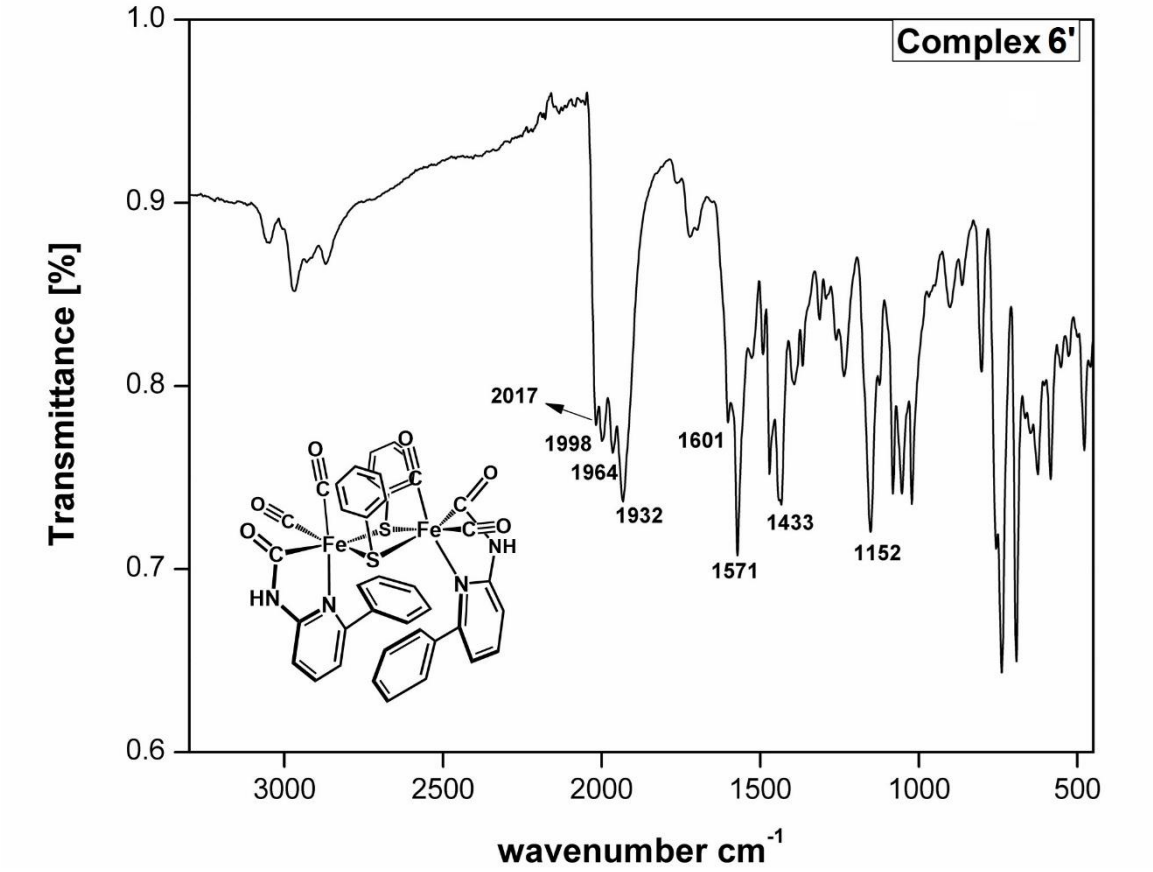

Figure A13 Comparison of the solid state ATR-IR spectra of the dimer analogues of type μ_2-$(PhS)_2$–$[(^{O=}C^{NH}N^{Ph})Fe(CO)_2]_2$ (**6'**).

APPENDIX B SUPPORTING INFORMATION FOR CHAPTER 3

B.1 Spectra of the ligands

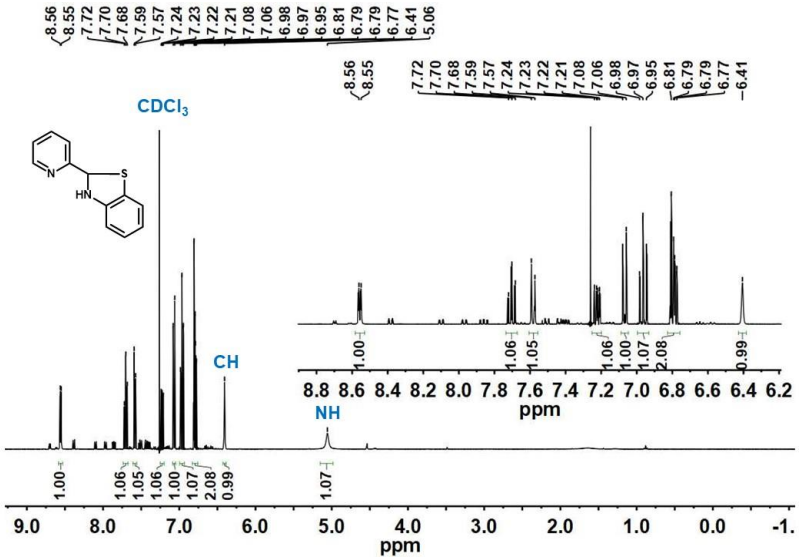

Figure B1 ^{1}H NMR spectrum of **L1** ($CDCl_3$, 400 MHz)

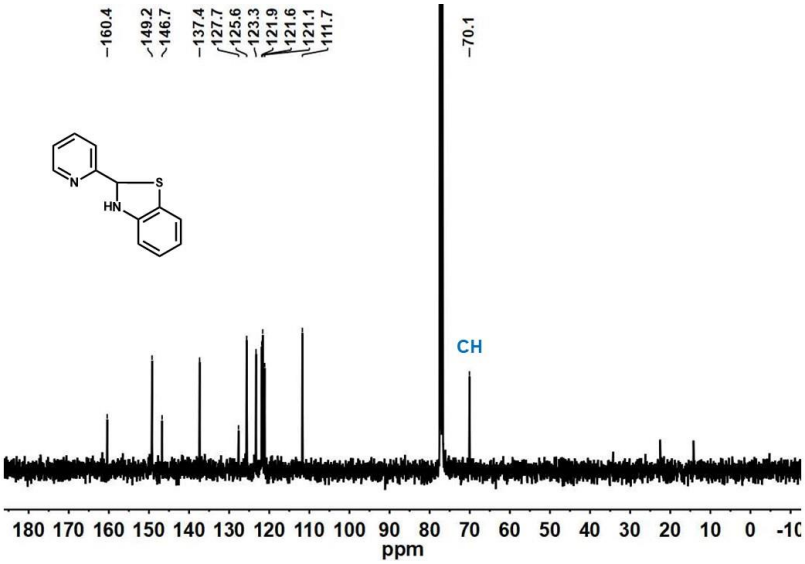

Figure B2 ^{13}C NMR spectrum of **L1** ($CDCl_3$, 100 MHz)

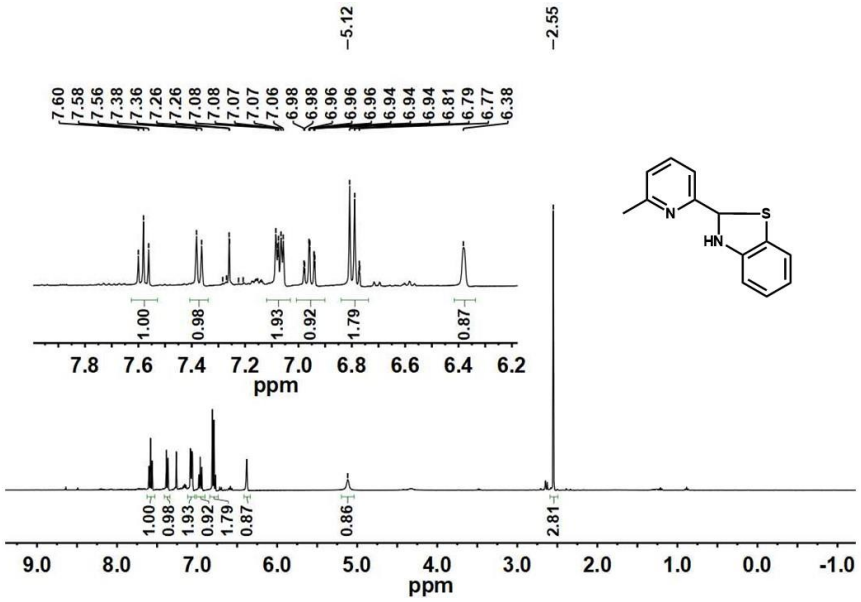

Figure B3 ^{1}H NMR spectrum of **L2** ($CDCl_3$, 400 MHz)

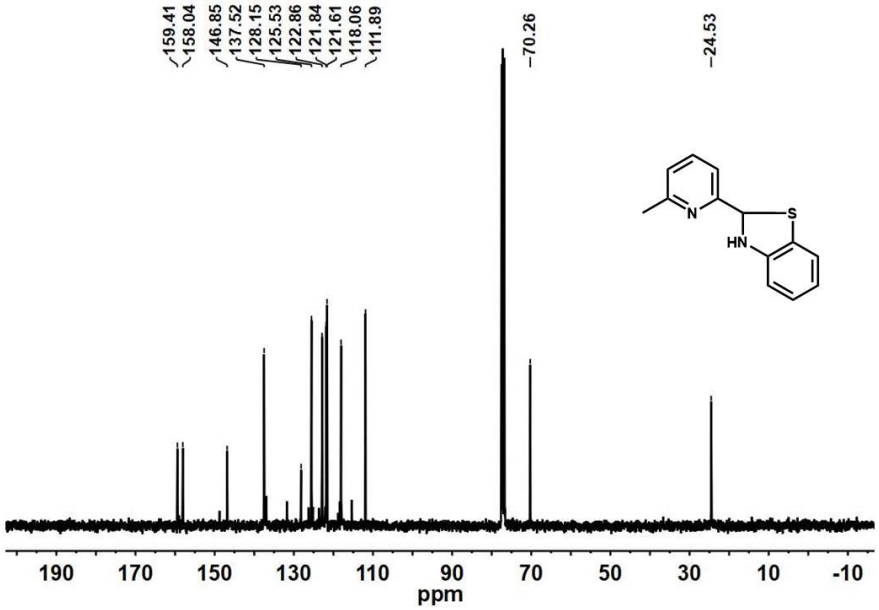

Figure B4 ^{13}C NMR spectrum of **L2** ($CDCl_3$, 100 MHz)

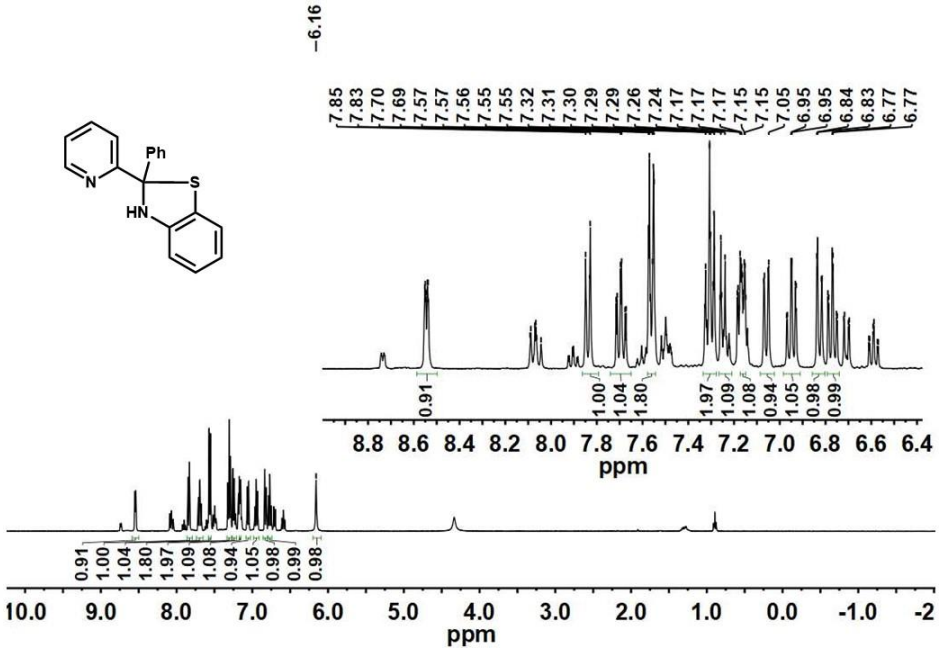

Figure B5 ^{1}H NMR spectrum of **L3** ($CDCl_3$, 400 MHz)

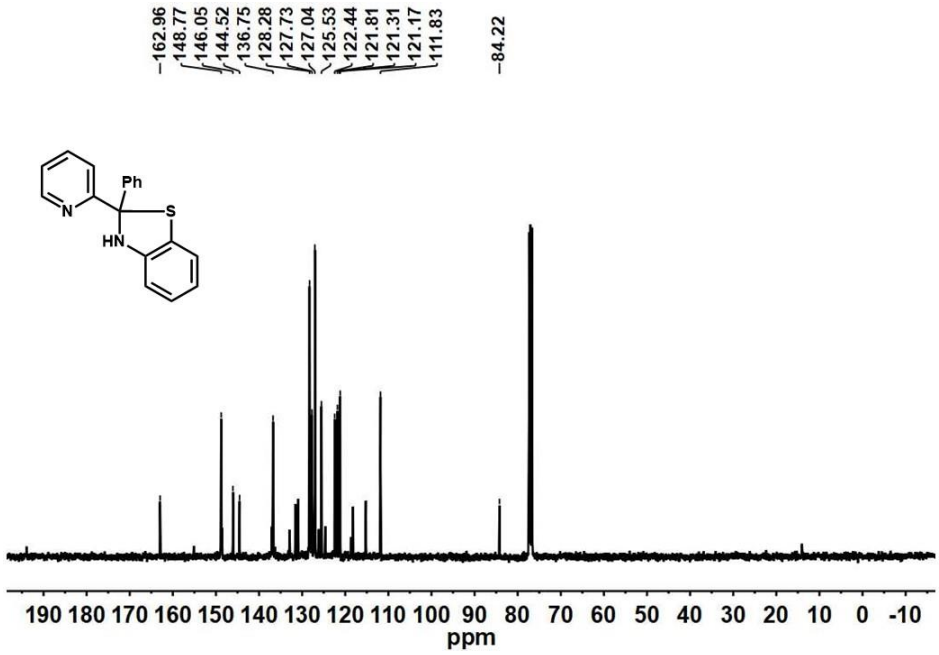

Figure B6 ^{13}C NMR spectrum of **L3** ($CDCl_3$, 100 MHz)

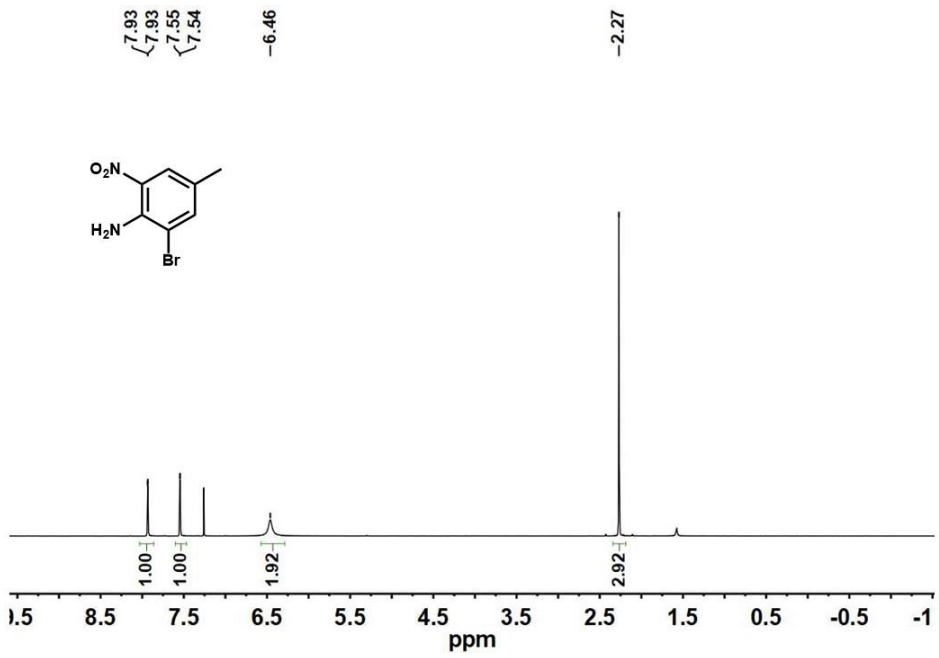

Figure B7 ^{1}H NMR spectrum of **a** ($CDCl_3$, 400 MHz)

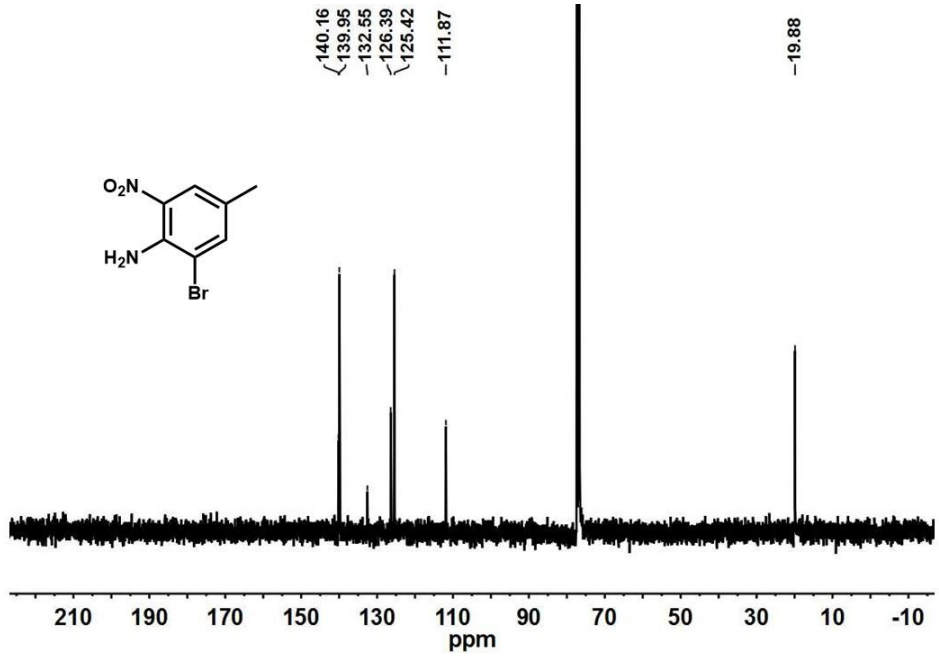

Figure B8 ^{13}C NMR spectrum of **a** ($CDCl_3$, 100 MHz)

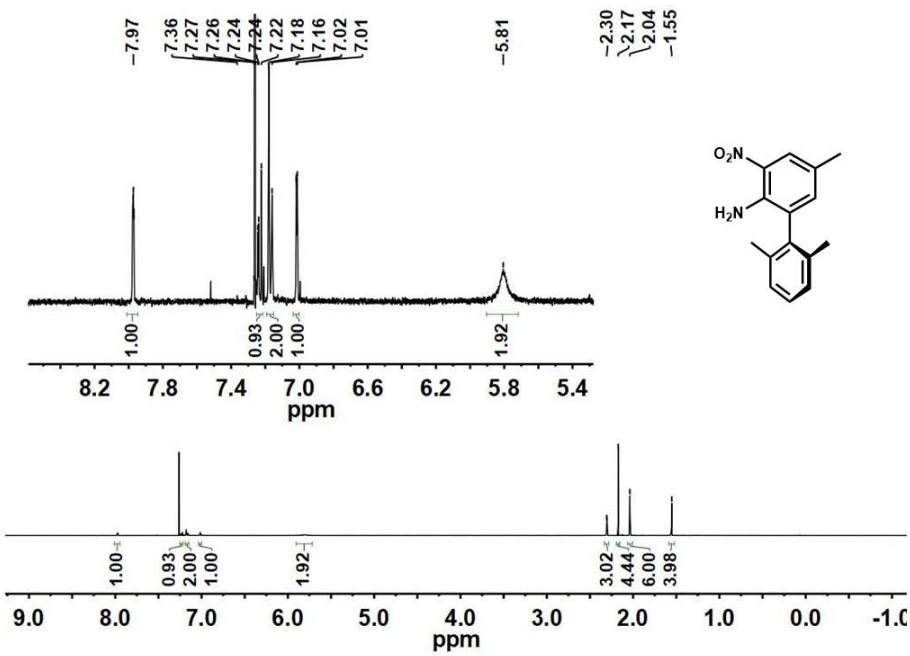

Figure B9 ^{1}H NMR spectrum of **b** ($CDCl_3$, 400 MHz)

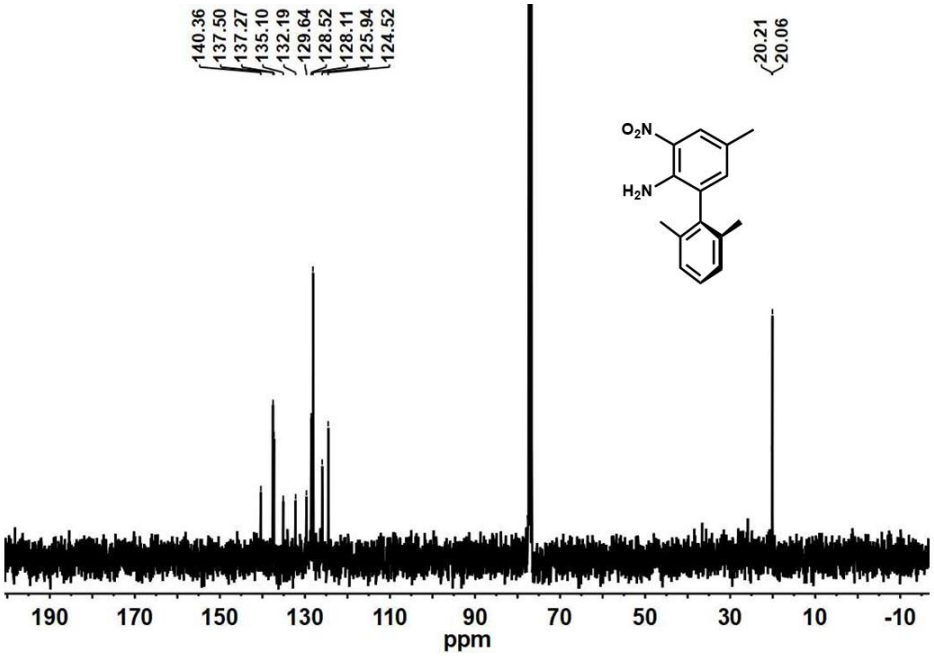

Figure B10 ^{13}C NMR spectrum of **b** ($CDCl_3$, 100 MHz)

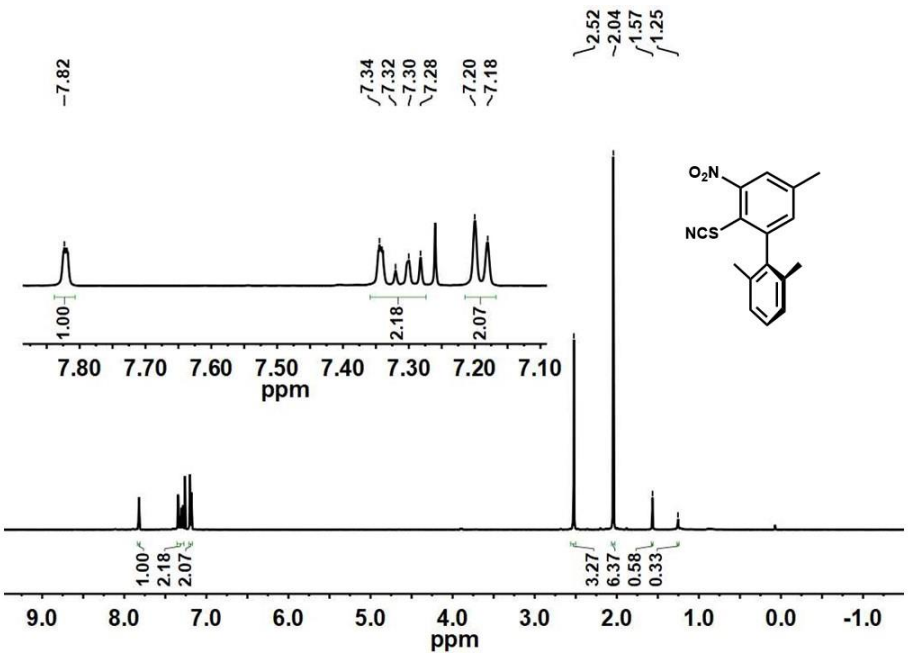

Figure B11 ^{1}H NMR spectrum of **c** ($CDCl_3$, 400 MHz)

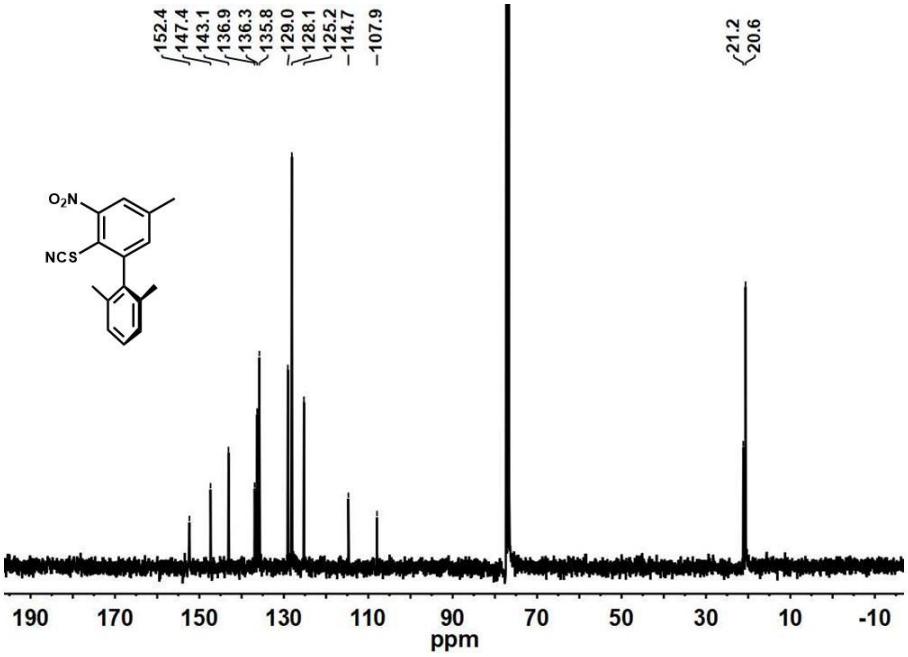

Figure B12 ^{13}C NMR spectrum of **c** ($CDCl_3$, 100 MHz)

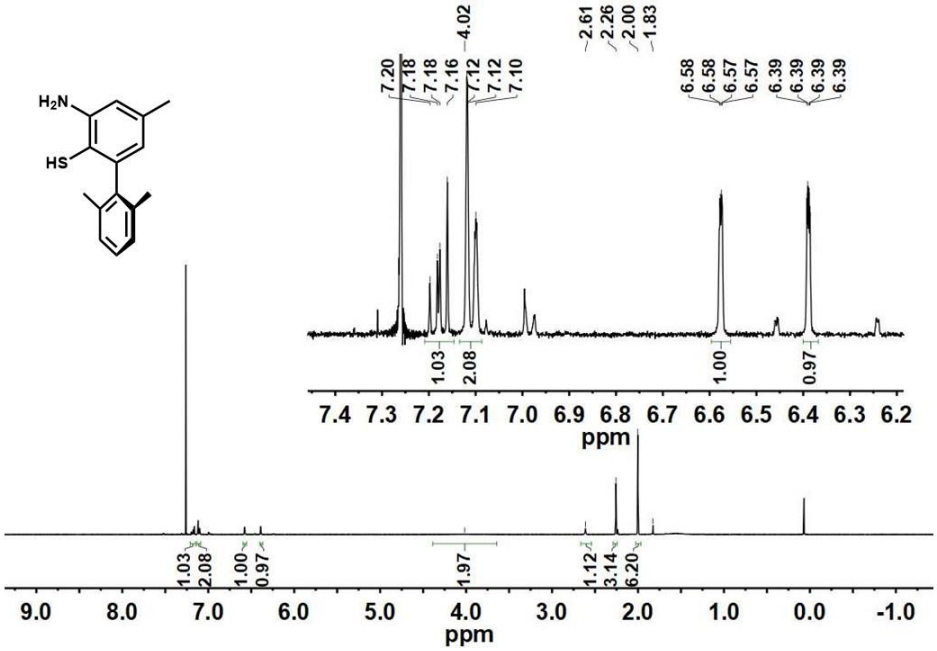

Figure B13 ^{1}H NMR spectrum of **d** ($CDCl_3$, 400 MHz)

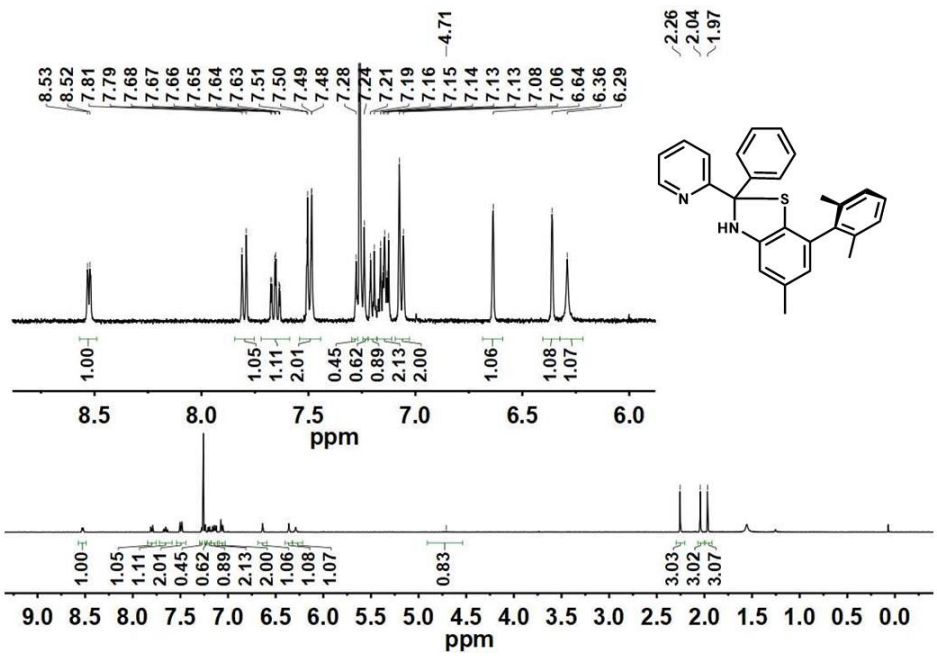

Figure B14 ^{1}H NMR spectrum of **L_B** ($CDCl_3$, 400 MHz)

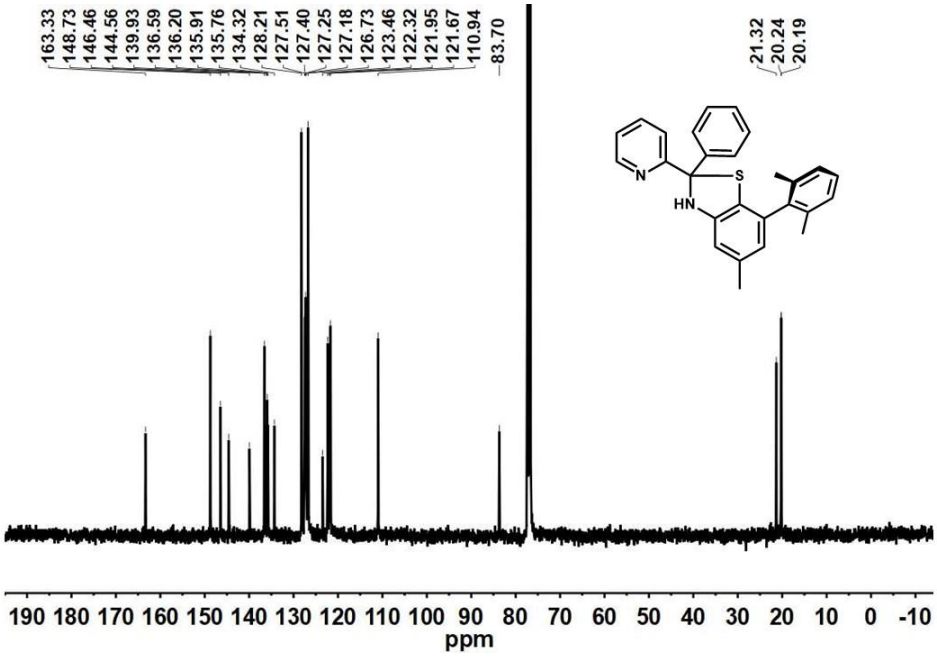

Figure B15 ^{13}C NMR spectrum of **L_B** ($CDCl_3$, 100 MHz)

B.2 Spectra of the Complexes

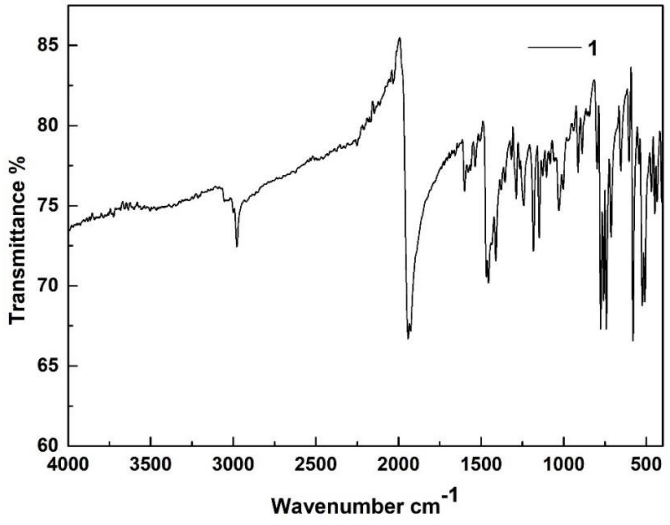

Figure B16 IR spectrum of **1**.

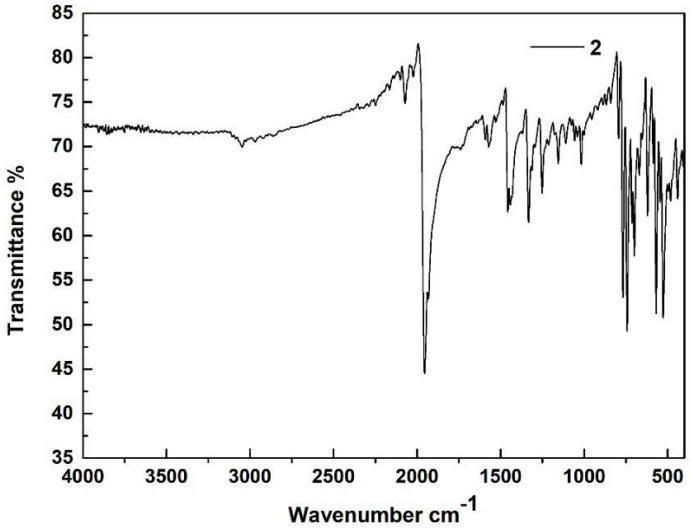

Figure B17 IR spectrum of **2**.

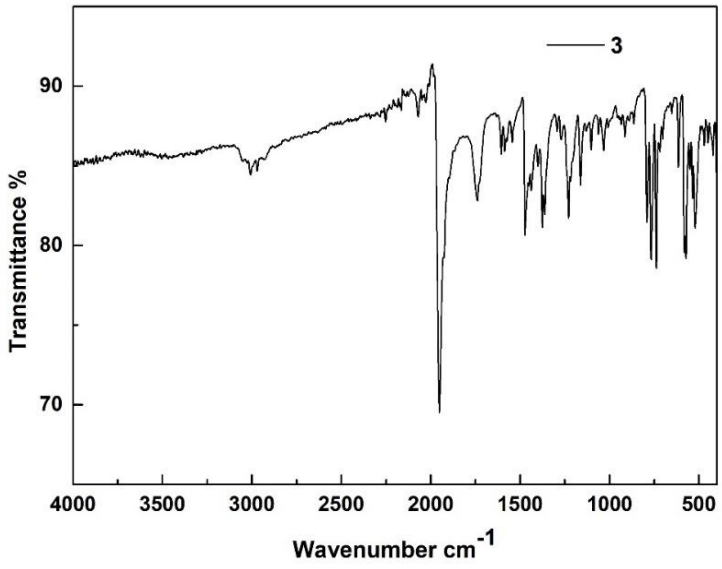

Figure B18 IR spectrum of **3**.

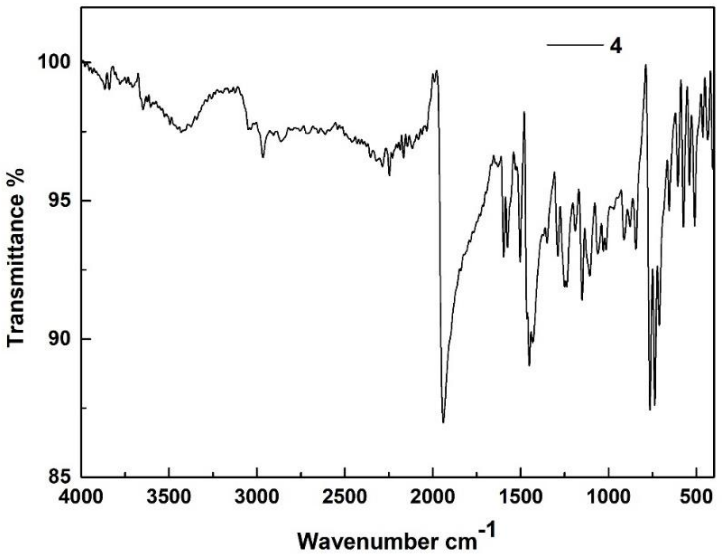

Figure B19 IR spectrum of **4**.

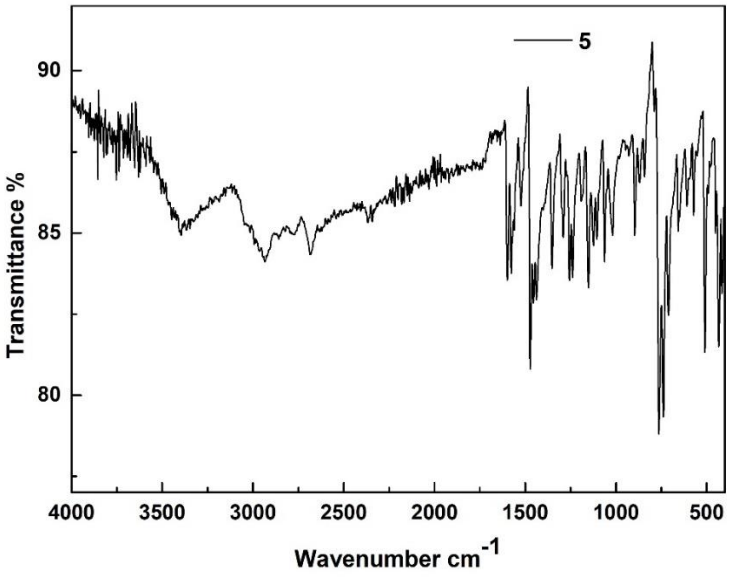

Figure B20 IR spectrum of **5**.

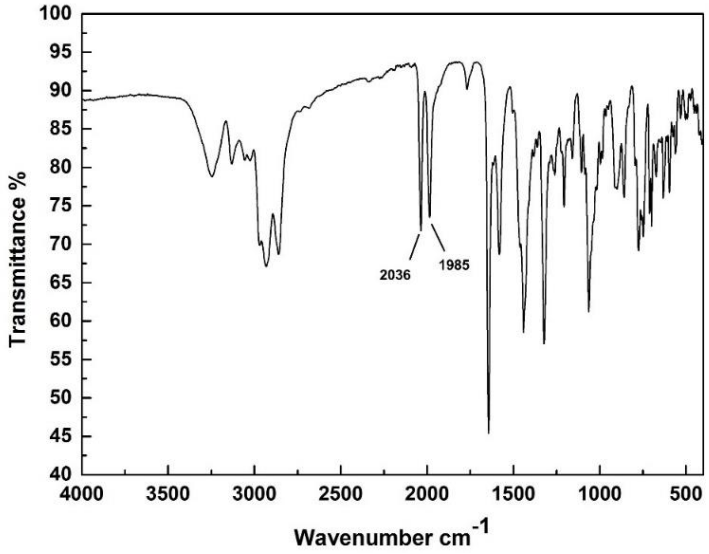

Figure B21 IR spectrum of **8**.

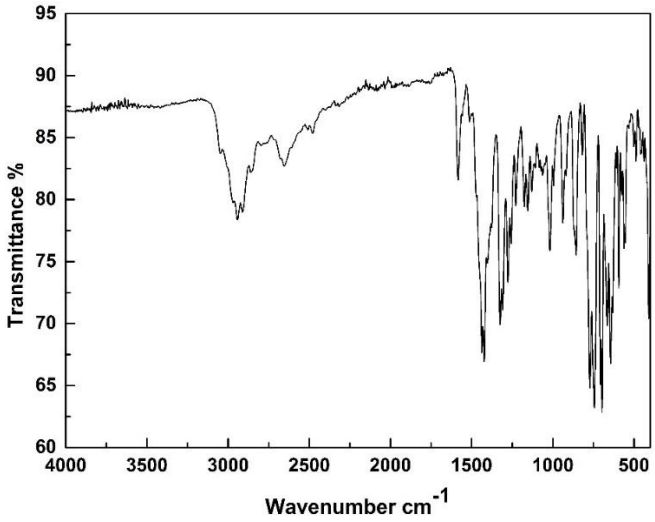

Figure B22 IR spectrum of **9**.

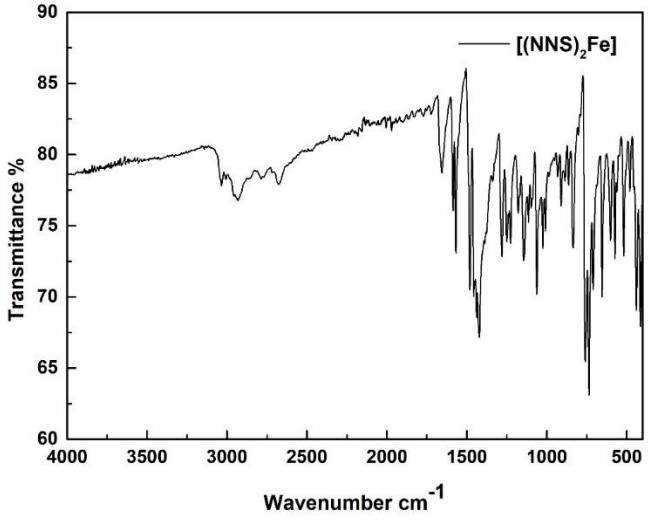

Figure B23 IR spectrum of $[(NNS)_2Fe]$.

B.3 X-ray Crystallography

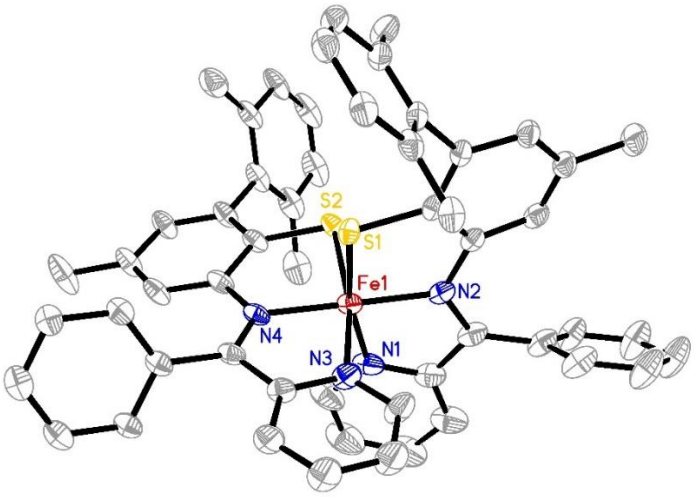

Figure B24 ORTEP plot (30% thermal ellipsoids) for [($N^{Ph}NS^{DMPh}$)$_2$Fe] (**9**). H-atoms are omitted for sake of clarity.

Table B1 Selected bond lengths (Å) and angles (°).

Cmpd	1	1_{DFT}	2	4	4_{DFT}^{+}	5	5^{+}_{DFT}	9	$[(NNS)_2Fe]$	8_{DFT}
Fe(1)–S(1)	2.2889(17)	2.333	2.259(4)	2.2888(11)	2.353	2.212(3)	2.251	2.2621(10)	2.290(3)	2.308
Fe(1)–S(2)/S(1)#1	2.3278(18)	2.408	2.312(4)	2.2972(10)	2.360	2.222(3)	2.251	2.2610(9)	2.294(3)	
Fe(1)–N(1)	1.979(5)	2.010	1.945(11)	1.961(3)	2.019	2.015(8)	2.047	1.946(4)	1.973(9)	2.006
Fe(1)–N(2)	1.982(5)	1.978	1.994(10)	1.903(3)	1.969	1.928(7)	1.971	1.924(4)	1.911(10)	2.003
Fe(1)–N(3)				1.964(3)	2.021	2.016(8)	2.047	1.966(3)	1.961(10)	
Fe(1)–N(4)				1.925(3)	1.968	1.930(7)	1.971	1.937(3)	1.902(9)	
Fe(2)–S(1)			2.306(4)	2.3061(10)	2.404					
Fe(2)–S(2)			2.312(4)	2.4026(11)	2.448					
Fe(2)–S(3)				2.2733(10)	2.342					
Fe(2)–N(3)			1.963(11)							
Fe(2)–N(4)			2.001(10)							
Fe(2)–N(5)				1.988(3)	2.040					
Fe(2)–N(6)				1.939(3)	1.975					
Fe–Ccarbonyl	1.789(8)	1.815	1.780(15)	1.774(5)	1.801					1.804
			1.762(14)							1.822
C≡O	1.114(8)	1.141	1.145(16)	1.115(5)	1.140					1.140
			1.148(15)							1.138
Fe–I/Br	2.642(3)	2.726	2.6676(19)							2.528
S(1)–Fe(1)–S(2)/S(1)#1	84.81(6)	85.18	82.76(13)	85.01(4)	85.69	96.46(10)	95.94	92.65(4)	91.05(12)	
Fe(1)–S(1)–Fe(2)/Fe(1)#1	95.10(6)	94.56	97.32(13)	97.73(4)	96.36					
Ccarbonyl–Fe(1)–S(1)	98.0(2)	95.32	94.9(4)							85.96

Symmetry transformations used to generate equivalent atoms: #1 -x+2,y,-z+3/2

Table B2 Crystal data and refinement parameters for thiolate complexes.

Cmpd	**1**	**2**	**4**	**5**	**9**	**$(NNS)_2Fe$**
CCDC number	1837368	1837371	1837369	1837370	1837372	1837373
Formula	$C_{13}H_9FeIN_2O_1S_1$	$C_{38}H_{26}Fe_2I_2N_4O_2S_2$, $C_2H_3N_1$	$C_{37}H_{27}Fe_2N_6O_1S_3^{1+}$, $0.66(I_1^{1-})$,$0.34(I1)$	$C_{24}H_{18}Fe_1N_4S_2^{1+}$, $(I_1^{1-})0.25(I_2)$	$2(C_{54}H_{46}Fe_1N_4S_2)$, $C_6H_5F_1$	$C_{24}H_{18}Fe_1N_4S_2$
FW	424.03	1041.3	453.21	672.74	1837.93	482.39
T (K)	100(2)	100(2)	100(2)	100(2)	100(2)	100(2)
size (mm^3)	0.07 × 0.05 × 0.04	0.11 × 0.09 × 0.07	0.14 × 0.05 × 0.04	0.145 × 0.022 × 0.012	0.5 × 0.2 × 0.1	0.174 × 0.024 × 0.015
System	Monoclinic	Orthorhombic	Monoclinic	Monoclinic	Triclinic	Orthorhombic
space group	*C 2/c*	*P 21 21 21*	*P 21/c*	*P 21/n*	*P-1*	*P n a 21*
Z	8	4	8	4	2	4
l (Å)	0.71073	0.71073	0.71073	1.54184	1.54184	1.54184
a (Å)	19.543	12.2989(18)	10.8949(11)	8.145	15.1617(3)	23.436(2)
b (Å)	8.922	15.752(2)	13.2081(15)	27.849	19.6764(6)	7.8953(11)
c (Å)	17.928	19.923(3)	30.117(3)	11.609	20.1569(6)	11.2967(12)
α (°)	90	90	90	90	94.991(3)	90
β (°)	117.75	90	99.060(2)	105.43	104.346(2)	90
γ (°)	90	90	90	90	107.317(2)	90
V ($Å^3$)	2766.5	3859.7(10)	4279.8(8)	2538.4	5477.1(3)	2090.2(4)
d_{calc} (mg/cm^3)	2.036	1.792	1.407	1.76	1.114	1.533
m (mm^{-1})	3.464	2.502	1.579	20.777	3.216	7.808
R(int)	0.0884	0.0993	0.0627	0.1067	0.0718	0.0773
GOF on F^2	1.067	1.065	1.109	1.100	1.024	1.063
*R*1/w*R*2 [*I*>2s(*I*)]	0.0454	0.0669	0.0467	0.0695	0.0678	0.0825
	0.1043	0.1218	0.1035	0.1563	0.1749	0.1909
*R*1/w*R*2 (all data)	0.057	0.0993	0.0596	0.0993	0.0913	0.1026
	0.1107	0.1368	0.1083	0.1708	0.1938	0.2115

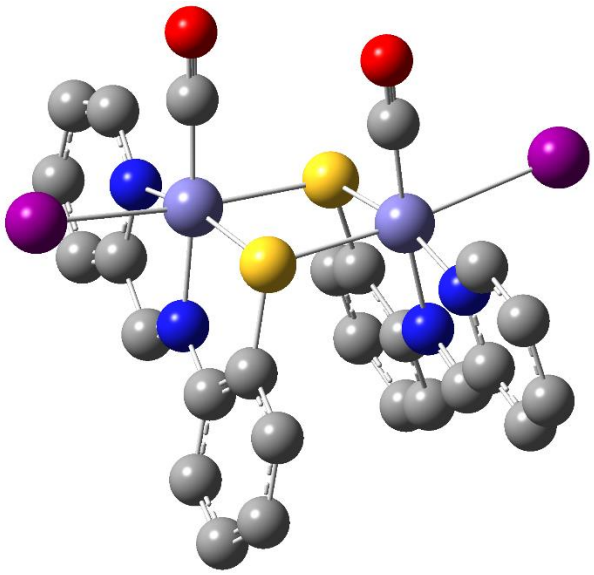

Figure B25 Calculated structure of **1**.

B.4 DFT Calculations

Table B3 Coordinates of the calculated structure **1.**

Tag	Symbol	X	Y	Z
1	C	-3.82123	-2.07752	-1.15325
2	H	-3.5049	-2.039	-2.18716
3	C	-4.83503	-2.93935	-0.74873
4	H	-5.31183	-3.58068	-1.47858
5	C	-5.22064	-2.95155	0.589336
6	H	-6.01224	-3.60747	0.930948
7	C	-4.57342	-2.10378	1.477308
8	H	-4.84059	-2.07719	2.526597
9	C	-3.56252	-1.2668	1.00094
10	C	-2.83423	-0.33817	1.83755
11	H	-3.08031	-0.26257	2.89208
12	C	-1.16636	1.369652	1.916137
13	C	-1.347	1.732273	3.258915
14	H	-2.10645	1.249928	3.861306
15	C	-0.56986	2.72812	3.82905
16	H	-0.72559	3.006193	4.864636
17	C	0.394992	3.384654	3.059957
18	H	0.990772	4.177823	3.497488
19	C	0.577152	3.038835	1.727239
20	H	1.303193	3.564234	1.119137
21	C	-0.19048	2.026524	1.139452
22	C	-1.72151	-0.06287	-2.49615
23	N	-3.19365	-1.25374	-0.30726
24	N	-1.92879	0.380284	1.258871
25	O	-1.71962	-0.15511	-3.63373
26	S	0.023354	1.604138	-0.57384
27	Fe	-1.7397	0.080947	-0.68731
28	I	-3.62823	1.999677	-1.1168
29	C	3.82118	2.077563	-1.1533
30	H	3.504906	2.038968	-2.18722
31	C	4.834896	2.939483	-0.74876
32	H	5.311688	3.580835	-1.47859
33	C	5.220426	2.951763	0.589331
34	H	6.011965	3.607765	0.930954
35	C	4.573235	2.10398	1.477301

36	H	4.840357	2.07745	2.526606
37	C	3.562422	1.266906	1.000912
38	C	2.834152	0.338243	1.837528
39	H	3.080203	0.262762	2.892066
40	C	1.166437	-1.36973	1.916105
41	C	1.347204	-1.73243	3.258843
42	H	2.106763	-1.25015	3.861164
43	C	0.570087	-2.72828	3.828995
44	H	0.725905	-3.00643	4.864549
45	C	-0.39487	-3.38473	3.059958
46	H	-0.99064	-4.17789	3.49751
47	C	-0.57712	-3.03886	1.727266
48	H	-1.30322	-3.56421	1.119199
49	C	0.190512	-2.02656	1.139461
50	C	1.7215	0.062824	-2.49619
51	N	3.193625	1.253771	-0.3073
52	N	1.928825	-0.38031	1.258843
53	O	1.719528	0.154957	-3.63377
54	S	-0.02336	-1.60415	-0.57383
55	Fe	1.739709	-0.08096	-0.68733
56	I	3.62825	-1.99968	-1.11683

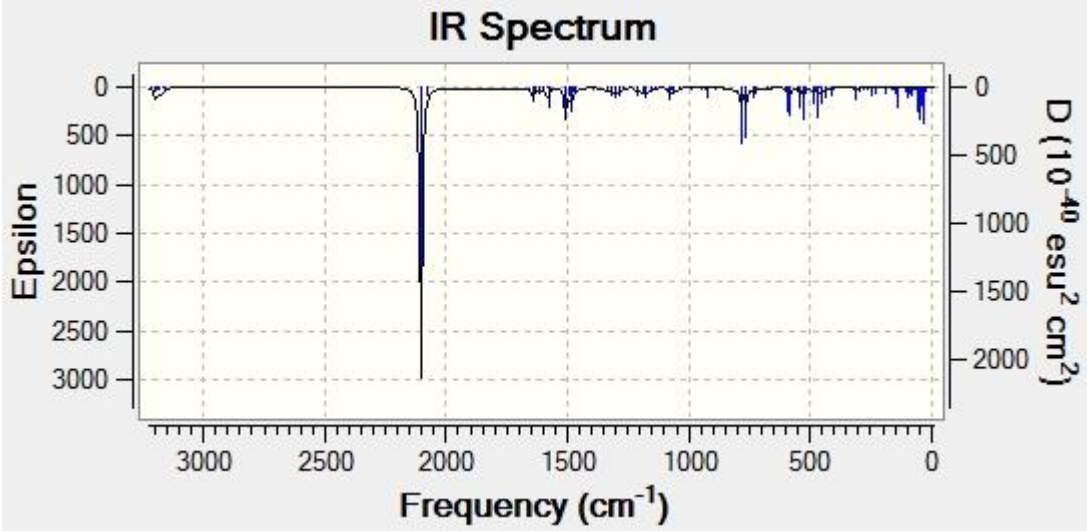

Figure B26 Calculated IR spectrum of **1**. (Scaling factor = 0.964)

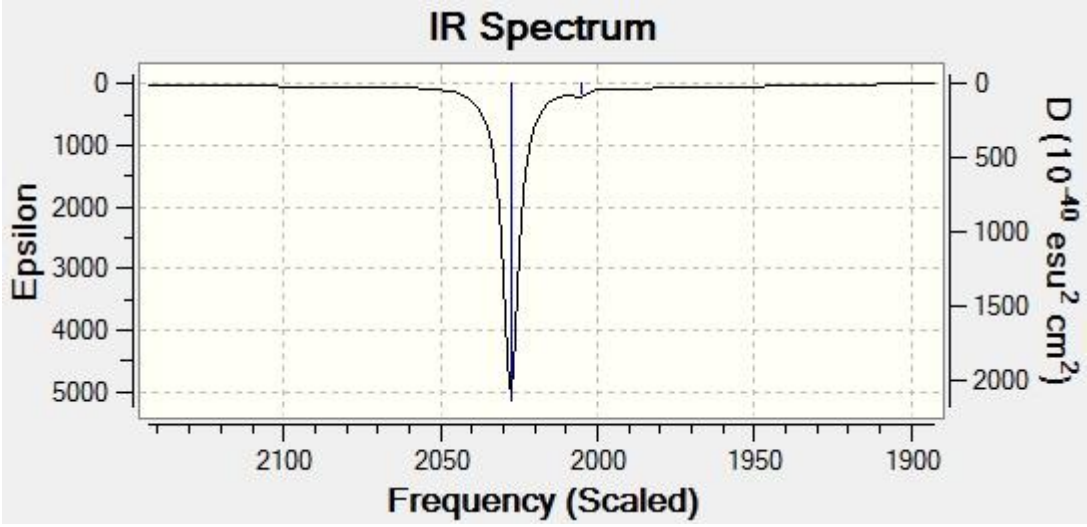

Figure B27 Carbonyl region of calculated IR spectrum of **1**. (Scaling factor = 0.964)

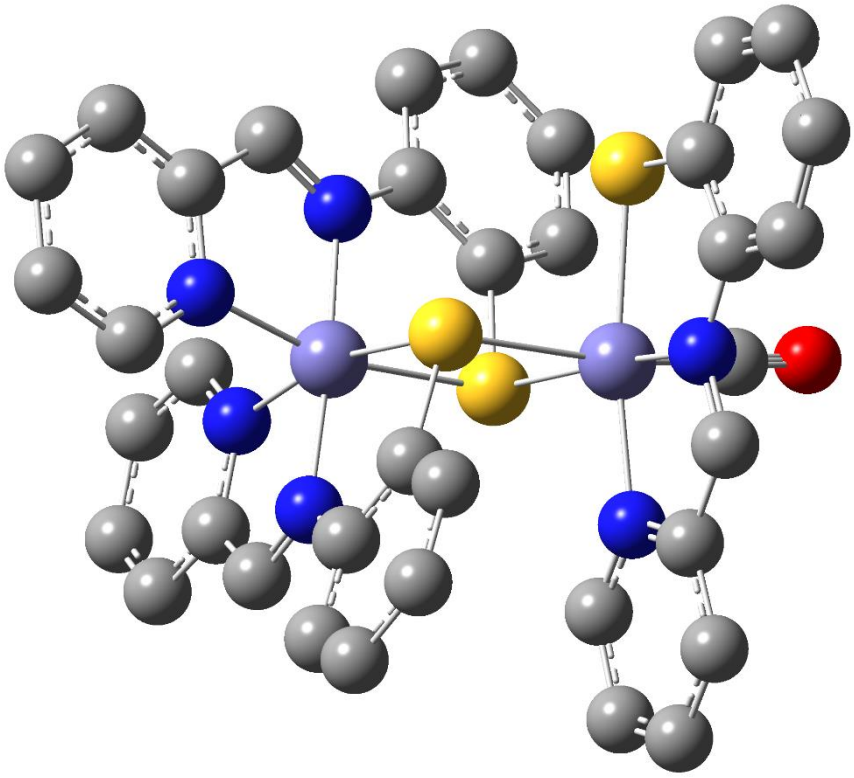

Figure B28 Calculated structure of **4**$^{+}$.

Table B4 Coordinates of the calculated structure **4$^+$.**

Tag	Symbol	X	Y	Z
1	C	2.8029	1.029331	2.914093
2	H	2.735672	2.025047	2.495695
3	C	3.226419	0.834886	4.225459
4	H	3.499434	1.689171	4.831244
5	C	3.284308	-0.45993	4.732985
6	H	3.603461	-0.6412	5.75197
7	C	2.924036	-1.51705	3.907327
8	H	2.952258	-2.54035	4.260774
9	C	2.514617	-1.24774	2.600689
10	C	2.14813	-2.27653	1.65047
11	H	2.199196	-3.32192	1.938458
12	C	1.513732	-2.75325	-0.60311
13	C	1.829133	-4.12083	-0.59418
14	H	2.291	-4.57467	0.273963
15	C	1.570751	-4.90359	-1.70786
16	H	1.818141	-5.95795	-1.69396
17	C	1.002795	-4.32939	-2.84858
18	H	0.804189	-4.9402	-3.72126
19	C	0.698722	-2.97428	-2.87267
20	H	0.264455	-2.52765	-3.75855
21	C	0.946123	-2.17337	-1.75453
22	C	4.307059	-0.66254	-1.09099
23	H	4.084611	-1.67807	-0.79189
24	C	5.452997	-0.37234	-1.82558
25	H	6.131691	-1.17151	-2.09388
26	C	5.700269	0.944282	-2.204
27	H	6.582211	1.198845	-2.77882
28	C	4.793092	1.926689	-1.82954
29	H	4.945537	2.963988	-2.10144
30	C	3.66597	1.562895	-1.09014
31	C	2.673359	2.509843	-0.63279
32	H	2.795442	3.565618	-0.85495
33	C	0.671515	2.835666	0.63448
34	C	0.730761	4.237871	0.697538
35	H	1.569189	4.775852	0.272187
36	C	-0.2719	4.952406	1.332774
37	H	-0.21357	6.03271	1.385855

38	C	-1.34292	4.273783	1.924017
39	H	-2.11844	4.830738	2.437134
40	C	-1.40561	2.88803	1.875547
41	H	-2.21965	2.358794	2.355714
42	C	-0.40735	2.146302	1.227952
43	C	-1.34324	2.278794	-2.45681
44	H	-0.42339	1.833372	-2.81534
45	C	-1.76761	3.521664	-2.9165
46	H	-1.16728	4.059339	-3.6388
47	C	-2.96815	4.042304	-2.44024
48	H	-3.32789	5.005184	-2.78239
49	C	-3.70338	3.300937	-1.52622
50	H	-4.64763	3.663954	-1.13966
51	C	-3.21888	2.057474	-1.10998
52	C	-3.93048	1.196389	-0.19295
53	H	-4.86517	1.535854	0.241095
54	C	-3.9757	-0.93174	0.904222
55	C	-5.187	-0.74166	1.60119
56	H	-5.73935	0.184543	1.500921
57	C	-5.68756	-1.73371	2.41719
58	H	-6.61907	-1.58214	2.948311
59	C	-4.98381	-2.94389	2.551633
60	H	-5.37795	-3.7267	3.189682
61	C	-3.79792	-3.14656	1.875111
62	H	-3.26196	-4.08246	1.977093
63	C	-3.26036	-2.14927	1.034734
64	C	-2.39134	-1.1163	-2.28796
65	N	2.450809	0.020563	2.109745
66	N	1.780871	-1.87819	0.474441
67	N	3.423827	0.273682	-0.72534
68	N	1.674327	2.032235	0.043871
69	N	-2.03906	1.558611	-1.57039
70	N	-3.41349	0.030645	0.055697
71	O	-2.8045	-1.64677	-3.20888
72	S	-1.7608	-2.42008	0.180928
73	S	-0.48278	0.371191	1.180499
74	S	0.53525	-0.43817	-1.74853
75	Fe	1.665544	0.074678	0.250488
76	Fe	-1.68661	-0.31266	-0.83808

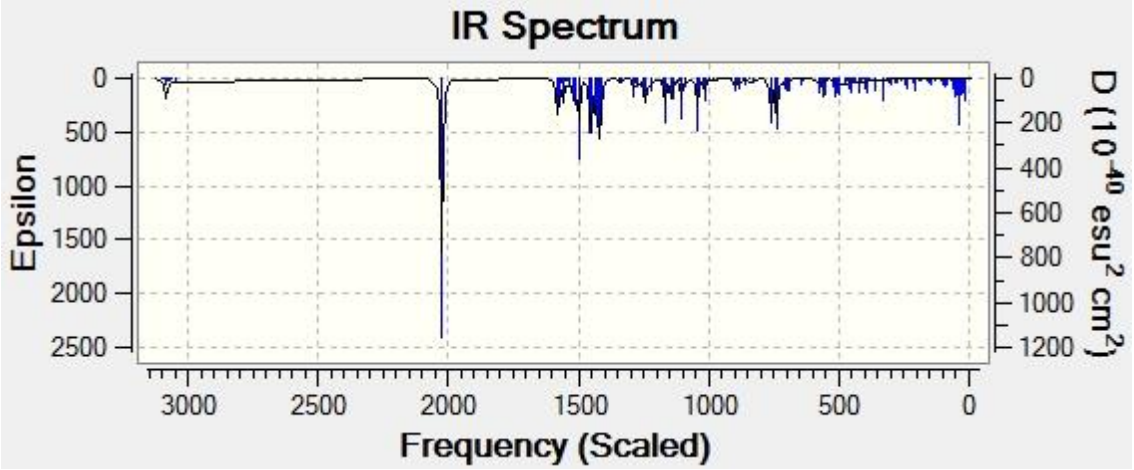

Figure B29 Calculated IR spectrum of $\mathbf{4}^{+}$. (Scaling factor = 0.964)

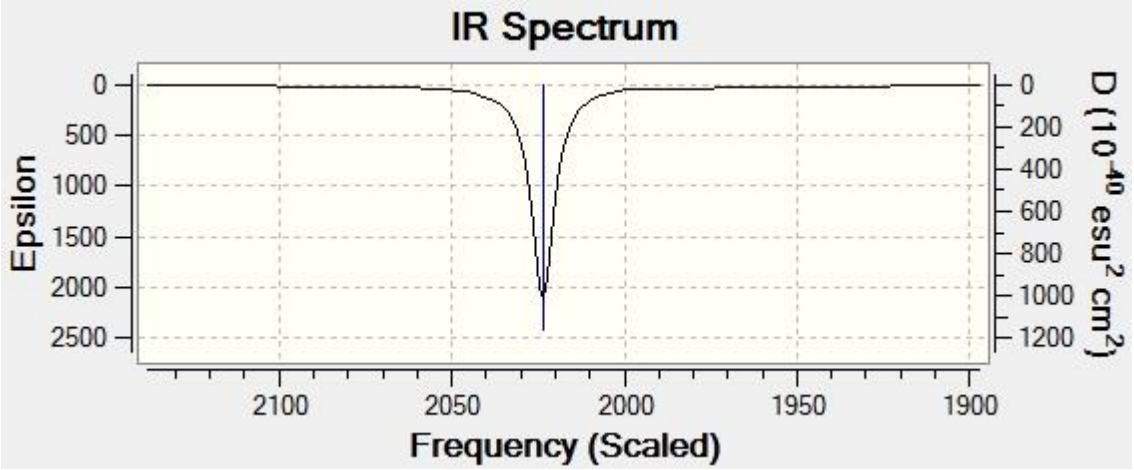

Figure B30 Carbonyl region of calculated IR spectrum of $\mathbf{4}^{+}$. (Scaling factor = 0.964)

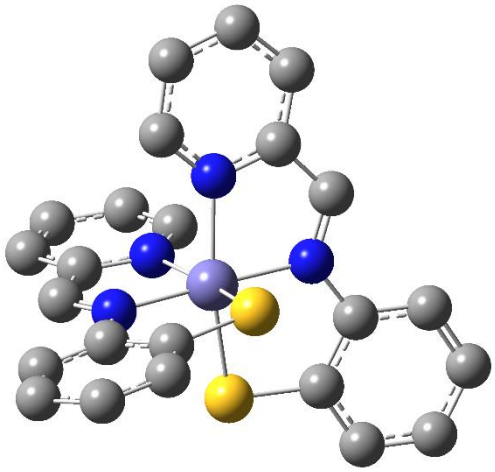

Figure B31 Calculated structure of $\mathbf{5}^{+}$.

Table B5 Coordinates of the calculated structure **5$^+$.**

Tag	Symbol	X	Y	Z
1	C	-1.40499	2.184043	1.578717
2	H	-2.24695	1.995827	0.924574
3	C	-1.47906	3.135198	2.591469
4	H	-2.3899	3.703025	2.728599
5	C	-0.37384	3.3278	3.416814
6	H	-0.40386	4.058624	4.215668
7	C	0.767437	2.56435	3.205819
8	H	1.644395	2.682392	3.830031
9	C	0.770772	1.624142	2.173394
10	C	1.894603	0.761098	1.876692
11	H	2.795691	0.824397	2.478197
12	C	2.725288	-0.99176	0.459412
13	C	3.974595	-1.17238	1.083145
14	H	4.241208	-0.60012	1.963196
15	C	4.869461	-2.09655	0.583005
16	H	5.827534	-2.23903	1.066816
17	C	4.530949	-2.85686	-0.54879
18	H	5.233844	-3.58472	-0.93665
19	C	3.30531	-2.6939	-1.16894
20	H	3.045464	-3.28938	-2.03557
21	C	2.377195	-1.76035	-0.67684
22	C	1.405094	2.183839	-1.57889
23	H	2.247078	1.995558	-0.92479
24	C	1.479171	3.134982	-2.59165
25	H	2.390048	3.702734	-2.72884
26	C	0.373905	3.327671	-3.41692
27	H	0.403935	4.058491	-4.21578
28	C	-0.76742	2.564312	-3.20585
29	H	-1.6444	2.682422	-3.83
30	C	-0.77076	1.624107	-2.17342
31	C	-1.89462	0.76113	-1.87666
32	H	-2.79575	0.824487	-2.47811
33	C	-2.7253	-0.99175	-0.45939
34	C	-3.97455	-1.17245	-1.0832
35	H	-4.2411	-0.6003	-1.96334
36	C	-4.86944	-2.09659	-0.58304
37	H	-5.82747	-2.23915	-1.06691

38	C	-4.53099	-2.8568	0.548846
39	H	-5.23389	-3.58463	0.936732
40	C	-3.30539	-2.69376	1.169064
41	H	-3.04559	-3.28917	2.035758
42	C	-2.37726	-1.76023	0.676942
43	N	-0.31177	1.446593	1.370639
44	N	1.7596	-0.07043	0.888614
45	N	0.311817	1.446479	-1.37073
46	N	-1.7596	-0.07043	-0.8886
47	S	0.819317	-1.54921	-1.45759
48	S	-0.81942	-1.54903	1.457749
49	Fe	-2E-06	-0.04196	0

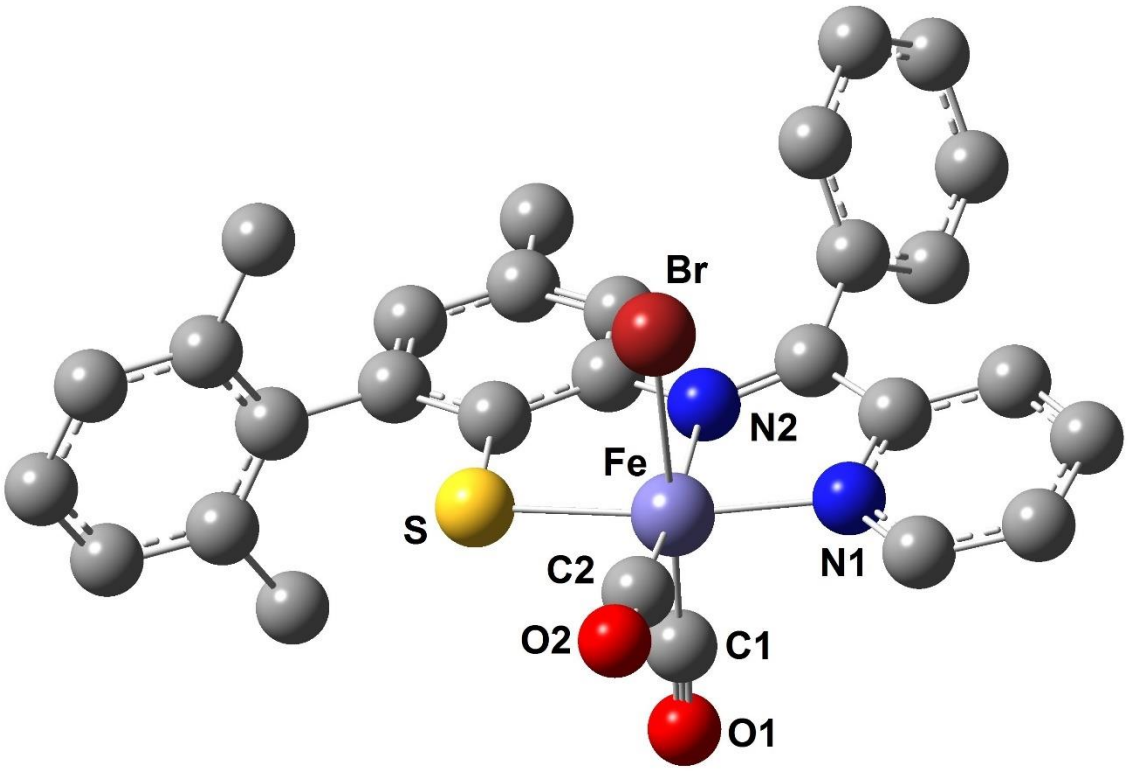

Figure B32 Calculated structure of **8**.

Table B6 Coordinates of the calculated structure **8.**

Tag	Symbol	X	Y	Z
1	C	-3.56562	-2.58027	0.69164
2	H	-3.14494	-3.57309	0.785503
3	C	-4.94188	-2.38733	0.681328
4	H	-5.60477	-3.23686	0.780164
5	C	-5.42758	-1.094	0.524441
6	H	-6.49392	-0.90391	0.495495
7	C	-4.52844	-0.04397	0.396293
8	H	-4.87681	0.96932	0.259251
9	C	-3.15437	-0.30549	0.432157
10	C	-2.1215	0.733223	0.312535
11	C	-2.57048	2.113623	-0.03378
12	C	0.290343	1.089149	0.412058
13	C	0.316379	2.487904	0.611408
14	H	-0.60044	3.022436	0.797862
15	C	1.499766	3.200225	0.595121
16	C	1.524701	4.69211	0.82225
17	C	2.695506	2.496051	0.358845
18	C	2.726623	1.121678	0.197219
19	H	3.63382	3.041486	0.31712
20	C	1.514556	0.382574	0.259141
21	C	-0.52422	-3.46568	0.070312
22	N	-2.69574	-1.57481	0.570351
23	N	-0.88553	0.314135	0.413272
24	O	-0.39333	-4.57732	-0.13527
25	S	1.574407	-1.35825	0.166957
26	Fe	-0.70073	-1.68013	0.387736
27	Br	-1.05746	-1.61176	-2.11409
28	C	6.514523	-0.78333	-0.46075
29	C	6.07547	-0.53778	0.834967
30	H	6.693555	-0.82438	1.67952
31	C	4.840211	0.070999	1.070109
32	C	4.04009	0.435148	-0.02978
33	C	4.377286	0.311408	2.488338
34	C	4.475231	0.186269	-1.34622
35	C	5.717364	-0.42306	-1.54084
36	C	-0.38456	-1.78862	2.159962
37	O	-0.1745	-1.85405	3.278122

38	H	7.475234	-1.25807	-0.62857
39	C	3.620683	0.553581	-2.53654
40	H	3.385209	1.621755	-2.55054
41	H	4.133141	0.308505	-3.46865
42	H	2.669246	0.013895	-2.52313
43	H	3.411111	-0.16624	2.674364
44	H	5.097172	-0.09297	3.202483
45	H	4.255007	1.377586	2.701153
46	H	0.517921	5.089945	0.96316
47	H	2.115003	4.9502	1.707495
48	H	1.97458	5.21462	-0.02797
49	C	-3.20472	2.941682	0.899296
50	H	6.056703	-0.61864	-2.55267
51	C	-3.63919	4.212177	0.527173
52	C	-3.45596	4.657648	-0.7807
53	C	-2.83973	3.828542	-1.71695
54	C	-2.39875	2.560724	-1.34908
55	H	-3.79523	5.645753	-1.06979
56	H	-4.11959	4.852352	1.258369
57	H	-2.70214	4.168378	-2.73698
58	H	-1.91863	1.909555	-2.07079
59	H	-3.3405	2.599868	1.919806

B.5 Stability Study

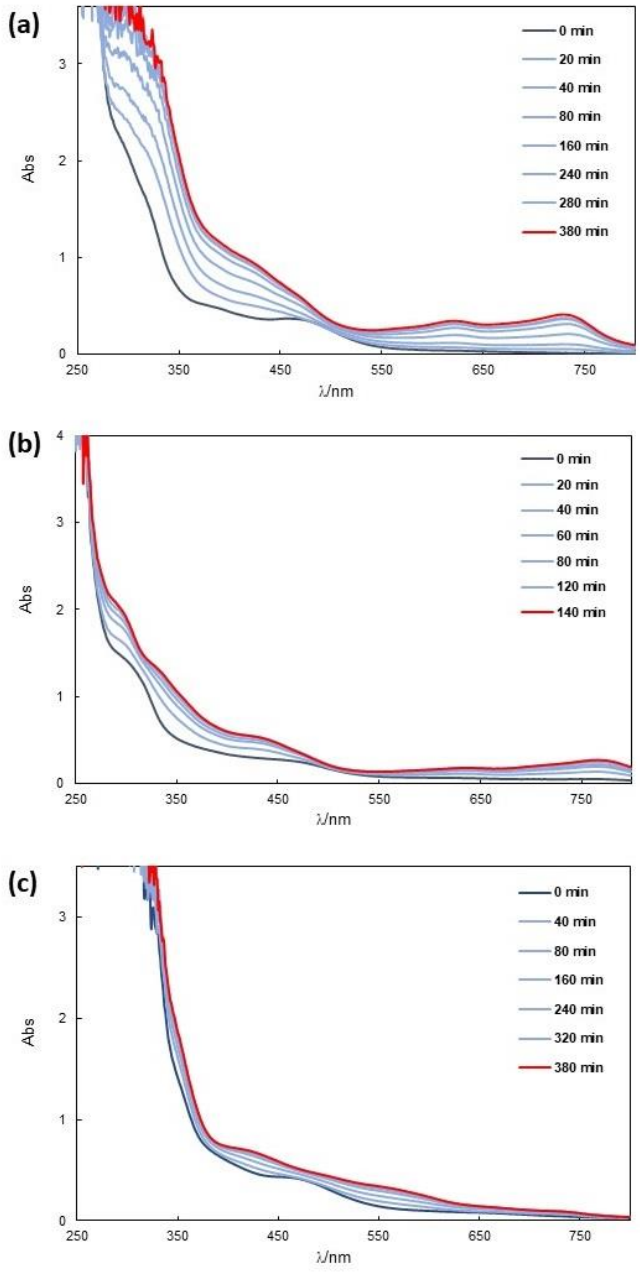

Figure B33 Changes in the UV/vis absorption spectra of **1** (a), **2** (b) and **3** (c) during conversion to the corresponding Fe(II) monocarbonyl, **4**, **6** and **7**, respectively, by dissociation of the CO ligand. *Conditions:* MeCN, 298 K, dark.

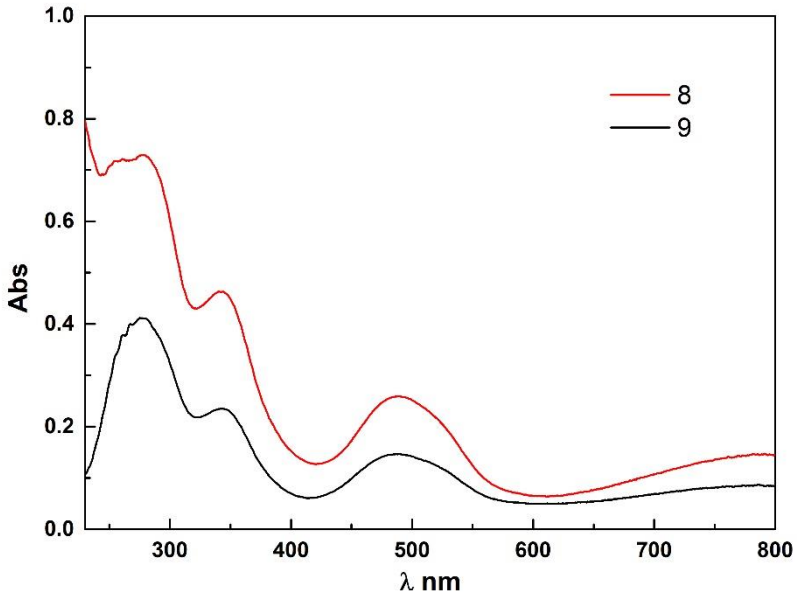

Figure B34 Comparison of UV/vis spectra of **8** and **9**. *Conditions:* THF, 298 K, dark.

APPENDIX C: SUPPORTING INFORMATION FOR CHAPTER 4

C.1 Spectroscopic Characterization of Synthons and Complexes

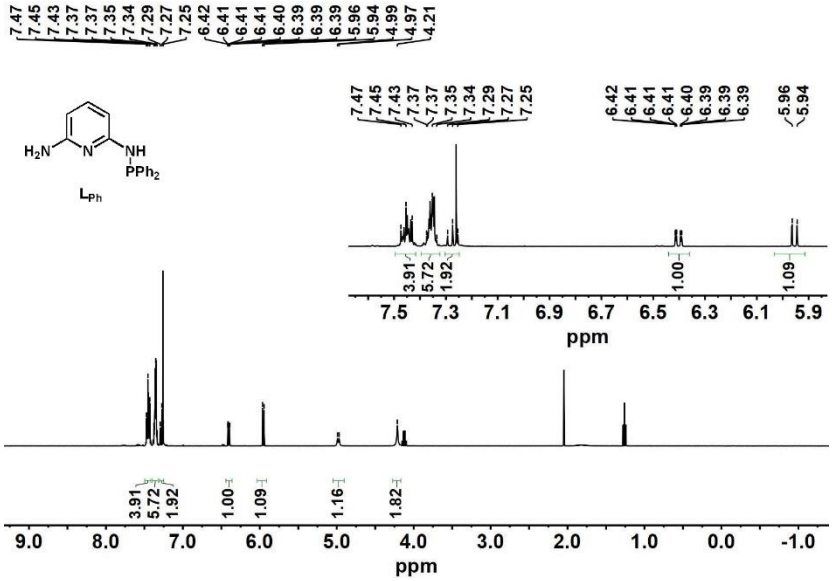

Figure C1 ^{1}H NMR spectrum of **L_{Ph}** (400 MHz, $CDCl_3$)

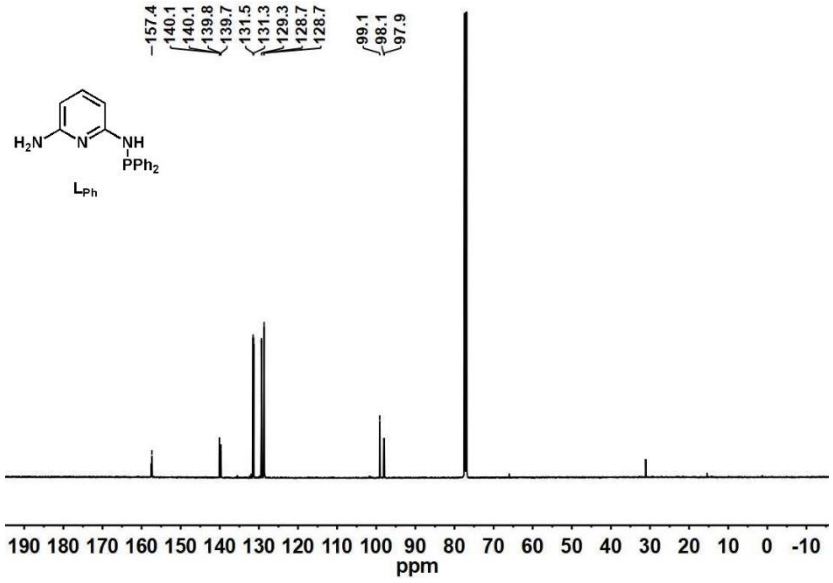

Figure C2 ^{13}C NMR spectrum of **L_{Ph}** (126 MHz, $CDCl_3$)

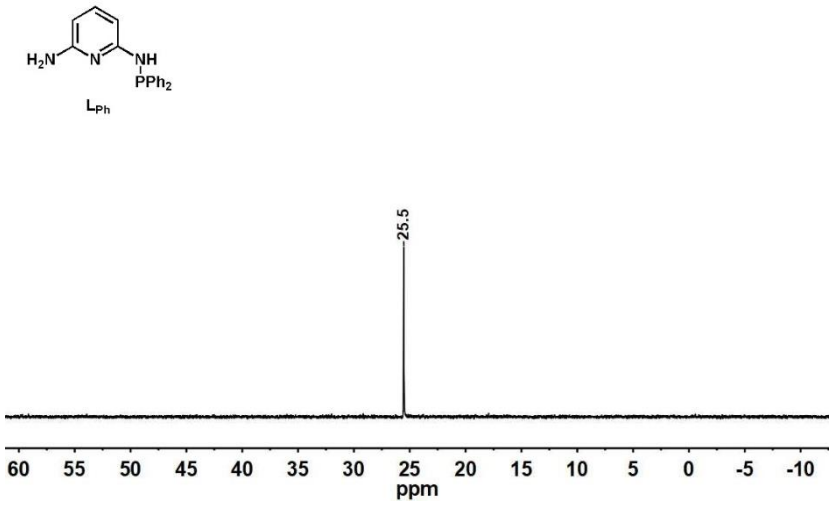

Figure C3 ^{31}P NMR spectrum of **L_{Ph}** (202 MHz, $CDCl_3$)

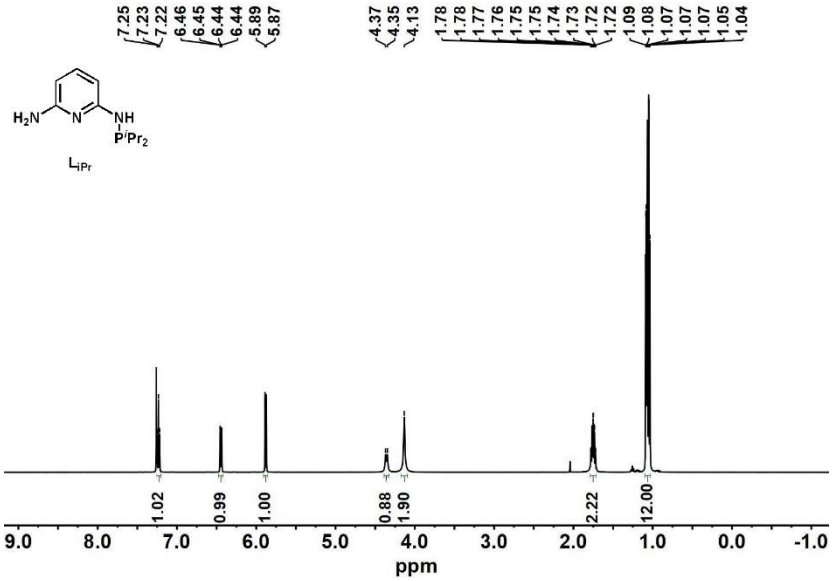

Figure C4 ^{1}H NMR spectrum of **L_{iPr}** (400 MHz, $CDCl_3$)

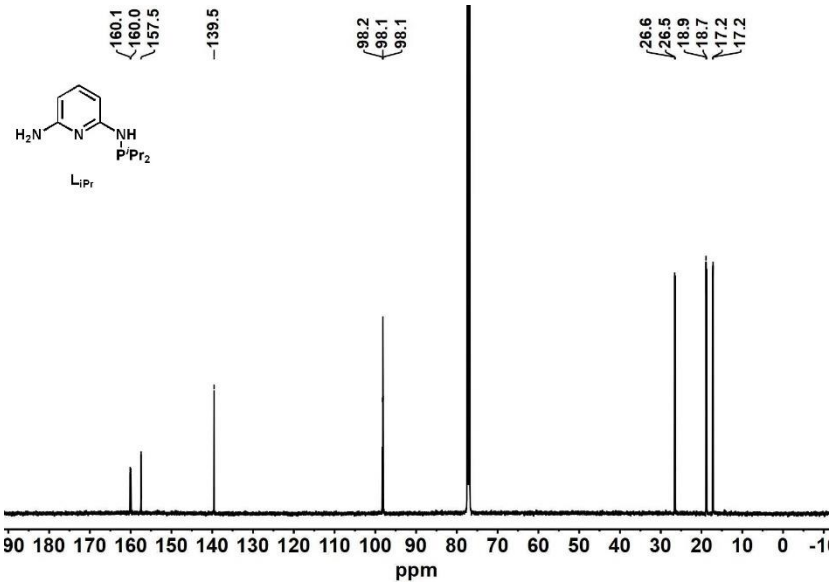

Figure C5 ^{13}C NMR spectrum of **L$_{iPr}$** (126 MHz, $CDCl_3$)

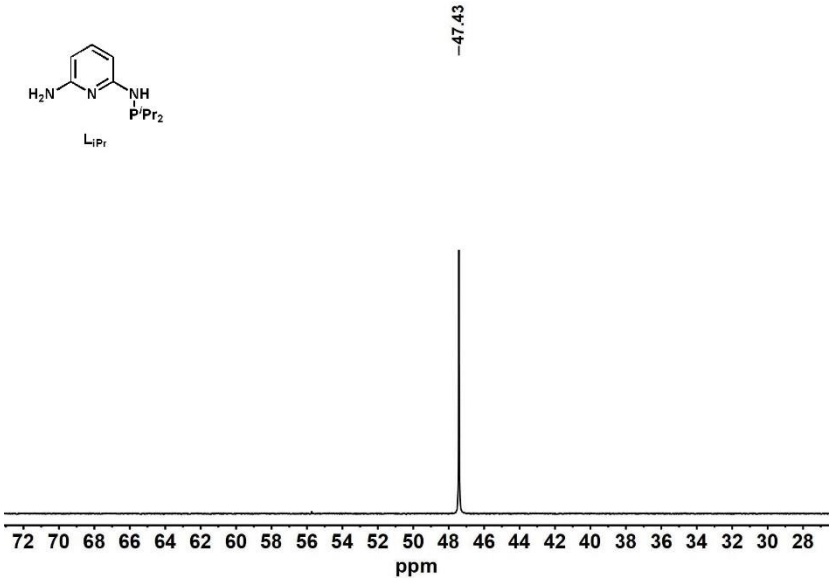

Figure C6 ^{31}P NMR spectrum of **L$_{iPr}$** (202 MHz, $CDCl_3$)

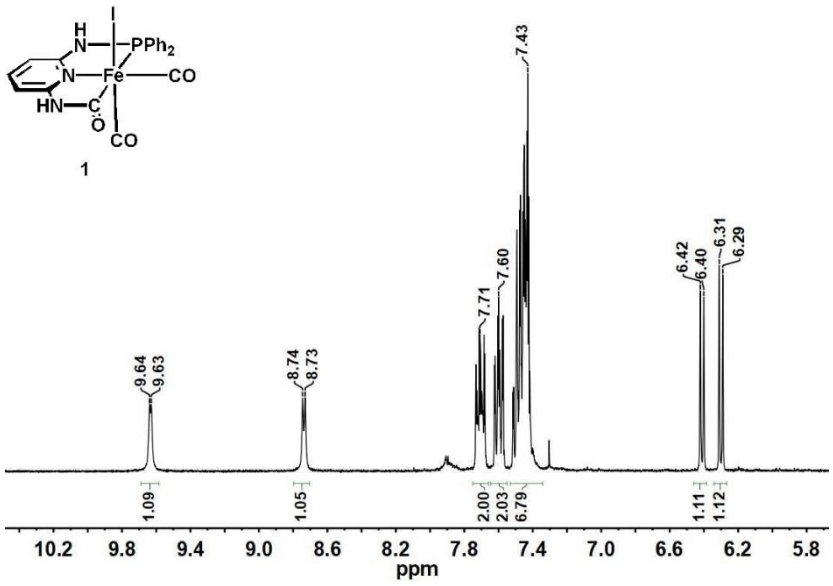

Figure C7 ^{1}H NMR spectrum of **1** (400 MHz, THF-d_8)

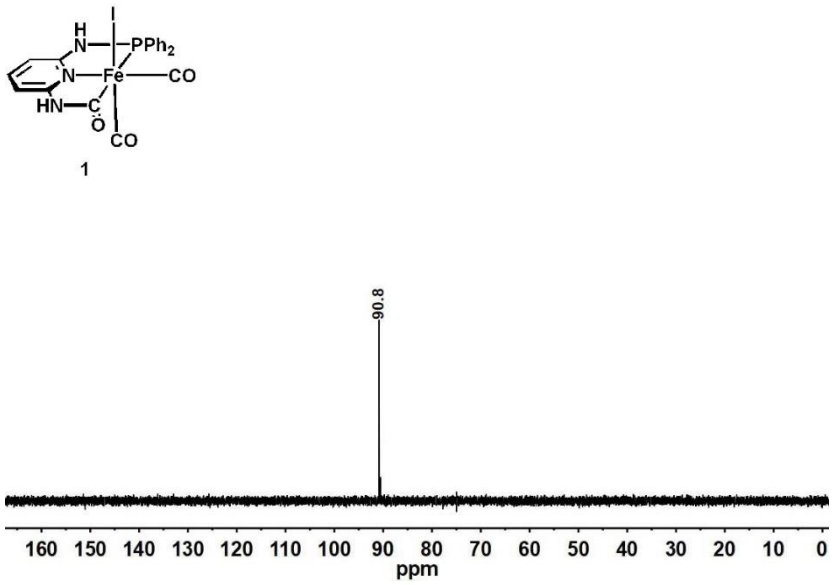

Figure C8 ^{31}P NMR spectrum of **1** (162 MHz, THF-d_8)

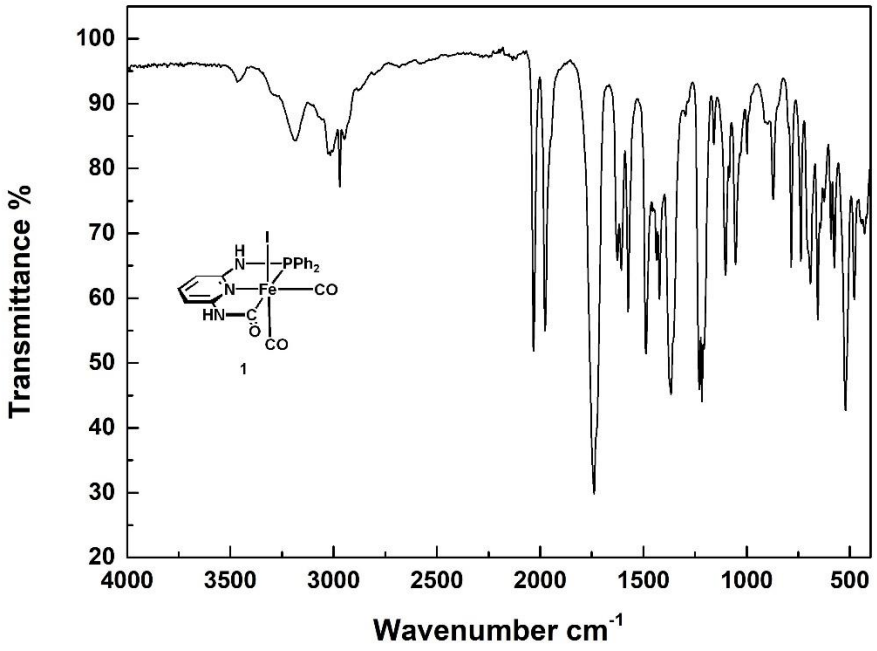

Figure C9 IR spectrum of **1** (neat)

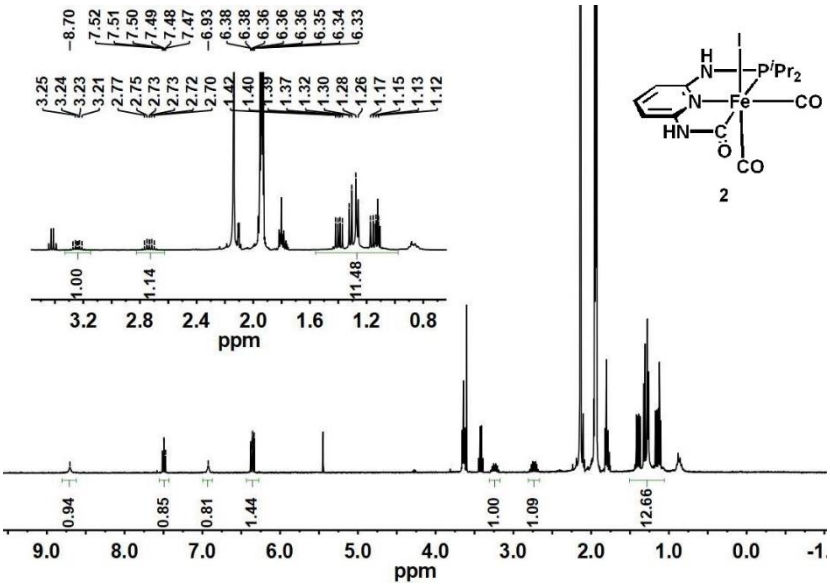

Figure C10 ^{1}H NMR spectrum of **2** (400 MHz, CD_3CN)

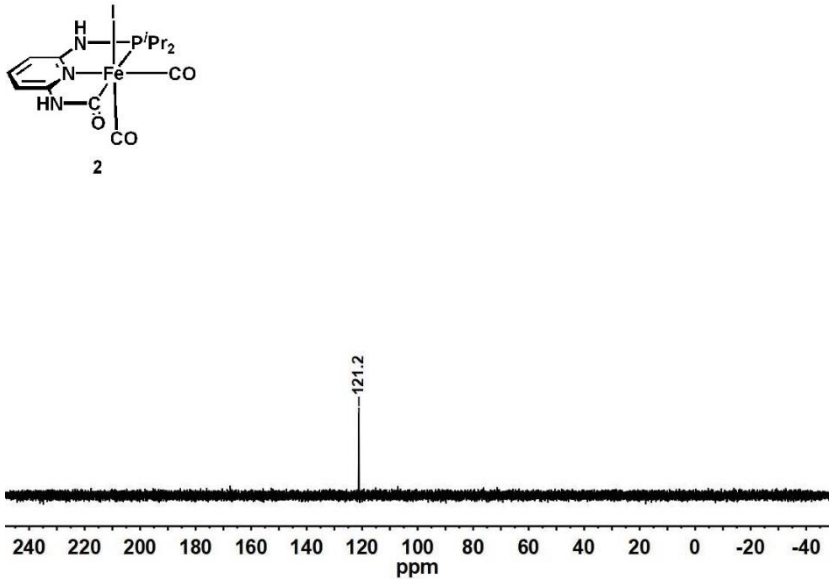

Figure C11 ^{31}P NMR spectrum of **2** (162 MHz, CD_3CN)

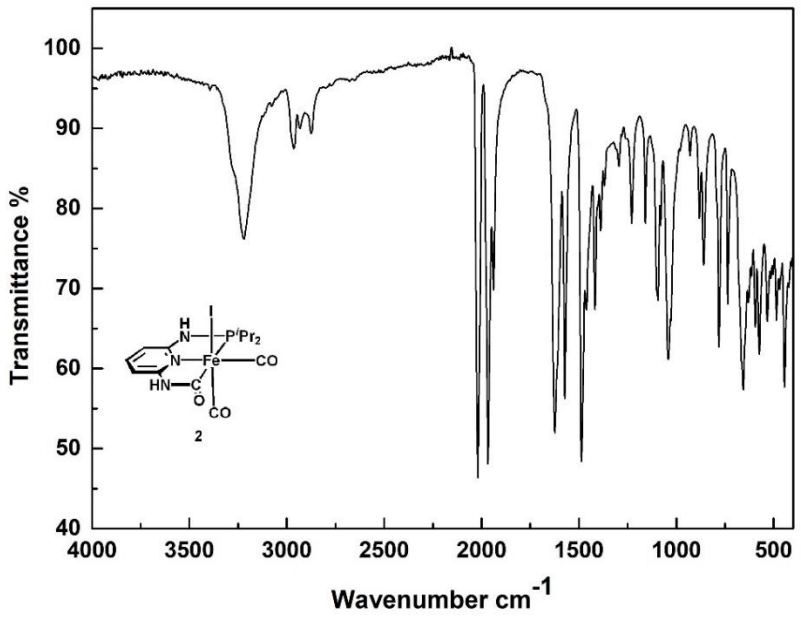

Figure C12 IR spectrum of **2** (neat)

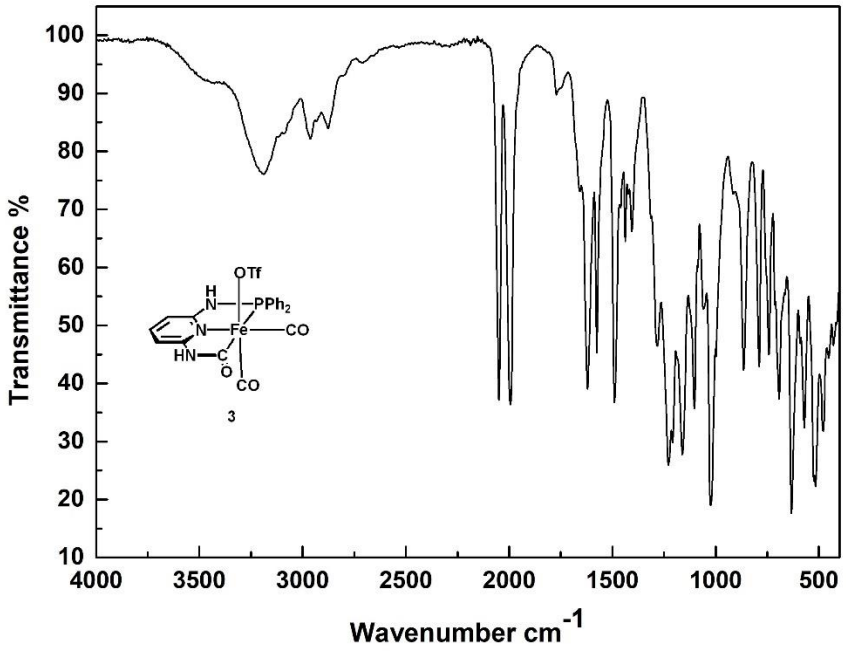

Figure C13 IR spectrum of **3** (neat)

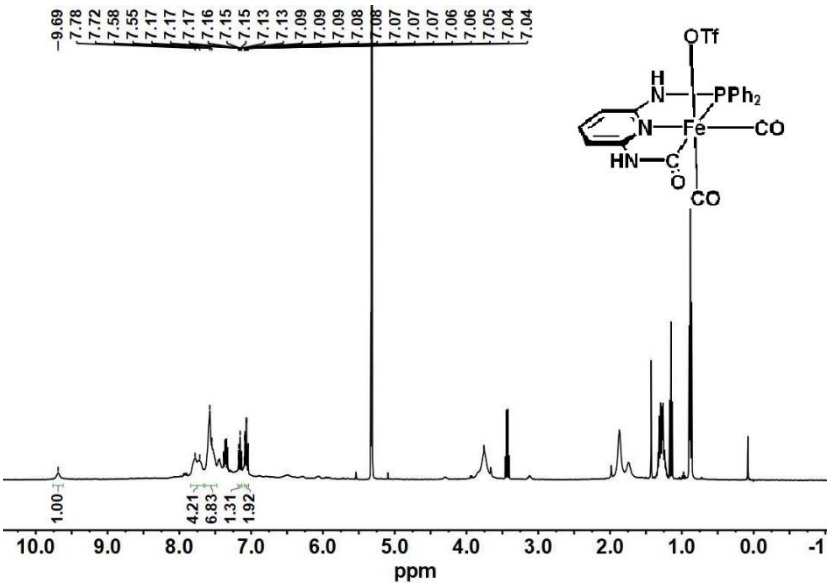

Figure C14 ^{1}H NMR spectrum of **3** (400 MHz, DCM-d_2)

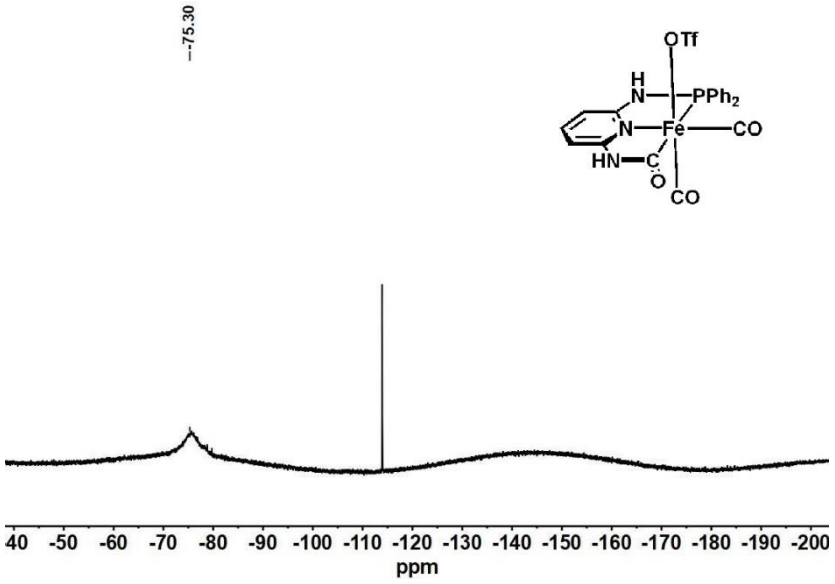

Figure C15 ^{19}F NMR spectrum of **3** (376 MHz, DCM-d_2)

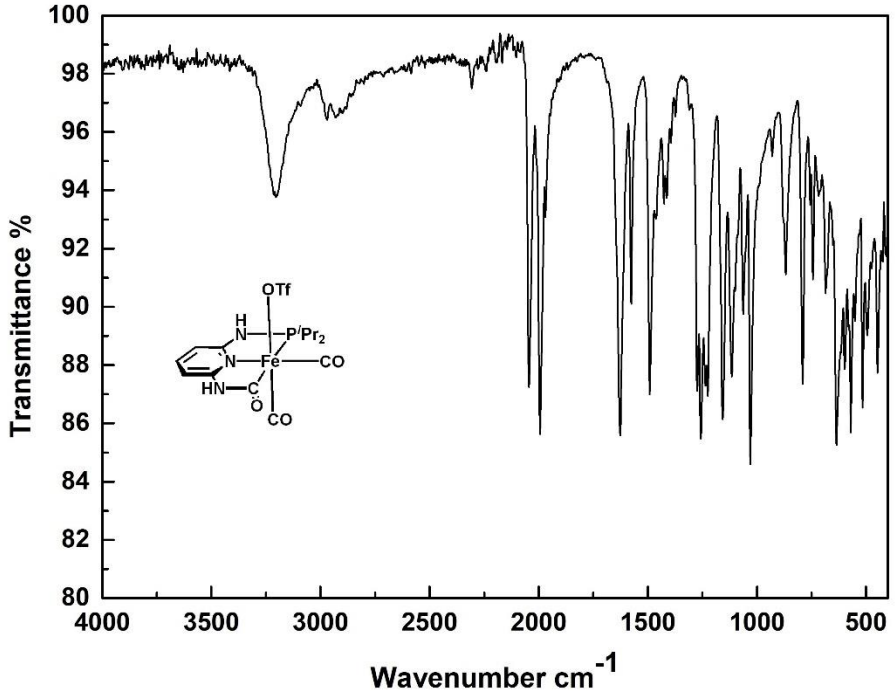

Figure C16 IR spectrum of **4** (neat)

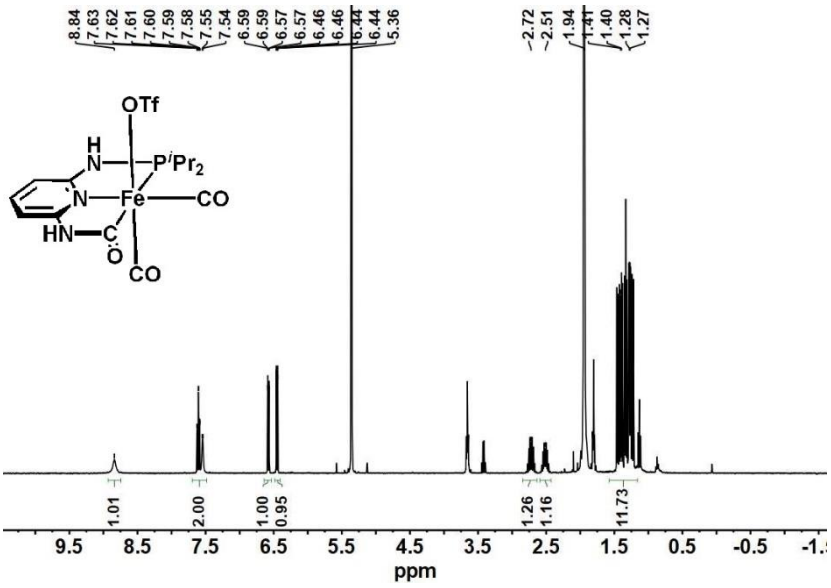

Figure C17 ^{1}H NMR spectrum of **4** (400 MHz, DCM-d_2)

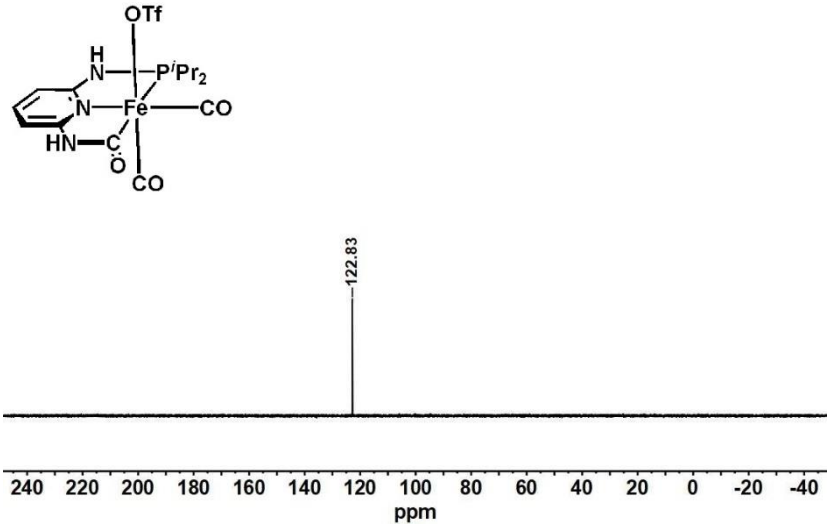

Figure C18 ^{31}P NMR spectrum of **4** (376 MHz, DCM-d_2)

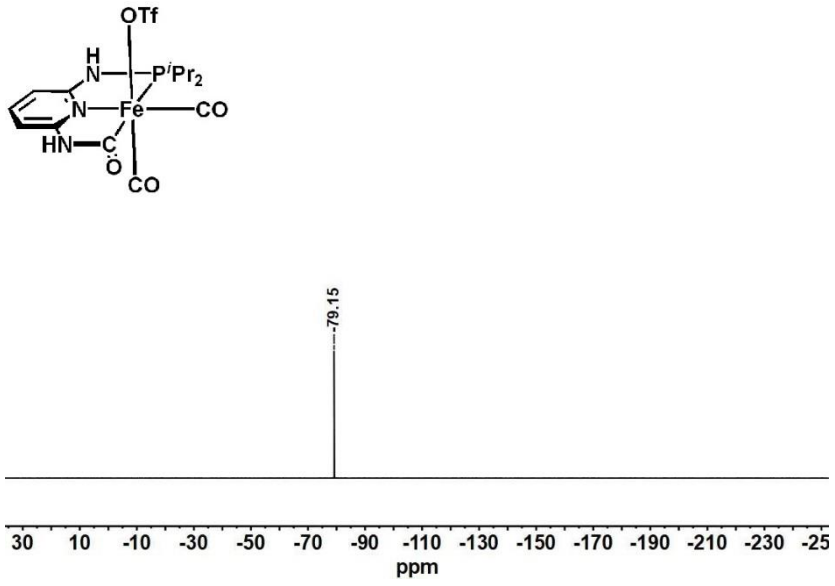

Figure C19 ^{19}F NMR spectrum of **4** (376 MHz, DCM-d_2)

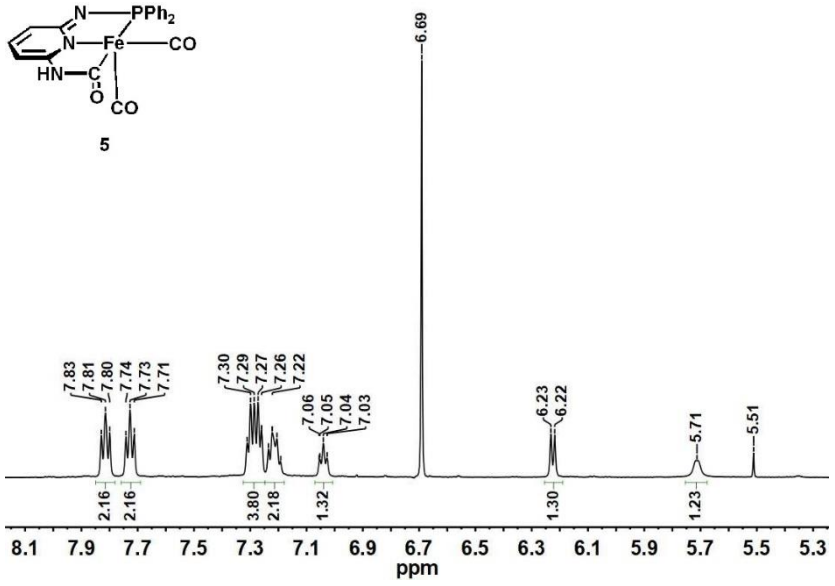

Figure C20 ^{1}H NMR spectrum of **5** (600 MHz, THF)

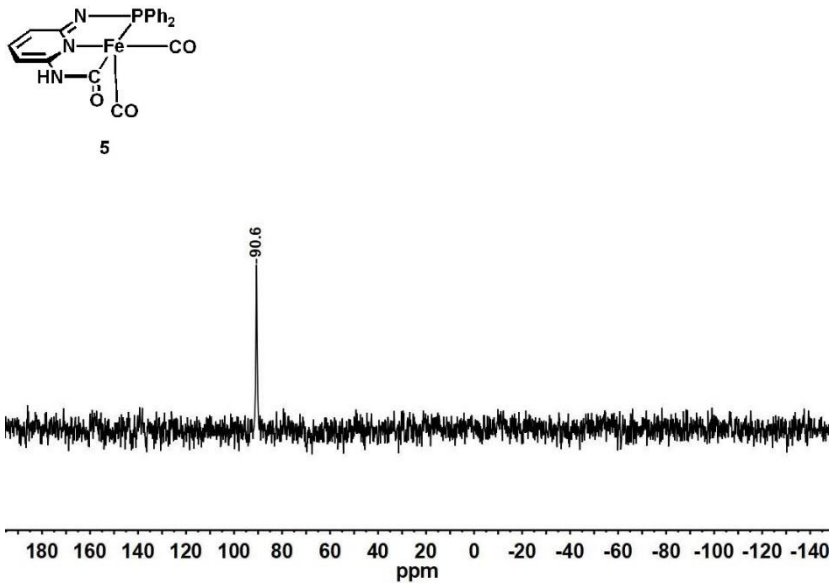

Figure C21 ^{31}P NMR spectrum of **5** (243 MHz, THF)

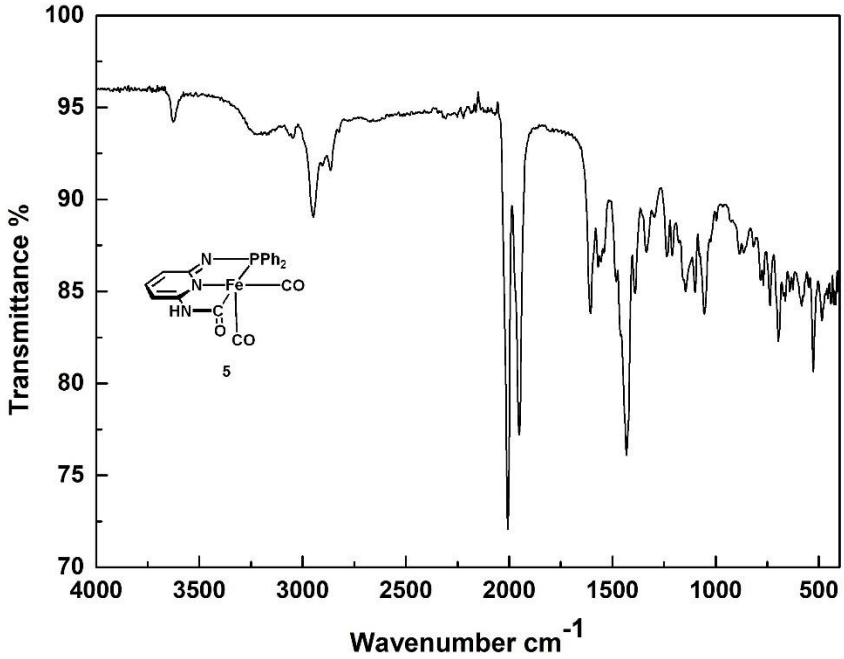

Figure C22 IR spectrum of **5** (neat)

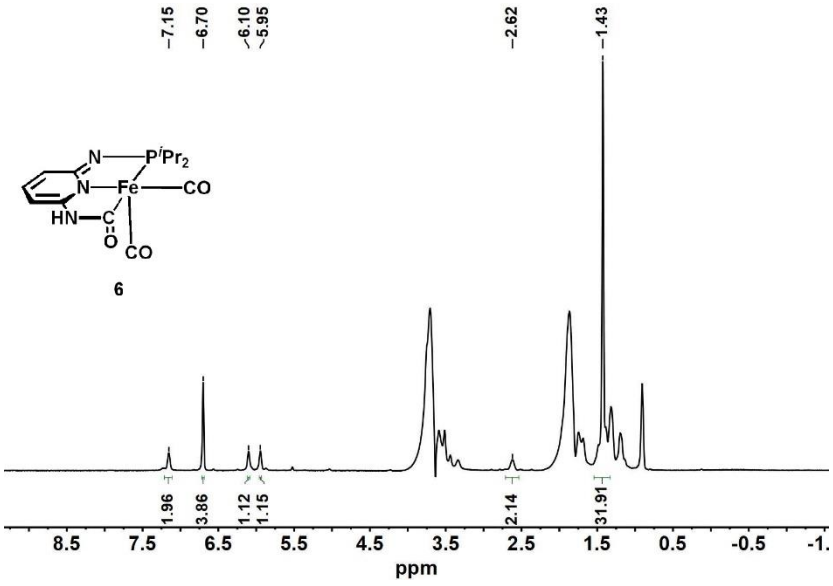

Figure C23 ^{1}H NMR spectrum of **6** (600 MHz, THF)

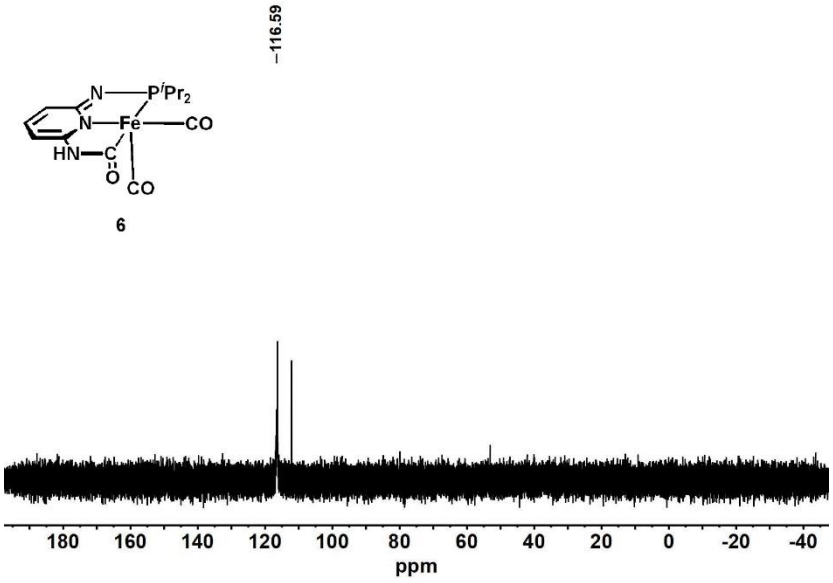

Figure C24 ^{31}P NMR spectrum of **6** (243 MHz, THF)

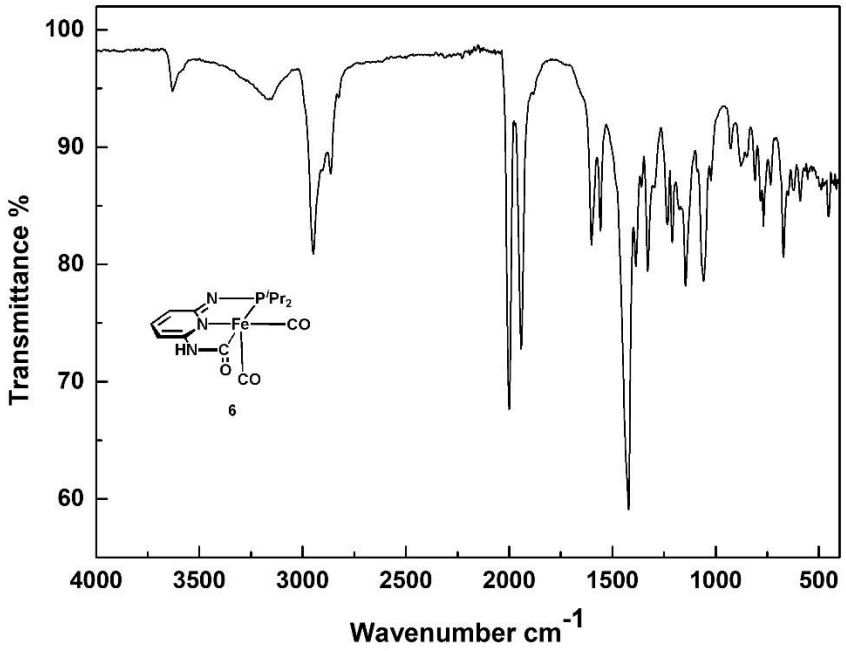

Figure C25 IR spectrum of **6** (neat)

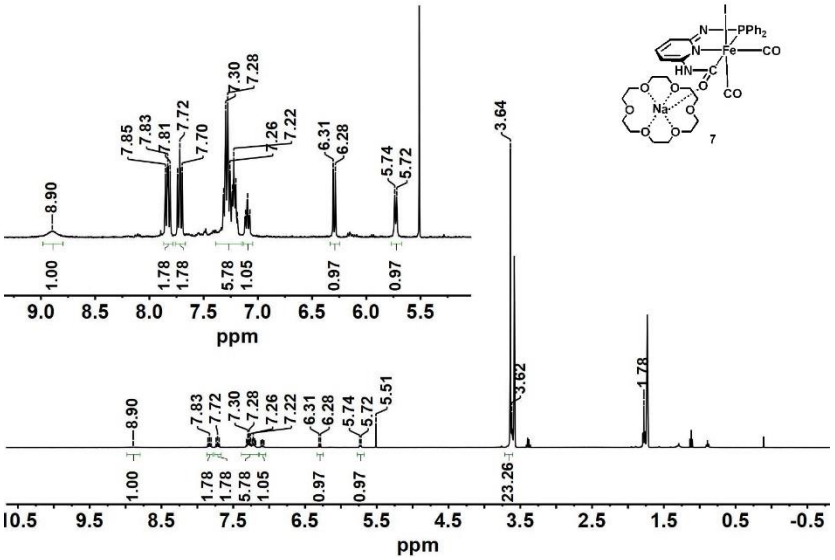

Figure C26 ^{1}H NMR spectrum of **7** (400 MHz, THF-d_8)

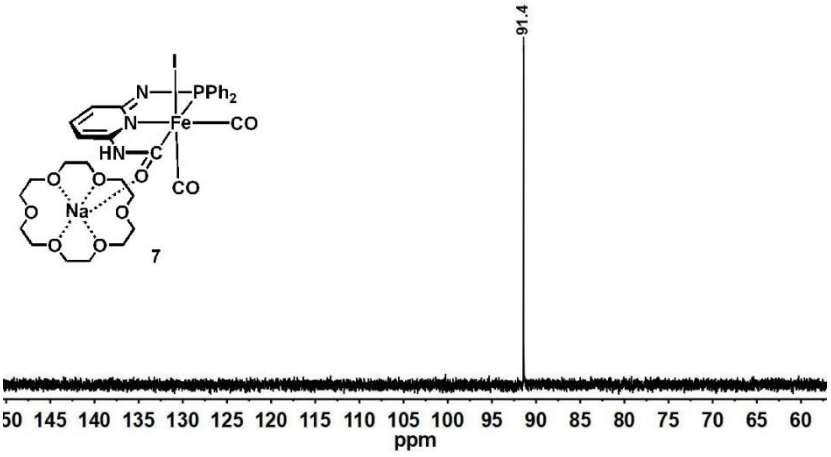

Figure C27 ^{31}P NMR spectrum of **7** (162 MHz, THF-d_8)

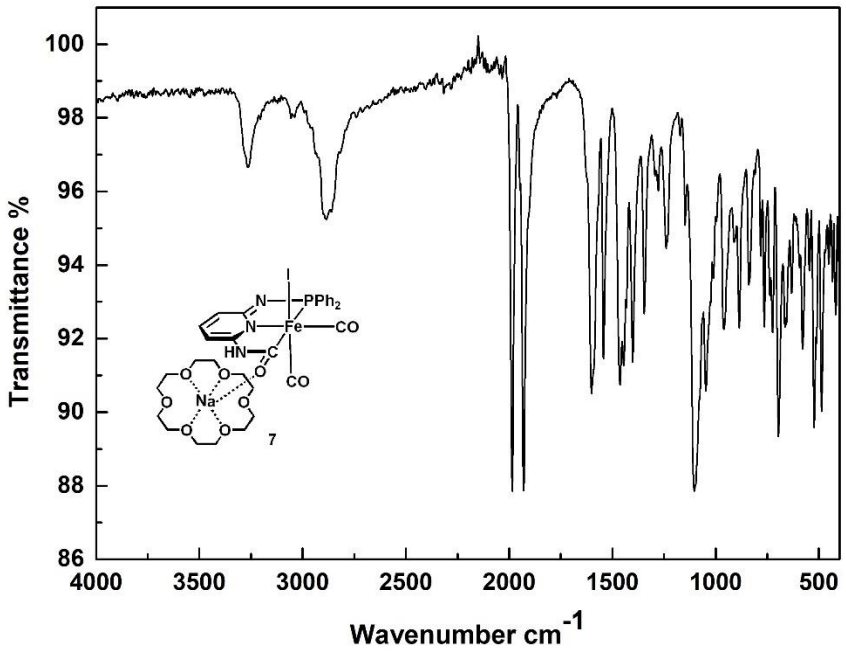

Figure C28 IR spectrum of **7** (neat)

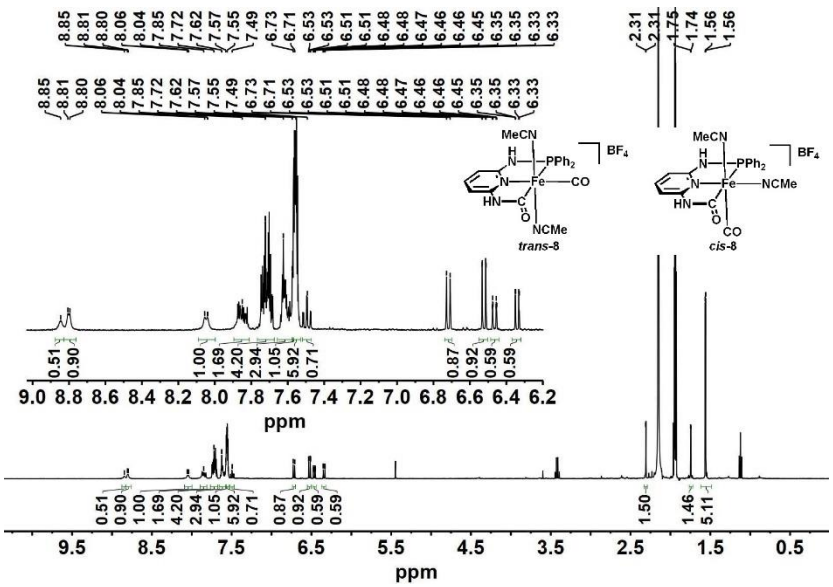

Figure C29 ^{1}H NMR spectrum of **8** (400 MHz, CD_3CN)

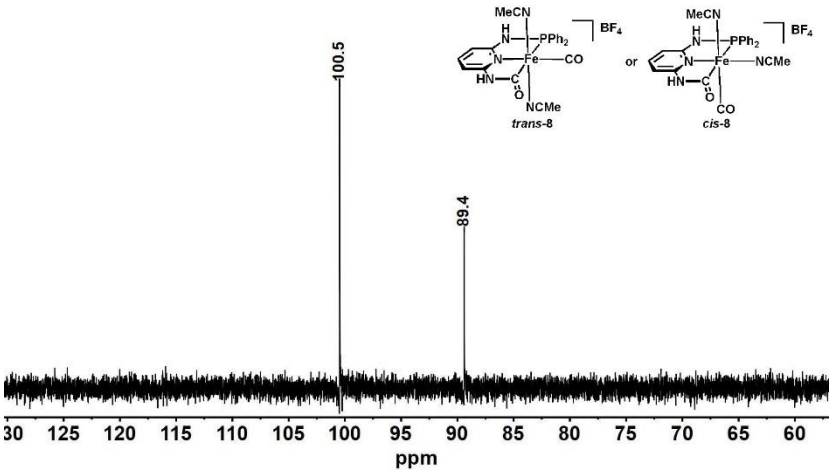

Figure C30 ^{31}P NMR spectrum of **8** (162 MHz, CD_3CN)

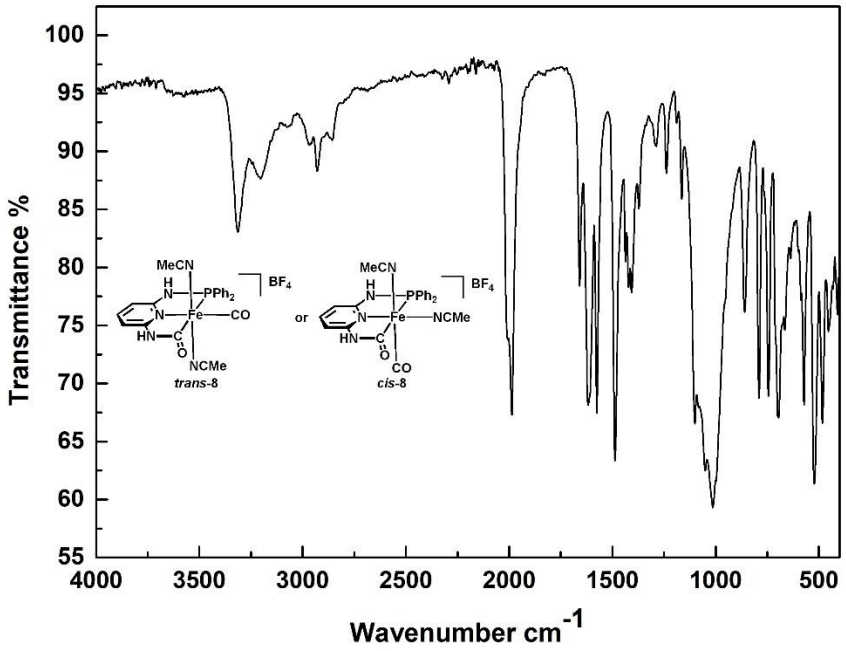

Figure C31 IR spectrum of **8** (neat)

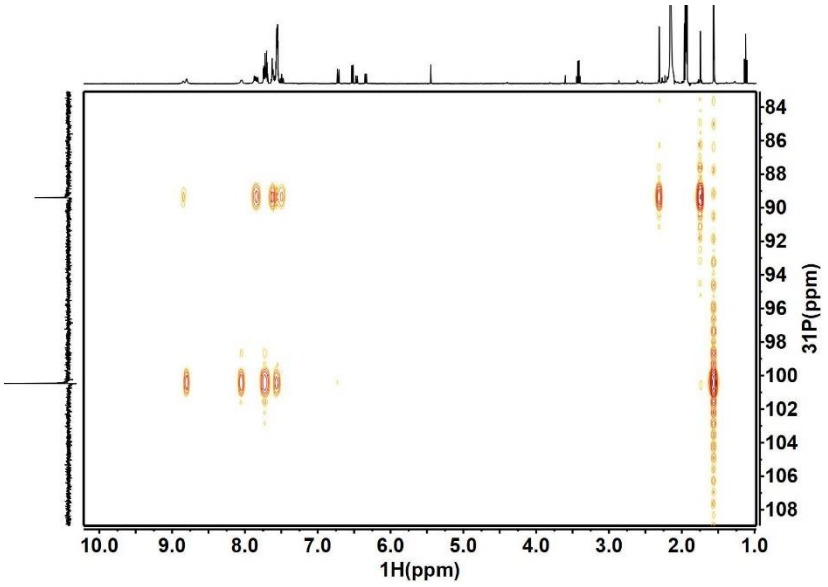

Figure C32 ^{1}H-^{31}P HMBC spectrum of ***cis*-8** and ***trans*-8** mixture (CD_3CN)

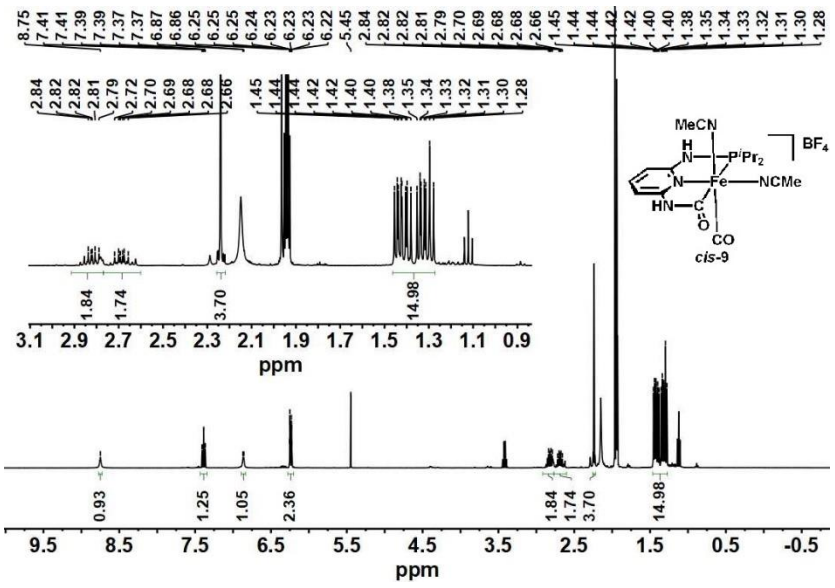

Figure C33 ^{1}H NMR spectrum of ***cis*-9** (400 MHz, CD_3CN)

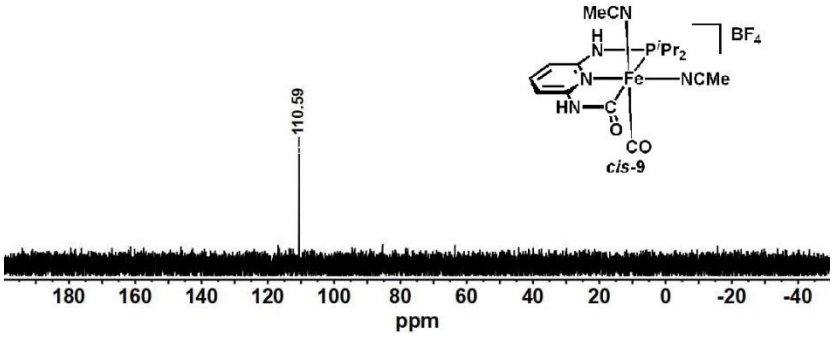

Figure C34 ^{31}P NMR spectrum of ***cis*-9** (162 MHz, CD_3CN)

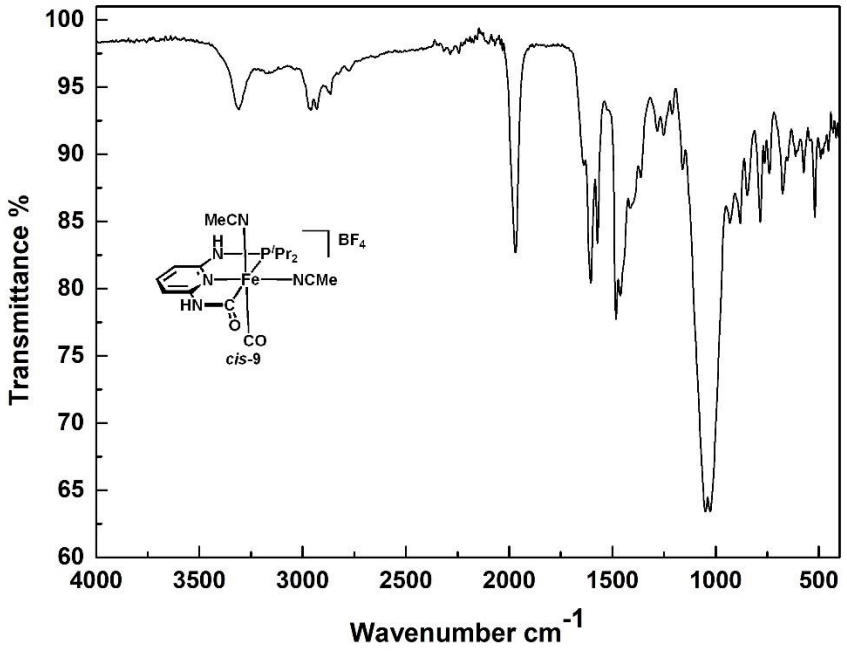

Figure C35 IR spectrum of ***cis*-9** (neat)

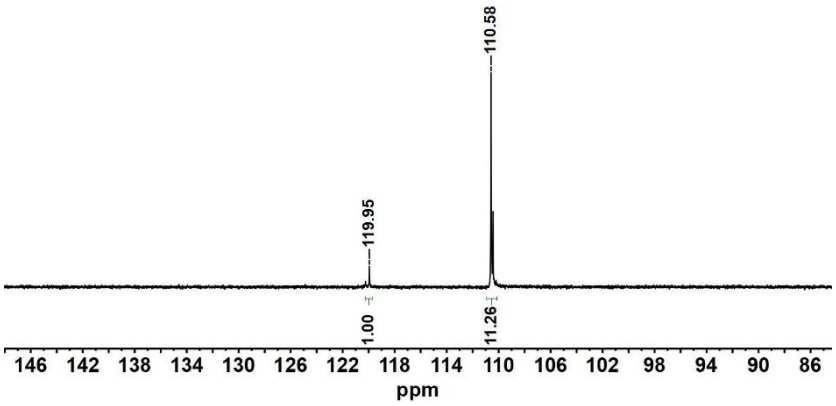

Figure C36 ^{31}P NMR spectrum of **9** (crude material, 162 MHz, CD_3CN)

C.2 X-ray Crystallography

Table C1 Crystal data and refinement parameters for CNP complexes.

Cmpd	**3**	**4-H_2O**	**7**	**8**	***cis*-9**
CCDC number					
Formula	$C_{25}H_{23}F_3FeN_3O_7PS$	$C_{15}H_{21}FeF_3N_3O_7PS$	$C_{24}H_{30.67}Fe_{0.67}I_{0.67}N_2Na_{0.67}O_{6.67}P_{0.67}$	$C_{8.73}H_{8.18}B_{0.36}F_{1.45}Fe_{0.36}N_2O_{0.73}P_{0.36}$	$C_{15.2}H_{20.8}B_{0.8}F_{3.2}Fe_{0.8}N_{4.8}O_{1.6}P_{0.8}$
FW	653.34	531.23	611.64	215.86	435.27
T (K)	100(2)	100(2)	100(2)	100(2)	100(2)
size (mm^3)	0.23 × 0.15 × 0.12	0.16 × 0.12 × 0.08	0.34 × 0.27 × 0.23	0.30 × 0.12 × 0.11	0.34 × 0.25 × 0.20
System	Triclinic	Monoclinic	Monoclinic	Triclinic	Monoclinic
space group	*P-1*	*P c*	*P 2₁/n*	*P-1*	*P 2₁/n*
Z	2	2	6	11	5
l (Å)	1.54184	1.54184	1.54184	1.54184	1.54184
a (Å)	8.5097(6)	8.5871(5)	10.17330(10)	8.5363(4)	8.48160(10)
b (Å)	12.0567(8)	11.5344(8)	21.21230(10)	16.4814(6)	22.4745(3)
c (Å)	15.7457(11)	15.0030(13)	18.73680(10)	22.2864(13)	13.8099(2)
α (°)	67.635(6)	90	90	98.533(4)	90
β (°)	74.850(6)	102.687(7)	97.5690(10)	100.411(4)	106.1410(10)
γ (°)	69.913(6)	90	90	90.030(3)	90
V ($Å^3$)	1387.13(19)	1449.72(19)	4008.15(5)	3048.5(3)	2528.67(6)
d_{calc} (Mg/cm^3)	1.392	1.192	1.520	1.293	1.429
m (mm^{-1})	6.140	5.112	10.034	4.939	5.898
R(int)	0.0420	0.0720	0.0746	0.0819	0.0370
GOF on F^2	0.992	0.990	1.205	0.969	1.051
*R*1/w*R*2 [$I>2\sigma(I)$]	0.0713 0.1834	0.0765 0.2017	0.0874 0.2179	0.0564 0.1340	0.0404 0.1114
*R*1/w*R*2 (all data)	0.0968 0.2055	0.0968 0.2268	0.0877 0.2181	0.0823 0.1489	0.0415 0.1126

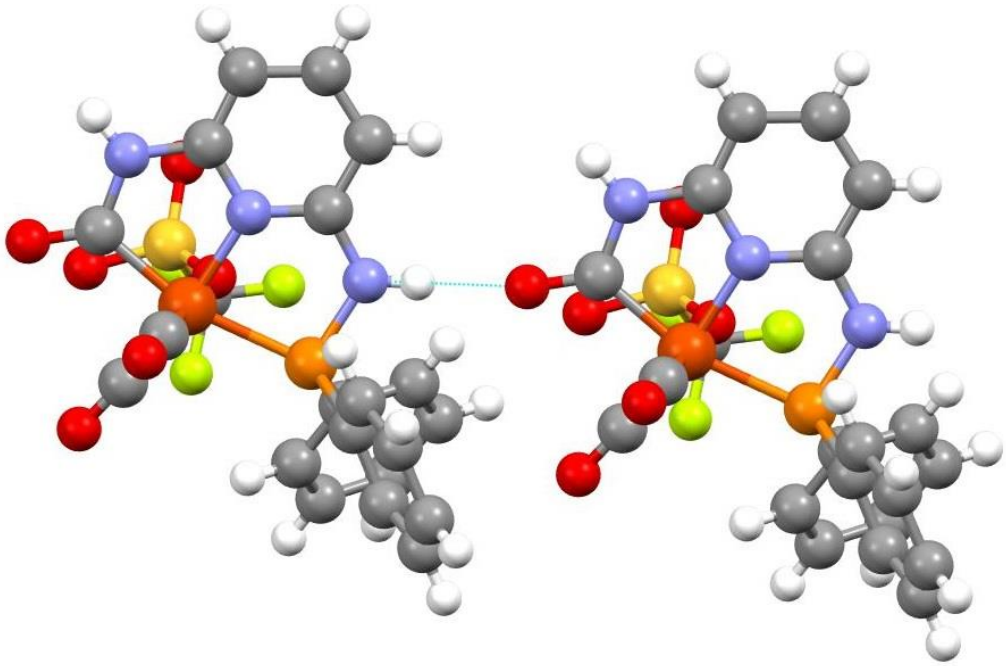

Figure C37 Hydrogen bonding diagram for complex **3**.

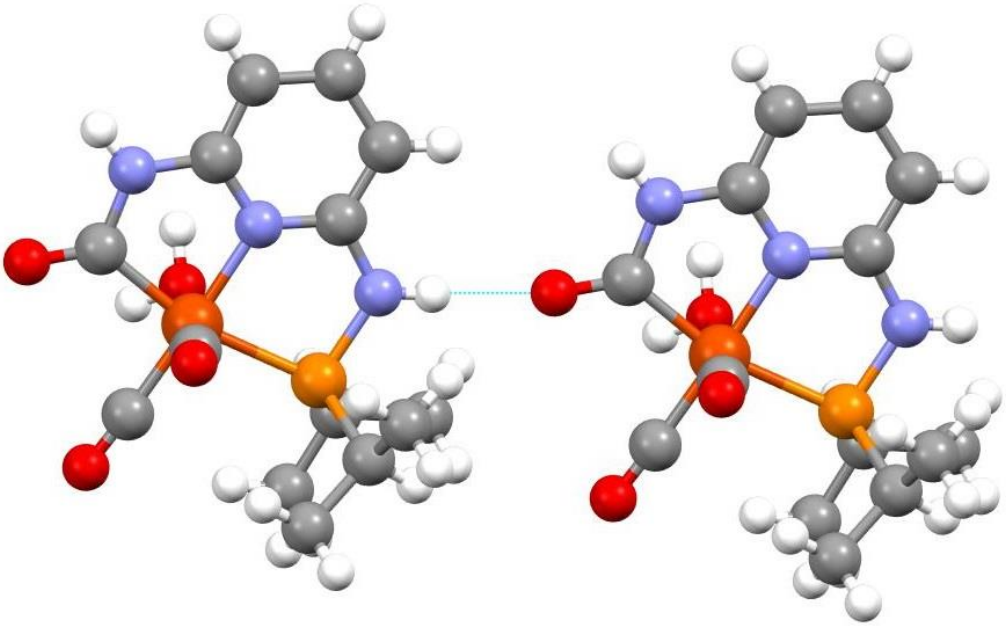

Figure C38 Hydrogen bonding diagram for complex **4**.

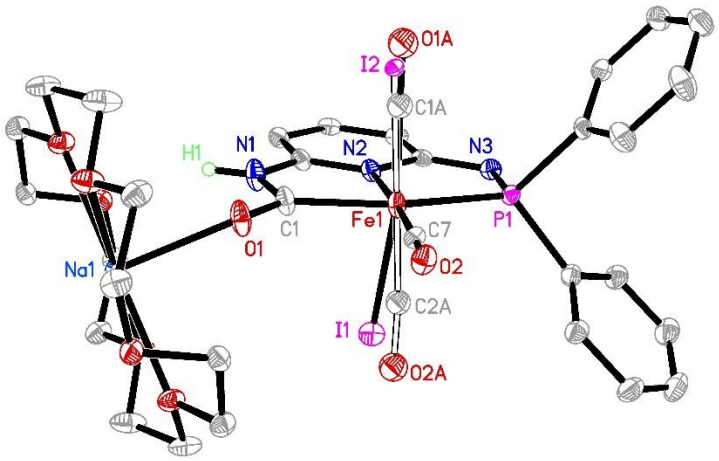

Figure C39 ORTEP diagram (30% thermal ellipsoids) for dearomatized [($C^{NH}N^{N=}P^{Ph2}$)Fe(CO)$_2$I][Na(18-crown-6)] (**7**) with disorder on iodide and carbonyl ligands. H atoms except for the N*H* proton are omitted for clarity.

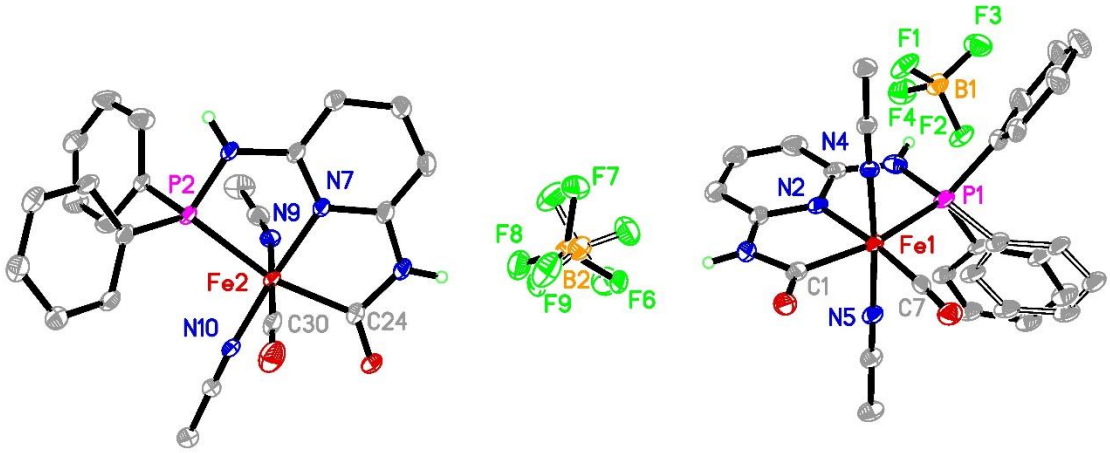

Figure C40 ORTEP diagram (30% thermal ellipsoids) for *cis*-[($C^{NH}N^{NH}P^{Ph2}$)Fe(CO)(MeCN)$_2$](BF_4) (***cis*-8**) and *trans*-[($C^{NH}N^{NH}P^{Ph2}$)Fe(CO)(MeCN)$_2$](BF_4) (***trans*-8**). Both complexes were found co-crystallized in the same unit cell. Disorder on the BF_4^- anion and phenyl rings is shown in the diagram. H atoms except for the N*H* proton are omitted for clarity.

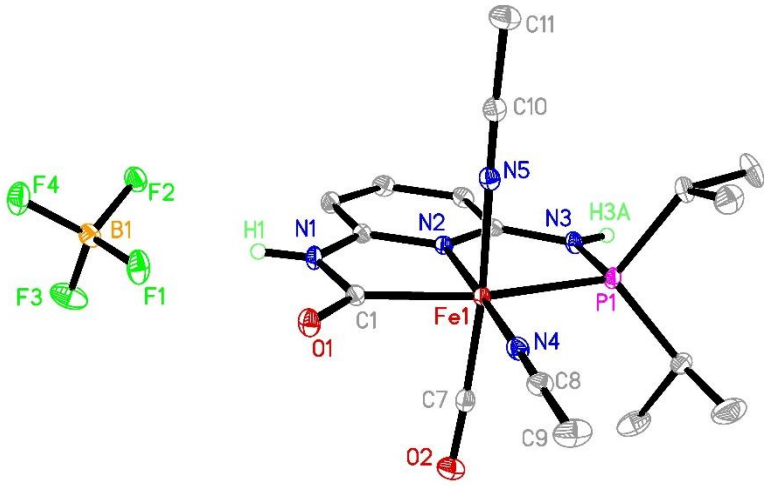

Figure C41 ORTEP diagram (30% thermal ellipsoids) for *cis*-[($C^{NH}N^{NH}P^{iPr2}$)Fe(CO)$(MeCN)_2$](BF_4) (***cis*-9**). H atoms except for the N*H* proton are omitted for clarity.

C.3 DFT Calculations

Atomic coordinates for all the optimized structure

5_{DFT}

C	-1.153317	2.024335	-0.607715
O	-1.214831	3.148117	-0.381248
C	-2.953631	0.367727	-1.575393
C	-3.310896	-0.339261	0.681957
C	-4.054976	-0.719708	1.777424
H	-5.136128	-0.763541	1.729915
C	-3.346317	-1.045123	2.950272
H	-3.904186	-1.346537	3.833002
C	-1.977251	-0.990979	3.006236
H	-1.423939	-1.235902	3.904084
C	-1.233575	-0.59731	1.856214
C	-0.371596	0.541753	-2.50414
C	2.000325	1.128415	0.685496
C	2.409055	1.380618	1.998202
H	1.946229	0.823368	2.807257
C	3.384088	2.342213	2.246484
H	3.698718	2.538421	3.267552
C	3.95313	3.053083	1.192695
H	4.711573	3.805041	1.390902
C	3.543217	2.807414	-0.115882
H	3.977869	3.367477	-0.938701
C	2.565419	1.851102	-0.370168
H	2.239756	1.675996	-1.392802
C	1.636015	-1.62254	-0.180422
C	1.69685	-2.737419	0.660513
H	1.218089	-2.683034	1.63397
C	2.368238	-3.88484	0.247098
H	2.41454	-4.748003	0.905124
C	2.980438	-3.926629	-1.002582
H	3.502372	-4.823576	-1.323546
C	2.921016	-2.817544	-1.844536
H	3.394797	-2.847776	-2.821454
C	2.247327	-1.670533	-1.438855
H	2.202591	-0.813772	-2.106287
N	-3.827567	0.019931	-0.538012
H	-4.821618	-0.024395	-0.721058
N	-1.950753	-0.289925	0.704264
N	0.089946	-0.527342	1.866444

O	-3.398628	0.613656	-2.678738
O	0.098663	0.675521	-3.541307
Fe	-1.106525	0.318161	-0.891376
P	0.724308	-0.132106	0.374126

5'$_{DFT}$

C	-1.629491	-1.898323	0.665366
O	-1.922381	-2.992737	0.445517
C	-3.002671	0.076379	1.551922
C	-3.321154	0.506024	-0.6175
C	-4.051953	0.821113	-1.785472
H	-5.129018	0.903378	-1.713737
C	-3.368781	1.043707	-2.959451
H	-3.920271	1.306088	-3.858237
C	-1.969518	0.943439	-3.027696
H	-1.429298	1.114947	-3.95139
C	-1.300821	0.599092	-1.86605
C	-0.434232	-0.694097	2.501389
C	1.892492	-1.250414	-0.504603
C	1.671201	-2.163817	-1.539792
H	0.853839	-1.999039	-2.235847
C	2.494031	-3.278732	-1.673933
H	2.317895	-3.982048	-2.48254
C	3.533858	-3.49415	-0.77389
H	4.172144	-4.366456	-0.879138
C	3.752272	-2.591531	0.264953
H	4.560378	-2.757503	0.971193
C	2.935854	-1.474514	0.402529
H	3.11527	-0.773255	1.213478
C	1.86418	1.569302	0.051945
C	3.093802	1.714721	-0.603524
H	3.454816	0.93052	-1.264165
C	3.865005	2.853175	-0.396531
H	4.818172	2.959817	-0.906335
C	3.419396	3.852015	0.467865
H	4.026667	4.737638	0.630991
C	2.201654	3.712666	1.127567
H	1.856146	4.485674	1.807366
C	1.427161	2.57463	0.921577
H	0.478689	2.46304	1.442367
N	-3.884874	0.352705	0.58202
N	-1.952925	0.392361	-0.701737
N	0.072605	0.425326	-1.786595
O	-3.070445	0.249861	2.750562
O	0.014172	-0.962961	3.523373
Fe	-1.129627	-0.270325	0.910643
P	0.754662	0.146073	-0.235578
H	0.626836	0.744363	-2.568514

***cis*-8$_{DFT}$**

C	-2.95696	-0.09123	1.166562
C	-3.10374	-0.74338	-1.13744
C	-3.73956	-1.11692	-2.32199
H	-4.81946	-1.18821	-2.37097
C	-2.93735	-1.39874	-3.41953
H	-3.40013	-1.69614	-4.35565
C	-1.55155	-1.30406	-3.34586
H	-0.92179	-1.51429	-4.20238
C	-0.99147	-0.92279	-2.12701
C	-1.37818	4.234761	-0.49312
H	-0.36765	4.614189	-0.66957
H	-1.84777	4.812172	0.30757
H	-1.96915	4.349336	-1.40554
C	-1.31044	2.836246	-0.12065
C	1.800402	1.32775	-0.72956
C	2.212187	2.098338	0.36625
H	2.043914	1.737142	1.378375
C	2.831999	3.327923	0.165687
H	3.160337	3.913779	1.019229
C	3.029053	3.807011	-1.12895
H	3.513466	4.766198	-1.28557
C	2.604997	3.053444	-2.22065
H	2.755387	3.424756	-3.23002
C	1.993341	1.817508	-2.0234
H	1.657527	1.240957	-2.88006
C	2.301924	-1.44366	-0.06458
C	3.612877	-1.03878	0.206868
C	4.590741	-1.98871	0.490247
C	4.27123	-3.34289	0.500501
H	5.037169	-4.08063	0.719436

C	2.967789	-3.75267	0.225352
H	2.714823	-4.80848	0.228066
C	1.985317	-2.80977	-0.05119
H	0.973828	-3.14232	-0.26718
N	-3.73105	-0.44098	0.034566
H	-4.74058	-0.45679	0.108569
N	-1.76028	-0.65594	-1.05808
N	0.364513	-0.79129	-1.91792
H	0.982965	-1.11795	-2.64713
N	-1.23425	1.723751	0.175851
O	-3.52024	0.212213	2.193759
P	0.958724	-0.25578	-0.3944
Fe	-1.06237	-0.15051	0.69243
H	5.607173	-1.66685	0.695572
H	3.877473	0.013665	0.186906
O	-1.11108	-2.92799	1.593374
C	-1.06649	-1.84204	1.229969
N	-0.57201	0.41908	2.467625
C	-0.47657	0.716087	3.578299
C	-0.40156	1.075758	4.979825
H	0.07563	2.051862	5.098074
H	-1.41399	1.11909	5.391228
H	0.175665	0.327031	5.528628

***trans*-8$_{DFT}$**

C	-2.93826	-0.03776	-1.31317
C	-3.13678	0.156057	1.076481
C	-3.80298	0.25483	2.299836
H	-4.88423	0.310596	2.338938
C	-3.02775	0.271414	3.45128
H	-3.51388	0.344807	4.419557
C	-1.64003	0.191877	3.392173
H	-1.03264	0.197622	4.289708
C	-1.05057	0.100952	2.130682
C	-0.53512	-0.27332	-2.52279
C	-1.54353	-4.5538	-0.37714
H	-0.5691	-5.03837	-0.27007
H	-2.04431	-4.94464	-1.2671
H	-2.1532	-4.78007	0.501578
C	-1.36873	-3.12079	-0.50181
C	-0.94679	4.393702	-1.351
H	-1.05024	4.618317	-2.41606
H	0.012001	4.779462	-0.99307
H	-1.75997	4.879919	-0.80575
C	-0.99759	2.960366	-1.14708
C	2.112112	-1.43309	0.318342
C	2.10831	-2.305	-0.77538
H	1.406368	-2.1492	-1.58927
C	3.010598	-3.36531	-0.83092
H	3.011028	-4.03068	-1.68917
C	3.912415	-3.56561	0.209583
H	4.61409	-4.39327	0.16852
C	3.925054	-2.69776	1.301373
H	4.636396	-2.8477	2.107792
C	3.036074	-1.63112	1.352503
H	3.077914	-0.94548	2.19525
C	2.028553	1.43085	0.26947
C	3.136079	1.446621	-0.58662
C	3.90989	2.596746	-0.70613
C	3.589517	3.736465	0.028204
H	4.202056	4.628762	-0.05906
C	2.489724	3.725914	0.883568
H	2.24839	4.606829	1.471838
C	1.70654	2.580364	1.000373
H	0.85311	2.574623	1.673249
N	-3.73417	0.106635	-0.14563
H	-4.74145	0.144181	-0.24096
N	-1.79211	0.09312	1.011492
N	0.310345	0.022596	1.931225
H	0.899717	0.063741	2.750548
N	-1.22226	-1.98076	-0.60922
N	-1.02432	1.817102	-0.99153
O	-3.49975	-0.10087	-2.38379
O	-0.22894	-0.39911	-3.61675
P	0.945419	-0.03574	0.331225
Fe	-1.0524	-0.08562	-0.80839
H	4.771264	2.598868	-1.36707
H	3.404375	0.557231	-1.15071

A_{MeCN}

C	8.4421	8.9524	6.692
C	8.1618	8.1564	8.9505
C	7.4681	7.6849	10.0562
C	8.2141	7.4284	11.2311
C	9.5783	7.6334	11.2839
C	10.2772	8.121	10.1334
C	11.023	9.2966	5.7791
C	10.0047	13.412	8.2144
C	10.0148	12.0082	7.8606
C	13.5282	7.7212	8.2404
C	14.021	7.6392	6.9257
C	15.0708	6.7646	6.6221
C	15.6244	5.9572	7.6229
C	15.124	6.0241	8.9296
C	14.08	6.9014	9.2413
C	13.0251	10.4646	8.9948
C	13.6855	11.1511	7.9592
C	14.2678	12.3997	8.1989
C	14.1868	12.9819	9.4719
C	13.5268	12.3045	10.5043
C	12.9463	11.0509	10.2697
Fe	10.291	9.0808	7.3538
H	6.3926	7.5145	10.011
H	7.6927	7.0566	12.1174
H	10.1575	7.4435	12.1869
H	9.8116	14.0346	7.327
H	10.9794	13.6986	8.643
H	9.2198	13.6166	8.9594
H	13.5798	8.2464	6.1316
H	15.4478	6.7064	5.598
H	16.4391	5.2694	7.3826
H	15.5482	5.3891	9.7115
H	13.6746	6.9567	10.2541
H	14.6422	13.9579	9.658
H	13.4683	12.7485	11.5014
H	12.4355	10.5083	11.0687
H	6.5994	8.3477	7.5464
H	14.7843	12.9208	7.3889
H	13.7434	10.7136	6.9587
N	7.6033	8.4715	7.7251
N	9.5227	8.3569	8.9619
N	11.5954	8.3544	10.1421
N	10.0894	10.8558	7.6076
O	7.9467	9.2038	5.589
O	11.5061	9.4055	4.7075
P	12.1696	8.8793	8.6541

B_{MeCN}

C	13.7362	6.1979	9.2502
C	11.3629	5.7336	9.4085
C	10.2326	4.9244	9.5241
C	8.9854	5.5767	9.5626
C	8.884	6.9578	9.486
C	10.0601	7.7562	9.3699
C	14.5398	8.8978	9.1773
C	12.8659	8.124	4.7236
C	12.9164	8.0094	6.1658
C	11.5943	11.0936	10.4754
C	12.8163	11.6661	10.8707
C	12.8451	12.6447	11.8711
C	11.6569	13.0507	12.4904
C	10.4392	12.4747	12.1075
C	10.4041	11.5004	11.104
C	11.4939	10.7975	7.6226
C	12.5921	11.5856	7.2328
C	12.5758	12.268	6.0113
C	11.464	12.1667	5.1631
C	10.3676	11.3842	5.5464
C	10.3818	10.6995	6.7689
Fe	13.0002	8.0596	9.2124
H	10.3229	3.8401	9.5873
H	8.0759	4.9775	9.6564
H	7.9207	7.4659	9.5175
H	13.8774	8.0364	4.2977
H	12.4453	9.1039	4.4445
H	12.2346	7.3315	4.2939
H	13.7533	11.34	10.4113
H	13.7998	13.0813	12.1743
H	11.6816	13.8083	13.2775

H	9.5104	12.7819	12.5948
H	9.4636	11.0322	10.8041
H	11.451	12.7018	4.2101
H	9.4932	11.3094	4.8941
H	9.5324	10.0881	7.0841
H	12.8861	4.2727	9.3676
H	13.4341	12.8786	5.7195
H	13.47	11.6667	7.8796
H	13.2821	7.6502	10.7102
H	12.8111	8.422	10.7431
N	12.6728	5.2775	9.3552
N	11.2827	7.089	9.3386
N	10.028	9.1034	9.2912
N	12.954	7.9695	7.3439
O	14.8931	5.7825	9.1711
O	15.5741	9.4613	9.1563
P	11.5247	9.8082	9.1718

TS_{MeCN}

C	13.6804	6.143	9.356
C	11.3524	5.7267	8.8783
C	10.1603	4.9906	8.8004
C	8.9586	5.679	9.0099
C	8.9401	7.0397	9.3404
C	10.1645	7.727	9.4126
C	14.5418	8.6642	9.8758
C	13.3878	8.169	4.8737
C	13.4157	8.0744	6.3195
C	11.8218	11.2134	10.5111
C	13.0721	11.745	10.8672
C	13.1498	12.8005	11.785
C	11.9837	13.3239	12.3546
C	10.7353	12.7912	12.0057
C	10.6512	11.7412	11.0877
C	11.2547	10.688	7.7513
C	12.2359	11.5315	7.1919
C	12.0265	12.1392	5.9517
C	10.8379	11.9019	5.2468
C	9.8613	11.0618	5.7948
C	10.0654	10.4538	7.0418
Fe	13.0183	8.0003	9.3249
H	10.1809	3.9123	8.6393
H	8.0164	5.1271	8.9645
H	8.0162	7.5617	9.5865
H	14.4028	8.1048	4.4531
H	12.9358	9.1264	4.5657
H	12.7853	7.3488	4.4519
H	13.9882	11.3217	10.4491
H	14.1261	13.2023	12.066
H	12.0466	14.1396	13.079
H	9.8229	13.1904	12.4559
H	9.6843	11.3047	10.829
H	10.6739	12.3758	4.276
H	8.9312	10.8803	5.2504
H	9.2975	9.8029	7.4668
H	12.8437	4.2432	8.8668
H	12.7919	12.7992	5.5353
H	13.1692	11.7149	7.7328
H	12.465	8.0583	10.8899
N	12.6437	5.2511	8.8895
N	11.3215	7.073	9.0692
N	10.3482	8.9876	9.9801
N	13.3722	8.0334	7.5007
O	14.7863	5.6498	9.5795
O	15.5644	9.0953	10.2742
P	11.692	9.8422	9.3112
H	11.5262	8.4674	10.6964

C_{MeCN}

C	13.8182	6.3334	9.182
C	11.4797	5.7515	9.474
C	10.3678	4.9296	9.7297
C	9.1189	5.5413	9.8546
C	8.9795	6.9289	9.7405
C	10.1318	7.6872	9.4773
C	14.558	8.9066	9.0776
C	12.9583	7.7927	4.4762
C	12.9224	7.8587	5.9237
C	11.7427	11.0848	10.4727
C	12.7332	10.9753	11.463
C	12.7852	11.8977	12.5156
C	11.8398	12.926	12.5969

C	10.844	13.0388	11.617
C	10.802	12.1304	10.555
C	11.3609	10.8876	7.6533
C	12.138	12.0408	7.4269
C	12.0056	12.7652	6.2382
C	11.0994	12.3485	5.2537
C	10.3296	11.1982	5.4649
C	10.4632	10.4693	6.6529
Fe	13.0173	8.103	8.9898
H	10.4908	3.8515	9.8348
H	8.2367	4.9285	10.0538
H	8.0107	7.4162	9.8535
H	13.9949	7.6661	4.1248
H	12.5504	8.7175	4.0367
H	12.364	6.9406	4.1101
H	13.4597	10.1616	11.4017
H	13.5685	11.8106	13.2723
H	11.8795	13.6433	13.4204
H	10.1051	13.8418	11.6758
H	10.0406	12.2465	9.7781
H	10.9924	12.9199	4.3287
H	9.6163	10.8682	4.7049
H	9.8629	9.5694	6.8086
H	13.0545	4.3627	9.4834
H	12.6106	13.6617	6.0817
H	12.8492	12.3769	8.1863
H	13.1616	8.1428	10.4994
H	9.2775	9.5733	9.5241
N	12.7821	5.3458	9.3656
N	11.3496	7.1003	9.3212
N	10.1516	9.0667	9.354
N	12.9281	7.9364	7.1057
O	14.9767	5.9108	9.1426
O	15.5955	9.4547	9.2127
P	11.6844	9.8396	9.1239

A_{diCO}

C	8.004	11.1666	8.1913
C	6.181	9.4997	7.3291
C	5.8247	8.7543	9.5892
C	5.0877	8.3632	10.6955
C	5.7994	8.0359	11.8754
C	7.1765	8.0899	11.928
C	7.9252	8.4845	10.7739
C	8.8249	9.6606	6.4529
C	11.1563	10.2245	9.5859
C	11.5742	10.4827	10.9035
C	12.554	11.4519	11.146
C	13.1231	12.163	10.0829
C	12.7043	11.9112	8.7705
C	11.7183	10.9508	8.5208
C	10.7927	7.465	8.721
C	10.8604	6.339	9.5608
C	11.5396	5.1907	9.1375
C	12.1541	5.1564	7.8805
C	12.0864	6.2753	7.0404
C	11.4027	7.4233	7.4531
Fe	8.0468	9.4632	8.0163
H	4.0003	8.3088	10.6493
H	5.2385	7.7325	12.763
H	7.7327	7.8459	12.8322
H	11.1203	9.9242	11.7246
H	12.8726	11.6515	12.172
H	13.8865	12.9203	10.2769
H	13.1359	12.4723	7.9385
H	11.3816	10.7795	7.4951
H	10.3851	6.38	10.5431
H	11.5902	4.3204	9.7965
H	12.6827	4.258	7.553
H	12.5588	6.2525	6.0556
H	11.347	8.2833	6.7814
H	4.2916	9.0846	8.1787
N	5.301	9.1249	8.3645
N	7.2016	8.8044	9.599
N	9.2591	8.5531	10.7736
O	7.9708	12.3333	8.3448
O	5.7348	9.7595	6.2106
O	9.3461	9.7937	5.4064
P	9.8798	8.9605	9.2723

B_{diCO}

C	11.033	7.4442	7.3829

C	11.8223	5.6657	9.1537
C	9.4651	5.117	9.2208
C	8.3645	4.2645	9.2605
C	7.0921	4.8681	9.2807
C	6.9401	6.2457	9.2676
C	8.0859	7.0934	9.2355
C	12.5126	8.4298	9.1373
C	9.4261	10.4343	7.8588
C	8.1946	10.7244	7.2455
C	8.1284	11.6807	6.226
C	9.2849	12.3511	5.8104
C	10.5149	12.0565	6.4114
C	10.5878	11.0996	7.4293
C	9.5237	10.252	10.7275
C	8.4221	10.2436	11.6001
C	8.463	10.9834	12.7881
C	9.5991	11.733	13.1141
C	10.6977	11.7477	12.2441
C	10.6624	11.0099	11.0565
Fe	11.0075	7.5148	9.1376
H	8.4947	3.1829	9.2761
H	6.2038	4.232	9.3079
H	5.9577	6.7165	9.283
H	7.3008	10.1887	7.5728
H	7.168	11.9	5.7532
H	9.2313	13.0958	5.0124
H	11.4236	12.5658	6.0821
H	11.5581	10.8684	7.8761
H	7.5442	9.6499	11.3344
H	7.6027	10.97	13.4624
H	9.6321	12.3023	14.0459
H	11.5891	12.3282	12.4947
H	11.5315	11.0221	10.3936
H	11.043	3.7149	9.1897
H	11.2878	7.0682	10.6952
H	10.8229	7.785	10.7568
N	10.793	4.7111	9.1904
N	9.3338	6.4714	9.2146
N	8.009	8.4387	9.228
O	11.0524	7.3954	6.2129
O	13.0002	5.3175	9.1375
O	13.5179	9.037	9.1282
P	9.4715	9.2099	9.2178

TS_{diCO}

C	11.9002	7.6601	7.9827
C	11.7585	5.5173	9.3111
C	9.5164	5.2252	8.4832
C	8.3598	4.5205	8.1284
C	7.1273	5.1619	8.3117
C	7.0441	6.4347	8.8834
C	8.2354	7.1022	9.2201
C	12.447	7.97	10.4391
C	9.2596	10.1756	8.0717
C	7.9147	10.4348	7.7523
C	7.6015	11.2261	6.6421
C	8.6226	11.7683	5.8514
C	9.9622	11.5105	6.1659
C	10.2821	10.7107	7.2682
C	9.7823	10.4196	10.8894
C	8.7071	10.6012	11.7765
C	8.7975	11.5598	12.7924
C	9.9501	12.3425	12.9258
C	11.0231	12.162	12.0434
C	10.9437	11.2	11.032
Fe	11.0814	7.3819	9.5006
H	8.4218	3.4924	7.771
H	6.2088	4.6347	8.0426
H	6.0884	6.912	9.0957
H	7.1221	10.0155	8.3767
H	6.5553	11.4225	6.3952
H	8.3741	12.3884	4.9869
H	10.7618	11.9245	5.5472
H	11.3297	10.4997	7.4969
H	7.8121	9.9858	11.6656
H	7.9611	11.694	13.4828
H	10.0165	13.0886	13.7212
H	11.9292	12.7627	12.1498
H	11.7935	11.0513	10.3601
H	11.0173	3.7537	8.3917
H	10.2867	7.2335	11.0143
N	10.8043	4.743	8.5703

N	9.441	6.5172	8.9039
N	8.3198	8.2563	9.9904
O	12.467	7.8665	6.9726
O	12.8263	4.993	9.6156
O	13.3477	8.3578	11.0843
P	9.693	9.1921	9.5464
H	9.4118	7.6386	10.8016

C_{diCO}

C	11.0979	7.4878	7.2084
C	11.8371	5.7323	9.1468
C	9.5019	5.0911	9.2754
C	8.3987	4.2297	9.3982
C	7.1268	4.8013	9.4416
C	6.9552	6.189	9.3808
C	8.101	6.9893	9.2618
C	12.5042	8.3418	9.2456
C	9.4088	10.4547	7.8882
C	8.1728	10.7699	7.2982
C	8.0947	11.7306	6.2831
C	9.2488	12.3924	5.8499
C	10.4851	12.0814	6.4284
C	10.5668	11.1136	7.4343
C	9.5782	10.2069	10.7375
C	8.4849	10.2194	11.6193
C	8.5328	10.9701	12.8005
C	9.6752	11.7124	13.1166
C	10.773	11.6985	12.2466
C	10.7277	10.9498	11.0674
Fe	10.997	7.5025	8.99
H	8.5449	3.1514	9.4593
H	6.2497	4.157	9.5332
H	5.9651	6.6428	9.4302
H	7.2595	10.2552	7.6054
H	7.1279	11.9565	5.8269
H	9.1868	13.1394	5.0553
H	11.394	12.5804	6.0846
H	11.5436	10.8549	7.8515
H	7.5939	9.6245	11.4058
H	7.6753	10.9657	13.4778
H	9.7155	12.291	14.0423
H	11.6759	12.262	12.4929
H	11.6041	10.9306	10.4147
H	11.1104	3.7419	9.3171
H	11.0934	7.4614	10.5236
H	7.1812	8.8406	9.3047
N	10.8195	4.7232	9.2368
N	9.3431	6.4419	9.1864
N	8.0895	8.3761	9.2191
O	11.2358	7.5058	6.0395
O	13.0074	5.3555	9.1659
O	13.51	8.9166	9.4567
P	9.6024	9.1921	9.2059

A_{CO}

C	8.7524	8.9565	6.518
C	8.3274	8.124	8.7341
C	7.5701	7.5904	9.7685
C	8.2237	7.3616	11.0005
C	9.5629	7.6535	11.1736
C	10.3281	8.2021	10.097
C	10.1262	10.8192	7.696
C	12.2032	10.0354	3.31
C	11.7304	9.7667	4.6508
C	13.6145	7.8357	8.4028
C	14.1384	7.7353	7.1012
C	15.1543	6.8151	6.8159
C	15.645	5.9777	7.8244
C	15.1143	6.0611	9.1183
C	14.1029	6.9827	9.4098
C	13.2274	10.5779	9.2051
C	14.0699	11.1855	8.2566
C	14.7131	12.3901	8.5545
C	14.5169	13.0031	9.7996
C	13.6805	12.4007	10.7459
C	13.0355	11.1927	10.4533
Fe	10.5267	9.2022	7.363
H	6.5148	7.3588	9.6248
H	7.6518	6.9473	11.8348
H	10.0725	7.4908	12.1229
H	11.7003	10.9294	2.9084
H	11.9711	9.187	2.6471

H	13.2913	10.2078	3.2949
H	13.7417	8.3702	6.3052
H	15.555	6.7438	5.8015
H	16.4339	5.2555	7.6006
H	15.4903	5.4038	9.9064
H	13.6755	7.051	10.4126
H	15.0134	13.9491	10.0281
H	13.5249	12.8735	11.7188
H	12.384	10.7096	11.1853
H	6.8815	8.2365	7.2015
H	15.3664	12.8549	7.8118
H	14.2268	10.7171	7.281
N	7.8549	8.4282	7.4681
N	9.6671	8.3992	8.8667
N	11.6225	8.5287	10.227
N	11.3272	9.5543	5.7445
O	8.3676	9.1614	5.3616
O	9.8379	11.9377	7.9424
P	12.2974	9.0597	8.7907

B_{CO}

C	8.7453	8.9203	6.4785
C	8.2836	8.1588	8.7239
C	7.4916	7.6826	9.7677
C	8.1338	7.4479	10.9987
C	9.4909	7.6771	11.1657
C	10.2771	8.162	10.0794
C	10.2216	10.7119	7.7067
C	12.138	10.2435	3.28
C	11.7235	9.8595	4.6128
C	13.6828	7.7843	8.4134
C	14.2127	7.6707	7.1159
C	15.2715	6.7919	6.858
C	15.8014	6.0106	7.892
C	15.2679	6.11	9.1836
C	14.2144	6.9924	9.447
C	13.1924	10.4849	9.1876
C	14.0574	11.0955	8.2617
C	14.692	12.3008	8.5764
C	14.4677	12.91	9.8184
C	13.6069	12.3074	10.7423
C	12.9688	11.1003	10.4307
Fe	10.5647	9.0489	7.3023
H	6.4259	7.5045	9.6254
H	7.5461	7.0764	11.8423
H	9.9928	7.4996	12.1167
H	11.5997	11.1516	2.966
H	11.901	9.4395	2.5656
H	13.2204	10.4438	3.239
H	13.7864	8.2613	6.3002
H	15.6774	6.7098	5.8465
H	16.6226	5.3187	7.6898
H	15.6719	5.4934	9.9907
H	13.7803	7.0672	10.4469
H	14.9625	13.8532	10.0626
H	13.4294	12.7778	11.7128
H	12.2999	10.6149	11.1455
H	6.8432	8.3484	7.1919
H	15.3638	12.7671	7.8512
H	14.2437	10.6269	7.2915
H	11.1627	7.5071	7.0779
H	10.4206	7.5197	6.6683
N	7.8335	8.4537	7.4437
N	9.6189	8.3811	8.8692
N	11.599	8.4125	10.1822
N	11.3526	9.5417	5.6892
O	8.3585	9.1793	5.3365
O	9.9912	11.8348	7.9656
P	12.2985	8.9384	8.7724

TS_{CO}

C	8.7523	9.1032	6.4415
C	8.2776	8.8313	8.7783
C	7.5232	8.5247	9.9176
C	8.2068	8.0436	11.0427
C	9.587	7.8248	11.0158
C	10.3019	8.1533	9.8491
C	10.4849	10.8279	7.2042
C	11.9071	9.2164	2.8954
C	11.5746	9.1173	4.301
C	13.9055	7.9264	8.112
C	14.1874	7.5683	6.7848

C	15.3099	6.7825	6.4897
C	16.1522	6.3495	7.5187
C	15.8731	6.702	8.8467
C	14.7569	7.4879	9.1437
C	13.0808	10.3009	9.4808
C	14.1293	11.0582	8.9221
C	14.5911	12.2097	9.5645
C	14.0083	12.6232	10.7695
C	12.967	11.8757	11.3309
C	12.5025	10.7191	10.692
Fe	10.5922	9.0938	7.1666
H	6.4368	8.6173	9.9046
H	7.6409	7.7968	11.9443
H	10.1219	7.3878	11.8582
H	11.3887	10.0809	2.4508
H	11.5866	8.3104	2.3579
H	12.9915	9.3467	2.7511
H	13.5166	7.8943	5.9877
H	15.521	6.5026	5.4546
H	17.0251	5.7334	7.289
H	16.5262	6.3598	9.6532
H	14.5313	7.7521	10.1796
H	14.3661	13.5269	11.2685
H	12.5105	12.1935	12.2714
H	11.6922	10.1393	11.1396
H	6.8067	9.1607	7.3094
H	15.4073	12.7863	9.1224
H	14.589	10.742	7.9815
H	10.8827	7.3695	7.3448
N	7.8117	9.1535	7.5231
N	9.6377	8.7397	8.7961
N	11.6208	7.7899	9.5942
N	11.2811	9.0672	5.4452
O	8.3173	9.1649	5.2898
O	10.428	12.0052	7.2551
P	12.4116	8.9018	8.5201
H	11.2412	7.2948	8.2984

Cco

C	8.8518	8.8697	6.4054
C	8.3085	8.0534	8.6123
C	7.5386	7.454	9.623
C	8.1494	7.2163	10.8554
C	9.4906	7.5504	11.0703
C	10.2017	8.1495	10.0178
C	10.1	10.9199	7.7214
C	12.104	10.2359	3.2549
C	11.6904	9.9323	4.6097
C	13.6447	7.857	8.3421
C	13.6437	7.1042	7.1563
C	14.6478	6.1574	6.9164
C	15.6506	5.9413	7.8678
C	15.6547	6.6809	9.0586
C	14.6658	7.6421	9.2885
C	13.2412	10.5226	9.2366
C	14.45	10.8949	8.6168
C	15.1166	12.0636	8.9999
C	14.5878	12.878	10.009
C	13.3824	12.5207	10.6253
C	12.7095	11.3566	10.238
Fe	10.5356	9.24	7.3225
H	6.5006	7.1794	9.4347
H	7.5763	6.7513	11.6607
H	9.983	7.3481	12.022
H	11.5927	11.1429	2.8951
H	11.8414	9.4046	2.5813
H	13.1913	10.4032	3.1973
H	12.8376	7.2617	6.4344
H	14.643	5.5848	5.9856
H	16.4308	5.1988	7.6833
H	16.4358	6.5137	9.8044
H	14.7006	8.2389	10.2049
H	15.111	13.7882	10.3114
H	12.9591	13.1535	11.4091
H	11.7605	11.0959	10.7129
H	6.9622	8.0762	7.0007
H	16.0557	12.3355	8.5113
H	14.8795	10.2628	7.8353
H	12.0534	8.2752	10.93
H	10.8069	7.7777	6.9041
N	7.9006	8.3258	7.334
N	9.6059	8.4207	8.8233

N	11.5357	8.514	10.0786
N	11.3117	9.6804	5.7003
O	8.4772	9.022	5.2397
O	9.7952	12.0333	7.9718
P	12.2923	9.076	8.6237

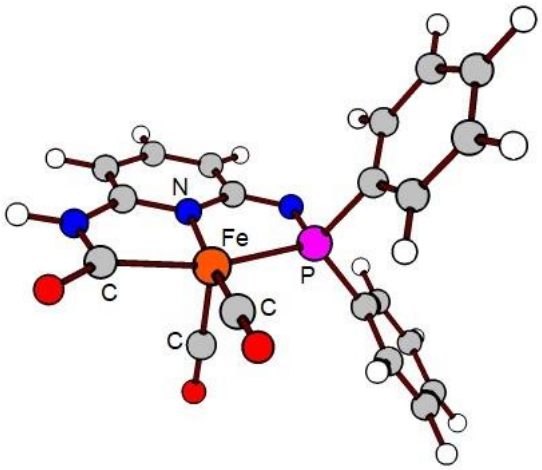

Figure C42 Optimized structure of **5**$_{DFT}$ (PBE0/opt).

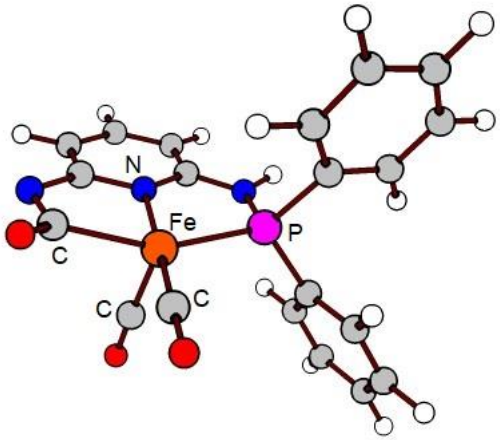

Figure C43 Optimized structure of **5'**$_{DFT}$ (PBE0/opt).

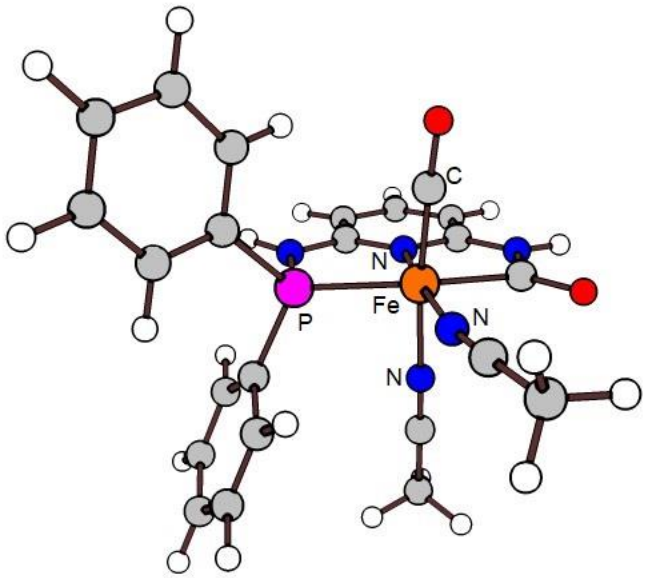

Figure C44 Optimized structure of ***cis*-8$_{DFT}^{+}$** cation (PBE0/opt).

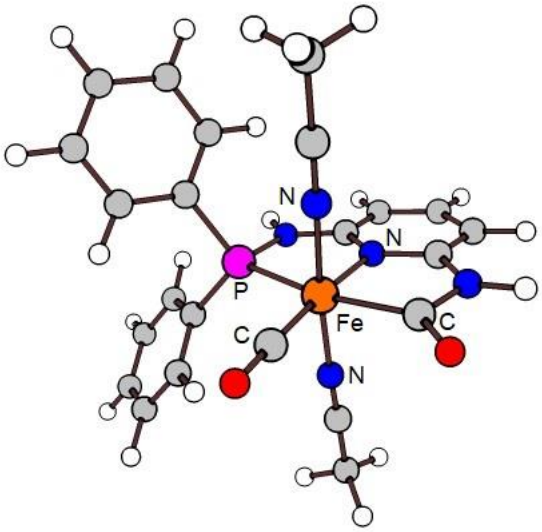

Figure C45 Optimized structure of ***tans*-8$_{DFT}^{+}$** cation (PBE0/opt).

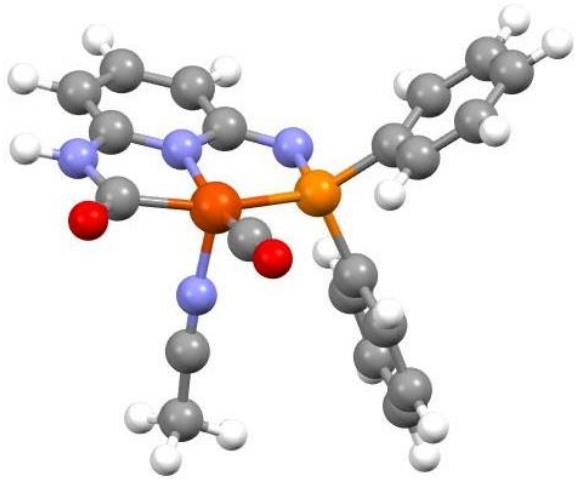

Figure C46 Optimized structure of $\mathbf{A}_{\mathbf{MeCN}}$.

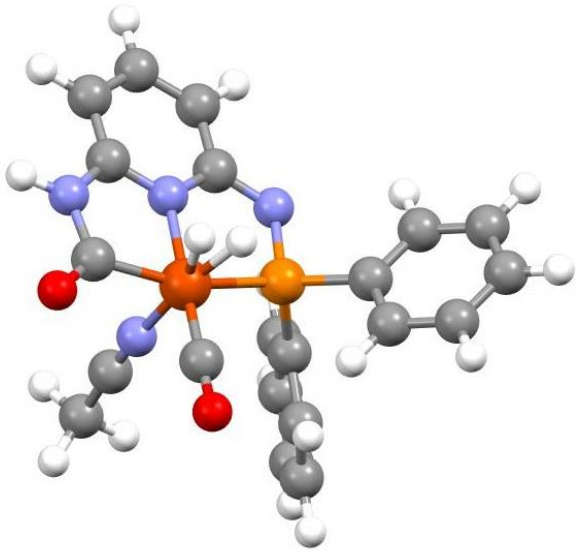

Figure C47 Optimized structure of $\mathbf{B}_{\mathbf{MeCN}}$.

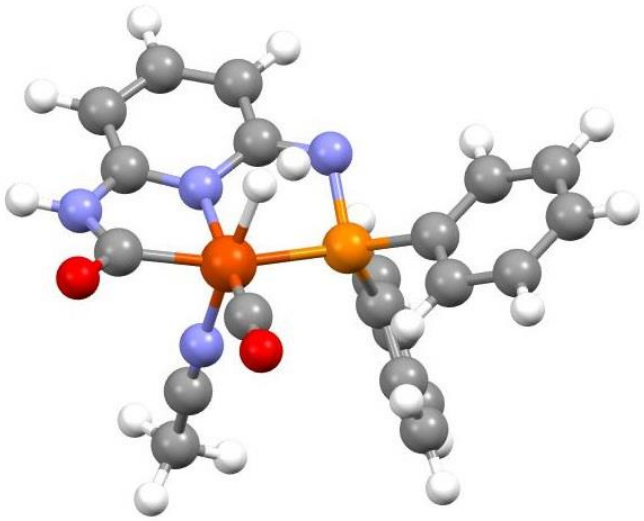

Figure C48 Optimized structure of **TS_{MeCN}.**

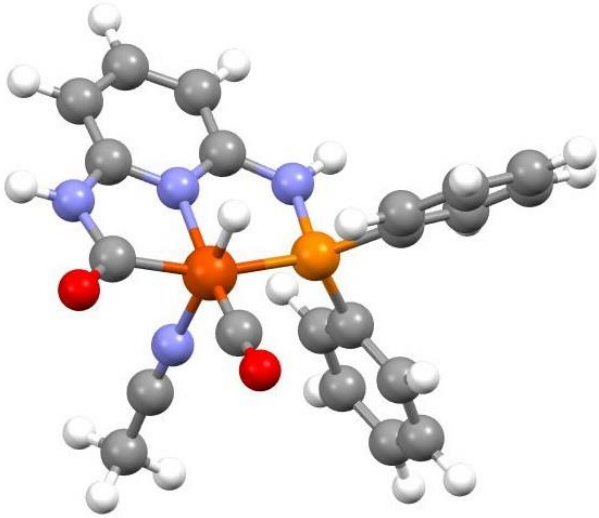

Figure C49 Optimized structure of **C_{MeCN}.**

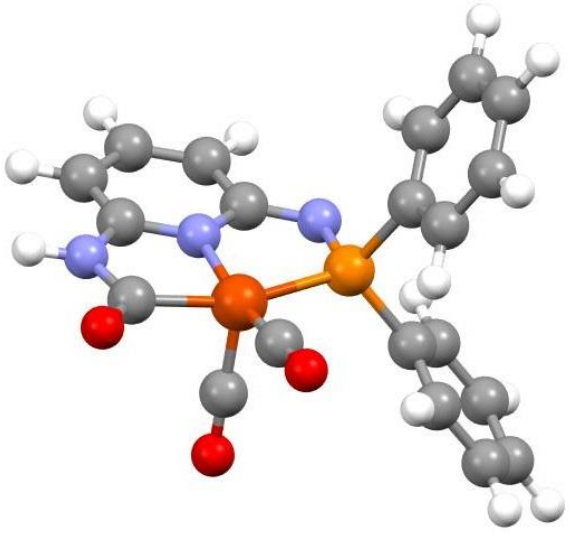

Figure C50 Optimized structure of $\mathbf{A}_{\mathbf{diCO}}$.

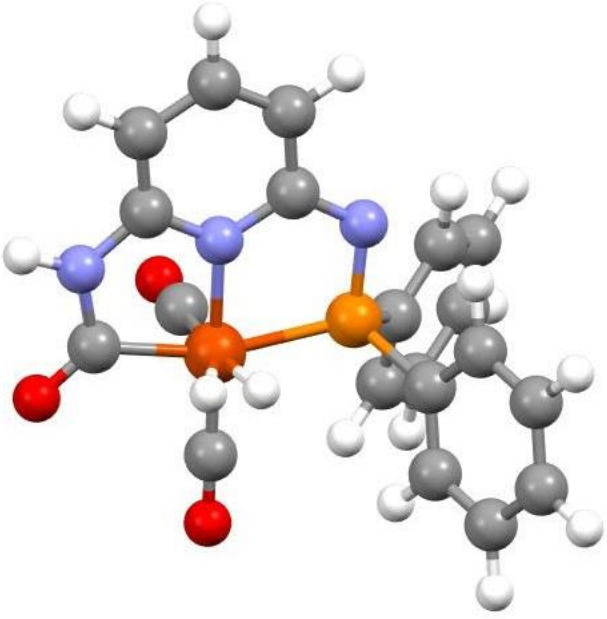

Figure C51 Optimized structure of $\mathbf{B}_{\mathbf{diCO}}$.

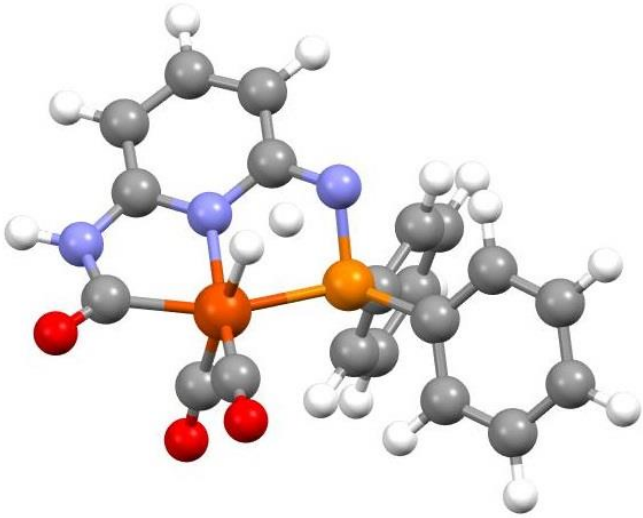

Figure C52 Optimized structure of **TS_{diCO}**.

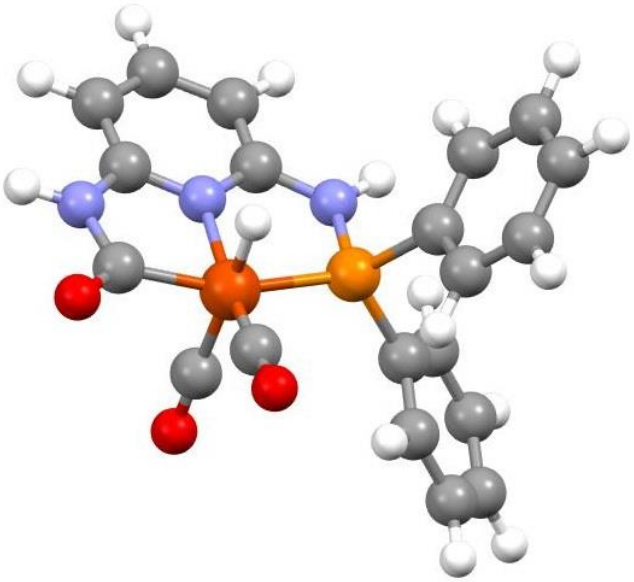

Figure C53 Optimized structure of **C_{diCO}**.

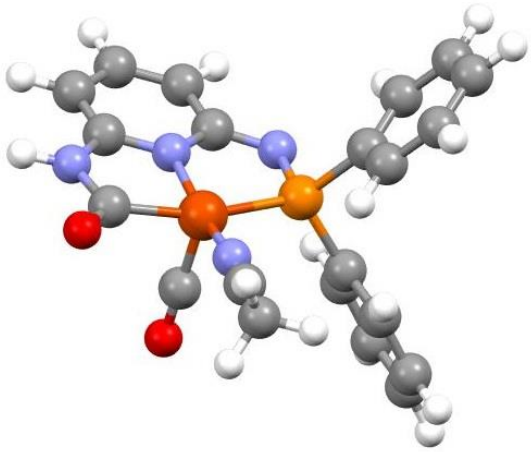

Figure C54 Optimized structure of **A**$_{CO}$.

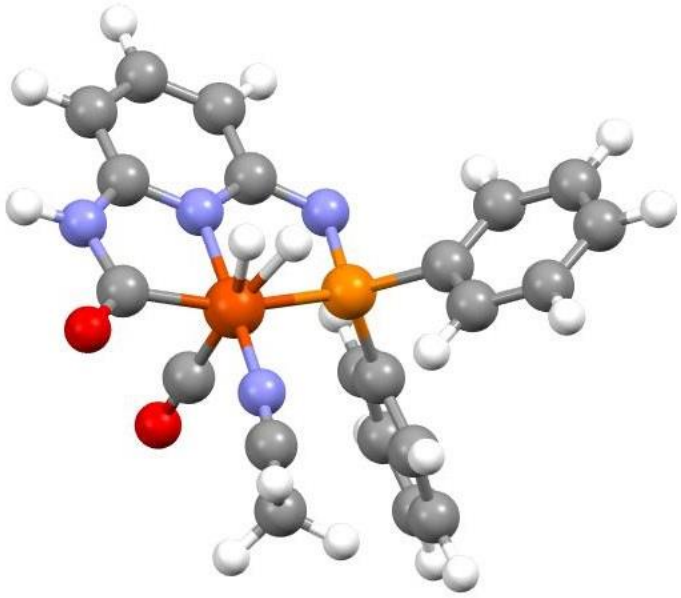

Figure C55 Optimized structure of **B**$_{CO}$.

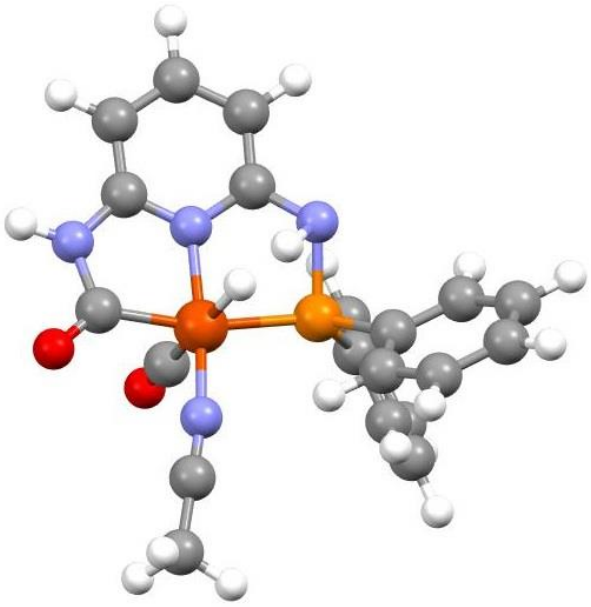

Figure C56 Optimized structure of **TS$_{CO}$**.

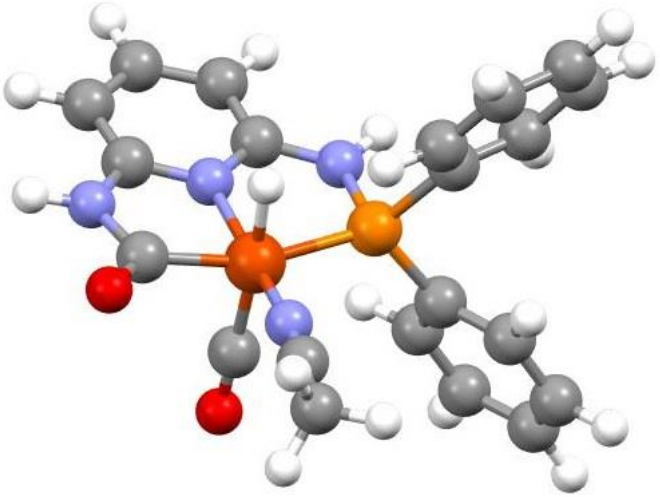

Figure C57 Optimized structure of **C$_{CO}$**.

Table C2. Electronic energy obtained from geometry optimization

Complex	E (Hartree)	ΔE (kcal/mol)
5$_{DFT}$	-1624.32125	0
5'$_{DFT}$	-1624.30166	12.3[a]
***cis*-8**$_{DFT}^{+}$	-1776.79230	0
***tans*-8**$_{DFT}^{+}$	-1776.78990	1.5[b]

[a]the energy difference between **5**$_{DFT}^{+}$ and C(=O)N*H* deprotonated **5**$_{DFT}^{+}$
[b]the energy difference between ***tans*-8**$_{DFT}^{+}$ and ***cis*-8**$_{DFT}^{+}$

References

Chapter 1

(1) Štefane, B.; Požgan, F. In *Hydrogen Transfer Reactions. Topics in Current Chemistry Collections.*; Guillena, G., Ramón, D., Eds.; Springer, Cham, 2016; pp 1–67.

(2) Perez, F.; Oda, S.; Geary, L. M.; Krische, M. J. In *Hydrogen Transfer Reactions. Topics in Current Chemistry Collections.*; Guillena, G., Ramón, D., Eds.; Springer, Cham, 2016; pp 365–387.

(3) Schöneich, C. In *Hydrogen-Transfer Reactions*; Hynes, J. T., Klinman, J. P., Limbach, H.-H., Schowen, R. L., Eds.; Wiley-VCH Verlag GmbH & Co. KGaA: Weinheim, Germany, 2006; pp 1013–1035.

(4) Crabtree, R. H. *The Organometallic Chemistry of the Transition Metals*; John Wiley & Sons, Inc.: Hoboken, NJ, USA, 2005.

(5) Bullock, R. M. *Chem. - A Eur. J.* 2004, *10* (10), 2366–2374.

(6) Balaraman, E.; Nandakumar, A.; Jaiswal, G.; Sahoo, M. K. *Catal. Sci. Technol.* 2017, *7* (15), 3177–3195.

(7) Møller, K. T.; Jensen, T. R.; Akiba, E.; Li, H. *Prog. Nat. Sci. Mater. Int.* 2017, *27* (1), 34–40.

(8) Singh, A. K.; Singh, S.; Kumar, A. *Catal. Sci. Technol.* 2016, *6* (1), 12–40.

(9) Kubas, G. J. *J. Organomet. Chem.* 2009, *694* (17), 2648–2653.

(10) Zhang, F.; Zhao, P.; Niu, M.; Maddy, J. *Int. J. Hydrogen Energy* 2016, *41* (33), 14535–14552.

(11) Holladay, J. D.; Hu, J.; King, D. L.; Wang, Y. *Catal. Today* 2009, *139* (4), 244–260.

(12) Young, J. F.; Osborn, J. A.; Jardine, F. H.; Wilkinson, G. *Chem. Commun.* 1965, *0* (7), 131–132.

(13) Wang, D.; Astruc, D. *Chem. Rev.* 2015, *115* (13), 6621–6686.

(14) Chirik, P. J. *Acc. Chem. Res.* 2015, *48* (6), 1687–1695.

(15) Chen, J. G.; Crooks, R. M.; Seefeldt, L. C.; Bren, K. L.; Bullock, R. M.; Darensbourg, M. Y.; Holland, P. L.; Hoffman, B.; Janik, M. J.; Jones, A. K.; et al. *Science* 2018, *360* (6391), eaar6611.

(16) Wodrich, M. D.; Hu, X. *Nat. Rev. Chem.* 2017, *2* (1), 0099.

(17) Dance, I.; Fisher, K. In *Progress in Inorganic Chemistry*; Kailin, K. D., Ed.; John Wiley & Sons, Ltd, 2007; pp 637–803.

(18) Bauer, I.; Knölker, H.-J. *Chem. Rev.* 2015, *115* (9), 3170–3387.

(19) Wei, D.; Darcel, C. *Chem. Rev.* 2019, *119* (4), 2550–2610.

(20) Lynch, T. J.; Banah, M.; Kaesz, H. D.; Porter, C. R. *J. Org. Chem.* 1984, *49* (7), 1266–1270.

(21) Frankel, E. N.; Emken, E. A.; Davison, V. L. *J. Org. Chem.* 1965, *30* (8), 2739–2745.

(22) Frankel, E. N.; Peters, H. M.; Jones, E. P.; Dutton, H. J. *J. Am. Oil Chem. Soc.* 1964, *41* (3), 186–191.

(23) Frankel, E. N.; Emken, E. A.; Peters, H. M.; Davison, V. L.; Butterfield, R. O. *J. Org. Chem.* 1964, *29* (11), 3292–3297.

(24) Emken, E. A.; Frankel, E. N.; Butterfield, R. O. *J. Am. Oil Chem. Soc.* 1966, *43* (1), 14–18.

(25) Schroeder, M. A.; Wrighton, M. S. *J. Am. Chem. Soc.* 1976, *98* (2), 551–558.

(26) Inoue, H.; Suzuki, M. *J. Chem. Soc. Chem. Commun.* 1980, *0* (17), 817–818.

(27) Nishiguchi, T.; Fukuzumi, K. *J. Chem. Soc. D Chem. Commun.* 1971, *0* (3), 139–140.

(28) Nishiguchi, T.; Fukuzumi, K. *Bull. Chem. Soc. Jpn.* 1972, *45* (6), 1656–1660.

(29) Markó, L.; Palágyi, J. *Transit. Met. Chem.* 1983, *8* (4), 207–209.

(30) Hoyt, J. M.; Shevlin, M.; Margulieux, G. W.; Krska, S. W.; Tudge, M. T.; Chirik, P. J. *Organometallics* 2014, *33* (20), 5781–5790.

(31) Villa, M.; Miesel, D.; Hildebrandt, A.; Ragaini, F.; Schaarschmidt, D.; Jacobi von Wangelin, A. *ChemCatChem* 2017, *9* (16), 3203–3209.

(32) Gorgas, N.; Stöger, B.; Veiros, L. F.; Pittenauer, E.; Allmaier, G.; Kirchner, K. *Organometallics* 2014, *33* (23), 6905–6914.

(33) Chakraborty, S.; Lagaditis, P. O.; Förster, M.; Bielinski, E. A.; Hazari, N.; Holthausen, M. C.; Jones, W. D.; Schneider, S. *ACS Catal.* 2014, *4* (11), 3994–4003.

(34) Wienhöfer, G.; Westerhaus, F. A.; Junge, K.; Ludwig, R.; Beller, M. *Chem. - A Eur. J.* 2013, *19* (24), 7701–7707.

(35) Sui-Seng, C.; Freutel, F.; Lough, A. J.; Morris, R. H. *Angew. Chem. Int. Ed.* 2008, *47* (5), 940–943.

(36) Tondreau, A. M.; Atienza, C. C. H.; Weller, K. J.; Nye, S. A.; Lewis, K. M.; Delis, J. G. P.; Chirik, P. J. *Science* 2012, *335* (6068), 567–570.

(37) Knölker, H.-J.; Goesmann, H.; Klauss, R. *Angew. Chem. Int. Ed.* 1999, *38* (5), 702–705.

(38) Ragsdale, S. W. *Chem. Rev.* 2006, *106* (8), 3317–3337.

(39) Hoffman, B. M.; Lukoyanov, D.; Yang, Z.-Y.; Dean, D. R.; Seefeldt, L. C. *Chem. Rev.* 2014, *114* (8), 4041–4062.

(40) Doukov, T. I.; Iverson, T. M.; Seravalli, J.; Ragsdale, S. W.; Drennan, C. L. *Science* 2002, *298* (5593), 567–572.

(41) Dobbek, H.; Svetlitchnyi, V.; Gremer, L.; Huber, R.; Meyer, O. *Science* 2001, *293* (5533), 1281–1285.

(42) Lubitz, W.; Ogata, H.; Rüdiger, O.; Reijerse, E. *Chem. Rev.* 2014, *114* (8), 4081–4148.

(43) van der Vlugt, J. I. *Eur. J. Inorg. Chem.* 2012, *2012* (3), 363–375.

(44) Kubas, G. J. *Chem. Rev.* 2007, *107* (10), 4152–5205.

(45) Robert H. Crabtree. *Chem. Rev.* 2016, *116* (15), 8750–8769.

(46) Kubas, G. J. *Acc. Chem. Res.* 1988, *21* (3), 120–128.

(47) Kubas, G. J. *J. Organomet. Chem.* 2001, *635* (1–2), 37–68.

(48) Zhang, L.; Peng, D.; Leng, X.; Huang, Z. *Angew. Chem. Int. Ed.* 2013, *52* (13), 3676–3680.

(49) Szymczak, N. K.; Tyler, D. R. *Coord. Chem. Rev.* 2008, *252* (1–2), 212–230.

(50) Aresta, M.; Giannoccaro, P.; Rossi, M.; Sacco, A. *Inorg. Chim. Acta* 1971, *5*, 115–118.

(51) Ashworth, T. V.; Singleton, E. *J. Chem. Soc., Chem. Commun.* 1976, *0* (18), 705–706.

(52) Kubas, G. J.; Ryan, R. R.; Swanson, B. I.; Vergamini, P. J.; Wasserman, H. J. *J. Am. Chem. Soc.* 1984, *106* (2), 451–452.

(53) Dewar, M. J. S. *Bull. Soc. Chim. Fr.* 1951, *18*, C71–C79.

(54) Chatt, J.; Duncanson, L. A. *J. Chem. Soc.* 1953, *0* (0), 2939–2947.

(55) Kubas, G. J.; Burns, C. J.; Eckert, J.; Johnson, S. W.; Larson, A. C.; Vergamini, P. J.; Unkefer, C. J.; Khalsa, G. R. K.; Jackson, S. A.; Eisenstein, O. *J. Am. Chem. Soc.* 1993, *115* (2), 569–581.

(56) Albinati, A.; Bakhmutov, V. I.; Caulton, K. G.; Clot, E.; Eckert, J.; Eisenstein, O.; Gusev, D. G.; Grushin, V. V.; Hauger, B. E. *J. Am. Chem. Soc.* 1993, *115* (16), 7300–7312.

(57) Abdur-Rashid, K.; Fong, T. P.; Greaves, B.; Gusev, D. G.; Hinman, J. G.; Landau, S. E.; Lough, A. J.; Morris, R. H. *J. Am. Chem. Soc.* 2000, *122* (38), 9155–9171.

(58) Morris, R. H. *Chem. Rev.* 2016, *116* (15), 8588–8654.

(59) Chinn, M. S.; Heinekey, D. M.; Payne, N. G.; Sofield, C. D. *Organometallics* 1989, *8* (7), 1824–1826.

(60) Cappellani, E. P.; Drouin, S. D.; Jia, G.; Maltby, P. A.; Morris, R. H.; Schweitzer, C. T. *J. Am. Chem. Soc.* 1994, *116* (8), 3375–3388.

(61) Junge, K.; Schröder, K.; Beller, M. *Chem. Commun.* 2011, *47* (17), 4849.

(62) Zell, T.; Milstein, D. *Acc. Chem. Res.* 2015, *48* (7), 1979–1994.

(63) Hale, L. V. A.; Szymczak, N. K. *ACS Catal.* 2018, 6446–6461.

(64) Morris, R. H. *Acc. Chem. Res.* 2015, *48* (5), 1494–1502.

(65) Bauer, G.; Kirchner, K. A. *Angew. Chem. Int. Ed.* 2011, *50* (26), 5798–5800.

(66) Clapham, S. E.; Hadzovic, A.; Morris, R. H. *Coord. Chem. Rev.* 2004, *248* (21–24), 2201–2237.

(67) Dub, P. A.; Scott, B. L.; Gordon, J. C. *J. Am. Chem. Soc.* 2017, *139* (3), 1245–1260.

(68) Dub, P. A.; Gordon, J. C. *ACS Catal.* 2017, *7* (10), 6635–6655.

(69) Filonenko, G. A.; van Putten, R.; Hensen, E. J. M.; Pidko, E. A. *Chem. Soc. Rev.* 2018, *47* (4), 1459–1483.

(70) Berggren, G.; Adamska, A.; Lambertz, C.; Simmons, T. R.; Esselborn, J.; Atta, M.; Gambarelli, S.; Mouesca, J. M.; Reijerse, E.; Lubitz, W.; et al. *Nature* 2013, *499* (7456), 66–69.

(71) Esselborn, J.; Muraki, N.; Klein, K.; Engelbrecht, V.; Metzler-Nolte, N.; Apfel, U. P.; Hofmann, E.; Kurisu, G.; Happe, T. *Chem. Sci.* 2016, *7*, 959–968.

(72) Schilter, D.; Rauchfuss, T. B. *Angew. Chem. Int. Ed.* 2013, *52* (51), 13518–13520.

(73) Esselborn, J.; Lambertz, C.; Adamska-Venkatesh, A.; Simmons, T.; Berggren, G.; Noth, J.; Siebel, J.; Hemschemeier, A.; Artero, V.; Reijerse, E.; et al. *Nat. Chem. Biol.* 2013, *9* (10), 607–609.

(74) Shima, S.; Chen, D.; Xu, T.; Wodrich, M. D.; Fujishiro, T.; Schultz, K. M.; Kahnt, J.; Ataka, K.; Hu, X. *Nat. Chem.* 2015, *7* (12), 995–1002.

(75) Xu, T.; Yin, C.-J. M.; Wodrich, M. D.; Mazza, S.; Schultz, K. M.; Scopelliti, R.; Hu, X. *J. Am. Chem. Soc.* 2016, *138* (10), 3270–3273.

(76) Murray, K. A.; Wodrich, M. D.; Hu, X.; Corminboeuf, C. *Chem. - A Eur. J.* 2015, *21* (10), 3987–3996.

(77) Gunanathan, C.; Milstein, D. *Chem. Rev.* 2014, *114* (24), 12024–12087.

(78) Mukherjee, A.; Milstein, D. *ACS Catal.* 2018, *8* (12), 11435–11469.

(79) Filonenko, G. A.; Conley, M. P.; Copéret, C.; Lutz, M.; Hensen, E. J. M.; Pidko, E. A. *ACS Catal.* 2013, *3* (11), 2522–2526.

(80) Yang, X. *Inorg. Chem.* 2011, *50* (24), 12836–12843.

(81) Yang, X. *ACS Catal.* 2011, *1* (8), 849–854.

(82) Morello, G. R.; Hopmann, K. H. *ACS Catal.* 2017, *7* (9), 5847–5855.

(83) Pryde, A.; Shaw, B. L.; Weeks, B. *J. Chem. Soc. Dalt. Trans.* 1976, *0* (4), 322.

(84) van Koten, G.; Timmer, K.; Noltes, J. G.; Spek, A. L. *J. Chem. Soc., Chem. Commun.* 1978, *0* (6), 250–252.

(85) van Koten, G. *Pure Appl. Chem.* 1989, *61* (10), 1681–1694.

(86) Werkmeister, S.; Neumann, J.; Junge, K.; Beller, M. *Chem. – A Eur. J.* 2015, *21* (35), 12226–12250.

(87) Peris, E.; Crabtree, R. H. *Chem. Soc. Rev.* 2018, *47* (6), 1959–1968.

(88) Langer, R.; Leitus, G.; Ben-David, Y.; Milstein, D. *Angew. Chem. Int. Ed.* 2011, *50* (9), 2120–2124.

(89) Langer, R.; Iron, M. A.; Konstantinovski, L.; Diskin-Posner, Y.; Leitus, G.; Ben-David, Y.; Milstein, D. *Chem. - A Eur. J.* 2012, *18* (23), 7196–7209.

(90) Chakraborty, S.; Dai, H.; Bhattacharya, P.; Fairweather, N. T.; Gibson, M. S.; Krause, J. A.; Guan, H. *J. Am. Chem. Soc.* 2014, *136* (22), 7869–7872.

(91) Schröder-Holzhacker, C.; Gorgas, N.; Stöger, B.; Kirchner, K. *Monatshefte fur Chemie* 2016, *147* (6), 1023–1030.

(92) Gorgas, N.; Stöger, B.; Veiros, L. F.; Kirchner, K. *ACS Catal.* 2016, *6* (4), 2664–2672.

(93) Mazza, S.; Scopelliti, R.; Hu, X. *Organometallics* 2015, *34* (8), 1538–1545.

(94) Zell, T.; Ben-David, Y.; Milstein, D. *Catal. Sci. Technol.* 2015, *5* (2), 822–826.

(95) Zell, T.; Ben-David, Y.; Milstein, D. *Angew. Chem. Int. Ed.* 2014, *53* (18), 4685–4689.

(96) Werkmeister, S.; Junge, K.; Wendt, B.; Alberico, E.; Jiao, H.; Baumann, W.; Junge, H.; Gallou, F.; Beller, M. *Angew. Chem. Int. Ed.* 2014, *53* (33), 8722–8726.

(97) Elangovan, S.; Wendt, B.; Topf, C.; Bachmann, S.; Scalone, M.; Spannenberg, A.; Jiao, H.; Baumann, W.; Junge, K.; Beller, M. *Adv. Synth. Catal.* 2016, *358* (5), 820–825.

(98) Garg, J. A.; Chakraborty, S.; Ben-David, Y.; Milstein, D. *Chem. Commun.* 2016, *52* (30), 5285–5288.

(99) Schneck, F.; Assmann, M.; Balmer, M.; Harms, K.; Langer, R. *Organometallics* 2016, *35* (11), 1931–1943.

(100) Rezayee, N. M.; Samblanet, D. C.; Sanford, M. S. *ACS Catal.* 2016, *6* (10), 6377–6383.

(101) Jayarathne, U.; Zhang, Y.; Hazari, N.; Bernskoetter, W. H. *Organometallics* 2017, *36* (2), 409–416.

(102) Benito-Garagorri, D.; Kirchner, K. *Acc. Chem. Res.* 2008, *41* (2), 201–213.

(103) Docherty, J. H.; Peng, J.; Dominey, A. P.; Thomas, S. P. *Nat. Chem.* 2017, *9* (6), 595–600.

(104) Sonnenberg, J. F.; Wan, K. Y.; Sues, P. E.; Morris, R. H. *ACS Catal.* 2017, *7* (1), 316–326.

(105) Bart, S. C.; Lobkovsky, E.; Chirik, P. J. *J. Am. Chem. Soc.* 2004, *126* (42), 13794–13807.

(106) Yu, R. P.; Darmon, J. M.; Hoyt, J. M.; Margulieux, G. W.; Turner, Z. R.; Chirik, P. J. *ACS Catal.* 2012, *2* (8), 1760–1764.

(107) Trovitch, R. J.; Lobkovsky, E.; Chirik, P. J. *Inorg. Chem.* 2006, No. 45, 7252–7260.

(108) Xu, R.; Chakraborty, S.; Bellows, S. M.; Yuan, H.; Cundari, T. R.; Jones, W. D. *ACS Catal.* 2016, *6* (3), 2127–2135.

(109) Srimani, D.; Diskin-Posner, Y.; Ben-David, Y.; Milstein, D. *Angew. Chem. Int. Ed.* 2013, *52* (52), 14131–14134.

(110) Chakraborty, S.; Bhattacharya, P.; Dai, H.; Guan, H. *Acc. Chem. Res.* 2015, *48* (7), 1995–2003.

(111) Langer, R.; Diskin-Posner, Y.; Leitus, G.; Shimon, L. J. W.; Ben-David, Y.; Milstein, D. *Angew. Chem. Int. Ed.* 2011, *50* (42), 9948–9952.

(112) Zell, T.; Butschke, B.; Ben-David, Y.; Milstein, D. *Chem. - A Eur. J.* 2013, *19* (25), 8068–8072.

(113) Rivada-Wheelaghan, O.; Dauth, A.; Leitus, G.; Diskin-Posner, Y.; Milstein, D. *Inorg. Chem.* 2015, *54* (9), 4526–4538.

(114) Mellone, I.; Gorgas, N.; Bertini, F.; Peruzzini, M.; Kirchner, K.; Gonsalvi, L. *Organometallics* 2016, *35* (19), 3344–3349.

(115) Bertini, F.; Gorgas, N.; Stöger, B.; Peruzzini, M.; Veiros, L. F.; Kirchner, K.; Gonsalvi, L. *ACS Catal.* 2016, *6* (5), 2889–2893.

(116) Zhang, Y.; MacIntosh, A. D.; Wong, J. L.; Bielinski, E. A.; Williard, P. G.; Mercado, B. Q.; Hazari, N.; Bernskoetter, W. H. *Chem. Sci.* 2015, *6* (7), 4291–4299.

(117) Bielinski, E. A.; Lagaditis, P. O.; Zhang, Y.; Mercado, B. Q.; Würtele, C.; Bernskoetter, W. H.; Hazari, N.; Schneider, S. *J. Am. Chem. Soc.* 2014, *136* (29), 10234–10237.

(118) Alberico, E.; Sponholz, P.; Cordes, C.; Nielsen, M.; Drexler, H.-J.; Baumann, W.; Junge, H.; Beller, M. *Angew. Chem. Int. Ed.* 2013, *52* (52), 14162–14166.

(119) Maity, A.; Teets, T. S. *Chem. Rev.* 2016, *116* (15), 8873–8911.

(120) Bernskoetter, W. H.; Hazari, N. *Acc. Chem. Res.* 2017, *50* (4), 1049–1058.

(121) Bielinski, E. A.; Förster, M.; Zhang, Y.; Bernskoetter, W. H.; Hazari, N.; Holthausen, M. C. *ACS Catal.* 2015, *5* (4), 2404–2415.

(122) Thauer, R. K.; Kaster, A.-K.; Seedorf, H.; Buckel, W.; Hedderich, R. *Nat. Rev. Microbiol.* 2008, *6* (8), 579–591.

(123) Thauer, R. K.; Kaster, A.-K.; Goenrich, M.; Schick, M.; Hiromoto, T.; Shima, S. *Annu. Rev. Biochem.* 2010, *79* (1), 507–536.

(124) Chen, D.; Scopelliti, R.; Hu, X. *Angew. Chem. Int. Ed.* 2010, *49* (41), 7512–7515.

(125) Tard, C.; Pickett, C. J. *Chem. Rev.* 2009, *109* (6), 2245–2274.

(126) Thauer, R. K. *Microbiology* 1998, *144* (9), 2377–2406.

(127) Berke, H. *ChemPhysChem* 2010, *11* (9), 1837–1849.

(128) Zirngibl, C.; Hedderich, R.; Thauer, R. K. *FEBS Lett.* 1990, *261* (1), 112–116.

(129) Shima, S.; Warkentin, E.; Thauer, R. K.; Ermler, U. *J. Biosci. Bioeng.* 2002, *93* (6), 519–530.

(130) Schilter, D.; Camara, J. M.; Huynh, M. T.; Hammes-Schiffer, S.; Rauchfuss, T. B. *Chem. Rev.* 2016, *116* (15), 8693–8749.

(131) Vogt, S.; Lyon, E. J.; Shima, S.; Thauer, R. K. *JBIC J. Biol. Inorg. Chem.* 2007, *13* (1), 97–106.

(132) Shima, S.; Pilak, O.; Vogt, S.; Schick, M.; Stagni, M. S.; Meyer-Klaucke, W.; Warkentin, E.; Thauer, R. K.; Ermler, U. *Science* 2008, *321* (5888), 572–575.

(133) Hiromoto, T.; Ataka, K.; Pilak, O.; Vogt, S.; Stagni, M. S.; Meyer-Klaucke, W.; Warkentin, E.; Thauer, R. K.; Shima, S.; Ermler, U. *FEBS Lett.* 2009, *583* (3), 585–590.

(134) Escalante-Semerena, J. C.; Rinehart, K. L.; Wolfe, R. S.; Escalante-Semerenas, J. C.; Rinehart, K. L.; Wolfe$ll, R. S. *J. Biol. Chem.* 1984, *259* (15), 9447—9455.

(135) Zirngibl, C.; Dongen, W.; Schworer, B.; Bunau, R.; Richter, M.; Klein, A.; Thauer, R. K. *Eur. J. Biochem.* 1992, *208* (2), 511–520.

(136) Klein, A. R.; Thauer, R. K. *Eur. J. Biochem.* 1995, *227* (1–2), 169–174.

(137) Geierstanger, B. H.; Prasch, T.; Griesinger, C.; Hartmann, G.; Buurman, G.; Thauer, R. K. *Angew. Chem. Int. Ed.* 1998, *37* (23), 3300–3303.

(138) Berkessel, A. *Curr. Opin. Chem. Biol.* 2001, *5* (5), 486–490.

(139) Lyon, E. J.; Shima, S.; Buurman, G.; Chowdhuri, S.; Batschauer, A.; Steinbach, K.; Thauer, R. K. *Eur. J. Biochem.* 2004, *271* (1), 195–204.

(140) Shima, S.; Lyon, E. J.; Sordel-Klippert, M.; Kauß, M.; Kahnt, J.; Thauer, R. K.; Steinbach, K.; Xie, X.; Verdier, L.; Griesinger, C. *Angew. Chem. Int. Ed.* 2004, *43* (19), 2547–2551.

(141) Lyon, E. J.; Shima, S.; Boecher, R.; Thauer, R. K.; Grevels, F.-W.; Bill, E.; Roseboom, W.; Albracht, S. P. J. *J. Am. Chem. Soc.* 2004, *126* (43), 14239–14248.

(142) Shima, S.; Lyon, E. J.; Thauer, R. K.; Mienert, B.; Bill, E. *J. Am. Chem. Soc.* 2005, *127* (29), 10430–10435.

(143) Wang, X.; Li, Z.; Zeng, X.; Luo, Q.; Evans, D. J.; Pickett, C. J.; Liu, X. *Chem. Commun.* 2008, *0* (30), 3555.

(144) Salomone-Stagni, M.; Stellato, F.; Whaley, C. M.; Vogt, S.; Morante, S.; Shima, S.; Rauchfuss, T. B.; Meyer-Klaucke, W. *Dalt. Trans.* 2010, *39* (12), 3057–3064.

(145) Korbas, M.; Vogt, S.; Meyer-Klaucke, W.; Bill, E.; Lyon, E. J.; Thauer, R. K.; Shima, S. *J. Biol. Chem.* 2006, *281* (41), 30804–30813.

(146) Guo, Y.; Wang, H.; Xiao, Y.; Vogt, S.; Thauer, R. K.; Shima, S.; Volkers, P. I.; Rauchfuss, T. B.; Pelmenschikov, V.; Case, D. A.; et al. *Inorg. Chem.* 2008, *47* (10), 3969–3977.

(147) Shima, S.; Schick, M.; Kahnt, J.; Ataka, K.; Steinbach, K.; Linne, U. *Dalt. Trans.* 2012, *41* (3), 767–771.

(148) Shima, S.; Vogt, S.; Göbels, A.; Bill, E. *Angew. Chem. Int. Ed.* 2010, *49* (51), 9917–9921.

(149) Shima, S.; Ermler, U. *Eur. J. Inorg. Chem.* 2011, *2011* (7), 963–972.

(150) Hiromoto, T.; Warkentin, E.; Moll, J.; Ermler, U.; Shima, S. *Angew. Chem. Int. Ed.* 2009, *48* (35), 6457–6460.

(151) Tamura, H.; Salomone-Stagni, M.; Fujishiro, T.; Warkentin, E.; Meyer-Klaucke, W.; Ermler, U.; Shima, S. *Angew. Chem. Int. Ed.* 2013, *52* (37), 9656–9659.

(152) Yang, X.; Hall, M. B. *J. Am. Chem. Soc.* 2009, *131* (31), 10901–10908.

(153) Finkelmann, A. R.; Senn, H. M.; Reiher, M. *Chem. Sci.* 2014, *5* (11), 4474–4482.

(154) Stephan, D. W.; Erker, G. *Angew. Chem. Int. Ed.* 2010, *49* (1), 46–76.

(155) Royer, A. M.; Rauchfuss, T. B.; Gray, D. L. *Organometallics* 2009, *28* (13), 3618–3620.

(156) Royer, A. M.; Salomone-Stagni, M.; Rauchfuss, T. B.; Meyer-Klaucke, W. *J. Am. Chem. Soc.* 2010, *132* (47), 16997–17003.

(157) Fujishiro, T.; Kahnt, J.; Ermler, U.; Shima, S. *Nat. Commun.* 2015, *6* (1), 6895.

(158) Chen, D.; Scopelliti, R.; Hu, X. *Angew. Chem. Int. Ed.* 2011, *50* (25), 5671–5673.

(159) Hu, B.; Chen, D.; Hu, X. *Chem. - A Eur. J.* 2014, *20* (6), 1677–1682.

(160) Song, L.-C.; Xie, Z.-J.; Wang, M.-M.; Zhao, G.-Y.; Song, H.-B. *Inorg. Chem.* 2012, *51* (14), 7466–7468.

(161) Song, L.-C.; Hu, F.-Q.; Wang, M.-M.; Xie, Z.-J.; Xu, K.-K.; Song, H.-B. *Dalt. Trans.* 2014, *43* (21), 8062–8071.

(162) Song, L.-C.; Hu, F.-Q.; Zhao, G.-Y.; Zhang, J.-W.; Zhang, W.-W. *Organometallics* 2014, *33* (22), 6614–6622.

(163) Song, L.-C.; Zhao, G.-Y.; Xie, Z.-J.; Zhang, J.-W. *Organometallics* 2013, *32* (9), 2509–2512.

(164) Song, L.-C.; Zhu, L.; Hu, F.-Q.; Wang, Y.-X. *Inorg. Chem.* 2017, *56* (24), 15216–15230.

(165) Song, L.-C.; Xu, K.-K.; Han, X.-F.; Zhang, J.-W. *Inorg. Chem.* 2016, *55* (3), 1258–1269.

(166) Turrell, P. J.; Wright, J. A.; Peck, J. N. T.; Oganesyan, V. S.; Pickett, C. J. *Angew. Chem. Int. Ed.* 2010, *49* (41), 7508–7511.

(167) Turrell, P. J.; Hill, A. D.; Ibrahim, S. K.; Wright, J. A.; Pickett, C. J. *Dalt. Trans.* 2013, *42* (22), 8140–8146.

(168) Manes, T. A.; Rose, M. J. *Coord. Chem. Rev.* 2017, *353*, 295–308.

(169) Seo, J.; Manes, T. A.; Rose, M. J. *Nat. Chem.* 2017, *9* (6), 552–557.

(170) Kerns, S. A.; Magtaan, A.-C.; Vong, P. R.; Rose, M. J. *Angew. Chem. Int. Ed.* 2018, *57* (11), 2855–2858.

(171) Kalz, K. F.; Brinkmeier, A.; Dechert, S.; Mata, R. A.; Meyer, F. *J. Am. Chem. Soc.* 2014, *136* (47), 16626–16634.

(172) Barik, C. K.; Ganguly, R.; Li, Y.; Leong, W. K. *Inorg. Chem.* 2018, *57* (12), 7113–7120.

(173) Barik, C. K.; Ganguly, R.; Li, Y.; Przybylski, C.; Salmain, M.; Leong, W. K. *Inorg. Chem.* 2018, *57* (19), 12206–12212.

Chapter 2

(1) Kubas, G. J. *Chem. Rev.* 2007, *107* (10), 4152–5205.

(2) Kubas, G. J. *J. Organomet. Chem.* 2009, *694* (17), 2648–2653.

(3) Kubas, G. J. *J. Organomet. Chem.* 2001, *635* (1–2), 37–68.

(4) Schilter, D.; Camara, J. M.; Huynh, M. T.; Hammes-Schiffer, S.; Rauchfuss, T. B. *Chem. Rev.* 2016, *116* (15), 8693–8749.

(5) Shima, S.; Ermler, U. *Eur. J. Inorg. Chem.* 2011, *2011* (7), 963–972.

(6) Thauer, R. K.; Kaster, A.-K.; Goenrich, M.; Schick, M.; Hiromoto, T.; Shima, S. *Annu. Rev. Biochem.* 2010, *79* (1), 507–536.

(7) Yang, X.; Hall, M. B. *J. Am. Chem. Soc.* 2009, *131* (31), 10901–10908.

(8) Finkelmann, A. R.; Senn, H. M.; Reiher, M. *Chem. Sci.* 2014, *5* (11), 4474–4482.

(9) Hedegård, E. D.; Kongsted, J.; Ryde, U. *Angew. Chem. Int. Ed.* 2015, *54* (21), 6246–6250.

(10) Shima, S.; Chen, D.; Xu, T.; Wodrich, M. D.; Fujishiro, T.; Schultz, K. M.; Kahnt, J.; Ataka, K.; Hu, X. *Nat. Chem.* 2015, *7* (12), 995–1002.

(11) Chen, D.; Scopelliti, R.; Hu, X. *Angew. Chem. Int. Ed.* 2011, *50* (25), 5671–5673.

(12) Hu, B.; Chen, D.; Hu, X. *Chem. - A Eur. J.* 2014, *20* (6), 1677–1682.

(13) Seo, J.; Manes, T. A.; Rose, M. J. *Nat. Chem.* 2017, *9* (6), 552–557.

(14) Lenton, T. N.; VanderVelde, D. G.; Bercaw, J. E. *Organometallics* 2012, *31* (21), 7492–7499.

(15) Coe, B. J.; Glenwright, S. J. *Coord. Chem. Rev.* 2000, *203* (1), 5–80.

(16) Turrell, P. J.; Wright, J. A.; Peck, J. N. T.; Oganesyan, V. S.; Pickett, C. J. *Angew. Chem. Int. Ed.* 2010, *49* (41), 7508–7511.

(17) Muthiah, K. A. T.; Durgaprasad, G.; Xie, Z.-L.; Williams, O. M.; Joseph, C.; Lynch, V. M.; Rose, M. J. *Eur. J. Inorg. Chem.* 2015, *2015* (10), 1675–1691.

(18) McKinley, S. G.; Vecchi, P. A.; Ellern, A.; Angelici, R. J. *Dalt. Trans.* 2004, *0* (5), 788.

(19) Ortega-Alfaro, M. C.; Hernández, N.; Cerna, I.; López-Cortés, J. G.; Gómez, E.; Toscano, R. A.; Alvarez-Toledano, C. *J. Organomet. Chem.* 2004, *689* (5), 885–893.

(20) Lyon, E. J.; Shima, S.; Boecher, R.; Thauer, R. K.; Grevels, F.-W.; Bill, E.; Roseboom, W.; Albracht, S. P. J. *J. Am. Chem. Soc.* 2004, *126* (43), 14239–14248.

(21) Hiromoto, T.; Ataka, K.; Pilak, O.; Vogt, S.; Stagni, M. S.; Meyer-Klaucke, W.; Warkentin, E.; Thauer, R. K.; Shima, S.; Ermler, U. *FEBS Lett.* 2009, *583* (3), 585–590.

(22) Shima, S.; Schick, M.; Kahnt, J.; Ataka, K.; Steinbach, K.; Linne, U. *Dalt. Trans.* 2012, *41* (3), 767–771.

(23) Lubitz, W.; Ogata, H.; Rüdiger, O.; Reijerse, E. *Chem. Rev.* 2014, *114* (8), 4081–4148.

(24) Kalz, K. F.; Brinkmeier, A.; Dechert, S.; Mata, R. A.; Meyer, F. *J. Am. Chem. Soc.* 2014, *136* (47), 16626–16634.

(25) Dey, A. *J. Am. Chem. Soc.* 2010, *132* (39), 13892–13901.

(26) Shima, S.; Pilak, O.; Vogt, S.; Schick, M.; Stagni, M. S.; Meyer-Klaucke, W.; Warkentin, E.; Thauer, R. K.; Ermler, U. *Science* 2008, *321* (5888), 572–575.

(27) Waleh, A.; Loew, G. H. *J. Am. Chem. Soc.* 1982, *104* (12), 3513–3515.

(28) Nguyen, D. H.; Hsu, H.-F.; Millar, M.; Koch, S. A.; Achim, C.; Bominaar, E. L.; Münck, E. *J. Am. Chem. Soc.* 1996, *118* (37), 8963–8964.

(29) Tolman, C. A. *J. Am. Chem. Soc.* 1970, *92* (10), 2956–2965.

(30) Song, L.-C.; Gu, Z.-C.; Zhang, W.-W.; Li, Q.-L.; Wang, Y.-X.; Wang, H.-F. *Organometallics* 2015, *34* (16), 4147–4157.

(31) Garrett, B. R.; Awad, A.; He, M.; Click, K. A.; Durr, C. B.; Gallucci, J. C.; Hadad, C. M.; Wu, Y. *Polyhedron* 2016, *103*, 21–27.

(32) Chen, C.-H.; Chang, Y.-S.; Yang, C.-Y.; Chen, T.-N.; Lee, C.-M.; Liaw, W.-F. *Dalt. Trans.* 2004, *0* (1), 137–143.

(33) Whaley, C. M.; Rauchfuss, T. B.; Wilson, S. R. *Inorg. Chem.* 2009, *48* (10), 4462–4469.

(34) Zell, T.; Milko, P.; Fillman, K. L.; Diskin-Posner, Y.; Bendikov, T.; Iron, M. A.; Leitus, G.; Ben-David, Y.; Neidig, M. L.; Milstein, D. *Chem. - A Eur. J.* 2014, *20* (15), 4403–4413.

(35) Turrell, P. J.; Hill, A. D.; Ibrahim, S. K.; Wright, J. A.; Pickett, C. J. *Dalt. Trans.* 2013, *42* (22), 8140–8146.

(36) Dance, I.; Fisher, K. In *Progress in Inorganic Chemistry*; Kailin, K. D., Ed.; John Wiley & Sons, Ltd, 2007; pp 637–803.

(37) Bichler, B.; Holzhacker, C.; Stöger, B.; Puchberger, M.; Veiros, L. F.; Kirchner, K. *Organometallics* 2013, *32* (15), 4114–4121.

(38) Zuo, W.; Tauer, S.; Prokopchuk, D. E.; Morris, R. H. *Organometallics* 2014, *33* (20), 5791–5801.

(39) Langer, R.; Diskin-Posner, Y.; Leitus, G.; Shimon, L. J. W.; Ben-David, Y.; Milstein, D. *Angew. Chem. Int. Ed.* 2011, *50* (42), 9948–9952.

(40) Langer, R.; Iron, M. A.; Konstantinovski, L.; Diskin-Posner, Y.; Leitus, G.; Ben-David, Y.; Milstein, D. *Chem. - A Eur. J.* 2012, *18* (23), 7196–7209.

(41) Zell, T.; Butschke, B.; Ben-David, Y.; Milstein, D. *Chem. - A Eur. J.* 2013, *19* (25), 8068–8072.

(42) Zell, T.; Milstein, D. *Acc. Chem. Res.* 2015, *48* (7), 1979–1994.

(43) He, L.-P.; Chen, T.; Gong, D.; Lai, Z.; Huang, K.-W. *Organometallics* 2012, *31* (14), 5208–5211.

(44) He, L.-P.; Chen, T.; Xue, D.-X.; Eddaoudi, M.; Huang, K.-W. *J. Organomet. Chem.* 2012, *700*, 202–206.

(45) Rigaku Americas Corporation, The Woodlands, TX: Woodlands, TX, 2008.

(46) Agilent Technologies UK Ltd.: Oxford, UK, 2013.

(47) Palatinus, L.; Chapuis, G. *J. Appl. Crystallogr.* 2007, *40* (4), 786–790.

(48) Sheldrick, G. M. *Acta Crystallogr. Sect. A Found. Crystallogr.* 2008, *64* (1), 112–122.

(49) van der Sluis, P.; Spek, A. L. *Acta Crystallogr. Sect. A Found. Crystallogr.* 1990, *46* (3), 194–201.

(50) Spek, A. L. *Acta Crystallogr. Sect. D* 2009, *65* (2), 148–155.

(51) Farrugia, L. J. *J. Appl. Crystallogr.* 1999, *32* (4), 837–838.

(52) Granovsky, A. A. Firefly version 8 http://classic.chem.msu.su/gran/gamess/index.html.

(53) Schmidt, M. W.; Baldridge, K. K.; Boatz, J. A.; Elbert, S. T.; Gordon, M. S.; Jensen, J. H.; Koseki, S.; Matsunaga, N.; Nguyen, K. A.; Su, S.; et al. *J. Comput. Chem.* 1993, *14* (11), 1347–1363.

(54) Perdew, J. P.; Chevary, J. A.; Vosko, S. H.; Jackson, K. A.; Pederson, M. R.; Singh, D. J.; Fiolhais, C. *Phys. Rev. B* 1992, *46* (11), 6671–6687.

(55) Perdew, J. P.; Chevary, J. A.; Vosko, S. H.; Jackson, K. A.; Pederson, M. R.; Singh, D. J.; Fiolhais, C. *Phys. Rev. B* 1993, *48* (7), 4978–4978.

(56) Bode, B. M.; Gordon, M. S. *J. Mol. Graph. Model.* 1998, *16* (3), 133–138.

(57) Feller, D. *J. Comput. Chem.* 1996, *17* (13), 1571–1586.

(58) Schuchardt, K. L.; Didier, B. T.; Elsethagen, T.; Sun, L.; Gurumoorthi, V.; Chase, J.; Li, J.; Windus, T. L. *J. Chem. Inf. Model.* 2007, *47* (3), 1045–1052.

(59) Mitin, A. V.; Baker, J.; Pulay, P. *J. Chem. Phys.* 2003, *118* (17), 7775–7782.

(60) McGrath, M. P. *J. Chem. Phys.* 2009, *130* (17), 176101.

(61) Andrienko, G. A. Chemcraft http://www.chemcraftprog.com.

(62) Glendening, E. D.; Badenhoop, J. K.; Reed, A. E.; Carpenter, J. E.; Bohmann, J. A.; Morales, C. M.; Landis, C. R.; Weinhold, F. Theoretical Chemistry Institute, University of Wisconsin: Madison 2013.

Chapter 3

(1) Shima, S.; Pilak, O.; Vogt, S.; Schick, M.; Stagni, M. S.; Meyer-Klaucke, W.; Warkentin, E.; Thauer, R. K.; Ermler, U. *Science* 2008, *321* (5888), 572–575.

(2) Hiromoto, T.; Ataka, K.; Pilak, O.; Vogt, S.; Stagni, M. S.; Meyer-Klaucke, W.; Warkentin, E.; Thauer, R. K.; Shima, S.; Ermler, U. *FEBS Lett.* 2009, *583* (3), 585–590.

(3) Yang, X.; Hall, M. B. *J. Am. Chem. Soc.* 2009, *131* (31), 10901–10908.

(4) Chen, D.; Scopelliti, R.; Hu, X. *Angew. Chem. Int. Ed.* 2012, *51* (8), 1919–1921.

(5) Finkelmann, A. R.; Senn, H. M.; Reiher, M. *Chem. Sci.* 2014, *5* (11), 4474–4482.

(6) Chen, D.; Scopelliti, R.; Hu, X. *Angew. Chem. Int. Ed.* 2011, *50* (25), 5671–5673.

(7) Shima, S.; Chen, D.; Xu, T.; Wodrich, M. D.; Fujishiro, T.; Schultz, K. M.; Kahnt, J.; Ataka, K.; Hu, X. *Nat. Chem.* 2015, *7* (12), 995–1002.

(8) Muthiah, K. A. T.; Durgaprasad, G.; Xie, Z.-L.; Williams, O. M.; Joseph, C.; Lynch, V. M.; Rose, M. J. *Eur. J. Inorg. Chem.* 2015, *2015* (10), 1675–1691.

(9) Durgaprasad, G.; Xie, Z.-L.; Rose, M. J. *Inorg. Chem.* 2016, *55* (2), 386–389.

(10) Xie, Z.-L.; Durgaprasad, G.; Ali, A. K.; Rose, M. J. *Dalt. Trans.* 2017, *46* (33), 10814–10829.

(11) Kerns, S. A.; Magtaan, A.-C.; Vong, P. R.; Rose, M. J. *Angew. Chem. Int. Ed.* 2018, *57* (11), 2855–2858.

(12) Carlson, L. J.; Welby, J.; Zebrowski, K. A.; Wilk, M. M.; Giroux, R.; Ciancio, N.; Tanski, J. M.; Bradley, A.; Tyler, L. A. *Inorg. Chim. Acta* 2011, *365* (1), 159–166.

(13) Lynn, M. A.; Carlson, L. J.; Hwangbo, H.; Tanski, J. M.; Tyler, L. A. *J. Mol. Struct.* 2012, *1011*, 81–93.

(14) Lindoy, L. F. *Coord. Chem. Rev.* 1969, *4* (1), 41–71.

(15) Xu, H.-J.; Liang, Y.-F.; Cai, Z.-Y.; Qi, H.-X.; Yang, C.-Y.; Feng, Y.-S. *J. Org. Chem.* 2011, *76* (7), 2296–2300.

(16) Fu, Y.; Wang, J.-Y.; Zhang, D.; Chen, Y.-F.; Gao, S.; Zhao, L.-X.; Ye, F. *Molecules* 2017, *22* (10), 1601.

(17) Plant, D.; Tarbell, D. S.; Whiteman, C. *J. Am. Chem. Soc.* 1955, *77* (6), 1572–1575.

(18) C. Noveron, J.; Herradora, R.; Olmstead, M. M.; Mascharak, P. K. *Inorg. Chim. Acta* 1999, *285* (2), 269–276.

(19) Li, B.; Liu, T.; Popescu, C. V.; Bilko, A.; Darensbourg, M. Y. *Inorg. Chem.* 2009, *48* (23), 11283–11289.

(20) Lyon, E. J.; Shima, S.; Boecher, R.; Thauer, R. K.; Grevels, F.-W.; Bill, E.; Roseboom, W.; Albracht, S. P. J. *J. Am. Chem. Soc.* 2004, *126* (43), 14239–14248.

(21) El-Azhary, A. A.; Suter, H. U. *J. Phys. Chem.* 1996, *100* (37), 15056–15063.

(22) Turrell, P. J.; Wright, J. A.; Peck, J. N. T.; Oganesyan, V. S.; Pickett, C. J. *Angew. Chem. Int. Ed.* 2010, *49* (41), 7508–7511.

(23) Shima, S.; Schick, M.; Kahnt, J.; Ataka, K.; Steinbach, K.; Linne, U. *Dalt. Trans.* 2012, *41* (3), 767–771.

(24) Chen, D.; Scopelliti, R.; Hu, X. *Angew. Chem. Int. Ed.* 2010, *49* (41), 7512–7515.

(25) Hieber, W.; Bader, G. *Ber. Dtsch. Chem. Ges.* 1928, *61* (8), 1717–1722.

(26) Rigaku Americas Corporation, The Woodlands, TX: Woodlands, TX, 2008.

(27) Agilent Technologies UK Ltd.: Oxford, UK, 2013.

(28) Palatinus, L.; Chapuis, G. *J. Appl. Crystallogr.* 2007, *40* (4), 786–790.

(29) *Acta Crystallogr. Sect. A* 2008, *64* (1), 112–122.

(30) Spek, A. L. *Acta Crystallogr. Sect. D* 2009, *65* (2), 148–155.

(31) Farrugia, L. J. *J. Appl. Crystallogr.* 1999, *32* (4), 837–838.

(32) Frisch, M. J.; Trucks, G. W.; Schlegel, H. B.; Scuseria, G. E.; Robb, M. A.; Cheeseman, J. R.; Scalmani, G.; Barone, V.; Petersson, G. A.; Nakatsuji, H.; et al. Gaussian, Inc.: Wallingford, CT, 2009.

(33) Becke, A. D. *J. Chem. Phys.* 1993, *98* (7), 5648–5652.

(34) Stephens, P. J.; Devlin, F. J.; Chabalowski, C. F.; Frisch, M. J. *J. Phys. Chem.* 1994, *98* (45), 11623–11627.

(35) Dolg, M.; Wedig, U.; Stoll, H.; Preuss, H. *J. Chem. Phys.* 1987, *86* (2), 866–872.

(36) Hay, P. J.; Wadt, W. R. *J. Chem. Phys.* 1985, *82* (1), 270–283.

(37) Hay, P. J.; Wadt, W. R. *J. Chem. Phys.* 1985, *82* (1), 299–310.

(38) Krishnan, R.; Binkley, J. S.; Seeger, R.; Pople, J. A. *J. Chem. Phys.* 1980, *72* (1), 650–654.

(39) McLean, A. D.; Chandler, G. S. *J. Chem. Phys.* 1980, *72* (10), 5639–5648.

(40) National Institute of Standards and Technology. Computational Chemistry Comparison and Benchmark DataBase. https://cccbdb.nist.gov/vibscalejust.asp (accessed Apr 26, 2018).

(41) Gross, E. K. U.; Kohn, W. *Adv. Quantum Chem.* 1990, *21*, 255–291.

(42) Gross, E. K. U.; Dobson, J. F.; Petersilka, M. In *Density Functional Theory II. Topics in Current Chemistry, vol 181*; Nalewajski, R. F., Ed.; Springer, Berlin, Heidelberg, 1996; pp 81–172.

(43) Tomasi, J.; Mennucci, B.; Cammi, R. *Chem. Rev.* 2005, *105* (8), 2999–3094.

(44) Dennington, R.; Keith, T.; Millam, J. Semichem Inc.: Shawnee Mission, KS, 2009.

(45) Lindoy, L. F.; Livingstone, S. E. *Inorg. Chim. Acta* 1967, *1*, 365–370.

Chapter 4

(1) Santhanam, K. S. V.; Press, R. J.; Miri, M. J.; Bailey, A. V.; Takacs, G. A. *Introduction to Hydrogen Technology*, 2nd ed.; Wiley: Hoboken, 2017.

(2) Momirlan, M.; Veziroglu, T. . *Renew. Sustain. Energy Rev.* 2002, *6* (1–2), 141–179.

(3) Zhang, F.; Zhao, P.; Niu, M.; Maddy, J. *Int. J. Hydrogen Energy* 2016, *41* (33), 14535–14552.

(4) Møller, K. T.; Jensen, T. R.; Akiba, E.; Li, H. *Prog. Nat. Sci. Mater. Int.* 2017, *27* (1), 34–40.

(5) U. S. DRIVE Partnership. *Hydrogen Production Technical Team Roadmap*; 2017.

(6) Holladay, J. D.; Hu, J.; King, D. L.; Wang, Y. *Catal. Today* 2009, *139* (4), 244–260.

(7) Lubitz, W.; Ogata, H.; Rüdiger, O.; Reijerse, E. *Chem. Rev.* 2014, *114* (8), 4081–4148.

(8) Schilter, D.; Camara, J. M.; Huynh, M. T.; Hammes-Schiffer, S.; Rauchfuss, T. B. *Chem. Rev.* 2016, *116* (15), 8693–8749.

(9) Evans, D. J.; Pickett, C. J. *Chem. Soc. Rev.* 2003, *32* (5), 268–275.

(10) Shima, S.; Pilak, O.; Vogt, S.; Schick, M.; Stagni, M. S.; Meyer-Klaucke, W.; Warkentin, E.; Thauer, R. K.; Ermler, U. *Science* 2008, *321* (5888), 572–575.

(11) Hiromoto, T.; Ataka, K.; Pilak, O.; Vogt, S.; Stagni, M. S.; Meyer-Klaucke, W.; Warkentin, E.; Thauer, R. K.; Shima, S.; Ermler, U. *FEBS Lett.* 2009, *583* (3), 585–590.

(12) Yang, X.; Hall, M. B. *J. Am. Chem. Soc.* 2009, *131* (31), 10901–10908.

(13) Finkelmann, A. R.; Senn, H. M.; Reiher, M. *Chem. Sci.* 2014, *5* (11), 4474–4482.

(14) Bichler, B.; Holzhacker, C.; Stöger, B.; Puchberger, M.; Veiros, L. F.; Kirchner, K. *Organometallics* 2013, *32* (15), 4114–4121.

(15) Gorgas, N.; Stöger, B.; Veiros, L. F.; Pittenauer, E.; Allmaier, G.; Kirchner, K. *Organometallics* 2014, *33* (23), 6905–6914.

(16) Langer, R.; Diskin-Posner, Y.; Leitus, G.; Shimon, L. J. W.; Ben-David, Y.; Milstein, D. *Angew. Chem. Int. Ed.* 2011, *50* (42), 9948–9952.

(17) Langer, R.; Leitus, G.; Ben-David, Y.; Milstein, D. *Angew. Chem. Int. Ed.* 2011, *50* (9), 2120–2124.

(18) Langer, R.; Iron, M. A.; Konstantinovski, L.; Diskin-Posner, Y.; Leitus, G.; Ben-David, Y.; Milstein, D. *Chem. - A Eur. J.* 2012, *18* (23), 7196–7209.

(19) Zell, T.; Ben-David, Y.; Milstein, D. *Angew. Chem. Int. Ed.* 2014, *53* (18), 4685–4689.

(20) Mazza, S.; Scopelliti, R.; Hu, X. *Organometallics* 2015, *34* (8), 1538–1545.

(21) Chen, D.; Scopelliti, R.; Hu, X. *Angew. Chem. Int. Ed.* 2011, *50* (25), 5671–5673.

(22) Hu, B.; Chen, D.; Hu, X. *Chem. - A Eur. J.* 2014, *20* (6), 1677–1682.

(23) Xu, T.; Yin, C.-J. M.; Wodrich, M. D.; Mazza, S.; Schultz, K. M.; Scopelliti, R.; Hu, X. *J. Am. Chem. Soc.* 2016, *138* (10), 3270–3273.

(24) Turrell, P. J.; Hill, A. D.; Ibrahim, S. K.; Wright, J. A.; Pickett, C. J. *Dalt. Trans.* 2013, *42* (22), 8140–8146.

(25) Turrell, P. J.; Wright, J. A.; Peck, J. N. T.; Oganesyan, V. S.; Pickett, C. J. *Angew. Chem. Int. Ed.* 2010, *49* (41), 7508–7511.

(26) Shima, S.; Chen, D.; Xu, T.; Wodrich, M. D.; Fujishiro, T.; Schultz, K. M.; Kahnt, J.; Ataka, K.; Hu, X. *Nat. Chem.* 2015, *7* (12), 995–1002.

(27) Durgaprasad, G.; Xie, Z.-L.; Rose, M. J. *Inorg. Chem.* 2016, *55* (2), 386–389.

(28) Seo, J.; Manes, T. A.; Rose, M. J. *Nat. Chem.* 2017, *9* (6), 552–557.

(29) Kerns, S. A.; Magtaan, A.-C.; Vong, P. R.; Rose, M. J. *Angew. Chem. Int. Ed.* 2018, *57* (11), 2855–2858.

(30) Schroeder-Holzhacker, C.; Stoeger, B.; Pittenauer, E.; Allmaier, G. G.; Veiros, L. F.; Kirchner, K.; Schröder-Holzhacker, C.; Stöger, B.; Pittenauer, E.; Allmaier, G. G.; et al. *Monatsh. Chem.* 2016, *147* (9), 1539–1545.

(31) Holzhacker, C.; Stoeger, B.; Carvalho, M. D.; Ferreira, L. P.; Pittenauer, E.; Allmaier, G.; Veiros, L. F.; Realista, S.; Gil, A.; Calhorda, M. J.; et al. *Dalt. Trans.* 2015, *44* (29), 13071–13086.

(32) Lackner-Warton, W.; Tanaka, S.; Standfest-Hauser, C. M.; Oeztopcu, O.; Hsieh, J.-C.; Mereiter, K.; Kirchner, K. *Polyhedron* 2010, *29* (16), 3097–3102.

(33) Gorgas, N.; Stöger, B.; Veiros, L. F.; Kirchner, K. *ACS Catal.* 2016, *6* (4), 2664–2672.

(34) Mastalir, M.; Glatz, M.; Gorgas, N.; Stöger, B.; Pittenauer, E.; Allmaier, G.; Veiros, L. F.; Kirchner, K. *Chem. - A Eur. J.* 2016, *22* (35), 12316–12320.

(35) Bertini, F.; Gorgas, N.; Stöger, B.; Peruzzini, M.; Veiros, L. F.; Kirchner, K.; Gonsalvi, L. *ACS Catal.* 2016, *6* (5), 2889–2893.

(36) Huber, R.; Passera, A.; Mezzetti, A. *Organometallics* 2018, *37* (3), 396–405.

(37) Tolman, C. A. *Chem. Rev.* 1977, *77* (3), 313–348.

(38) Robert H. Crabtree. In *The Organometallic Chemistry of the Transition Metals*; John Wiley & Sons, Inc.: Hoboken, NJ, USA, 2005; pp 87–124.

(39) Gorgas, N.; Alves, L. G.; Stöger, B.; Martins, A. M.; Veiros, L. F.; Kirchner, K. *J. Am. Chem. Soc.* 2017, *139* (24), 8130–8133.

(40) Benito-Garagorri, D.; Becker, E.; Wiedermann, J.; Lackner, W.; Pollak, M.; Mereiter, K.; Kisala, J.; Kirchner, K. *Organometallics* 2006, *25* (8), 1900–1913.

(41) Hale, L. V. A.; Szymczak, N. K. *ACS Catal.* 2018, *8* (7), 6446–6461.

(42) Xie, Z.-L.; Durgaprasad, G.; Ali, A. K.; Rose, M. J. *Dalt. Trans.* 2017, *46* (33), 10814–10829.

(43) Nakahara, Y.; Toda, T.; Kuwata, S. *Polyhedron* 2018, *143*, 105–110.

(44) Aloisi, A.; Berthet, J.-C.; Genre, C.; Thuéry, P.; Cantat, T. *Dalt. Trans.* 2016, *45* (37), 14774–14788.

(45) Sui-Seng, C.; Freutel, F.; Lough, A. J.; Morris, R. H. *Angew. Chem. Int. Ed.* 2008, *47* (5), 940–943.

(46) Zell, T.; Ben-David, Y.; Milstein, D. *Catal. Sci. Technol.* 2015, *5* (2), 822–826.

(47) Li, H.; Zheng, B.; Huang, K.-W. *Coord. Chem. Rev.* 2015, *293–294*, 116–138.

(48) Kalz, K. F.; Brinkmeier, A.; Dechert, S.; Mata, R. A.; Meyer, F. *J. Am. Chem. Soc.* 2014, *136* (47), 16626–16634.

(49) Wenrui Chai. University of Texas at Austin, 2019.

(50) Coe, B. J.; Glenwright, S. J. *Coord. Chem. Rev.* 2000, *203* (1), 5–80.

(51) Ouali, A.; Majoral, J.-P.; Caminade, A.-M.; Taillefer, M. *ChemCatChem* 2009, *1* (4), 504–509.

(52) Clapham, S. E.; Hadzovic, A.; Morris, R. H. *Coord. Chem. Rev.* 2004, *248* (21–24), 2201–2237.

(53) Wiedner, E. S.; Chambers, M. B.; Pitman, C. L.; Bullock, R. M.; Miller, A. J.; Appel, A. M. *Chem. Rev.* 2016, *116* (15), 8655–8692.

(54) Agilent Technologies UK Ltd.: Oxford, UK, 2013.

(55) Palatinus, L.; Chapuis, G. *J. Appl. Crystallogr.* 2007, *40* (4), 786–790.

(56) *Acta Crystallogr. Sect. A* 2008, *64* (1), 112–122.

(57) Spek, A. L. *Acta Crystallogr. Sect. D* 2009, *65* (2), 148–155.

(58) Farrugia, L. J. *J. Appl. Crystallogr.* 1999, *32* (4), 837–838.

(59) Frisch, M. J.; Trucks, G. W.; Schlegel, H. B.; Scuseria, G. E.; Robb, M. A.; Cheeseman, J. R.; Scalmani, G.; Barone, V.; Petersson, G. A.; Nakatsuji, H.; et al. Gaussian, Inc.: Wallingford, CT, 2009.

(60) Adamo, C.; Barone, V. *J. Chem. Phys.* 1999, *110* (13), 6158.

(61) Ernzerhof, M.; Scuseria, G. E. *J. Chem. Phys.* 1999, *110* (11), 5029.

(62) Veillard, A. *Quantum Chemistry: The Challenge of Transition Metals and Coordination Chemistry*; Veillard, A., Ed.; Springer Netherlands: Dordrecht, 1986.

(63) Dolg, M.; Wedig, U.; Stoll, H.; Preuss, H. *J. Chem. Phys.* 1987, *86* (2), 866–872.

(64) Ditchfield, R.; Hehre, W. J.; Pople, J. A. *J. Chem. Phys.* 1971, *54* (2), 724–728.

(65) Hehre, W. J.; Ditchfield, R.; Pople, J. A. *J. Chem. Phys.* 1972, *56* (5), 2257–2261.

(66) Francl, M. M.; Pietro, W. J.; Hehre, W. J.; Binkley, J. S.; Gordon, M. S.; DeFrees, D. J.; Pople, J. A. *J. Chem. Phys.* 1982, *77* (7), 3654–3665.

(67) Blöchl, P. E. *Phys. Rev. B* 1994, *50* (24), 17953–17979.

(68) Tasker, P. W. *J. Phys. C Solid State Phys.* 1979, *12* (22), 4977–4984.

(69) Henkelman, G.; Uberuaga, B. P.; Jónsson, H. *J. Chem. Phys.* 2000, *113* (22), 9901–9904.

(70) Trygubenko, S. A.; Wales, D. J. *J. Chem. Phys.* 2004, *120* (5), 2082–2094.

(71) Nørskov, J. K.; Bligaard, T.; Logadottir, A.; Kitchin, J. R.; Chen, J. G.; Pandelov, S.; Stimming, U. *J. Electrochem. Soc.* 2005, *152* (3), J23–J26.